Titre: Title:	Synthesis and their Theranostic Applications of Plasmonic Gold-Silver Alloy Nanoparticles and Porous Nanostructures
Auteur: Author:	Lu Wang
Date:	2021
Type:	Mémoire ou thèse / Dissertation or Thesis
Référence: Citation:	Wang, L. (2021). Synthesis and their Theranostic Applications of Plasmonic Gold-Silver Alloy Nanoparticles and Porous Nanostructures [Thèse de doctorat, Polytechnique Montréal]. PolyPublie. https://publications.polymtl.ca/9950/

POLYTECHNIQUE MONTRÉAL

affiliée à l'Université de Montréal

Synthesis and their Theranostic Applications of Plasmonic Gold-Silver Alloy Nanoparticles and Porous Nanostructures

LU WANG

Département de génie Physique

Thèse présentée en vue de l'obtention du diplôme de *Philosophiae Doctor*

Génie des matériaux

Novembre 2021

POLYTECHNIQUE MONTRÉAL

affiliée à l'Université de Montréal

Cette thèse intitulée :

Synthesis and their Theranostic Applications of Plasmonic Gold-Silver Alloy Nanoparticles and Porous Nanostructures

présentée par **Lu WANG**

en vue de l'obtention du diplôme de *Philosophiae Doctor*

a été dûment acceptée par le jury d'examen constitué de :

Ludvik MARTINU, président
Michel MEUNIER, membre et directeur de recherche
Frédéric LEBLOND, membre
Dongling MA, membre externe

DEDICATION

To my family and Siyu

ACKNOWLEDGEMENTS

Foremost, I would like to thank my supervisor, Prof. Michel Meunier, for his valuable guidance and unconditional support during my study. I am grateful for his trust and patience and I appreciate for offering me the great opportunity to study and develop myself in LP^2L.

I would like to extend my sincere thanks to Prof. Ludvik Martinu, Prof. Dongling Ma, Prof. Frédéric Leblond for accepting being members of my thesis committee and offering their time and efforts. I wish to acknowledge the financial support from the Natural Sciences and Engineering Research Council of Canada.

I have been fortunate to be part of the supportive and cheerful group of LP2L. I would like to thank all my colleagues who gave me help and support: Dr. Sergiy Patskovsky, Cécile Darviot, Jennyfer Zapata-Farfan, Leonidas Agiotis, Isabelle Largillière, Dr. Morteza Hasanzadeh Kafshgari, Yves Drolet, David Rioux, Mengjiao Qi, Audrey Nsamela, Paule Marcoux-Valiquette and the rest members of our group. The group members of LP2L are like my family in Canada, encouraging me to continue my journey.

I am exceptionally grateful to my close friends, Lianjia Wu, Rui Tao, and Liyuan Ge for their continuous support. Special thanks to my parents, brother, and grandparents for their unconditional support and care. The completion of my dissertation would not have been possible without the support and nurturing of all of you. Finally, I would like to express my love and appreciation to my boyfriend, Siyu Tu. Thanks for the unparalleled support on my study and life during the most difficult time.

RÉSUMÉ

La recherche sur les nanoparticules (NP) métalliques plasmoniques est florissante au cours des dernières décennies. Parmi les NP plasmoniques, les NPs d'or (Au) et d'argent (Ag) et d'autres métaux nobles sont les plus étudiées en raison de leurs propriétés optiques exceptionnelles et de leur polyvalence. Leur interaction avec la lumière, la diffusion et la concentration de la lumière à proximité de la particule augmentent leur contraste sous illumination, ainsi que l'amélioration du champ de surface proche a permis la détectabilité dans le champ proche. Ces propriétés uniques peuvent promouvoir et permettre des applications dans divers domaines, notamment l'imagerie et la détection biomédicales, le domaine énergétique pour les cellules solaires et les catalyseurs ainsi que le stockage et le cryptage d'informations.

Certes, les NPs Au et Ag ont été exploitées dans diverses applications, tandis que leur alliage avec une autre dimension d'ajustabilité offre plus d'opportunités. Le rapport de composition réglable permet des propriétés optiques réglables, résultant directement en des couleurs contrôlables, et peut être appliqué pour la construction de structures plus complexes. Sur la base de la dépendance structurelle des propriétés optiques, diverses nanostructures et le contrôle de la synthèse ont été explorés. Les NP plus grandes (> 50 nm) avec une forte diffusion et une capacité d'amélioration ont été synthétisées par notre précédent collègue David Rioux, ce qui a ouvert la voie à leur utilisation en imagerie et potentiellement pour d'autres applications. Sur la base de l'approche de synthèse déjà publiée, il y a plus d'optimisation à faire pour un contrôle fin, ce qui facilite des applications plus pratiques. En outre, l'applicabilité de l'imagerie doit être prouvée dans des diagnostics pratiques tels que des tests de cytopathologie clinique. De plus, les NP Au-Ag de dimension et de composition ajustables contiennent un potentiel beaucoup plus important dans la construction de structures irrégulières, ce qui peut apporter des propriétés plus sophistiquées et une plus grande multifonctionnalité. L'amélioration du champ est la propriété la plus attendue des NP plasmoniques, et l'amélioration amplifie fortement le signal du champ proche, ce qui entraînerait des sondes ou des détecteurs sensibles.

Cette thèse porte sur l'optimisation de la synthèse de NPs d'alliages Au-Ag, et les applications de multiplexage des NPs solides, explorer la spectroscopie Raman exaltée en surface (SERS) par la

conception de la structure avec des NPs d'alliage Au-Ag et leur potentiel pour une plateforme multifonctionnelle.

La première partie de cette thèse se concentre sur l'optimisation de la synthèse à travers l'étude du mécanisme détaillé de croissance et de coréduction ensemencées d'Au-Ag. Pour faciliter une application ultérieure, l'approche de synthèse standard et le contrôle précis de la taille et de la composition doivent être effectués. Certaines modifications ont été apportées en analysant différents paramètres de réaction et la cinétique du processus depuis la fabrication des germes jusqu'aux étapes de croissance. Des étapes multiples à chaque étape de croissance, la modification de l'ordre d'ajout du sel métallique et de l'agent réducteur, ainsi qu'une configuration automatique ont été proposées et testées. La taille des NP d'alliages synthétisés entraîne une distribution encore plus étroite 10 % comparée avec 15 % que celles publiées précédemment, et l'approche proposée améliore la reproductibilité et l'automatisation du processus, facilitant des applications plus larges.

Les NP Au-Ag contrôlées avec précision ont été appliquées comme biomarqueurs chromatiques pour l'imagerie multiplexée avec des échantillons cellulaires. Selon le composant d'éclairage latéral LED rouge-vert-bleu (RVB), les NP Au-Ag ont été conçues sur la base de la théorie de Mie pour des pics de diffusion parallèles avec éclairage et pour trois milieux représentatifs, avec un indice de réfraction différent, pour différentes situations pratiques. Selon les résultats conçus, les NP Au-Ag ont été synthétisées pour les NP vertes et bleues pour trois milieux, et les nanobâtons Au sont choisies pour les rouges. Pour équilibrer l'intensité de trois couleurs dans chaque support, la taille et la composition des alliages NP et la dimension des nanobâtons sont délicatement ajustées. Pour éviter l'oxydation de l'Ag, la composition en Ag des NP bleues est limitée à 90 %, et les 10 % d'Au améliorent grandement la stabilité des NP. Avec l'éclairage LED économique qui peut être facilement installé avec des microscopes optiques courants, les échantillons cellulaires marqués NPs ont prouvé l'imagerie rapide et directe, avec un grand contraste de biomarqueurs chromatiques et une morphologie cellulaire claire. Cette application de multiplexage facilite l'application des NPs plasmoniques dans la cytopathologie pratique traditionnelle, et l'approche présente un potentiel pour des diagnostics quantitatifs et même numériques.

Le sondage SERS basé sur Au-Ag a été exploré, et les NPs poreuses Au-Ag se sont avérées être la solution. Les NPs poreuses sont synthétisées par réaction de remplacement galvanique à partir d'alliages solides préalablement synthétisés et de précurseurs de NPs. Les NPs sont conçues avec

un noyau Au ou Ag pour obtenir des NPs poreux avec un noyau solide ou un intérieur creux, respectivement. Le processus de désalliage a été étudié en détails de la structure aux propriétés optiques pour des solutions colloïdales et des NPs poreuses seuls. La structure ajustable et les propriétés optiques sont contrôlées par la composition de l'enveloppe en alliage des précurseurs NPs et des réactifs de désalliage. Un pic de plasmon décalé vers le rouge, une surface rugueuse et une densité élevée de points chauds avec des amplifications de champ localisées, ainsi que des structures de pores, ont créé d'excellents substrats multifonctionnels avec un facteur d'amplification élevé, une capacité de charge de médicaments améliorée et une biocompétence. L'extraordinaire activité Raman permet même le niveau de détection d'une particule unique et la surveillance quantitative du médicament chargé, offrant ainsi une plate-forme multifonctionnelle prometteuse pour le diagnostic et la thérapeutique, connue sous le nom de théranostic.

Principalement, cette thèse explore l'optimisation de la synthèse des NPs d'alliage Au-Ag et leur application pratique en tant que biomarqueurs dans le diagnostic. Les NPs Au-Ag structurées poreuses ont été proposées comme sondes SERS au niveau d'une seule particule, et avec la capacité de charge de médicament, elles fournissent une plate-forme théranostique multifonctionnelle potentielle. L'ajustabilité et les propriétés optiques des NPs en alliage Au-Ag incitent à davantage d'applications en biomédecine et dans d'autres domaines.

ABSTRACT

The research on plasmonic-metal nanoparticles (NPs) is thriving during the last several decades. Among plasmonic NPs, gold (Au) and silver (Ag) NPs and other noble metals are the most studied due to their exceptional optical properties and versatility. Indeed, upon their interaction with light, strong scattering and concentration of light near the particle can boost their contrast in imaging, as well as the near surface field enhancement enabled the detectability in the near field. These unique properties can promote and enable applications in diverse fields, including biomedical imaging and sensing, energy for solar cells and catalysts as well as information storage and encryption.

Even if Au and Ag NPs have been exploited in various applications, the synthesis of their alloys open up another dimension of adjustability, thus offering more opportunities. Indeed, the regulatable composition ratio enables tunable optical properties, directly resulting in controllable colors, and can be applied for more complexed structure building. Based on the structure dependence of optical properties, various nanostructures and the control of synthesis have been explored. The larger (> 50 nm) NPs with strong scattering and enhancing ability has been synthesized by our previous colleague David Rioux, which opened the window for the new strategies in imaging and other applications. Based on the published synthesis approach, more optimization is needed for finely control the process and nanostructures propreties, thus facilitating more practical applications. Indeed, for example, the imaging applicability has to be proven in practical diagnostics such as clinical cytopathology tests. Moreover, the Au-Ag NPs with adjustable dimension and composition contain much greater potential in irregular structure building, which may bring more unique properties and multifunctionality. In addition, the field enhancement is the most anticipated property of the plasmonic NPs, and the enhancement strongly amplifies the signal from near field, which would result in sensitive probes or detectors.

This thesis focuses on the optimization of Au-Ag alloy NPs synthesis, and the multiplexing applications of the solid NPs; exploring surface enhanced Raman spectroscopy (SERS) probing by structural design with Au-Ag alloy NPs and their potential for multifunctional platform.

The first part of this thesis focuses on the optimization the synthesis through studying the detailed mechanism of seeded growth and coreduction of Au-Ag. To facilitate further applications, the standard synthesis approach and the precise control on the size and composition has been developed in details. Some modification has been brought up by analysing different reaction parameters, and

the kinetics of the process from seeds fabrication to the growth stages. Multistep in each growth stage, changing the addition order of metal salt and reducing agent, as well as automatic setup have been proposed and tested. The size of synthesized alloy NPs results in even narrower distribution to even 10 %-12 % standard deviation than 15 % of the previously published ones, and the proposed approach improves reproducibility and automation of the process, facilitating broader applications.

The precisely controlled Au-Ag NPs have been applied as chromatic biomarkers for multiplexing imaging with cell samples. According to the red-green-blue (RGB) LED side-illumination component, the Au-Ag NPs have been designed based on Mie theory for parallel scattering peaks with illumination, and for three representative media, with different refractive index, for different practical situations. According to the designed results, Au-Ag NPs have been synthesized for green and blue NPs for three media, and Au nanorods are chosen for the red ones. To balance the intensity of three colors in each medium, the size and composition of alloy NPs and the dimension of nanorods are delicately adjusted. To avoid the oxidation of Ag, the Ag composition in blue NPs is restricted to 90 %, and the 10 % of Au greatly improves the stability of NPs. With the cost-effective LED illumination which can be easily installed with common optical microscopes, the NPs labeled cell samples have proved the fast and direct imaging, with great contrast of chromatic biomarkers and clear cell morphology. This multiplexing application facilitates the application of plasmonic NPs in traditional practical cytopathology, and the approach exhibit potential for quantitative and even digital diagnostics.

The Au-Ag based SERS probing has been explored by developing porous Au-Ag NPs. These particular nanostructures are synthesized through galvanic replacement reaction from previously synthesized solid alloy NPs and NP-precursors. The NPs are designed with Au or Ag core to attain porous NPs with solid core or hollow interior, respectively. The dealloying process have been studied thoroughly from structure to optical properties, and from colloidal to single NP. The adjustable structure and optical properties are controlled by the composition of alloy shell of NP-precursors and dealloying reagents. Red-shifted plasmon peak, rough surface and high density of hot spots with localized field enhancements, as well as pore structures, have created great multifunctional substrates with high enhancement factor, improved drug loading capacity and bio competency. The extraordinary Raman activity even enables the single-particle level of sensing,

and quantitative monitoring of loaded drug, providing promising multifunctional platform for diagnostics and therapeutics, which are known as theranostics.

Principally, this thesis explores the optimization of Au-Ag alloy NPs synthesis, and practical application as biomarkers in diagnostics. The porous structured Au-Ag NPs have been proposed as SERS probes at single-particle level, and with the drug loading capacity, they provide potential multifunctional theranostic platform. The adjustability and optical properties of Au-Ag alloy NPs prompt more application in biomedicine and other fields.

TABLE OF CONTENTS

LIST OF TABLES

LIST OF FIGURES

LIST OF SYMBOLS AND ABBREVIATIONS

This list presents the symbols and abbreviations used in the thesis or dissertation in alphabetical order, along with their meanings. Examples:

CTAB	Cetyltrimethylammonium bromide
CSI	Circular side-illumination
DFM	Dark field microscopy
DOX	Doxorubicin
FDTD	Finite difference time domain
FEM	Finite element methods
FWHM	Full width at half maximum
GRR	Galvanic replacement reaction
HAADF	High-angle annular dark field
HRTEM	High-resolution transmission electron microscopy
K_H	Release constant for Higuchi model
LED	Light-emitting diode
LSPR	Localized surface plasmon resonance
MM	Vectashield mounting medium
NA	Numerical aperture
NIR	Near infrared
NP	Nanoparticle
PA	Photoacoustic
PEDOT:PSS	Poly(3,4-ethylenedioxythiophene)-poly(styrenesulfonate)
PBS	Phosphate-buffered saline
RGB	Red-green-blue

RI	Refractive index(es)
SEF	Surface-enhanced fluorescence
SERS	Surface-enhanced Raman spectroscopy
SHE	Standard hydrogen electrode
STEM	Scanning transmission electron microscopy
NaCit	Sodium citrate
TEM	Transmission electron microscopy
UV	Ultraviolet

LIST OF APPENDICES

CHAPTER 1 INTRODUCTION

In recent decades, plasmonic nanomaterials are attracting enormous attention due to their unique optical properties, which allow the plasmonic NPs applied in energy and information technology, as well as in the biomedical field.[1, 2] The interaction between the incident light and plasmonic nanoparticles (NPs) generates the oscillation of collective electrons, and when the oscillation of free electrons reaches resonance, the localized surface plasmon resonance (LSPR) induces strong absorption, scattering, and surface enhancement.[3] The LSPR properties are dependent on the dimension, morphology, composition, as well as surrounding medium of plasmonic NPs. The optical properties make plasmonic NPs stand out in theranostics, which integrates both diagnostics and therapeutics, and have been the most urgent tasks for the health of human beings.[4, 5] With the increasing burden of cancer, and the accurate and efficient treatment requirements, theranostics has become a trend for the next generation of personalized medicine.[6] To have *in situ* guide for the surgery, enable targeting treatment, and monitor the response during treatment, the platforms with therapeutic potential have attracted much attention, such as the ones with bioimaging, biosensing, photothermal, or delivery abilities.[7] Plasmonic NPs stand out with their unique optical properties, as well as their flexible design. The intrinsic large scattering intensity and high field enhancement empower the contrast of biomarker and sensitivity of biosensing. Moreover, the photothermal properties and the adjustable plasmonic peak enlarges the possibility for various conditions. For example, the absorption in the transparent biological window, in near-infrared (NIR) range, and structural design for high loading capacity, can be addressed by the high flexibility of plasmonic nanostructures.

The development of nanotechnology has accelerated the progress of plasmonics. The design on intrinsic size, structure, and composition of NPs has introduced vast possibilities and high flexibility of LSPR properties, and the exploited different plasmonic peaks and surface enhancement behavior has been employed in various applications.[8] Among the plasmonic particles, the structure diversifies vastly at nanoscale. Besides the most common spherical NPs, nanorods, nanotriangles, nanocubes, and many non-spherical structures are invented. Due to the high sensitivity to dimension, morphology, and composition, plasmonic NPs require well-control and high monodisperses for appropriate properties, as well as applicability. The controllable synthesis becomes important for the LSPR properties. Liquid-phase synthesis is more robust

among all the approaches since flexible conditions in liquid-phase synthesis can easily adjust the size and structure of NPs, and the colloidal synthesis requires no special equipment and can scale up for cost-efficient and wide applications.[9] Controllable liquid-phase synthesis determines the properties of plasmonic NPs, and the ease of further applications.

Different from the flexibility in size and structure, the plasmonic materials are relatively limited. Although semiconductor crystals, two-dimension materials, and some conductive polymers show plasmonic properties, metallic materials are still dominant in plasmonics due to their mature theory and versatile synthesis approaches.[10] Noble metals such as Au and Ag have strong plasmonic effects in visible-near infrared wavelength, which is the most interesting range in research and applications. Due to the chemical stability and biocompatibility, Au is the most widely accepted plasmonic materials. While Ag exhibits the strongest plasmonic effects in visible range, which is valuable for the application. Moreover, their similar lattice constants and crystal structures allow the Au-Ag alloy in arbitrary composition. Therefore, Au-Ag alloy provides flexibility in composition, and the compositional dependence of plasmonics allows the alloy to generate plasmonic peaks adjustable between pure Au and Ag. Combining with the adjustable plasmonic resonance, ease to be functionalized and multifunctionality facilitates the application of Au-Ag alloy NPs in diagnostic and therapy.

Despite the great advantages of Au-Ag alloy NPs, the exploration on the structure based on the alloy and their applications are still limited. The control in colloidal synthesis, design of more structures of Au-Ag alloy NPs and their biomedical applications become the research topic of this doctorate thesis.

1.1 Problems and hypothesis

In this doctorate thesis, the focus is on Au-Ag alloy nanoparticles, including understanding and optimizing the synthesis, designing nanostructures, and exploring their biomedical applications. The research establishes three parts of the study based on Au-Ag alloy NPs.

First, it is essential to understand the synthesis of spherical Au-Ag alloy NPs and control the process. Thermodynamics and kinetics during the co-reduction and seeded-growth get complicated. The study will help with the well-controlled size, composition, and spherical morphology of Au-

Ag alloy NPs, thus regulating their plasmonic properties. To establish practical applications, the plasmonic properties should be well-defined, and at the same time, reproducible synthesis is crucial. Colloidal synthesis eases the modification of parameters in the reaction, providing flexible synthesis conditions, and the modification and optimization allow precise control and great quality. Automation in the process is introduced to eliminate the variance from human factors and benefit quality control for large-scale fabrication.

Then, to advance the potential applications of Au-Ag alloy NPs with their outstanding plasmonic properties, it is important to establish their use in facile and efficient ways. The adjustable size and composition of spherical alloy NPs provide biomarkers with tunable plasmon peaks as well as optical efficiency. The optical properties can be easily adjusted for various biological mounting mediums, suitable for diverse situations. Au-Ag alloy NPs implemented as multiplexing biomarkers will vastly improve the efficiency of bioimaging in pathology. Besides, the implementation compatible with the biomarkers is essential in clinical application, for example, the sample preparation in various situations and customized illumination for observation.

Finally, Au-Ag alloy creates more possibilities for various nanostructures, due to the different reduction potentials of the two components. Flexible colloidal synthesis manages to provide templates with various compositions and adjustable distribution. Dealloying through the deliberated rection will generate the controllable porous structure, which provides the large rough surface and hollow interior, thus inducing a shift of plasmonic peaks and a high density of “hot spots”. The porous Au-Ag structure is supposed to benefit from both the structural features and plasmonic properties, and the synergic effects will boost the application as a multifunctional therapeutic platform.

1.2 Objectives and thesis plan

With the problems and hypotheses discussed previously, this doctorate thesis focuses on the following objectives:

1. Understanding and optimizing the colloidal synthesis of Au-Ag alloy nanospheres;
2. Facilitating the multiplexing bioimaging with Au-Ag alloy NPs in cytopathology;
3. New structure designing based on Au-Ag alloy for the multifunctional therapeutic platform.

The plan of the thesis is the following:

Chapter 2 is the literature review about the liquid-phase synthesis methods of bimetallic nanoparticles, and Chapter 3 is the review published in the journal *Advanced Functional Materials*, entitled "Optical Properties and Applications of Plasmonic-Metal Nanoparticles". The optical properties of plasmonic are reviewed, and the applications of metallic plasmonic nanoparticles are summarized, especially the ones in biomedical fields.

Chapter 4 discusses the synthesis methodology of Au-Ag nanospheres, addressing the first objective of the thesis. First, understanding the nucleation and growth in the process provides the view to control the size, morphology, and dispersity of NPs. Based on that, different parameters in synthesis are kinetically controlled to optimize the properties and control qualities. At last, automation setup is proposed to scale up the synthesis and facilitate wide applications.

Chapter 5 is the published research article in the *Journal of Biophotonics*, entitled "Designable Nanoplasmonic Biomarkers for Direct Microscopy Cytopathology Diagnostics", which addresses the second objective. The work facilitates the clinical cytopathology application through designing Au-Ag alloy nanoparticles as multiplexing biomarkers and implemented for bioimaging with the customized illumination component.

Chapter 6 is a paper published in *Small*, entitled "Porous Au-Ag Nanoparticles from Galvanic Replacement Applied as Single-particle SERS Probe for Quantitative Monitoring", focusing on the third objective. Controllable porous Au-Ag structures are accomplished by dealloying Au-Ag alloy nanospheres through galvanic replacement reaction. The hot spots in high density with strong enhancement enable the *in situ* monitoring of drug release at single-particle level.

Chapter 7 generally discusses the dealloying process of Au-Ag alloy NPs, *in vitro* test and biofunctionalization of porous Au-Ag NPs, and their future applications in the fields of energy and information technology.

CHAPTER 2 LITERATURE REVIEW

The literature review contains two parts: one is a review (Chapter 3) recently published in *Advanced Functional Materials*, including the optical properties and applications of plasmonic-metal nanoparticles; and the other part in this chapter reviews the synthesis methods of bimetallic nanoparticles. The synthesis methods of plasmonic NPs have been focused on bimetallic ones in liquid-phase, concentrating on the alloy structure fabrication.

2.1 Liquid-phase synthesis of bimetallic NPs

Compared to pure metallic NPs, the bimetallic ones introduced the combined properties from two components, and the synergy effects from the combination can create new attractive properties and capabilities. In plasmonics, the composition effects eliminate the limitation from single materials and enlarge the flexibility for adjusting optical properties. Providing more possibilities, the bimetallic NPs are more interesting for wider applications.[11] The synthesis of bimetallic NPs involves different metal sources in the same environment, making the situation more complex. Many efforts have been made in this area,[12] and in this section, we will review the progress made in the synthesis of bimetallic NPs.

The synthesis of monometallic nanostructures has been well developed, while the controllable synthesis of bimetallic NPs is still challenging. The most direct way to get alloys is by heating different metals to melt them together. These solid-phase methods require high temperature for heating and long-time for annealing, and the resulting structure have usually limited surface area. Others use gas-phase synthesis to introduce the metal in the vapor phase and control the NPs formation in a cold environment. These methods require complicated instruments, e.g., pulsed laser, arc, and sputtering, leading to limited production. Besides the high energy consumption and low production, both solid and gaseous states are restricted in terms of nanostructure control, which has a significant influence on plasmonic properties. Liquid-phase synthesis typically involves metallic salts as the source of metal atoms, through chemical reduction to form the desired nanostructure by adjusting different parameters in the process. The colloidal synthesis can easily adjust the reaction and create more possibilities for nanostructure design. Moreover, compared to solid and gas-phase synthesis, liquid-phase methods are cost-efficient and more powerful for scale-up.[13]

For colloidal synthesis, metallic NPs are constructed from individual atoms through chemical reduction, usually called chemical synthesis methods. Similar to the monometallic synthesis, a proper chemical reaction should be chosen. For the synthesis of bimetallic NPs, two different metals will be reduced in the same system, therefore, proper reducing agents, surfactants, and solvents are required to balance the two components. Moreover, the reaction parameters should consider the thermodynamics and kinetics of both metals. On one side, during the colloidal synthesis, it is highly flexible to adjust the ratio between respective metal salts, the concentration of them and the reducing agents, the choice of stabilizer and solvent, as well as the reaction conditions, such as temperature and time.[14, 15] The colloidal synthesis results in a robust control in the composition, size, and structure of NPs, and shows high potential for scale-up fabrication. On the other side, the colloidal dispersions of NPs, especially the aqueous ones similar to the bio environment, exhibit tremendous possibilities for subsequent functionalization and implementation in further applications. Therefore, colloidal methods are the most developed for their versatility and applicability for a wide range of practical applications. We will review the most used synthesis methods for bimetallic NPs, especially AuAg alloy, focusing on co-reduction, seeded-growth, and galvanic replacement reaction. In practice, many approaches have employed more than one method.

2.1.1 Co-reduction

The colloidal synthesis of metallic NPs is usually performed in solution with metallic precursors, suitable reducing agents, and stabilizers. For bimetallic NPs, there are two types of metallic precursors for both components. Typically, there are three main stages in NPs formation: I) reduction, II) nucleation, and III) growth. The reduced metal atoms nucleate into seeds and continue growing on the seeds to form NPs, controlled by shape-directing agents and other reaction conditions. For producing bimetallic or alloy NPs, co-reduction combines the reduction of different metals in the same environment. Compared with a single metal, it is more difficult to reduce two kinds of metals simultaneously and control their nucleation and growth. Due to the different redox potential of the two components, the metal atoms can be reduced and nucleate separately. The order of reduction contributes to the structure, including the composition distribution within the NPs. Usually, metals with higher activities are reduced initially, followed by the reduction of the other

species. Core-shell structures are developed with symmetric deposition on the surface, while heterostructures can be generated through deposition with facet selection. During the growing process, interdiffusion between metals can lead to alloy or intermetallic NPs.[16]

The mechanism of the NPs formation has been explained with the concentration of monomers (Figure 2.1).[17] With the reduction of metal salts, the concentration of monomers increases rapidly until saturation. When the concentration is over critical value (S_C), nucleation burst in a short time, generating many nuclei. The nucleation consumes rapidly the monomers, reducing the concentration under S_C, so that the nucleation is ceased. The monomers attach to the generated nuclei for growth.

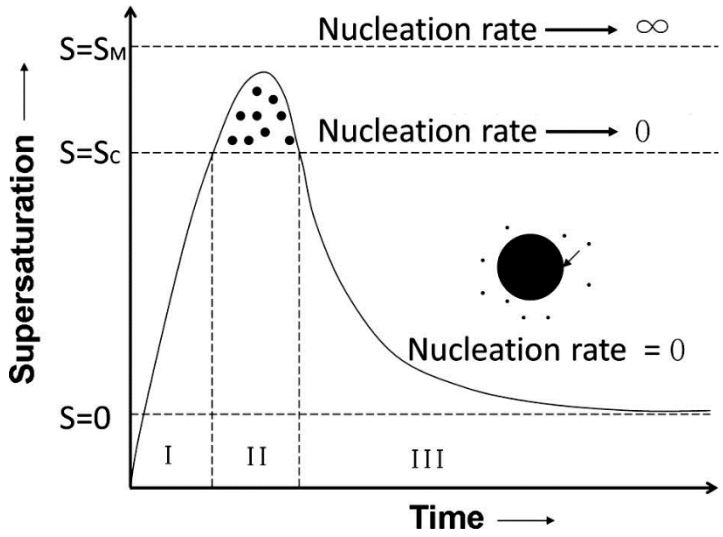

Figure 2.1 LaMer diagram of (I) reduction, (II) nucleation, and (III) growth, as a function of monomer supersaturation. Reproduced with permission.[17] Copyright 2014, Elsevier.

In the following stages in NPs formation, LaMer et al. proposed that the preparation of monodispersed NPs requires only homogeneous nucleation and avoiding heterogeneous ones, which is to say, the nucleation and growth should be separated.[18, 19] When the reducer is strong, reduction and nucleation will be very fast and the growth will also be out of control, especially when the redox potential, e.g., potential over standard hydrogen electrode (SHE) (listed in Table 2.1) of two metals in specific reaction conditions are significantly different from each other. Therefore, proper reducing agents and reaction conditions are necessary for controlling the nanostructure and size distribution.[11, 16] Several reducing agents have been employed in the

synthesis of bimetallic NPs, for instance, citrate, borohydride, ascorbic acid, polyol, and so on. Slower reduction and nucleation are relatively easier to control in kinetics so that the relatively mild reducers are preferred. In fact, some stronger reducers are needed due to the intrinsic chemical properties of some metals, as well as for the efficiency. Recent studies shed light on surfactants and surface ligands. Besides reducer and surfactants, other reaction conditions are also explored. As the boiling temperature of the solvent limits the heating temperature, different solvent systems are studied besides the aqueous one. With the exploration of reducing agents, surfactants, and surface ligands, as well as solvent, co-reduction synthesis manages to control the bimetallic NPs in size, morphology and composition.

Table 2.1 Redox potential and physicochemical properties of metals.[11, 20]

Metal	**Reduction reaction**	**E_0 (V vs SHE)**	**Crystal lattice**	**Lattice constant (Å)**	**Surface free energy (J m^{-2})**
Fe	$Fe^{2+}+2e^- \rightarrow Fe$	-0.44	*bcc*	2.87	0.98, 1.27, 1.80
Co	$Co^{2+}+2e^- \rightarrow Co$	-0.28	*hcp*	a=2.51, c=4.07	2.78, 3.04, 3.79
Ni	$Ni^{2+}+2e^- \rightarrow Ni$	-0.25	*fcc*	3.52	2.01, 2.43, 2.37
Cu	$Cu^{2+}+2e^- \rightarrow Cu$	0.34	*fcc*	3.61	1.95, 2.17, 2.24
Rh	$Rh^{3+}+3e^- \rightarrow Rh$	0.76	*fcc*	3.80	2.47, 2.80, 2.90
Pd	$Pd^{2+}+2e^- \rightarrow Pd$	0.95	*fcc*	3.89	1.92, 2.33, 2.23
Ag	$Ag^{+}+e^- \rightarrow Ag$	0.80	*fcc*	4.09	1.17, 1.20, 1.24
Pt	$Pt^{2+}+2e^- \rightarrow Pt$	1.18	*fcc*	3.92	2.30, 2.73, 2.82
Mn	$MnO^{4-}+8H^{+}+5e^- \rightarrow Mn^{2+}+4H_2O$	1.49	fcc	3.53	1.04
Au	$Au^{3+}+3e^- \rightarrow Au$	1.50	*fcc*	4.08	1.28, 1.63, 1.70

Co-reduction synthesis is efficient in bimetallic NPs production, and this liquid-phase approach normally regulates NPs size through changing the concentration of the reagents and the ratio between them and surfactants or ligands. With the simple co-reduction reaction, bimetallic nanospheres within certain dimensions can be produced, while the use of surfactants or surface ligands is necessary to fabricate NPs of large size or irregular morphologies. El-Sayed's group

employed relatively weak reducer citrate to synthesize Au-Ag NPs, through substituting a certain proportion of $HAuCl_4$ (precursor of Au) by an equivalent amount of $AgNO_3$ (precursor of Ag). They successfully synthesized Au-Ag alloy NPs, about 20 nm in diameter, and the single plasmon peak proves the formation of alloy NPs instead of the mixture of Au NPs and Ag ones.[21] However, the method is not applicable for larger NPs, because the size variation will raise a problem with different plasmonic properties for final products. Besides dimension, for metals with large differences in terms of reduction potential, it is also challenging to control the bimetallic structures with co-reduction. Loiseau and her co-workers reported co-reduction method in Ni-Pt NPs synthesis, where the two metals have a large difference in redox potential.[22] They managed to control the size distribution and composition, and avoid phase segregation by employing oleylamine and oleic acid as surfactants in benzyl ether. The solvent system enables heating up to 275 °C, and the temperature affects the redox potential and accelerates the diffusion of the two metals. Figure 2.2 shows the size distribution and spatial distribution of Pt and Ni within the bimetallic NPs. Both surfactants and the high temperature contribute to the alloy phase, and the ratio between surfactants and metal precursors adjusts the size.

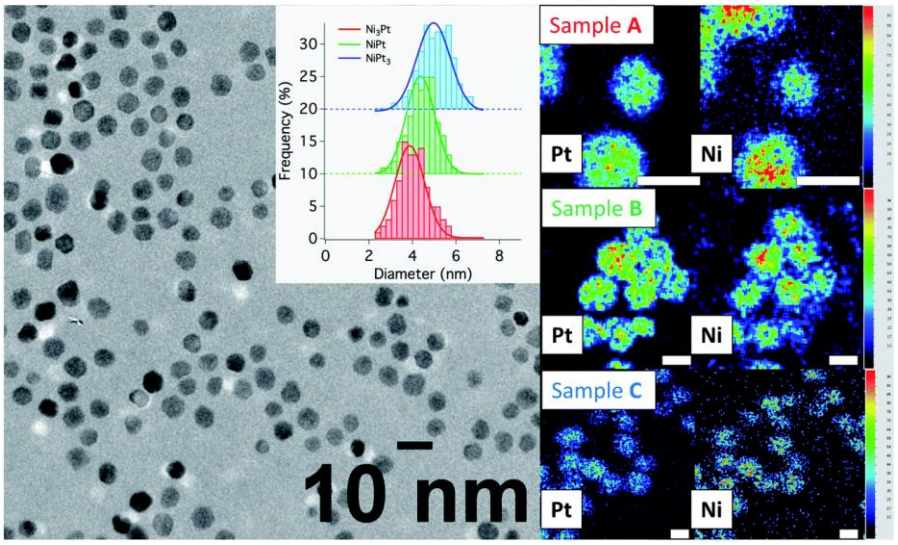

Figure 2.2 (left) TEM image of Pt-rich Ni-Pt NPs as representative, and inserted size distribution histograms for Ni-rich (sample A), equiatomic (sample B) and Pt-rich (sample C) Ni-Pt NPs. (right) EDX mapping of sample A-C, exhibiting spatial correlation between Ni and Pt (scale bar = 5 nm). Reproduced with permission.[22] Copyright 2020, Royal Society of Chemistry.

In addition to size, co-reduction approaches can control the morphology of bimetallic NPs through different crystallographic facets. Anisotropic growth occurs due to the different surface energy between facets, or surface directing agents, including capping agents or surfactants. For example, Zhang et al. applied decylamine as a coordinating ligand to control the co-reduction synthesis of Cu-Pd NPs.[23] The addition of decylamine narrowed down the reduction velocity difference between the two metals, facilitating the control in co-reduction, and meanwhile the decylamine selectively absorbed on {111} facets, directing the growth for tetrahedral structure. Figure 2.3 shows the influence of decylamine amount in the co-reduction for Cu-Pd bimetallic NPs. In the co-reduction, not only surface ligands affect the morphology of produced NPs, the effects of reducing agents and reaction temperature are studied. Glucose is the reducer in the synthesis of Cu-Pd NPs, and its concentration directly affects both size and morphology. Higher concentration accelerates the growth, especially the preferential one, which stimulates protrusion and generates rhombohedral tetrapods instead of terahedrons. The reaction temperature changes both reduction and diffusion rates, which induce different nucleation mechanisms and lead to distinct sizes and morphology. Combination and optimization of all the parameters are essential for co-reduction to produce designated bimetallic NPs.

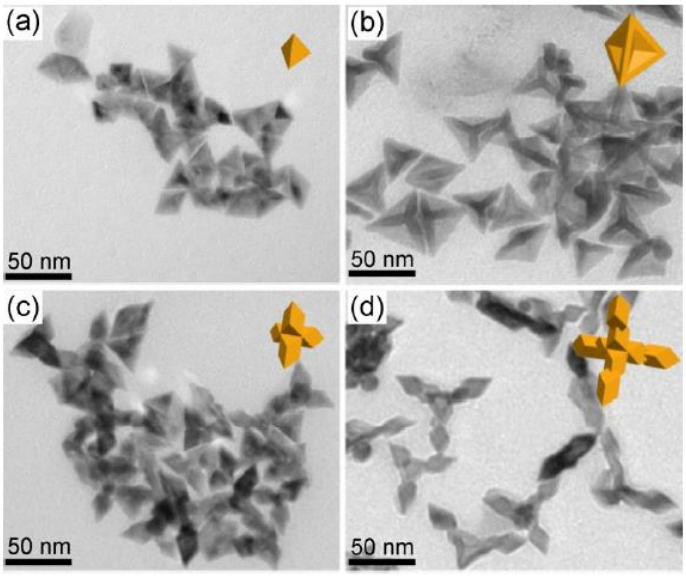

Figure 2.3 TEM images of Cu-Pd NPs obtained in the same co-reduction conditions, with only increasing amount of decylamine from (a) to (d). The inserted three-dimensional geometric models show the terahedron for NPs from (a), concave terahedron for NPs from (b), along with

rhombohedral tetrapods and grown ones for the NPs from (c) and (d) respectively. Reproduced with permission.[23] Copyright 2015, Springer Nature.

In co-reduction, the composition can be flexibly regulated by varying the ratio between metal precursors. For alloy or intermetallic NPs, composition regulation is crucial. If the precursors are completely reduced and all the metal atoms deposit onto the NPs during the co-reduction, the composition can be tuned correspondingly by simply changing the ratio of metal precursors. As shown in Figure 2.4, Yu et al. successfully produced monodispersed Co-Pt alloy NPs with oleylamine at 300 °C, where oleylamine perform as not only reducer but also surfactant and solvent.[24] The composition reaches linear fit when keeping $Pt(acac)_2$ at 0.5 mmol, and varying the amount of Co(acac)2 (Figure 2.4c), and leading to linear changes in lattice constants due to the alloying (Figure 2.4d). However, not all the metal elements can be tuned so smoothly for bimetallic NPs due to the difference of redox potential in certain reaction systems. Therefore, the choice of reducing agents and reaction conditions is important, especially in the absence of surfactants or foreign ions facilitating the deposition.

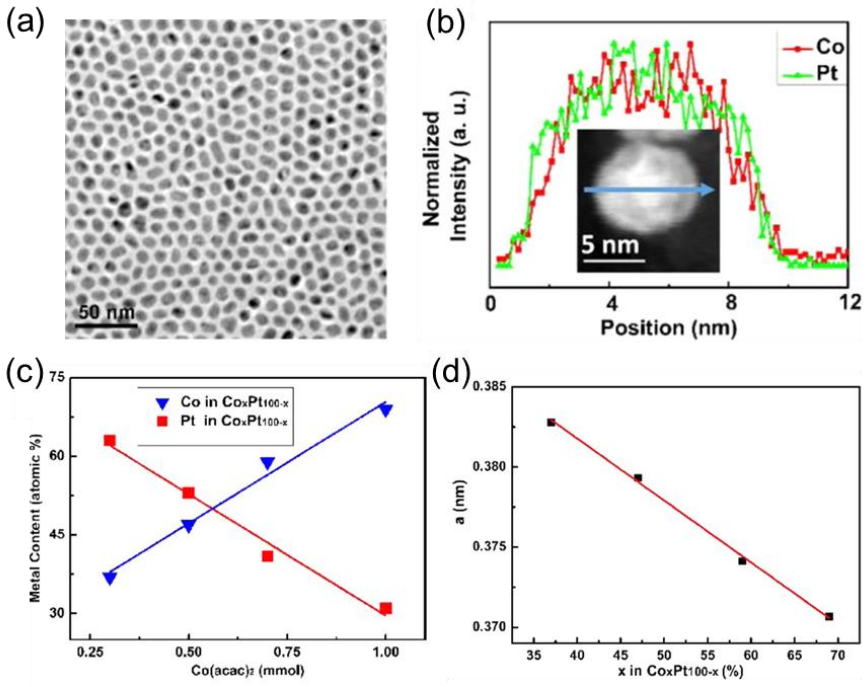

Figure 2.4 (a) TEM image of $Co_{47}Pt_{53}$ NPs and (b) HAADF-STEM image and EDS line scan from an individual one. Relationship between (c) the amount of Co precursor and the atomic contents of the NPs at Pt precursor of 0.5 mmol and (d) the lattice constants and the Co

compositions in alloy NPs. Reproduced with permission.[24] Copyright 2014, American Chemical Society.

Besides using chemical reducers, there are different routes with the assistance from sonochemistry or microwave in co-reduction,[25-27] eliminating the limitation from normal redox reactions. The ultrasound or microwave facilitates a fast synthesis process under lower temperature with better control. Gümeci et al. applied sonochemistry in the synthesis of Pt-Cu NPs, and successfully controlled the $PtCu_3$ stoichiometry, and achieved uniformly alloyed NPs.[28] Kwon's group reported many types of Pd-M (M= Ni, Co, Fe, Mn) bimetallic NPs synthesized by ultrasound-assisted polyol method.[29] Among the alloy NPs, Pd-Fe and Pd-Mn NPs were reported for the first time. Kalyva et al. reported a fast (13 min) microwave-assisted synthesis method for Pt-Cu NPs, and they employed polyvinylpyrrolidone as a capping agent in the ethylene glycol system to get "near-monodispersed" bimetallic NPs.[30] Sonochemistry and microwave irradiation have advantages in rapid reaction rate, mild condition (room temperature), and high purity of products, providing efficient synthesis approaches. However, with high kinetics of sonochemistry, the control over shape and size is more difficult, and for microwave-assisted approaches have limitations in terms of the size and cost of the dedicated reactor, as well as the difficulty of monitoring during the process.[31]

2.1.2 Seeded growth

Seeded growth methods separate nucleation and overgrowth step, and enlarge NPs gradually, with better control of size and morphology of NPs.[32] In the process, preformed seeds provide sites for the heterogeneous nucleation of newly formed metal atoms. As the seeds provide the surface for the reduced atoms to nucleate and deposit with lower surface energy than forming new nucleates, seeded-growth manages to synthesize well-controlled nanostructures. In general, from monomers to NPs, there are two types of nucleation: 1) homogeneous nucleation, which occurs when the concentration of monomers increases over a critical value, they tend to nucleate to form the NPs; 2) heterogeneous nucleation, which happens when there are nucleation sites from the certain solid surface, monomers deposit onto the existing particles. Heterogeneous nucleation occurs at the certain surface with lower surface energy, so that it is easier compared with homogeneous nucleation, which requires a much higher concentration of monomers, as stage II and III shown in

LaMer diagram (Figure 2.1). In general, homogeneous nucleation happens in a burst, while heterogeneous one is relatively slow. Therefore, the seeded-growth method is more controllable, and mono-dispersed nanostructures can be resolved by avoiding self-nucleation during the growth stage. Ideally, the growth of new monomers achieves equal distribution to each seed, thus the deviation of final NPs only comes from the seeds, and the growth becomes quantitative.[11] The amounts of precursors, as well as the size and shape of the produced NPs become precisely controlled with the determined amount of seeds.

The bimetallic structures include not only the homogeneously mixed alloy and intermetallic structures, but also core/shell and heterostructures where the two components segregate from each other, involving the hetero spatial distribution of composition. Seeded growth strategy enables controlled synthesis for all of those structures, especially the ones difficult to achieve through other approaches. With seeded growth approaches, the size and the composition of the alloy and intermetallic NPs are efficiently regulated, eliminating the limitation of other routes. Moreover, the structures with segregation of the constituents in nano-scale can be readily designed with one element for the seeds, the second one deposit to develop into various structures. If the deposition of the secondary metal atoms is equally distributed over the whole surface of seeds, core/shell structure will be resolved; if the deposition is selective to certain surfaces or directions, the heterostructure will be attained.[16] For the synthesis of a wide range of bimetallic structure, the seeded growth method provides high versatility, for instance, seeds structure, capping agents, and precursors, as well as their concentration and ratio among them.

In seeded growth methods, seeds formed at the first stage play an important role in the growth process with their surface energy, morphology, and facets. The formation of seeds can be controlled by playing with the ratio among precursors, reducing agent, and stabilizer, as well as changing the experimental conditions, as discussed in co-reduction synthesis. Considering the surface with high curvature usually exhibits high surface energy, their high activity facilitates the deposition in the growth. Meanwhile, the surface energy of facets from the same crystal system varies, for example, in fcc metals, $\gamma\{111\} < \gamma\{100\} < \gamma\{110\}$. This facilitates anisotropic growth and enables a wide range of non-spherical nanostructures. Therefore, seeded growth methods have been successfully proved in bimetallic NPs synthesis, with narrow-distributed nanorods, nanocubes, branched NPs, and other exotic shaped NPs.[33-36] For instance, a commonly used surfactant,

cetyltrimethylammonium bromide (CTAB), exhibits a strong affinity to {110} compared to the other facets, impeding the growth on its surface. Accordingly, the different growth rates in different directions induced orange slice-like shape and dumbbell-like Au@Ag core-shell nanorods.[33, 37] Seeded growth method offers a simple and efficient way for a large range of NPs synthesis, and the control of synthesis is crucial to tailor and enhance NPs properties in various applications like catalysis and SERS, which are sensitive to the facets and shapes.

Besides the seeds, the interaction between seeds and deposited atoms is also decisive for the seeded growth synthesis of bimetallic NPs. Growth is highly affected by the physicochemical properties, including crystal lattice, surface energy, and electronegativity of different types of metals, as listed in Table 2.1.[16] In seeded growth, to form the bimetallic NPs, the deposition tends to establish heteroepitaxial growth at the interface with similar lattice constants (difference less than 5%) and crystalline structure between the seeds and deposited metals, while amorphous or polycrystalline growth occurs with large mismatches or different crystal structures.[38] Epitaxial growth exhibits high potential in the synthesis of well-controlled heterostructure with precise control of crystalline orientations, facets, and interfaces relative to the seeds crystal structure.[39] The epitaxial growth is applied in many heterostructures for bimetallic systems, such as Pd-Pt, Ag-Cu, Ni-Cu, Au-Ag, and so on.[40-43] For example, with kinetic control, Neretina et al. have defined the growth of Ag onto the surfactant-free Au seeds with different orientations (Figure 2.5), and achieved expected core-shell bimetallic structure, including heterodimer, octahedron, and conformal core-shell.[43] However, there are still limitations for the epitaxial growth: besides the matching lattice constants, the deposition metal should have lower electronegativity and smaller bond energy than the metal of the seed.[38] With large lattice mismatches, the bimetallic structures are formed with anisotropic growth and result in polycrystalline, proved in Pt-Au and Cu-M (M=Au, Pt or Pd).[44-46] Taking advantage of the optical properties of some metals, Mirkin et al. introduced the concept of plasmon-mediated seeded growth synthesis and demonstrated it with Au@Ag core-shell nanorods and icosahedra.[47] The photomediated method employed plasmonic properties and efficiently controlled the epitaxial and nonepitaxial growth, with both size and structure control.

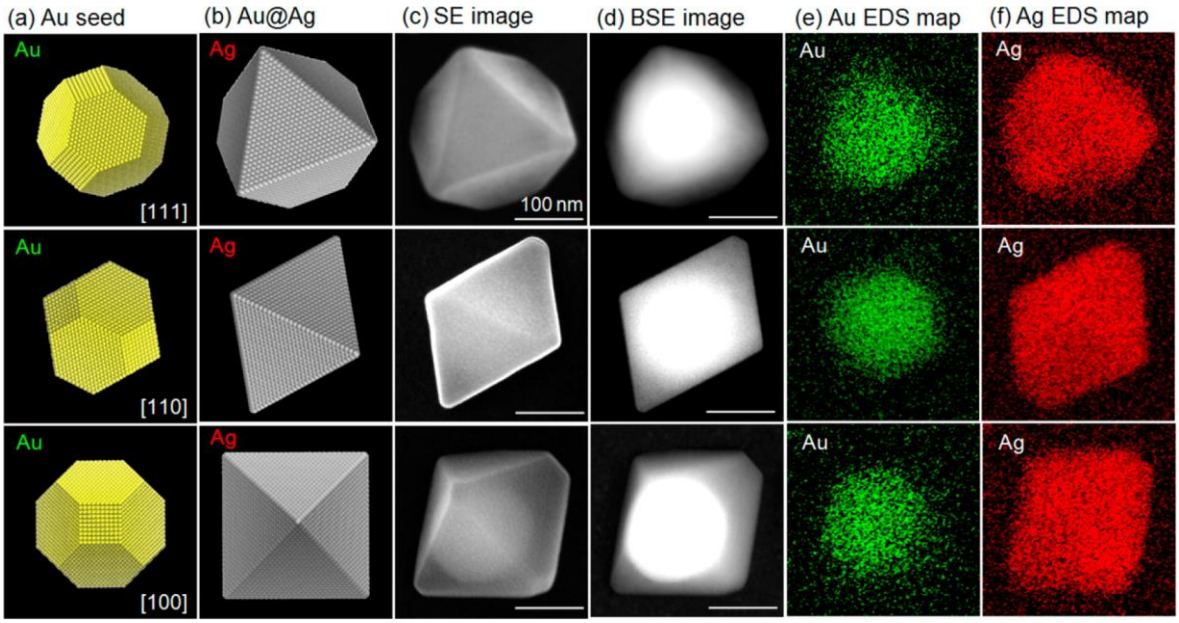

Figure 2.5 Schemes of (a) [111]-, [110]-, and [100]-oriented Au seeds and (b) respective bimetallic Au@Ag NPs after seeded growth. (c) Secondary electron and (d) backscatter modes SEM images of experimental results and their (e) Au and (f) Ag elemental mapping. Reproduced with permission.[43] Copyright 2014, American Chemical Society.

In addition to core-shell and heterostructures with segregation of metals, seeded growth routes have involved significant alloy structure in bimetallic NPs, regardless of epitaxial or amorphous and polycrystalline growth. Seeded growth combined with co-reduction allows simultaneous reduction and deposition of two types of metals and the alloy forms on the preadded seeds. The method has been applied to both lattice-matched and dismatched bimetallic structures.[48, 49] After proving with Au-Pd (4 % mismatch), Skrabalak and co-workers applied the seed-mediated co-reduction to Pd-Cu (7 % mismatch), and through kinetically control, they managed to control the composition distribution and produced branched alloy structure and polyhedral.[49] Our group has developed the synthesis of large Au-Ag alloy NPs with precise control in size and composition with the combination of seeded growth and co-reduction methods.[50] Au seeds (~15 nm) made through the Turkevich method are added to the "growth" solution with $HAuCl_4$ (precursor of Au) and $AgNO_3$ (precursor of Ag) and citrate (as reducing agent and stabilizer) to continue growing for larger NPs with co-reduction of Au and Ag (Figure 2.6). The fabricated NPs can be served as seeds for another step of growth. With multistep of growth, monodispersed Au-Ag alloy NPs are obtained

with controllable size and composition, resulting in wide tunable plasmonic properties. Alloy NPs of any composition between pure Au and pure Ag in the range of 30-150 nm can be synthesized with the deviation of less than 15 %.[50] The versatile seeded growth approaches enabled a wide range of bimetallic nanostructures with controllable and designable features.

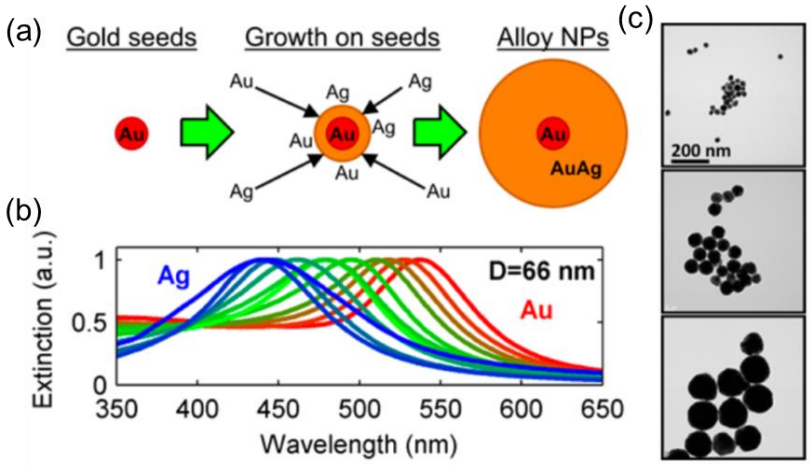

Figure 2.6 (a) Scheme of multistep seeded growth method in Au-Ag alloy NPs synthesis, (b) extinction spectra of 66 nm-diameter NPs of composition from pure Ag to pure Au, and (c) TEM images of Au seeds and Au@Au-Ag alloy NPs after one and two stages of growth. Reproduced with permission.[50] Copyright 2016, American Chemical Society.

Heterogeneous nucleation is thermodynamically favored compared to homogeneous nucleation, which provides the foundation for seeded growth approaches. The reaction parameters, such as temperature, reducing agents, and surfactants, should be designed to satisfy the hetero deposition while avoiding the homogeneous one. Moreover, during the deposition, thermodynamics and kinetics play important role in the structural control of bimetallic NPs, thus the reaction parameters must be adjusted rationally. In general, under high temperature, thermodynamically stabled structures are favored, and they are the most stable ones, but normally with less specific surface area. Xia and co-workers explained the thermodynamically and kinetically controlled surfactant-based growth with the concept of deposition rate (V_{dep}) and surface diffusion rate (V_{diff}).[51] If $V_{dep} > V_{diff}$, the deposition tends to be site-selective, and results in kinetically favored structures; in reverse, when $V_{dep} < V_{diff}$, the deposited atoms tend to diffuse across the surface and generate the conformal core-shell structures favored by thermodynamics. Neretina and co-workers controlled the surfactant-free deposition with slow, moderate, or fast kinetics, and produced Au-

Ag heterodimers, octahedra, and seeds-conformal core-shell structures.[43] Therefore, the morphology of bimetallic NPs can be controlled by adjusting the rates of deposition as well as diffusion. Considering the physical and chemical properties of different metals listed in Table 2.1 will be beneficial for designing the reaction conditions for certain bimetallic structures.[11]

2.1.3 Galvanic replacement reaction

Galvanic replacement reaction (GRR), also known as galvanic exchange, is an electrochemical process between two metals in presence of electrolytes. In GRR process, the metal as the sacrificial template is oxidized by the metal ions with higher reduction potential in the electrolytes, and the reduced metal deposits on the remaining template. GRR has been proved as a promising approach for hollow bimetallic nanostructures with high efficiency and versatility.[52, 53] GRR is driven by the different redox potentials between two metals, as the standard redox potential of some metals is shown in Table 2.1. The GRR between Au^{3+} and Ag is a notable one, especially when it occurs in an aqueous solution, which involves the oxidation of Ag and the reduction of $HAuCl_4$. The overall reaction is described as:

$$3Ag(s) + AuCl_4^-(aq) \rightarrow Au(s) + 3AgCl(s) + Cl^-(aq)$$

Due to the poor solubility of AgCl, the reaction is even easier as AgCl/Ag (0.22V vs. standard hydrogen electrode (SHE)) compared to Ag^+/Ag (0.8V vs. SHE). Therefore, the reaction leads to the replacement of each three Ag atoms by one Au atom.[54]

For porous and hollow bimetallic NPs, especially with noble metals, Ag is the ideal template material and have been widely reported because of the low reduction potential of silver ions, Ag^+/Ag (0.8V vs. SHE) compared with Pd^+/Pd (0.95V vs. SHE), Pt^+/Pt (1.18V vs. SHE), and Au^+/Au (1.5V vs. SHE).[55-58] Moreover, other metals with relatively low reduction potential, including Cu, Ni, Co, have also been applied as templates.[59-61] Various well-controlled morphologies have been applied as GRR templates, such as nanospheres, nanocubes, nanorods, nanobelts, and even heterostructures.[53, 56, 59, 62] Due to the intrinsic mechanism of GRR, the final hollow structures are dependent on the templates, forming a thin shell or frame surrounding the templates during the process. Combined with various template morphologies and related bimetallic structures, GRR has been proved great advantages in the synthesis of hollow and porous

structures over other approaches discussed previously. This route expands the exploration into the internal structure of NPs, which leads to more possibility and applicability. Among all the variations, Au-Ag bimetallic nanostructures are the most classic ones. Xia and co-workers have thoroughly studied the galvanic replacement between $AuCl_4^-$ and Ag, and also achieved fine-tuned nanoboxes, nanocages, and cubic frames from Ag nanocubes.[63] Figure 2.7 illustrates the whole process from silver cube to porous nanocage and finally cubic nanoframe through galvanic reaction and etching method. The added amount of $HAuCl_4$ and NH_4OH or $Fe(NO_3)_3$ as etching agents, drives the morphology transition. In GRR, the metals interdiffusion into each other, and the replacement can penetrate into the interior of NPs, as the dissolution amount can be controlled by the added metal ions ($AuCl_4^-$ in this case). Usually, partial metal atoms from the template will remain, which requires stronger etching agents to complete the removal if needed, for example, Fe^{3+}, HNO_3, H_2O_2, and NH_4OH assist in removing the residual Ag.[63, 64] The combination of GRR and etching facilitates the porous bimetallic structures design, beyond the classic thin shell and frame. However, the relatively harsh etching will cause the aggregation problem when the etching agents disturb the environment and change the surface electricity of the NPs, and the instability limits the extensive use in the colloidal phase. Deliberate adjustment of parameters can be one way for controlling, and surface coating, like PVP and other kinds of water-soluble polymers, has also been involved in tackling this problem.[64, 65]

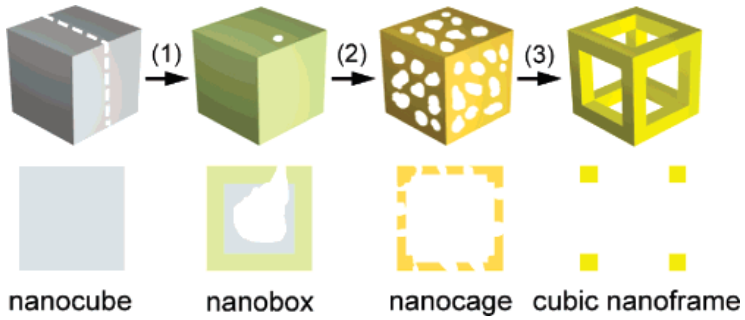

Figure 2.7 Schematic of galvanic replacement and etching process to build hollow structure from Ag nanocube. Reproduced with permission.[63] Copyright 2007, American Chemical Society.

During GRR, while bimetallic nanostructures form, the different rates of atomic migration are involved in the formation of voids, which is known as the Kirkendall effect.[54] Sometimes this effect is combined with GRR to achieve more complex hollow or multilayer structures.[66, 67] Kirkendall effect induces void formation and coalescence at nanoscale, to form the hollowness in

the interior of NPs. The process related with the interdiffusion of metal atoms is strongly related to temperature. Mirsaidov and co-workers directly observed the Kirkendall effect during GRR through liquid cell TEM.[54] Figure 2.8 shows the TEM images taken *in situ* during the GRR under room temperature 23 °C and at the heating of 90 °C, respectively. GRR creates vacancies due to the loss of atoms, and the Kirkendall effect nucleates the voids driven by the concentration gradient. At 23 °C (Figure 2.8a), following the deposition of Au onto Ag nanocube, Kirkendall effect induced voids at the interface of Au and Ag, and the gap formed between core and shell, as GRR continued dealloying Ag core in an isotropic way. While at 90 °C (Figure 2.8b), the void diffusion rate became much higher, leading to fast merge of voids. Following the formation of thicker shell compared with lower temperature, a large void propagated within the shell by dealloying Ag core. To regulate GRR and coexisting Kirkendall effect can provide more possibilities in designing bimetallic nanostructures.

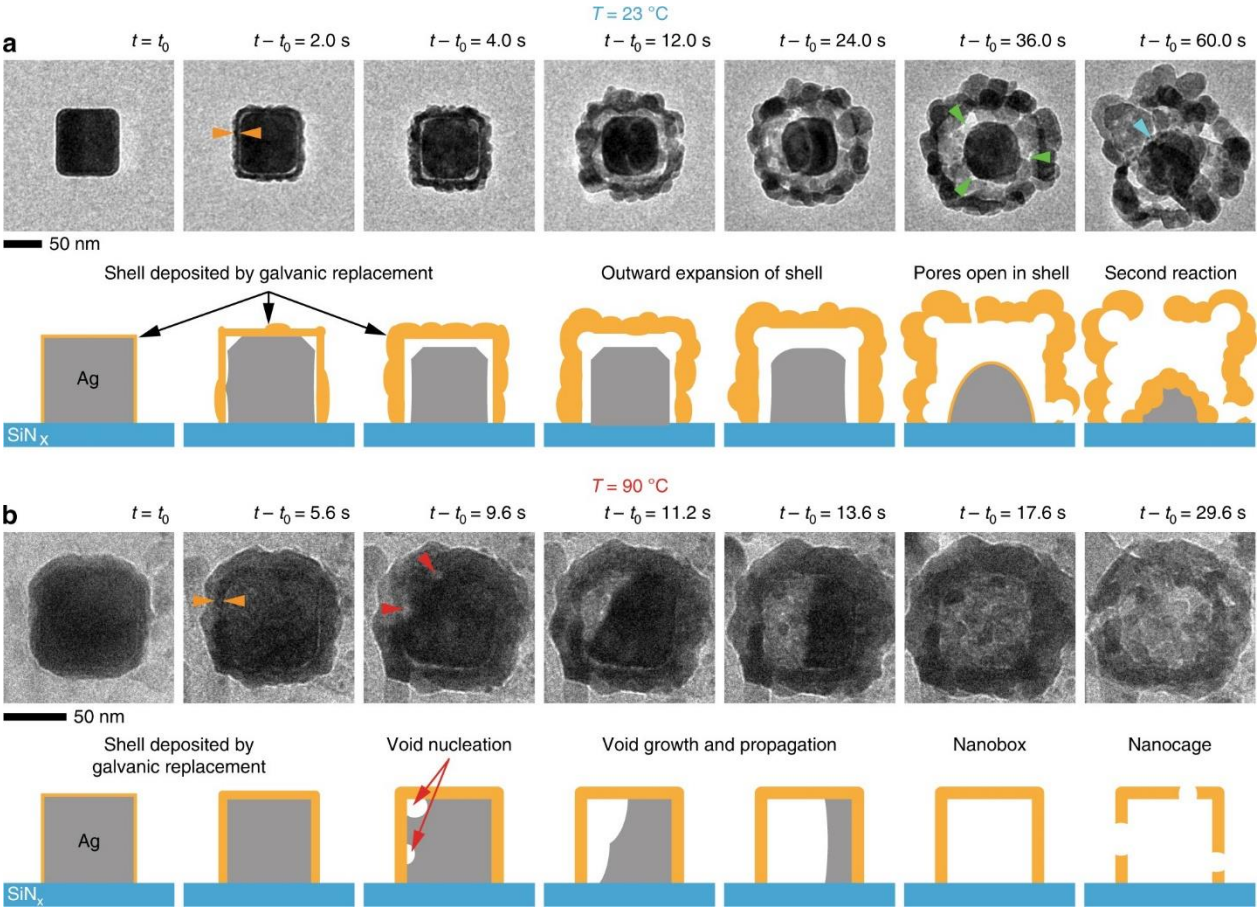

Figure 2.8 In situ TEM images and corresponding schemes of the GRR process of Ag nanocubes under the temperature of (a) 23 °C and (b) 90 °C. Reproduced with permission.[54] Copyright 2017, the authors.

For bimetallic nanostructures, GRR can be also combined with co-reduction by simply introducing a reducer during the GRR process. Xia and co-workers used the precursor of Pt, and reducing agents during the GRR of Pd nanocubes.[68] The combination of these two methods has resolved many bimetallic structures with superior catalytic performance, such as triangular Ag-Pd and dendritic Pt-Cu for the oxygen reduction reaction.[69, 70] For plasmonic Au-Ag NPs, Qin's group employed ascorbic acid during the GRR, and the co-reduction enhanced structural stability of Au-Ag hollow nanostructures.[71] Yue et al. also combined co-reduction with GRR, and successfully synthesized Au-Ag bimetallic nanostructures with tunable cavity size, through regulating the kinetics.[72] The combination of the GRR and co-reduction enhanced the stability of hollow structures, and the simultaneous processes facilitate high efficiency in synthesis while attaining good control of the structure and composition distribution.

CHAPTER 3 ARTICLE 1: OPTICAL PROPERTIES AND APPLICATIONS OF PLASMONIC-METAL NANOPARTICLES

The review published in *Advanced Functional Materials* explained the plasmonic properties of metallic NPs with the classic theory model. The biomedical applications have been discussed depending on the optical properties, and the applications in the energy field and information technology have also been summarized.

3.1 Authors

Lu Wang, Morteza Hasanzadeh Kafshgari, and Michel Meunier

3.2 Contribution of the authors

The author of this thesis, Lu Wang, carried out the complete writing of the manuscript as well as the composition of the figures. Morteza Hasanzadeh Kafshgari and Michel Meunier participated in the discussions as well as in the revision of the article.

3.3 Abstract

Noble metal nanoparticles due to their unique optical properties arising from their interactions with an incident light have been intensively employed in a broad range of applications. This review comprehensively describes fundamentals behind plasmonics, used to develop applications in the fields of biomedical, energy and information technology. Basic concepts (electromagnetic interaction and permittivity of metals) are discussed through Mie theory presented as the main model for interpreting phenomena of optical absorption and scattering. The effects of near-field enhancement, shape, composition, and surrounding medium of nanoparticles on optical properties are described in detail. The review explores and identifies the potential of plasmonic nanoparticles based on their optical properties (e.g., light absorption, scattering and field enhancement) for developing different applications (biomedical, energy and information technologies). Due to a significant impact of plasmonic nanoparticles on medicine and healthcare products and technologies, the review initially focuses on developed biomedical applications extensively benefited from the optical features of these nanoparticles. Advantages of the optical properties outstandingly implemented are also briefly discussed in other applications, including energy and

information technologies. This review concisely summarizes the explored areas based on plasmonic properties, compares advantages of plasmonic nanoparticles over other types of nanomaterials and highlights challenges.

3.4 Introduction

Metallic nanoparticles (NPs) are among the most popular nanomaterials, stimulated by an incident light, to spark a wide range of applications to well-established performances.[3, 73] Noble metal NPs exhibit a number of properties that make them attractive for a wide range of applications in biomedical, energy, and information technologies. Due to the interaction of these metallic nanostructures with an incident light, a collective oscillation of free electrons, called plasmon, becomes dominant and generates the surface plasmon resonance. A large number of these electrons, participating in the surface plasmon resonance, causes a strong absorption and scattering, as well as the near-field enhancement at the natural frequency of plasmonic-metal nanoparticles.[74] The localized surface plasmon resonance (LSPR) phenomena acquired by noble metal NPs are well known due to their resonance frequency in both visible and near-infrared ranges and studied to further biomedical, energy, and information technologies (e.g., bioimaging, biosensing, nanosurgery, photocatalysis, and data storage).[3, 75-79] To achieve an adaptable and application-oriented LSPR peak, physical features, including size, morphology, and composition of noble metal NPs have to be precisely designed by considering the permittivity of the surrounding medium.

Understanding physics behind the LSPR phenomena also plays a critical role in the fabrication and implementation of plasmonic NPs for developing various applications, and therefore many calculation approaches (e.g., Mie theory and numerical simulations) have been proposed to describe the LSPR phenomena of metallic NPs. Metallic NPs such as Ag, Au, and Pt with their tunable LSPR can easily be combined with other materials (e.g., titanium, silicon, carbon, and a wide range of polymers) for synergizing specific applications.[80-82] Synthesis of almost all metallic NPs is environmentally friendly compared to other nanomaterials (e.g., carbon-based materials), requiring harsh chemical agents for the reduction and oxidation.

Compared to other nanomaterials, plasmonic properties of noble metal NPs outstand from most other nanomaterials. The optical properties, including enormous absorption, scattering, and field

enhancement, enable a wide range of applications associated with opto-signal or enhanced chemical signals for imaging and sensing. Moreover, their reproducible fabrication protocols and tunable optical properties are outstanding due to an adaptable relation between plasmonic structures and optical properties.[83, 84] The irreplaceable and valuable optical properties of noble metal can be evaluated by precise plasmonic theories, assisting a reproducible fabrication of application-oriented plasmonic nanomaterials, followed by their feasible surface modification tackling problems related to functionality in complex environments compared to other nanomaterials.[85-87]

In this review, we summarize fundamental aspects of the surface plasmonics employed to design elaborated nanoparticles and implement their application-oriented plasmonic properties (Figure 3.1). A comprehensive description and comparison of different optical properties related to the electromagnetic interaction, composition, shape, and permittivity of plasmonic nanoparticles as well as the surrounding medium are given. The fundamentals of scattering and extinction cross sections based on 'Mie theory' are also presented to interpret a broad range of application-oriented plasmonic spherical nanoparticles. Applications of plasmonic-metal nanoparticles in three important fields (biomedical, energy, and information technology) based on light absorption, scattering, and field enhancement are summarized and discussed. Owing to their remarkable properties, such as optical responses, surface reactivity, and long-term physicochemical stability *in vitro* and *in vivo*, we extensively focus on biomedical applications of novel approaches, which can eventually be translated into clinical settings. We then continue discussing the use of plasmonic properties in developing energy technologies by taking advantage of their large scattering cross section, field enhancement at the surface, and carrier generation in the substrate. The major potential of plasmonic NPs is examined in energy technologies (e.g., photovoltaic energy conversion and photocatalysis), and their unsolved challenges are highlighted. In the final part, our attention is focused on current achievements of plasmonic nanoparticles in information technology. We briefly discuss important roles of plasmonic nanoparticles for furthering data storage and encryption and outline limitations and challenges that need to be addressed in order to accelerate their practical outcomes in information technology.

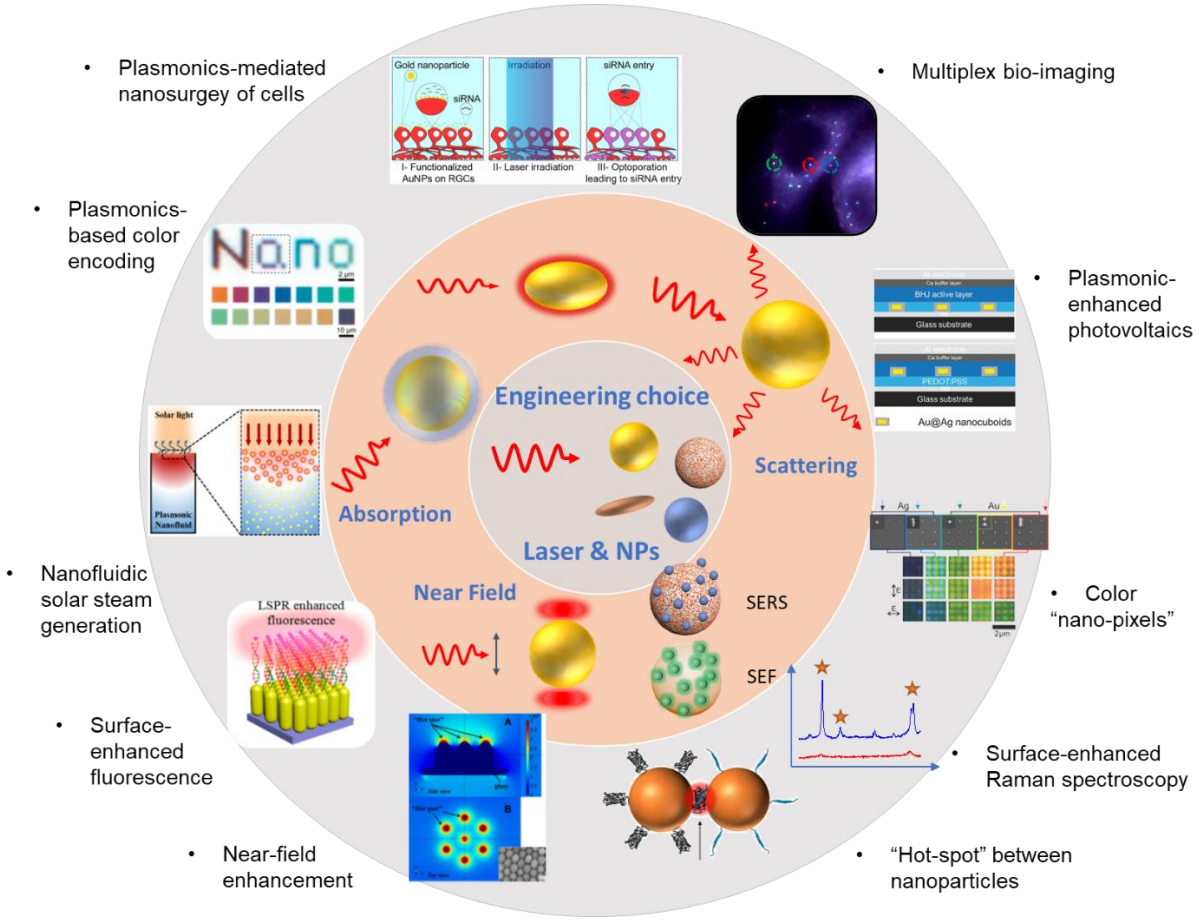

Figure 3.1 Schematic representation from plasmonic nanostructure design to applications. The center circle shows the engineering choice of the plasmonic nanostructures (geometry and composition) and irradiation light (wavelength, pulse width, energy, etc.). The second inner circle represents the main phenomena namely absorption, scattering, and near field. The outside circle shows examples of various applications exploiting specific phenomena, based on the engineering choices. Reproduced with permission.[88] Copyright 2018, American Chemical Society. Reproduced with permission.[89] Copyright 2019, John Wiley & Sons, Inc. Reproduced with permission.[90] Copyright 2016, Royal Society of Chemistry. Reproduced with permission.[91] Copyright 2016, John Wiley & Sons, Inc. Reproduced with permission.[92] Copyright 2018, Springer Nature Limited. Reproduced with permission.[93] Copyright 2017, American Chemical Society. Reproduced with permission.[94] Copyright 2017, Elsevier B.V. Reproduced with permission.[95] Copyright 2016, American Chemical Society.

3.5 Plasmonic nanoparticles

As explained in the introduction, LSPR phenomenon is the intrinsic characteristic of plasmonic materials. Besides noble metals mostly developed for a wide range of applications, there exist other types of plasmonic nanomaterials.[96-102] LSPR has also been discovered in other materials, including heavily-doped semiconductors, metal oxides, 2D materials, conducting polymers, summarized in Table 3.1. These materials have their intrinsic resonance wavelength range, tunable by adjusting morphology and size in order to cover a broad-spectrum range. Depending on the purpose of an application as well as cost-effectiveness, these materials offer more and more choices that can be designed in combination with other different materials.[96, 100, 101] In general, semiconductors have resonance redshifted compared to the visible and near-infrared (NIR) range of most metallic materials, and small size (< 10 nm) of semiconductor particles, like quantum dots, can be applied in biomedical applications. However, metallic NPs, especially Ag, have the highest resonance intensity, facilitating the on-resonance applications. Each kind of nanomaterials have their advantages and disadvantages, and specific material suitable for all applications has not been found. Nowadays, metallic plasmonic NPs have the dominant position in plasmonics, in terms of theoretical study and practical applications. These metallic NPs show significant advantages due to their large scattering and absorption cross section, strong field enhancement, as well as easy formation of different reproducible morphologies. Therefore, our review focuses on metallic plasmonic nanostructures and summarizes valuable details for understanding plasmonic properties, which may accelerate the utilization of other nonmetallic plasmonic materials.

Table 3.1 Properties of different plasmonic materials.

Materials	**Mechanism**	**Examples**	**LSPR range**	Advantages	Comments
Metallic nanostructures	Free electrons	Au, Ag, Cu and their alloys	UV-visible	Mature theory of optical properties, various structures, controllable synthesis methods, strong plasmonic effects	Costly, limited permittivity
Semiconductor nanocrystals	Free holes	$Cu_{2-x}S$,[103, 104] $Cu_{2-x}Se$[105-107], ITO[108], TiN[109]	Visible-NIR	smaller size (< 10 nm), broader NIR absorbance	Difficult to dope
2D materials	Electrons and holes	Graphene,[110, 111] MoS_2[112, 113]	NIR	strong plasmonic effect	Tedious synthesis processing, high-demanding synthesis instrument
Conductive polymers	Polaronic charge carriers	poly(3,4-ethylenedioxythiophene:sulfate)[114]	NIR	Switchable state, low cost, flexibility, biocompatibility	Limited to fundamental study, low electrical conductivity, high defect density

3.6 Optical Properties of Plasmonic Nanoparticles

3.6.1 Electromagnetic Interaction with Plasmonic Nanoparticles

Upon incidence of an electromagnetic wave, free electrons of metallic NPs are driven to the surface opposite to the direction of the electric field, resulting in positively and negatively charged sides for each particle. The electron distribution counteracts the incident electric field inside the particle and only enhances the field at its surface to generate well-performance conductors.[3] At a specific wavelength, LSPR peak, the charge-induced field, results in an induced dipole that may be

considered to be spatially invariant within.[3] At a specific wavelength, LSPR peak, the charge-induced field may be considered to be spatially invariant within small NPs with diameters smaller than approximately 20 nm, but varying with time, following the electric field of the incident electromagnetic wave. For larger NPs, higher orders poles or multipoles must be considered to describe the charge-induced field.

The collective oscillation of the electrons yields a large optical extinction cross section (σ_e) of NPs, including the contributions of both scattering and absorption. As a consequence of the interaction with a light, the induced dipole oscillator emits the light at the same frequency as the incident light, being scattered in all directions. The effective area of the particle, scattering the light, is defined as the scattering cross section (σ_{scat}).[115] In addition, the electric resistance of NPs is responsible for the absorption of the incident light, since the metallic NPs are not perfect conductors and therefore the oscillating electrons lose some of their energy in the form of heat. The corresponding effective area of absorbing light is the absorption cross section (σ_{abs}). The absorption feature can efficiently be used for a localized heating application, for example, hyperthermia in cancer therapy.[116, 117] In short, the extinction cross section is defined as:

$$\sigma_{ext} = \sigma_{scat} + \sigma_{abs} \tag{1}$$

It corresponds to the total loss (by scattering and absorption) when the light is incident on NPs. The optical cross sections are dependent upon the induced dipole, controlled by multiple factors (e.g., composition, size, and shape of NPs, the surrounding medium, and the wavelength of the incident electromagnetic wave). Certainly, plasmonics is of great importance because the scattering, absorption, and extinction cross sections can become tremendous when the incident light reaches the resonance condition.[116, 118, 119] The phenomenon results in one or more peaks in the scattering, absorption, or extinction spectra, known as plasmonic resonance peaks.

3.6.2 Permittivity of Metals

The optical properties of metal NPs primarily depend upon the permittivity, $\varepsilon(\omega)$, which is composed of both real ($\varepsilon_r(\omega)$) and imaginary parts ($\varepsilon_i(\omega)$) :

$$\varepsilon(\omega) = \varepsilon_r(\omega) + i\varepsilon_i(\omega) \tag{2}$$

where ω is the radial frequency. In general, the position of the resonance peak is mostly determined by the real part, while the dephasing depends on the imaginary part.[3]

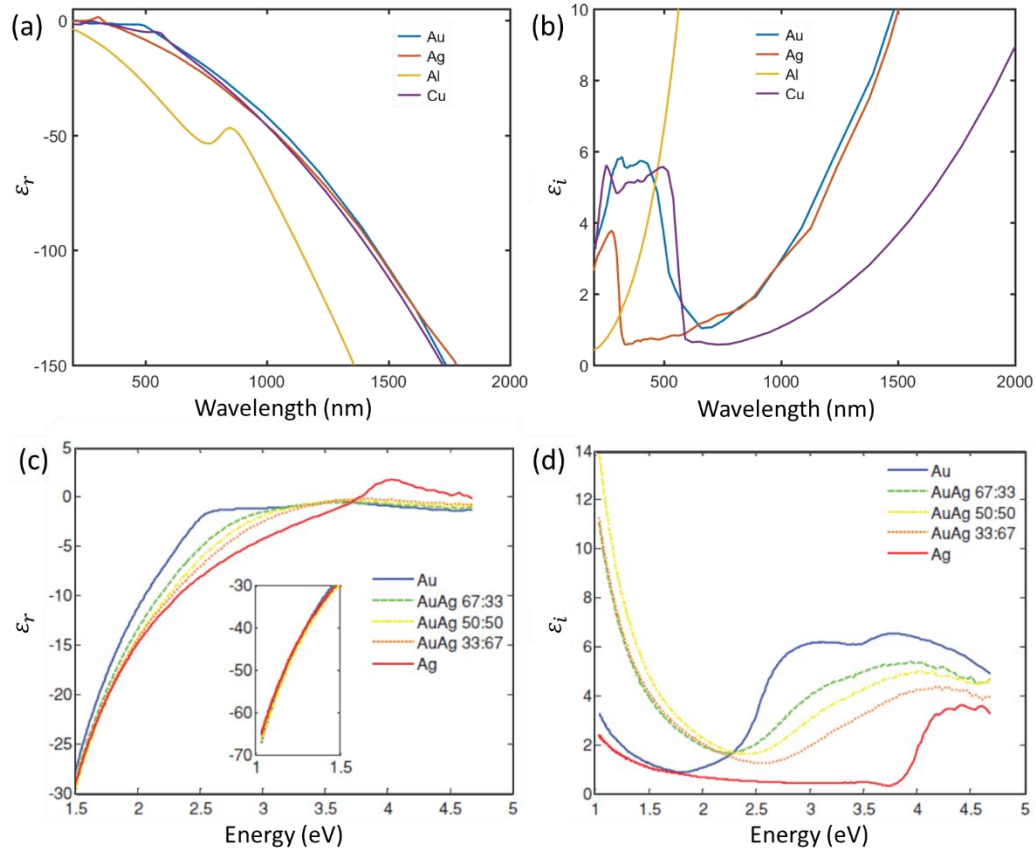

Figure 3.2 (a) Real and (b) imaginary parts of permittivity as a function of wavelength for Au, Ag, Al and Cu as obtained experimentally. (c) Real and (d) imaginary part of dielectric constants of Au, Ag and Au/Ag alloy thin films as a function of energy. Reproduced with permission.[120] Copyright 2014, John Wiley & Sons, Inc.

Figure 3.2a,b show the experimental real and imaginary parts of Ag, Au, Al, and Cu.[121, 122] The behavior of these curves can be described by many contributions, including the ones from free electrons and interband transitions. The simplest model to describe the permittivity of metal is the Drude model in which conduction electrons are considered to be free electrons.[123] Therefore, it can be expressed as:

$$\varepsilon(\omega) = 1 - \frac{\omega_p^2}{\omega(\omega + i\gamma_b)} \tag{3}$$

where ω_p is the plasma frequency and γ_b is the bulk damping constant related to the Fermi velocity v_F and the mean free path l_m, as:

$$\gamma_b = \frac{v_F}{l_m} \tag{4}$$

The Fermi velocity is calculated by using the electron density, vacuum permittivity, and effective mass of the electrons. It varies with the electron density of different metals. The mean free path depends upon the effects of various factors, such as phonons and impurities. For example, v_F and γ_b for Au are $v_F=1.4\times10^6$ ms^{-1} and $\gamma_b=(15\text{ fs})^{-1}$, resulting in a mean free path of l_m = 21 nm at room temperature.[3, 123] When the diameter of NPs is smaller than the l_m, the surface effect should be taken into consideration.

$$\gamma(l_{eff}) = \gamma_b + \frac{Av_F}{l_{eff}} \tag{5}$$

where l_{eff} is the effective path length, which is the average distance the electrons travel before scattering off a surface, and A is a dimensionless constant representing the electron-surface interaction.[3] The value of l_{eff} is related to the shape of NPs, and can be calculated by volume V and surface S of the NP, as $l_{eff}=4V/S$.[124]

Interband transitions are obtained from the lower-energy electrons compared to free electrons, and their effect only becomes large when the incident energy is high enough. Some interband transition energies are, for example, 3.9 eV for Ag, 2.4 eV for Au, and 2.1 eV for Cu. The interband transition will affect the frequency dependence of damping and can be taken into account by adding a term to the permittivity:

$$\varepsilon(\omega) = \varepsilon^{ib}(\omega) + 1 - \frac{\omega_p^2}{\omega\left(\omega + i\gamma(l_{eff})\right)} \tag{6}$$

This term can be separated into real and imaginary parts, as $\omega \gg \gamma$:

$$\varepsilon_r(\omega) \approx \varepsilon_r^{ib}(\omega) + 1 - \frac{\omega_p^2}{\omega^2} \tag{7}$$

and

$$\varepsilon_i(\omega) \approx \varepsilon_i^{ib}(\omega) + \frac{\omega_p^2\,\gamma(l_{eff})}{\omega^3} \tag{8}$$

Since l_{eff} does not appear in the real part for small NPs, it is almost the same as for bulk: $\varepsilon_r(\omega) \approx \varepsilon_r^b(\omega)$. The imaginary part depends strongly on $\gamma(l_{eff})$, indicating that the most significant size factor influences the damping with an electron surface scattering.

The condition for considering surface scattering of electrons depends on the dimension of NPs that should be smaller than the mean free path, l_m. Due to the quantum confinement, very small particles are no longer conductors, and therefore the Drude model is no longer the appropriate description.

In addition to pure metals, their alloys can also play a significant role in terms of permittivity Au/Ag alloy permittivity.[125] for example, have recently been determined. The real and imaginary parts measured by ellipsometry for several compositions are shown in Figure 3.2c,d. Interband transitions shift progressively from Au (~2.5 eV) to Ag (~4 eV) and result in a similar shape for the real part, unlike the imaginary part. The alloys exhibit higher absorption than pure metals at low energy.[120] Meunier and co-workers developed an analytical model for the prediction of the dielectric functions of Au/Ag alloys.[120] These multi-parametric equations are based on the modification of the Drude-Lorentz model, considering the band structure of the different Au and Ag metals.

3.6.3 Scattering and Absorption of Spherical Nanoparticles

Gustav Mie was the first, in the early 1900s, who calculated the optical cross sections, σ_{sca}, and σ_{ext}, of spherical NPs.[126] Mie theory is a precise calculation based on Maxwell's equations for spherical particles, using the permittivity of NPs and their surroundings. The general expression for scattering and extinction cross sections are:

$$\sigma_{sca} = \frac{2\pi}{\left|\vec{k}\right|^2} \sum_{l=1}^{\infty} (2l+1)(|a_l|^2 + |b_l|^2) \tag{9}$$

$$\sigma_{ext} = \frac{2\pi}{\left|\vec{k}\right|^2} \sum_{l=1}^{\infty} (2l+1)(a_l + b_l) \tag{10}$$

where

$$a_l = \frac{\varepsilon_m m^2 j_l(x)[x j_l(x)]' - \varepsilon j_l(x)[mx j_l(mx)]'}{\varepsilon_m m^2 j_l(mx)\left[x h_l^{(1)}(x)\right]' - \varepsilon h_l^{(1)}(x)[mx j_l(mx)]'}, \tag{11}$$

$$b_l = \frac{\varepsilon j_l(x)[x j_l(x)]' - \varepsilon_m j_l(x)[mx j_l(mx)]'}{\varepsilon j_l(mx)\left[x h_l^{(1)}(x)\right]' - \varepsilon_m h_l^{(1)}(x)[mx j_l(mx)]'}, \quad (12)$$

j_l and h_l are respectively Bessel and Hankel functions. $x = |\vec{k}|$R, $\vec{k}$ is the wave vector, and R is the geometric radius of NP; ε_m is the permittivity of the medium, and ε is the permittivity of the NP and $m = n/n_m$, where n is the complex refractive index of NP and n_m is that of the surrounding medium. The number *"l"* corresponds to dipole (*l = 1*), quadrupole (*l = 2*), octupole *(l = 3*), and so on. Dipole theory can give cross sections when the size of spherical NPs is small compared to the wavelength of the incident light, typically when $R < \lambda/20$. The absorption and scattering cross section can be calculated in the dipolar approximation:

$$\sigma_{abs} = \frac{24\pi^2 R^3 \varepsilon_m^{\frac{3}{2}}}{\lambda} \frac{\varepsilon_i}{|\varepsilon + 2\varepsilon_m|^2} \quad (13)$$

$$\sigma_{scat} = \frac{32\pi^4 R^6 \varepsilon_m^2}{\lambda^4} \left|\frac{\varepsilon - \varepsilon_m}{\varepsilon + 2\varepsilon_m}\right|^2 \quad (14)$$

where the permittivity of NPs, ε, is composed of real and imaginary parts, as $\varepsilon = \varepsilon_r + i\varepsilon_i$, and ε_m is the permittivity of the surrounding medium. According to these equations, for ε_i close to zero, the resonance condition occurs when $\varepsilon_r = -2\varepsilon_m$, resulting in extremely large σ_{ext}.[32] The two requirements are satisfied only by a few metals, such as Au, Ag, Cu. For very small NPs, $R \ll \lambda$, the extinction is essentially the absorption, $\sigma_{ext} \approx \sigma_{abs}$, as the scattering is negligible ($\sigma_{scat}/\sigma_{abs} \propto (R/\lambda)^3$). In the dipole approximation, the internal field is considered to be proportional to the incident field, with a frequency-dependent factor, the local field factor, f:

$$f(\omega) = \frac{3\varepsilon_m}{\varepsilon + 2\varepsilon_m} \quad (15)$$

This factor indicates that there may be an important field enhancement inside and around the particle as the different permittivities of the particle and the media vary with the irradiating wavelength. This also indicates that the resonance condition is $\varepsilon_r = -2\varepsilon_m$.

In the dipole approximation, the plasmon peak occurs at $\frac{\omega_p}{\sqrt{1+2\varepsilon_m}}$. When the NPs become larger, $R > \lambda/20$, the internal field in the NPs cannot be assumed to be uniformly distributed into the NPs

and. multipoles must be considered. The plasmon peak for the corresponding *"l"* can be approximated by:

$$\omega_l = \frac{\omega_p}{\sqrt{1 + \frac{l+1}{l}\varepsilon_m}} \tag{16}$$

Only noble metals (e.g., Ag, Au, and Cu) have their LSPR in the range of ultraviolet (UV)-visible and NIR, while most other metals have resonance frequencies in the deep UV range or higher frequencies.[32, 84] Based on Mie theory, Meunier and co-workers have developed the NFMie program in order to theoretically calculate the optical cross section and field enhancement of arbitrary spherical NPs.[120, 127, 128] For example, plasmon peaks, σ_{abs}, and σ_{scat} vary with the diameter and composition of Au and Ag NPs (Figure 3.3a-i,b-i).

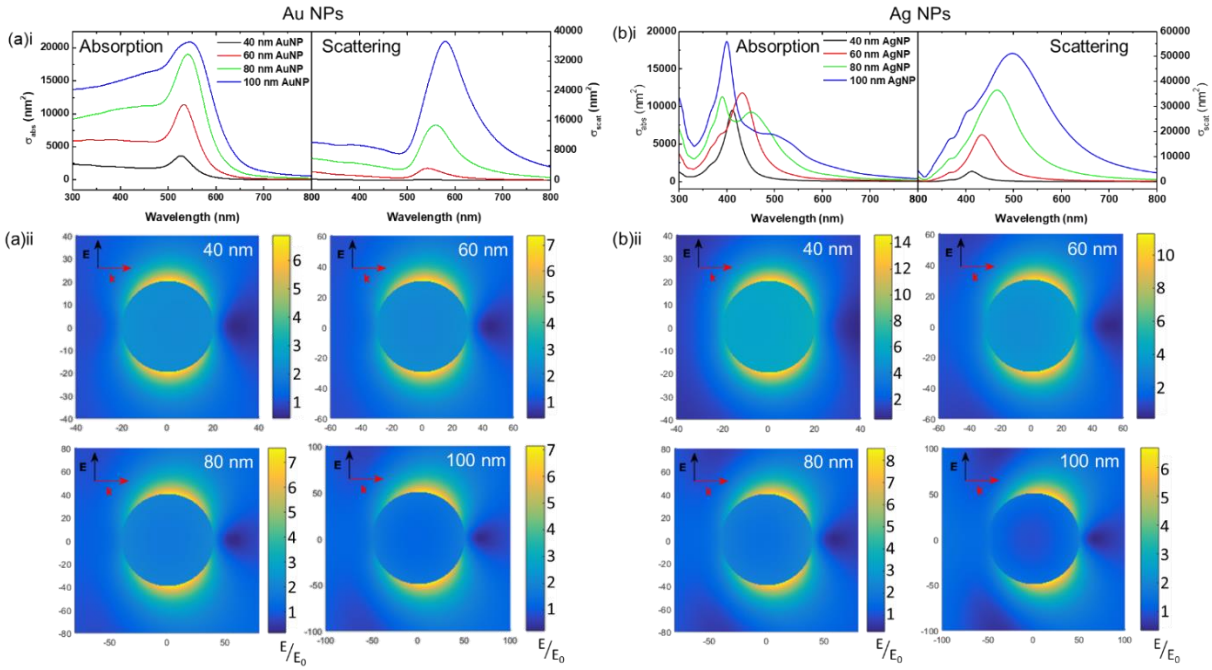

Figure 3.3 Absorption and scattering cross sections, σ_{abs} and σ_{scat}, of (a-i) AuNPs and (b-i) AgNPs in water with diameter of 40, 60, 80 and 100 nm, and (a-ii) and (b-ii) show their electric field enhancement (E/E_0) at the wavelength of scattering resonance, respectively. Calculations done by using Rioux and Meunier's developed NFMie program.[128]

3.6.4 Surface Enhanced Effects

The plasmonic resonance leads to way larger optical cross sections when compared to the real dimensions of NPs, resulting from the amplification of the electromagnetic field around the NPs. Indeed, upon the irradiation by the incident light, the oscillation of free electrons generates an additional electric field near the surface of NPs, and enhances the original field if the phase delay is relatively small. For example, Figure 3.3a-ii,b-ii show the electric field distribution of Au and Ag nanosphere (40-100 nm in diameter) at resonance frequency with a field amplification E/E_0 reaching close to ~7 for Au and ~14 for Ag.[127, 128]

When some molecules are in the near-field amplification of NPs, their fluorescence or Raman spectra can dramatically be enhanced. These phenomena lead to a greater surface-enhanced Raman scattering (SERS) and surface-enhanced fluorescence (SEF). This field enhancement effect is related to the intrinsic properties of plasmonic NPs and the incident light. In the case of SEF-based applications, the molecule must not be too close in order to avoid quenching of the signal by the nearby presence of the metallic NP. However, this limitation is relatively minor for SERS-based applications, and the enhancement of the Raman signal near the surface of the NP can reach many orders magnitudes. Both the absorption of incident light and Raman signal depend on the locally enhanced field. The amplification factor G is given by:

$$G = |E_{local}(\omega_L, r)|^2 |E_{local}(\omega_R, r)|^2 \quad (17)$$

where ω_L is the frequency of the incident light and ω_R is that of the Raman signal. As the Raman signal shift is very small, it may possible to assume that $\omega_L \approx \omega_R$, thus:

$$G = |E_{local}(\omega_R, r)|^4 \quad (18)$$

For spherical nanoparticles, as the field enhancement may be near 10, and G may be 10^4-10^6. The enhancement also depends on the shape of the metallic nanostructures, especially the narrow gap and high curvature of the surface.[129, 130] In general, sharp angles may lead to far bigger field enhancement of 100 to even 1000, resulting in G with an approximate value from 10^8 to 10^{12}, which has been implemented for a wide range of applications.[131-133]

3.6.5 Shape Effects

Mie theory has been extended to other types of spheroidal NPs, including core-shell geometry with different metals or dielectric components.[134-136] Considering the size-dependent electron surface scattering features of the shell, the effective free path can be modified in order to bring the scattering on the surface between core and shell into play. As confirmed by Mie theory, NPs composed of both metallic core or shell show significant resonance shifts in a size-dependent manner. Encina and Coronado have applied Mie theory for simulating the extinction spectra of iron oxide@noble metal core-shell nanostructures. In their study, α-Fe_2O_3@Ag core-shell NPs, for example, have been designed for obtaining an adaptable resonance peak and photothermal effect shift by varying the dimension of the core or the shell. Figure 3.4 illustrates a dimension-dependent heating effect under different irradiant wavelengths for α-Fe_2O_3@Ag core-shell NPs.[135] Mie theory has been found beneficial for the prediction of optimized size and structure required to improve photothermal applications.

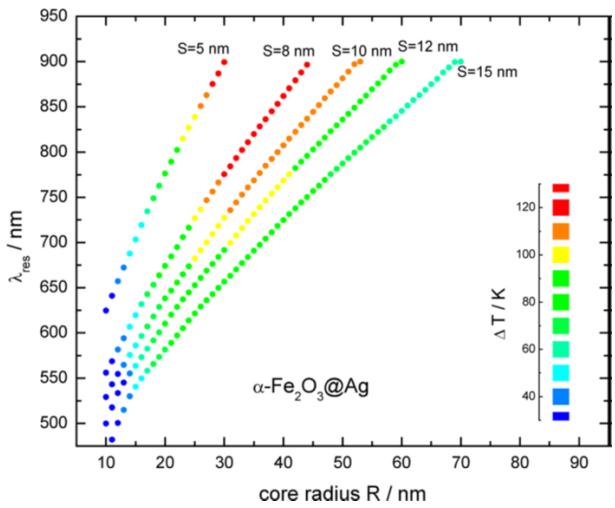

Figure 3.4 Resonance peak of α-Fe_2O_3@Ag core-shell NPs with different core radius R (in nm) and shell thicknesses S (in nm), and corresponding photothermal effect indicated by color, when dispersed in water and irradiated at their respective resonance wavelength (λ_{res}) with an irradiance of 1 mW μm^{-2}. Reproduced with permission.[135] Copyright 2016, American Chemical Society.

For nanorods, two resonance peaks corresponding to the longitudinal and transverse oscillations are observed. The resonance derived from the transverse band is weak and located in the visible range while the longitudinal resonance is strong and located in the red or NIR region (e.g.,

beneficial for biomedical applications since the biological transparency window is in the NIR region), showing a redshift with an increase of the aspect ratio.[137, 138] The longitudinal resonance is more sensitive to the aspect ratio compared to the transverse mode, which can be approximately described by the Gans theory,[139] and recently simulated by numerical methods.[140, 141]

In the case of non-spherical NPs, Mie theory is not applicable, and therefore sophisticated numerical approaches including finite difference time domain (FDTD), finite element methods (FEM), and DDA are needed to calculate optical properties from Maxwell's equations.[73, 142]

FDTD is based on Maxwell's equations, which are discretized both in time and space. This method has several advantages, including a simple implementation and flexibility in terms of the geometry-dependent properties, and can be applied to either 2D or 3D simulations. However, this method simulates a space domain larger than that of the NPs and requires the emulation of an infinite domain. At the same time, it may provide transient results but not steady-state.

FEM is based on Helmholtz vector equations and yields approximate results at discrete points over the domain. This method is useful to accurately represent various structures and solve multiphysics problems. Compared to FDTD, this approach generates results in steady-state terms and shows limitations for transient ones. It is more complex to implement and mesh the structure due to the simulation of a larger domain than the particle and a requirement for the emulation of an infinite domain.

Another widely used approach, DDA, is a frequency domain method derived from Maxwell's equations. The calculation is an approximation generated from the interaction between a finite array of discrete points in a continuum target. DDA is flexible in geometry and only simulates the domain of the particles. In this case, only steady-state conditions can be obtained and it is not possible to simulate transient ones. The solution accuracy shows a little improvement by adding more dipoles. Since both DDA and FEM simulate at a specific wavelength, calculations may take time for the whole spectrum.

Irregular nanostructures (i.e., nanocubes and nanoprisms), result in a more complicated interaction with light, are typically accompanied by wider peaks over a broad range of wavelengths.[143] As shown for silver nanostructures (Figure 3.5), shape and geometry greatly affect the LSPR spectra.[32] In another study, Kottmann et al. found that these resonances and associated strong

fields can come from the accumulated polarization charges on the surface of plasmonic NPs.[144] The field distribution around non-spherical nanostructures can be extremely stronger near sharp tips, suitable for near-field enhancement applications.

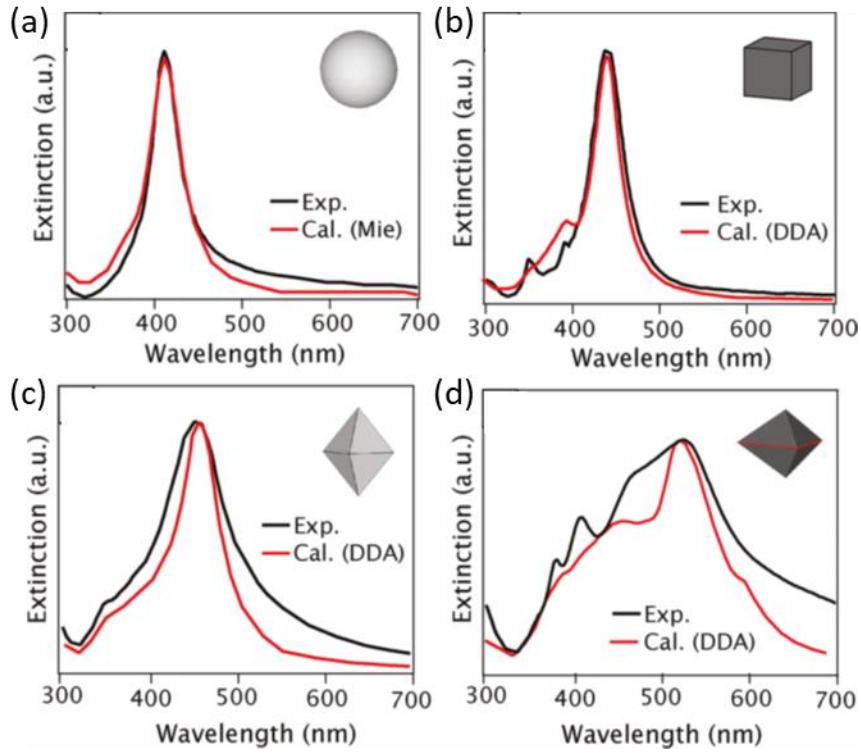

Figure 3.5 Experimental (black) and calculated (red) extinction spectra of AgNPs, (a) spheres, (b) cube, (c) octahedron, (d) right bipyramid. Reproduced with permission.[32] Copyright 2011, American Chemical Society.

3.6.6 Composition Effects

The chemical composition of nanostructures directly affects the interaction with light, leads to different optical properties (e.g., influencing the position and width of the resonance peaks). Noble metals, including Au, Ag, and Cu, dominate such promising properties in both visible and NIR ranges due to their intrinsic permittivity.

As a conclusion of Mie theory in the dipole approximation, the resonance happens when the real part of the metal's permittivity and the surrounding medium meets the condition $\varepsilon_r \approx -2\varepsilon_m$. Since the typical environment is air or water with a positive dielectric permittivity, for such NPs the

negative real part is required. In addition, the imaginary part, ε_i, of the metal may affect the quality of the plasmonic resonance peak, and it should be small at the resonance condition to confine the choice to several types of metals (e.g., Au, Ag, Cu, etc.).[32, 145] This approach works for spherical NPs, whereas the structure of nanomaterials should be taken into consideration for most of LSPR-based applications.

To evaluate the performance of metals, it is necessary to consider not only their plasmonic efficiency and wavelength range but also their stability. Al, Mg, In, and Ga are mostly functional in the UV region due to the high frequency of plasma, and although Li can be used for a broader region, its extraordinary activity limits any utilization.[32, 146] Therefore, Ag (narrow and intense plasmonic peaks), Au (visible to NIR plasmon range, chemical stability, and inertness), and Cu (a range from red to NIR and relatively inexpensive) are the most commonly used metals for different applications in the visible and NIR region.[143]

Alloy provides opportunities for tuning resonance by changing the permittivity through composition.[120] There are many combinations of different metals, showing higher flexibility over pure metals. Alloy enlarges the choice of potential metals (e.g., Pt and Pd) to be combined with Au or Ag.[147, 148] Meunier and co-workers have developed a unique approach to synthesized Au/Ag alloy by fine controlling both composition and size.[50, 149] In the case of alloys, since the resonance peak can be adjusted between that of the pure metals, Au/Ag alloy nanoparticles, for example, can cover nearly all visible wavelengths with proper size and dimension, enabling imaging applications.[50, 89, 150]

3.6.7 The Effect of Surrounding Media

The plasmonic resonance occurs at $\varepsilon_r \approx -2\varepsilon_m$, which emphasizes the importance of the surrounding medium of the light interacting NPs. The surrounding medium not only determines the resonance wavelength of the electromagnetic wave and modifies the geometry of the electric field around NPs, but also affects the polarization within individual particles.[151] The electric field resulting from oscillating electrons in the particle induces the polarization of the surrounding medium by generating charge accumulation around the interface within the particle. The accumulated charges may reduce the conduction electrons in oscillation, as larger ε_m results in a dramatic reduction.[151] As a result of reducing oscillating electrons, the plasmon peak resonance can shift to a longer

wavelength, and the intensity of the resonance peak increases, for example, as in the dipole approximation, the absorption cross section proportional to $\varepsilon_m^{3/2}$. Figure 3.6 illustrates the extinction cross section and the electric field around AuNPs and AgNPs (60 nm in diameter) imbedded in surrounding media with different RI calculated by using NFMie program (Mie theory).[127, 128]

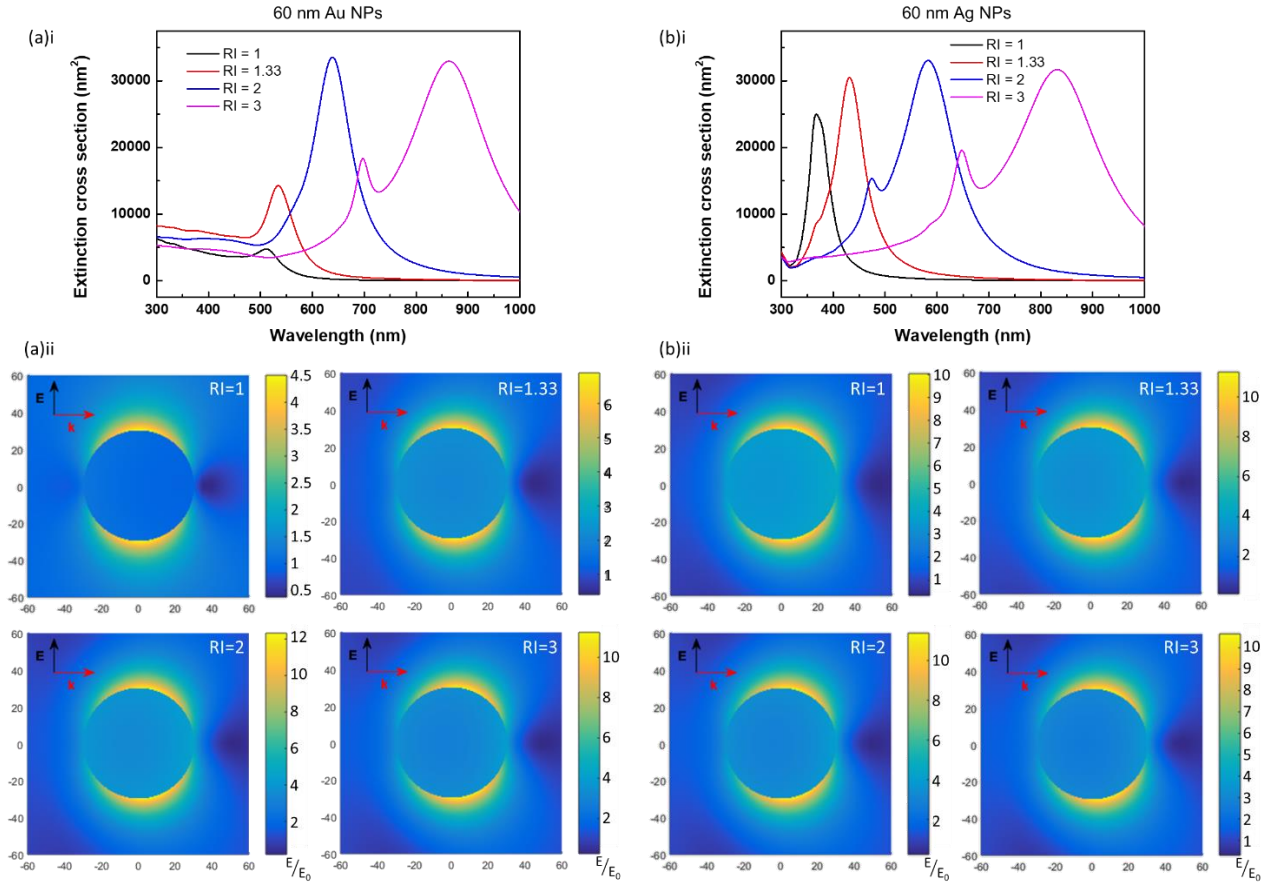

Figure 3.6 Calculated extinction cross section (a-i and b-i) and their electric field enhancement of NPs (a-ii and b-ii) at extinction resonance for 60 nm AuNPs and AgNPs in media with different refractive indices (RI) as given in the legend. Calculations done by using Rioux and Meunier's developed NFMie program.[128]

Based on the effect of the surrounding medium on plasmonic properties of NPs, multiple metallic and dielectric materials can behave as a surrounding medium to enhance and adjust plasmonic peaks. Indeed, a dielectric core and multilayer materials with different permittivities have been designed and synthesized to obtain specific plasmonic properties.[152] Nanomatryushka, a

multiple nanoshell, is an interesting structure showing an enhanced plasmonic peak.[153-155] Silica is typically involved in the core or certain layers within the structure as dielectric spacers. Such nanostructures enable a way to control the resonance peak and its amplitude by playing with the "medium" within the NPs, without changing the size of particles. NPs are also required to be stabilized by using capping agents, such as different molecules and polymers in order to be suitable for real situations. The capping agents strongly affect the surface plasmon of NPs (e.g., resonance peak shift, amplitude increases or decreases, as well as the accessibility and effectiveness of the field enhancement) by changing the medium permittivity that significantly influences the performance of application-oriented plasmonic NPs [75, 156, 157]

3.7 Applications of Plasmonic NPs

LSPR phenomenon causes strong absorption and scattering effects at the resonance frequency near the NPs surface and triggers the generation of particular physiochemical features suitable for advancing a wide range of cutting-edge applications. Other than the optical cross sections, LSPR also creates a great field enhancement, which improves Raman and fluorescent signals. All these specific plasmonic properties, exploited in the field of biomedical, energy, catalysis, and information technologies, are summarized and comprehensively discussed in this section.[78, 158-161]

3.7.1 Biomedical Technology

3.7.1.1 Absorption-Based Applications

The absorption cross section of plasmonic NPs dramatically increases the localized energy absorption and directly generates thermal phenomena associated to the surface plasmon.[116, 137] The strong absorption of plasmonic NPs induces different fascinating effects (e.g., a local temperature rise, acoustic wave, and bubble formation), which lead to new clinical theranostic techniques.[162, 163]

- **Hyperthermia**

Irradiation of plasmonic NPs at their resonance wavelength can cause a local temperature rise suitable for a wide range of therapies. Hyperthermia is a non-invasive approach owing to the

generation of a confined thermal effect around the irradiated NPs and high thermal contrast between NPs and tissue. With a surface functionalization (e.g., biomolecule and ligand conjugations), NPs can selectively target specific abnormal cells, and generate an effective thermal gradient on the cells to influence cellular activity and integrity. With an intense irradiation, the temperature rise of the cellular binding NPs can destroy the target cells by melting membrane and destructing the cytoskeleton and the nucleus, and cause an intracellular release of biomolecules and protein denaturation.[164] Due to the effective thermal contrast caused by the irradiated NPs, the intensity of laser light required for the hyperthermia of abnormal cells can be minimized to avoid any unnecessary damages to surrounding healthy tissue. For example, AuNP-mediated nanosecond laser has been used in eliminating retinoblastoma cancer cells. The localized heat generated by using a small fluence (e.g., 20 J cm^{-2} from a nanosecond laser) has shown an effective cellular death up to 80 % for both adherent and floating cells without harming other normal cells.[165] The plasmonic NPs have also been widely applied to combat and eliminate bacterial infections due to their photothermal feature. Antibody-conjugated NPs specifically bind to the target bacteria, and after laser irradiation, the localized heating generates an efficient antibacterial effect.[166-168]

Taking advantage of the deep tissue penetration of NIR laser light, plasmonic NPs with a resonance peak in the NIR region show a significant capability for clinical treatments. Certain morphologies, such as nanorod, nanoshell, and nanostar, with NIR resonance have been developed to target deep tissues with long-wavelength lasers.[169-171] Plasmonic nanorods, for example, are one of the promising candidates for photothermal therapy due to their redshift resonance peak compared to the nanospheres at the similar dimension.[172] Yeh and co-workers explored the second biological transparency widow, around 1000-1350 nm with longer wavelengths than the first window (650-950 nm) by developing a rod-in-shell structure (with a dimension less than 100 nm) to cover both two transparency windows, and thus greater cancer cell killing efficiency has been gained in both *in vitro* and *in vivo* compared to simple nanorods.[169] Due to the minimum light loss (absorption and scattering) through tissue and biomolecules, both first and second NIR window can penetrate deeper than other wavelength ranges. Studies have explored the two biological windows in phototherapy, bioimaging, and biosensing including field-enhanced fluorescent and Raman.[173-175]

Highly localized photothermia effects based on plasmonic absorption in NIR region has been tested in human. Rastinehad et al, applied Au-silica nanoshells, with NIR absorption, in photothermal treatment for localized prostate cancer. In the clinical trial, they reported safe parameters and high-efficient results with plasmonic NPs infusion and focused laser ablation in human.[176] Au-silica nanoshells in the treatment provides highly localized hyperthermia platform to control prostate cancer while avoiding the deleterious side effects. The pilot clinical trial demonstrated safety and efficiency of photothermal cancer treatment based on plasmonic NPs applied in human.

Photothermal effects have been elaborately adapted to generate a local stimuli-responsive therapeutic release. Chemotherapeutic molecules assembled in nanoshells, nanocages, or porous plasmonic NPs can precisely be released at the target tissue using a laser light at the corresponding plasmon resonance.[177-179] The generated local heat on the irradiated NPs can induce a phase transition or degradation of chemical linkers (e.g., polymers and micelles) on the surface of nanocarriers, thus releasing the bound cargos. Figure 3.7a illustrates the process of drug loading into Au nanocage, cancer cell membrane coating, and anticancer drug doxorubicin (DOX) release triggered by NIR irradiation for a homotypic targeting and treatment *in vivo*.[177] DOX was initially loaded in the porous Au nanocages (DAuNs), then coated with the cell membrane of 4T1 cells (CDAuNs). Afterwards, the prepared CDAuNs (nanocarriers), which were injected into mice adapted with the breast cancer, selectively targeted the tumor cells through the homotypic targeting. Quantitative analysis of DOX distribution *in vivo* has been performed at 1, 4, and 24 h after the injection (Figure 3.7b). NIR laser (at 808 nm) irradiated the NPs generated the photothermal heating and the stimuli-triggered drug release locally in the tumor site (Figure 3.7c, d). In fact, the cell membrane coating on the plasmonic nanocarriers promoted a site-specific targeting in tumor for treatment *in vivo*. The thermal-responsive capping by using the cell membrane also improved biocompatibility, reduced the therapeutic leakage in the physiological environment, and decreased the drug releasing temperature to 43 ℃, achieving a synergy of thermo- and chemo-therapy with a precise spatiotemporal control.

Plasmonic NPs, especially those carriers with a NIR resonance (e.g., nanocages, nanorods, nanostars), have a leading advantage over other materials, such as carbon-based or polymer-based nanomaterials, for cancer therapy due to the localized hyperthermia effect for release control and thermotherapy. Loading capacity may become a limitation for solid plasmonic NPs, because of the

high density of metal NPs; however, the fabrication of porous nanostructures as well as the selectively local release effect can make up for that, to gain higher efficiency in chemo- and thermo-therapy.

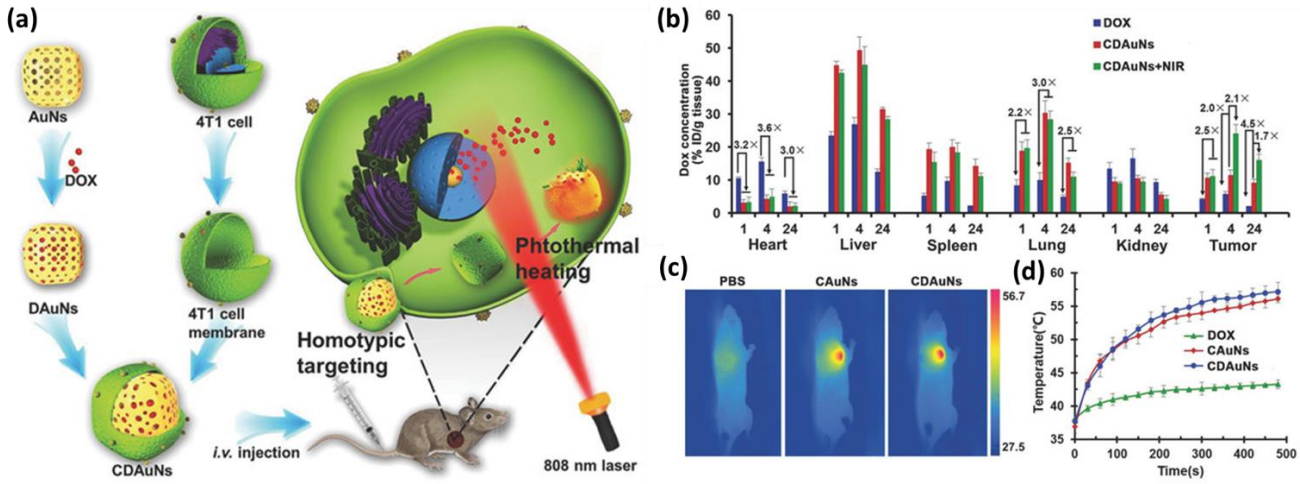

Figure 3.7 (a) Schematic describing drug loading and cancer cell membrane-coating of Au nanocage for the hyperthermia-triggered release of DOX and *in vivo* treatment of breast tumor. (b) Quantitative DOX distribution analysis *in vivo* after 1, 4, and 24 h post-injection, (c) infrared thermographic images of breast tumor bearing mice with different injection (PBS, cell membrane of 4T1 cells-coated Au nanocages (CAuNs), cell membrane of 4T1 cells-coated DAuNs (CDAuNs)), and (d) temperature increase of the tumor tissues *in vivo* with injection of DOX, CAuNs and CDAuNs under NIR irradiation. Reproduced with permission.[177] Copyright 2016, John Wiley & Sons, Inc.

- **Photoacoustic Imaging:**

Photoacoustic phenomenon is one of the functional approaches for deep-tissue high-resolution bioimaging.[92, 180-182] Since ultrasound wave has longer wavelength compared to that of the optical signal, it can easily penetrate into deep tissues without the degradation.[183] However, the use of ultrasound without the contrast agents, such as metallic NPs, can only reflect the mechanical properties of the target tissue due to lack of the optical contrast.[184] Plasmonic NPs owing to their strong absorption of the incident light, the temperature of and around the targeted NPs can rapidly increase, thus generating an acoustic wave during the heat transfer. The triggered acoustic signal can be subsequently detected from the body surface (superficial skin layer) by ultrasonic

transducers and converted to high-resolution images. In most cases, short pulsed lasers have been employed to generate transient thermal expansions from the local area of NPs at the tissue, as a photoacoustic excitation caused by a thermoelastic expansion.[185] Placing the ultrasound transducers near the target tissue can freely receive the acoustic signals reaching the body surface, and the images can be constructed with the distribution and intensity of the light absorption. On the other hand, the use of detectors at different locations from the target tissue can elaborately generate the photoacoustic tomography accompanied by complexed structures. The intensity of the photoacoustic signals, which are proportional to the heat generated by the absorption of electromagnetic wave, can be adjusted to facilitate high-resolution 2D and 3D image processing.[183, 186] Photoacoustic phenomenon is an interesting approach in high-resolution bioimaging obtained by the combination of the ultrasound and differentiable contrast given by cellular binding plasmonic NPs.[92, 180-182]

Au nanostructures as photoacoustic contrast agents have been applied for cancer diagnosis, brain vasculature and function, as well as the image-guided therapy.[187] Among which, Au nanostructures accompanied by the NIR resonance (e.g., nanorods, nanoshells, nanoprisms, nanostars, and nanocages) are preferable for visualizing deeper tissues by using elaborated photoacoustic devices. For example, Au nanostars with a tunable NIR resonance can also improve the contrast of photoacoustic imaging (Figure 3.8).[188] Post-fabrication with cyclic Arg-Gly-Asp (RGD) peptides has shown a great potential for targeting of endothelial cells with overexpressed integrin $\alpha_v\beta_3$, which associates with neovessels in tumor. The gold nanostars (GNS), prepared with an extinction peak ~790 nm, interestingly keep their intrinsic optical properties after the functionalization with RGD peptides as well. Therefore, the specific targeting and high photoacoustic contrast enabled RGD-GNS to improve the quality of photoacoustic imaging by providing high specificity and sensitivity. Meanwhile the absorption of plasmonic NPs at the resonance largely enhances the localized photothermal effect, that may be used for tumor treatment ((Figure 3.8e). This elaborate development of multifunctional plasmon-based nanomaterials demonstrates great potential in theranostics due to the high contrast created by site-specific cellular binding NPs over the target tissue, as well as precise localized photothermal therapy. Besides nanostars, nanorods have been widely applied in photoacoustics as contrast agents.[189, 190] Ultra-small Au nanorods coated with an organic dye (IR780) and anticancer drug DOX have also

shown their ability to enhance photoacoustic and therapeutic effects.[182] Therefore, the imaging contrast agent (e.g., plasmonic nanostars as an “on-spot” theranostic platform) helps to detect and identify the target tissues for proceeding an effective therapeutic hyperthermia, which only omits the cancer cells without inducing side effects to healthy organs.[188]

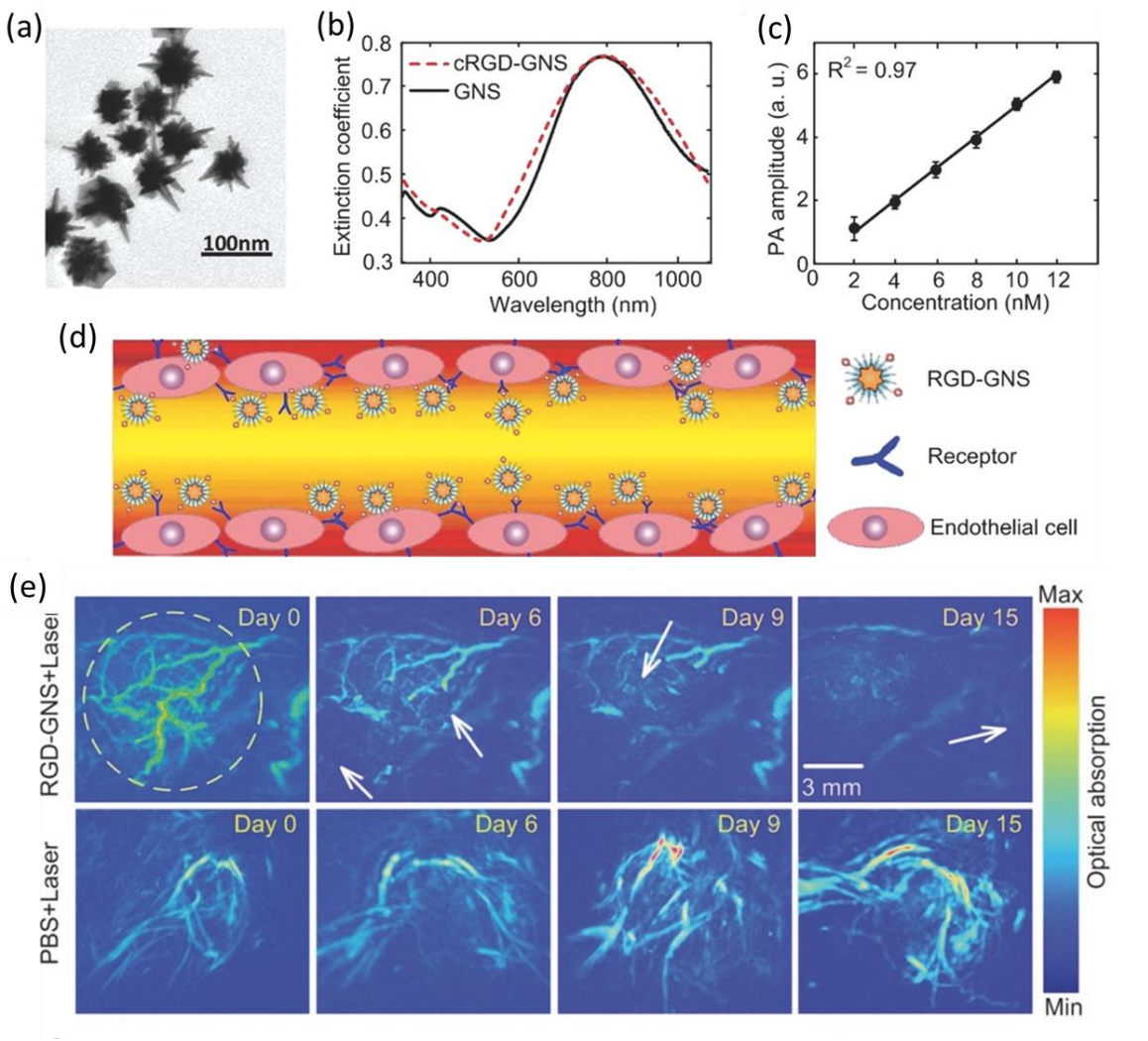

Figure 3.8 (a) TEM image of gold nanostars (GNS), (b) extinction spectra of GNS and RGD-GNS, with peak at ~790 nm, and (c) experimental relation between photoacoustic (PA) amplitude and concentration of NPs. (d) Schematic of RGD-GNS specifically targeted on endothelial cells. Photoacoustic images (e) for therapy monitoring in 15 days with Au nanostars and PBS injection. The white arrows in figure (e) point out the obvious changes after treatment with RGD-GNS. (RGD-GNS: Cyclic Arg-Gly-Asp (RGD) peptides conjugated plasmonic gold nanostars; PBS:

phosphate-buffered saline). Reproduced with permission.[188] Copyright 2013, John Wiley & Sons, Inc.

- **Optoporation:**

Transfection is an alternative effective approach for disease treatments. The optical transfection, known as optoporation, triggers a mild cellular perforation to directly deliver therapeutics into the cytoplasm of the target cells. This optical approach (physical) illustrates certain great advantages over other non-physical transfection strategies (viral and non-viral) due to the high transfection rate and less toxicity.[191] Photostability and their ability to be functionalized with biomolecules and ligands allow plasmonic NPs specifically attach to targeted cells for the optoporation. Compared to other physical approaches (e.g., mechanical and physical transfection) limited for gene delivery *in vivo*, plasmonic properties combined with the pulsed laser realize optoporation as the most precise and accurate transfection method *in vivo*; however, it still needs attention for improving the transfection of deep tissues. High compatibility with optical microscopy, as well as the possibility of focusing beam on the layer of interest and employing short pulse, optoporation can be performed in a real time accompanied by the control and precision.[192] Since the physical disruption of the lipid bilayer of cellular membrane does not activate immune responses compared to that observed from the administration of viral vectors, optoporation can avoid the immunogenicity problems.[193]

Taking advantage of their corresponding practical responses to the incident light, plasmonic NPs-assisted laser optoporation and perforation have been developed for the transfection of living cells. A weakly focused laser irradiation of cellular binding plasmonic NPs on targeted cells can transiently permeabilize the lipid bilayer of cellular membrane and facilitate the internalization of exogenous molecules (e.g. drugs, oligonucleotides, proteins, and plasmids).[162] A short pulse laser irradiation (e.g., picosecond or femtosecond laser) can generate a rapid temperature raise, followed by the formation of nanobubbles around plasmonic NPs.[193, 194] This bubble formation process can precisely cause transient, highly localized holes on the cell membrane close to the irradiated plasmonic NPs, thus allowing various exogenous biomolecules to be delivered into target cells.[191, 195, 196]

In the early stage, fluorescent dyes (e.g., calcein, propidium iodide, and fluorescein isothiocyanate -dextran, etc.) have been frequently employed to analyze permeability mechanisms of the targeted cell membrane and improve the cellular transfection.[197, 198] AuNP-mediated picosecond laser optoporation, for example, has been found highly practical due to achieving a therapeutic level (up to 88% *in vitro*) of transfection efficiency (fluorescent labeled siRNA) into canine pleomorphic adenoma ZMTH3 cells with maintaining high cell viability (over 90%).[199]

Non-specific optoporation, conducted by a simple and random sedimentation of plasmonic NPs on the cells (*in vitro*), has truly shown inefficient therapeutic effects, and therefore an elaborated surface functionalization by means of antibodies and other biomolecules needs to be developed in order to obtain site-specific therapeutic delivery.[199] To achieve a therapeutic effects, Meunier and co-workers, for example, have developed anti-CD44 functionalized AuNPs for a selective perforation of MDA-MB-231 breast cancer cells under femtosecond laser irradiation (at 800 nm) to analyze involving mechanisms for an effective site-specific therapeutic delivery. Polyethylene glycol as a bifunctional linker (thiol and N-hydroxysuccinimide ester) can bind functional antibodies and anchor them on the surface of the plasmonic NPs. In this case, Ab_{CD44} functionalized NPs bound on the cellular membrane of MDA-MB-231^{+CD44} and ARPE-19^{+CD44} cells 150 times more than that of $661W^{-CD44}$ cells, and enabled a successful selective optoporation without influencing other cells in the co-culture.[157]

Taking advantage of site-specific therapeutic delivery for future clinical translation, Meunier and co-workers have demonstrated an effective femtosecond laser optoporation of retina (*in vivo*) by using $K_v1.1$-functionalized AuNPs (100 nm in diameter) to deliver Cyanine 3-tagged siRNA (a scramble fluorescent labeled siRNA) to retinal ganglion cells without reducing their cell viability (Figure 3.9).[88] In this case, an intravitral injection assisted the delivery of functional AuNPs and fluorescent labeled molecules (siRNA or fluorescein isothiocyanate-dextran) to the target retinal tissue. The optical path (Figure 3.9b) was administrated for the optoporation *in vivo*, with a femtosecond laser at 800 nm, locally focused on the retina (ganglion cells) of rat (Figure 3.9c,d) incubated with the pre-injected functional AuNPs and biomolecules. The results certainly prove the successful functionalization of NPs that a large number of these well-distributed NPs bound on the targeted retina tissue/explant (Figure 3.9e,f). Significant efforts are still being put to achieve the highest therapeutic effects via plasmonic NPs-assisted optoporation by reducing the fluence

threshold for the unharmful bubble formation *in vitro* and *in vivo*.[196, 200] A theoretical model has been also developed to simulate the effects of different kinds of plasmonic nanostructures participated in the optoporation. For example, silica-Au core-shell NPs designed as one of the effective nanostructures, which lowered 51 % of the cavitation threshold at the NIR irradiation (at 800 nm) compared to that of the homogeneous AuNPs.[200] The nanoshell composed by SiO_2 core (42 nm radius) and Au shell (29 nm thickness) was theoretically determined and experimentally verified as an optimum nanostructure, which reduces the cavitation threshold to ~35 mJ/cm^2.[196] This non-invasive optoporation technique may lead to an efficient cell-specific therapy in clinics.

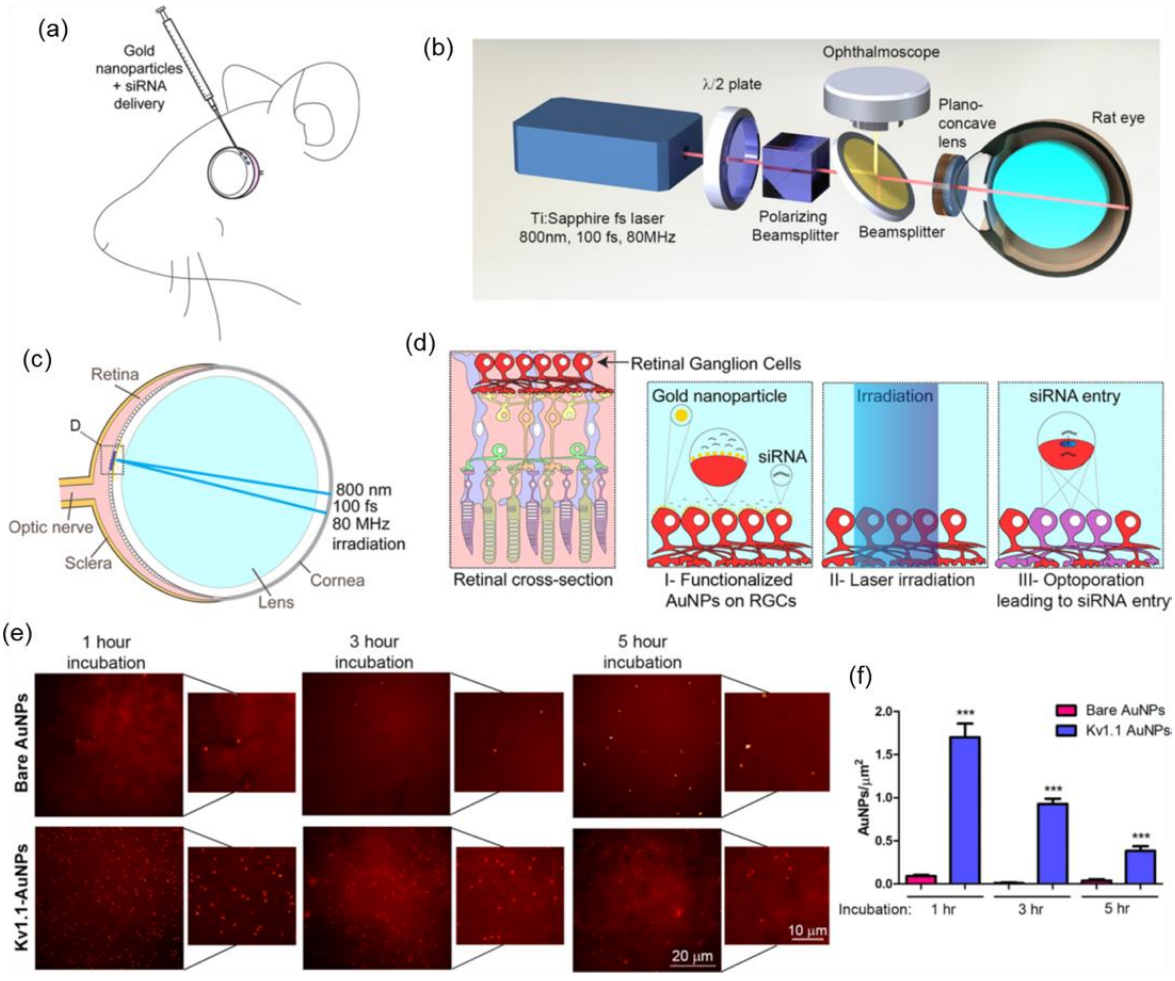

Figure 3.9 AuNP-mediated femtosecond laser irradiation for *in vivo* treatment of retina cells. (a) Schematic of the injection of NPs and siRNA to the back of the eye *in vivo*, (b) optical setup for femtosecond laser optoporation, (c) laser-beam path in the eye, and (d) detail of NPs targeted retinal cells at different steps during the treatment. Cell membrane binding and distribution of

bare and $K_v1.1$ functionalized AuNPs on retina explants (e) visualized and (f) quantified under an enhanced dark-field microscopy at different incubation periods. Reproduced with permission.[88] Copyright 2018, American Chemical Society.

3.7.1.2 Scattering-Based Applications

Light scattered from plasmonic nanoparticles of different composition, geometry and composition may be collected and analyzed for different types of biomedical applications. In addition, the light propagation due to the scattering cross sections of plasmonic NPs can also be manipulated at the nanoscale range to provide unique opportunities for specific biomedical applications. Moreover, the use of different nanostructures and surface modifications (e.g., antibodies, ligands, and peptides, etc.) can generate an alternative robust protocol in order to produce high-efficient biosensing and bioimaging devices. Biocompatibility and specific targeting are highly required in these applications, and thus substantial attentions have been paid to design elaborated surface modifications for creating highly stable imaging contrast agents.[157, 201, 202] For example, heterobifunctional polyethylene glycol is one of the widely applied polymers effectively reducing nonspecific cellular adsorption and aggregation of plasmonic NPs and improving their biocompatibility for a broad range of bioimaging and biosensing applications.[157]

- **Bioimaging and Diagnosis**

The role of plasmonic NPs as promising contrast agents has been thoroughly proven for bioimaging and detection of for example cancer cells and cellular biomolecules (e.g., expressed proteins and antigens, etc.) due to their large scattering cross sections, high-resolution, and chemical- and photo-stability compared to traditional fluorescent agents.[203] The strong scattering generated by the interaction with the incident light even makes plasmonic NPs visible under normal optical microscopes (e.g., dark field and back scattering mode), and this promising feature can be elaborately employed to simply create a quantitative multiplexing imaging process.[204, 205] The stable and strong scattering signal from the plasmonic NPs easily enables the fabrication of highly sensitive and cost-effective bioimaging and biosensing devices, desperately needed in clinical diagnosis and therapeutic monitoring.

In case of bioimaging, scattering signals from plasmonic NPs are composition- and shape-dependent and adjustable for obtaining different intensities and colors. The plasmonic NPs with different chromatic spectra can facilitate a multiplex imaging system as contrast agents.[89, 206] For example, Au/Ag alloy NPs are one of practical contrast agents providing a range of tunable chromatic spectra by adjusting their composition and size and improving current multiplex imaging systems. As shown in Figure 3.10a, the composition of the spherical alloy NPs (at the same size range) has been precisely adjusted from pure Ag to pure Au, resulting in different extinction spectra.[50] The Red-Green-Blue (RGB) illumination and scattering spectra of NPs for different media are shown in Figure 3.10b. Figure 3.10c,e shows breast cancer cells labeled with specifically designed plasmonic NPs for RGB (blue: 10:90 Au/Ag, green: 50:50 Au/Ag, and red: Au nanorod) under a dark-field optical microscope in different mediums (PBS, mounting medium and oil).[89] Scattering spectra from plasmonic NPs have also been applied in hyperspectral imaging, providing more detailed spectral information for a quantitative analysis.[150, 207] Furthermore, a large number of nanostructures, composed of pure metals and their alloys, have been developed to specifically scatter light at the NIR resonance for a high-resolution deep tissue bioimaging.[208] Besides cells, the use of functionalized plasmonic NPs enables a quick recognition of viral organisms and other pathogens under darkfield microscopy.[209-211]

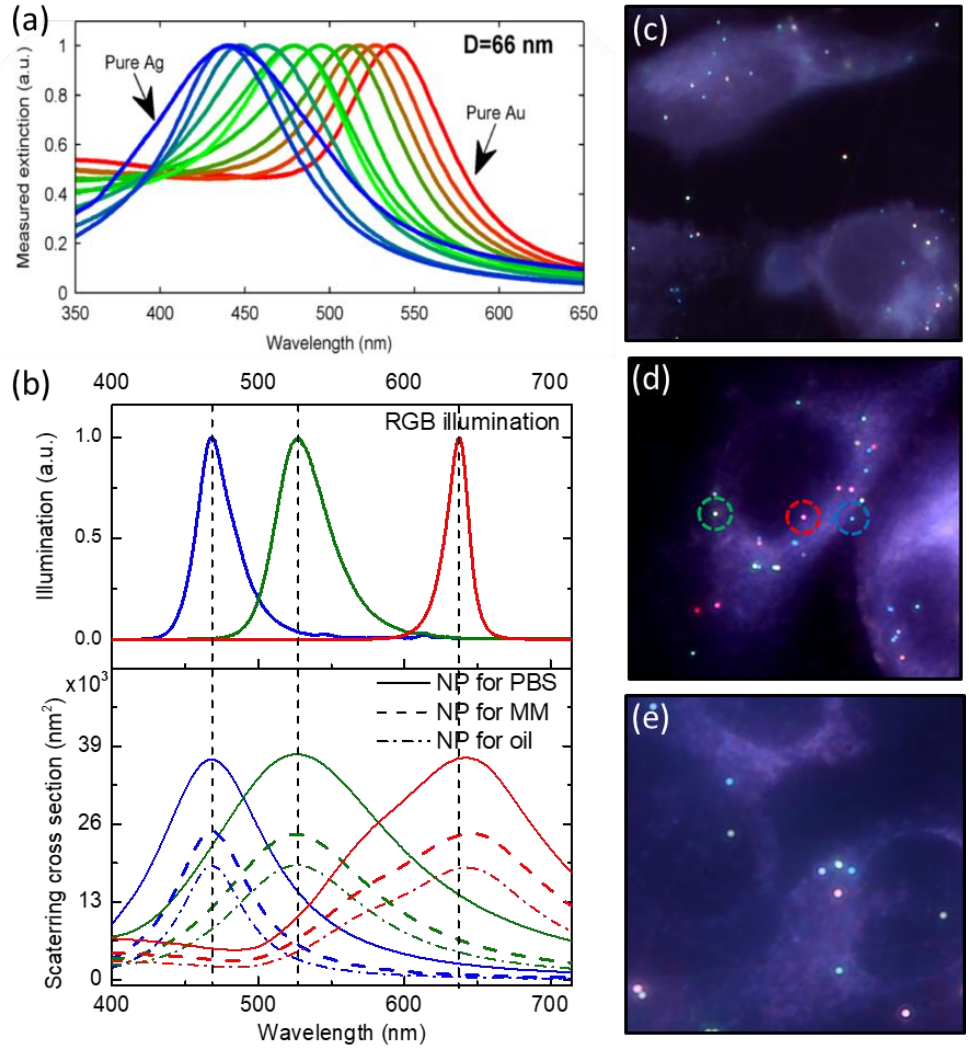

Figure 3.10 (a) Extinction spectra of Au/Ag NPs of different composition. Reproduced with permission.[50] Copyright 2015, American Chemical Society. (b) The RGB (red-green-blue) light source spectrum and theoretical scattering cross section of Au/Ag NPs designed for the illumination in phosphate buffered saline (PBS), mounting medium (MM), and microscope immersion oil for a dark field bioimaging. The representative dark-field side-illumination images of Au/Ag NPs (Red, green, and blue scattering light) on the cell membrane in (c) PBS, (d) MM, and (e) the immersion oil. Reproduced with permission.[89] Copyright 2019, John Wiley & Sons, Inc.

An elaborate combination of differentiable scattered lights (RGB colors) as well as specific cellular binding features (surface functionalization) of plasmonic NPs can be further used in many

applications in bioimaging, diagnosis, and therapy.[84, 212] Scattering lights from functionalized plasmonic NPs can provide a facilitated chromatic way to substitute current complex diagnostic strategies in regard to the common detection kits (e.g., pregnancy, cancer, and infection). With the development of metallic NPs, typically AuNPs and others (e.g., Ag, Pt, and Pd, etc.) by employing a specific surface functionalization (e.g., antibodies, peptide, and aptamers), these functional plasmonic NPs can be assembled as a rapid and sensitive detection kit for a wide range of diseases.[213, 214] Even with such progresses, critical challenges are being addressed in terms of signal intensity, penetration depth, and resolution needed to be thoroughly considered before moving towards clinical translation.

- **Biosensing**

LSPR is highly sensitive to the refractive index near the surface of plasmonic NPs, strongly influencing the LSPR peak, and the phenomenon can be served to improve spectral sensors. Due to the easy surface modifications of plasmonic NPs with biological and chemical molecules as receptors, the spectral sensors can selectively detect analytes and precisely report plasmonic peak shifts or broadening as a definite response.

Both single and assembled plasmonic particles can be implemented for the construction of a platform as a biosensor with a tunable feature based on the intrinsic morphology and composition, as well as the refractive index of surrounding medium.[215] Particle's size shows a direct impact on the detection spectrum range. An ultra-sensitive plasmonic platform can therefore be obtained by using smaller particles (due to their small local volume), while bigger particles in diameter can be assembled to detect analytes on a wider spectral range. In fact, smaller particles can mostly be influenced by the absorption, while the larger particles by scattering features, and both size ranges can facilitate a precise analysis for the detection of analytes through the extinction spectrum. The light-matter interaction (based on plasmonic NPs) can confine the detection range to an ultra-thin layer near the surface of the particle to provide a local supersensitive lab-on-a-chip device working at a very low concentration of analytes.[216]

Traditionally, plasmon peak shift is the main tracking point to evaluate the detection sensitivity, but these plasmon responses are subjected to lose their sensitivity due to an unsymmetrical broaden spectrum. In this case, the refractive index-based sensitivity can be improved by evaluating the

shift of the inflection points origin from the second derivative of the extinction spectrum, because the inflection point at the longer wavelength region with a similar refractive index change enables a noticeable shift (Figure 3.11).[215] By using the inflection point method, different types of AuNPs (e.g., nanospheres, nanorods with different dimensions, and nanostars) are able to improve bulk refractive index (RI) sensitivity around 18-55%.[217] Based on the similar method, the refractive index sensitivity of single AuNP is also found to be shape-dependent. The plasmonic NPs with sharp vertices and edges (e.g. nanocubes compared to nanospheres of same size range) possess higher RI sensitivity.[215] Instead of the inflection point, a curvature of the extinction peak can also be employed to improve the signal-to-noise ratio and the reliability of LSPR sensors by eliminating instrumental noises.[218] Plasmon-based bioimaging and biosensing rely on structural features of plasmonic NPs, substrates, as well as data analysis strategies. To achieve ultra-sensitive and accurate plasmon-based biosensing devices, our knowledge as a proof-of-concept regarding plasmonic properties certainly needs to be developed in order to accelerate a quick and accurate data analysis and affordable clinic translation, as well as other regulations required to facilitate their utilization in everyday life.

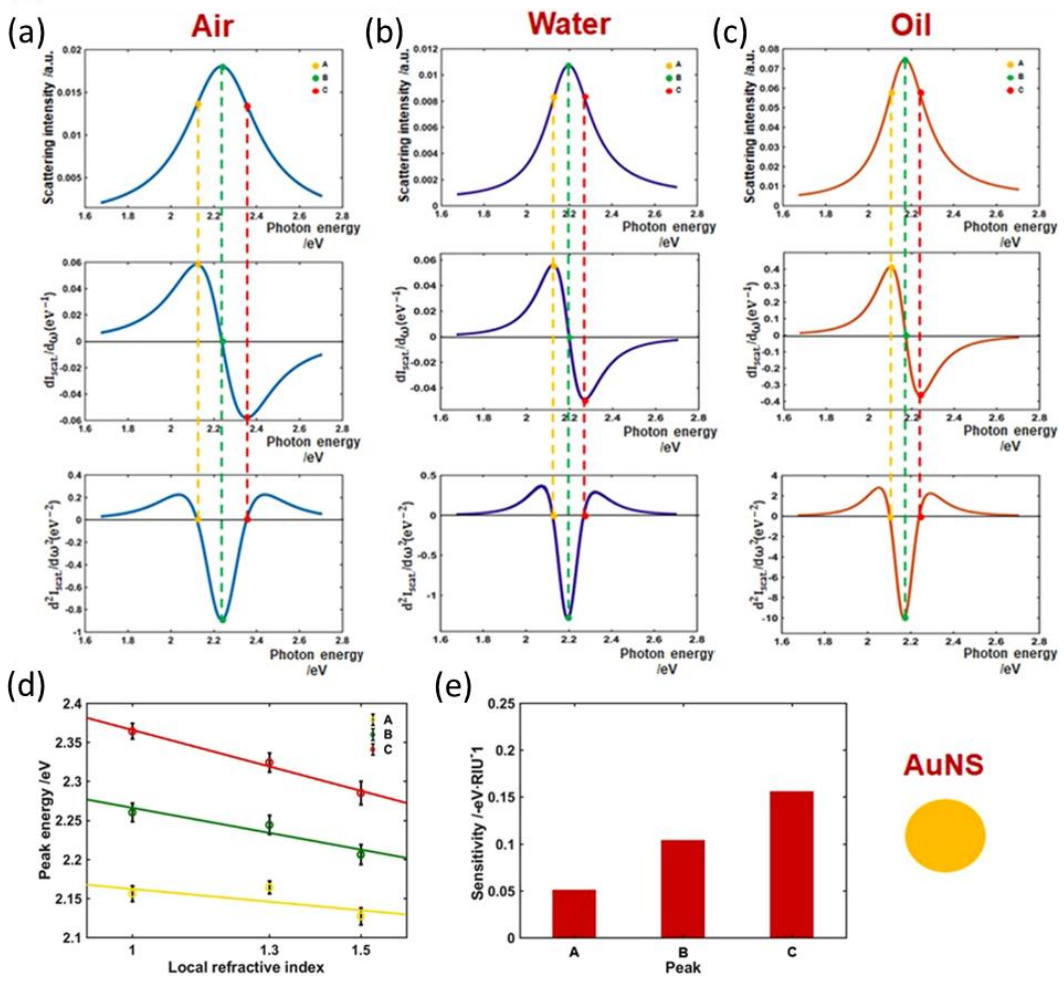

Figure 3.11 Extinction spectra (first row), their first derivative (second row), and second derivative (third row) of Au nanosphere (AuNS) in (a) air, (b) water, and (c) oil. The inflection points indicated with dash lines as A (yellow dashed line), B (green dashed line), and C (red dashed line). (d) Peak energy dependence on the local refractive index at the inflection points. (e) The sensitivity to refractive index at the inflection points. Reproduced with permission.[215] Copyright 2019, Springer Nature Limited.

3.7.1.3 Field Enhancement Applications

The field enhancement effect enables a passive bioimaging and detection by enhancing the emission signal from the emitter, placed in the near field of targeted plasmonic NPs. The field enhancement provides opportunities for an ultra-sensitive detection, even at the molecular level. Among various types of signals, Raman- and fluorescent signals are the most advanced

spectroscopic and microscopic strategies, developed for the field enhancement detection and imaging.

- **Surface-Enhanced Raman Spectroscopy (SERS)**

Since initially observed in 1973 by Fleischmann, SERS has attracted lots of attention due to the dramatic enhancement of Raman signals, thus achieving an ultrahigh sensitivity in the detection of small molecules.[219] Taking advantage of plasmonic field enhancement that may reach up to four orders of magnitude in certain nanostructures, Raman signals can remarkably be enlarged by 10^8 to even 10^{15}, opening up the possibility to detect single molecules.[220, 221]. The molecular specificity of Raman spectroscopy combining with the surface plasmon resonance from plasmonic NPs can generate highly sensitive "fingerprint" SERS platforms.[159] SERS-based platforms mainly involve two basic mechanisms for the signal enhancement. The most privileged mechanism is based on the influential electromagnetic mechanism caused by the concentrated electric field in the LSPR around plasmonic NPs (e.g., Raman signal enhancement up to 10^{10}). The second mechanism with a much smaller enhancement feature (e.g., up to 100) is attributed to the chemical enhancement caused by an interaction between molecules and NPs.[32, 159]

SERS based platforms are highly sensitive and responsive to the geometry of implemented nanostructures (e.g., sharp angles and clusters) in which plasmonic hot spots with large near-field enhancements can be used for the low concentration molecular detection.[222] According to both experimental and modeled field enhancement effect of plasmonic NPs, the highest enhancement comes from three types of nanostructures, including I: gaps, II: tips, and III: crevices. Therefore, many nanostructures transcend spherical ones, including nanocubes, nanoshells, nanosponges and other assemblies, which harvest gaps between each individual particle and their clusters.[223-226] Figure 3.12a illustrates the simulation of the resulted field enhancement between a pair of AgNPs, irradiated by a polarized light, and indicates the gap between the pair of particles with the highest field intensity. For example, a well-designed porous structure consisting of AgNPs embedded in silica coating around Au nanorod (Figure 3.12b) were used to gain a quantified SERS signal of probing molecules (1,2-bis(4-pyridyl) ethylene) at different concentrations (Figure 3.12c).[227] Following the same concept, Köker et al. designed SERS "hot spot" by coupling a pair of AuNPs between deposited an activated Raman reporter to be specifically differentiated. This tiny gap

around 2 nm created between the two particles can enable the highest SERS signal emits from the green fluorescent protein for a cellular bioimaging and spectral sensing (Figure 3.12d-f).[92] Due to the sensitivity and extremely small volume of the field enhancement, assembling Raman reporters into the hot spots is critical in order to generate a reproducible and controllable enhanced signal.

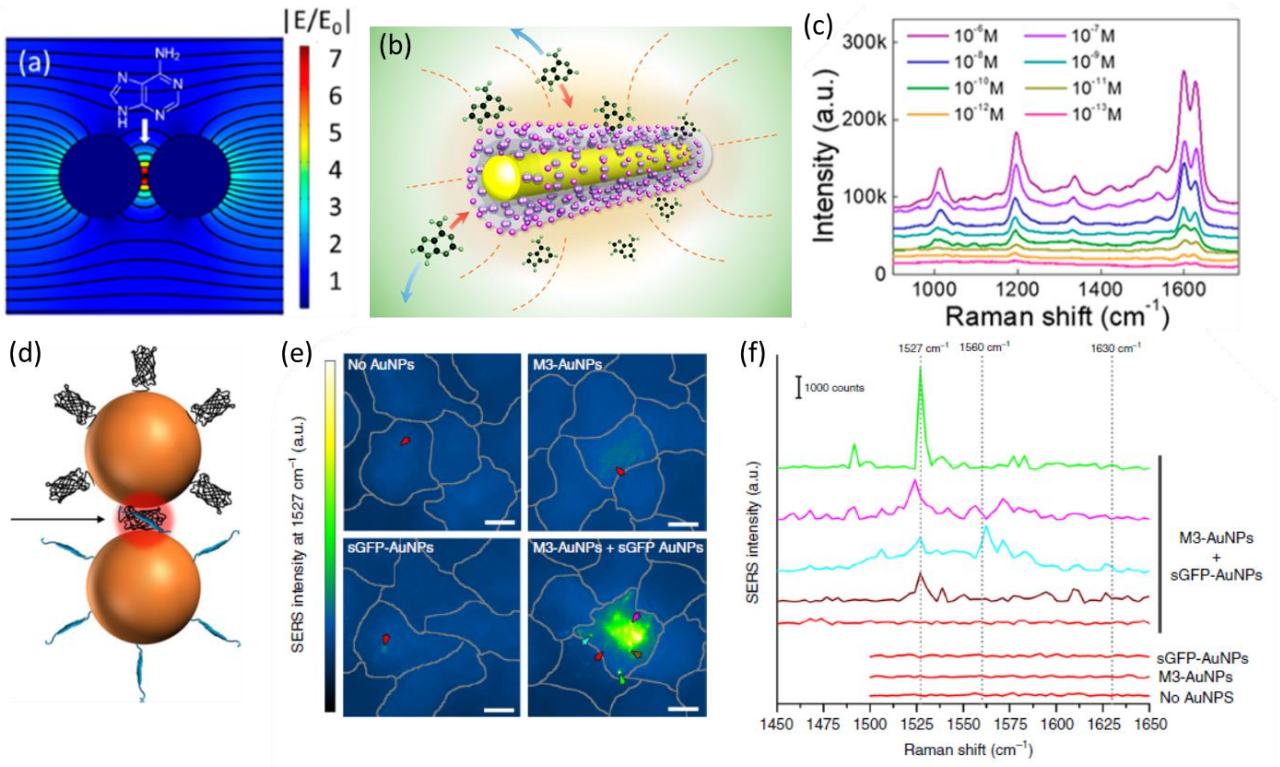

Figure 3.12 (a) Simulation of electric field enhancement of AgNPs pair with reporter molecule at the gap, (b) schematic of the sensing process with designed porous particle as Raman sensor, and (c) the SERS signal of 1,2-bis(4-pyridyl) ethylene in different concentrations enhanced by the designed particles. Reproduced with permission.[227] Copyright 2018, American Chemical Society. (d) Schematic of "hot spot" created by assembling of two AuNPs through the surface function with green fluorescent protein and peptide fragments, as well as (e) SERS image and (f) spectra of differently functionalized NPs with peptide (M3) and split green fluorescent protein (sGFP). Reproduced with permission.[92] Copyright 2018, Springer Nature Limited.

An elaborated assembly of plasmonic nanostructures, including disordered nano-islands formed by nanoaggregates and close-packed mono- or multi-layers of nanospheres, provides high

performance SERS substrates required to generate a highly sensitive platform for the detection of chemical and biological analytes.[228, 229] However, the reproducibility of the high performance SERS substrates privileged by the assembled plasmonic nanostructures has been an engineering challenge, prohibiting a wide range of applications. To fabricate the sensitive SERS substrates, thermally or electrokinetically driven deposition of aggregates can be a practical approach in order to control the disorder degree of these assemblies compared to the other techniques (e.g. flame spray pyrolysis and magnetron sputtering deposition).[228, 230] The control and optimization of fabrication parameters during the assembly of plasmonic nanostructures can directly contribute to the generation of hot spots of different densities, and facilitate a cost-effective production and utilization of the ultrasensitive SERS platforms. Compared to the disordered assemblies, the well-designed SERS substrates, for example, covered by a closed-packed nanospheres layer (with an optimized diameter and interparticle gap) shown a narrower plasmonic peak, sustain way better predictable field enhancement properties, influencing the enhance factor of the detection technique. Based on close-packed plasmonic NPs mono- and bilayers, the theoretical calculation exhibits enhancement factor up to 10^7 and with accompanying hot spots intensity up to $1000/\mu m^2$. The theoretical outcome together with well-developed synthesis techniques confirms the potential of plasmonic assembled nanoarrays for SERS applications.[229]

DNA origami technology, besides the above-mentioned approaches, is able to generate an accurate spatial assembly of plasmonic NPs in a large-scale (up to 500 nm) with the sub-nanometric precision, important for designing application-oriented plasmonic properties.[231, 232] With the structure programming, DNA origami technology shapes a reproducible and biocompatible scaffold, which precisely controls the distance and angle among the assembled plasmonic NPs. Wang et al. created reconfigurable diastereomers with DNA origami platform for assembling Au nanorods.[233] The complex can have up to three chiral centers, through DNA strand-displacement reaction, the L- and R-chiral center can switch from one to another, displaying different circular dichroism spectra. The spatial gap is one of the most promising SERS structures due to the sensitivity of the enhancement effect to the distance between NPs. In this case, DNA origami nano-assemblies, enable a reproducible and precise gap between plasmonic NPs, offering a perfect technology to couple pairs of NPs as gap-enhanced SERS substrates. Thacker et al. created AuNP dimers with reliable sub-5 nm via DNA origami to detect SERS signals from not only external

analytes absorbed molecules, but also the composition change of single-strand DNA attached to the NPs.[234]

Both Au and Ag nanostructures have been widely studied in SERS based applications because i) Ag has the most prominent effect for the Raman enhancement in a broad spectral range (400-1200 nm) and ii) Au has valuable enhancement behavior combined with good chemical stability and biocompatibility.[32, 158] Wang et al. have theoretically investigated aspects of Au/Ag hybrid nanoparticles in terms of the composition and structure to improve SERS performance. Au/Ag alloy NPs showed higher field enhancement compared to both pure Au- or Ag-based particles at the certain incident wavelength ranges (e.g., ≈420-520 nm) because of the different intrinsic plasmonic peaks of pure Au and pure Ag and the peak shift effect with chemical composition change. Au/Ag nanoshells with silica core have interestingly shown a stronger field enhancement in a broader range of spectrum than all others (e.g., Au/Ag alloy, AuNPs, and AgNPs), due to the modulation of environmental RI and variety of both chemical composition and shell thickness, and can be considered as a practical composition and structure applicable for future clinical translations.[158]

Due to tremendous progress in the fabrication of plasmonic NPs for SERS based platforms, it is highly possible to detect small molecules (e.g., a single nucleic acid) in the local environment of particles and tag markers on the surface of the particles to build sensing and imaging biomarkers (in *vitro* and *in vivo*).[223, 235, 236] For example, Olivo et al. tagged various SERS markers on functionalized AuNPs for multiplex detection *in vivo* (Figure 3.13). The peaks at 1120, 1175, and 1650 cm^{-1} are corresponding to Cyanine 5, malachite green isothiocyanate, and rhodamine 6G attached to the particles, respectively. SERS signals obtained from the treated mice (Figure 3.13 b, c) indicate that the SERS markers can quickly be vanished in the control groups (the healthy organs, less than 4 h), whereas the cellular binding AuNPs stayed much longer (more than 2 days) in the targeted tumor site, detectable via the long-term emitting signals.[237] Meanwhile, the high sensitivity SERS substrates provide a promising platform for an accurate trace detection of bacteria as a key point for the diagnosis of bacterial infections in early stages. Depending on chemical compositions, characteristic SERS signal provides information of various bacteria, and their detection.[238]

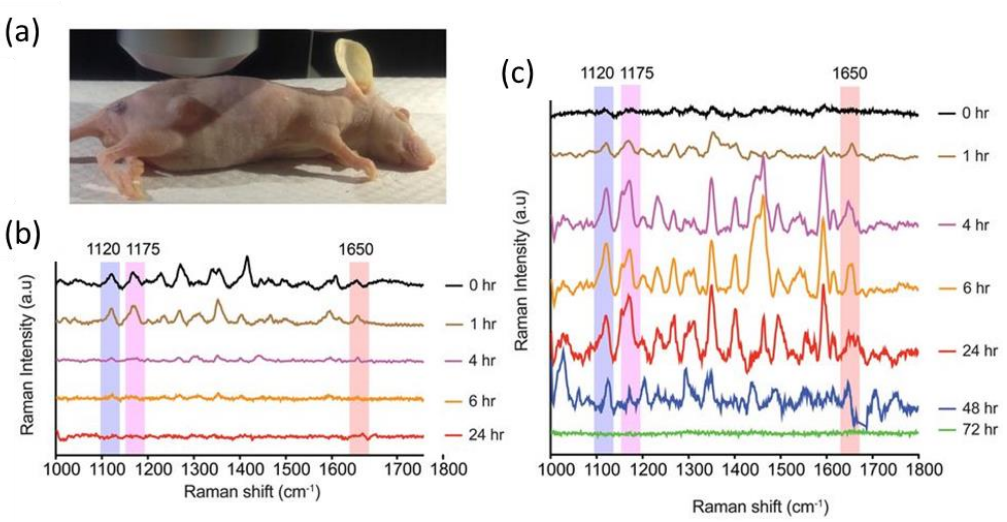

Figure 3.13. (a) Animal model for SERS experiment for tumor detection, (b) SERS spectra from tumor site in control mice with non-functionalized markers, and (c) in test mice with functionalized markers. Raman spectra were taken at the tumor after different incubation periods as indicated in the legend. Functionalized makers remain more than two days after the biomarker injection. Reproduced with permission.[237] Copyright 2014, Springer Nature Limited.

- **Surface-Enhanced Fluorescence:**

Fluorophores are widely used in biomedical applications due to their great accessibility and easy utilization. However, the deficiency, caused by their small cross section and their tendency for a quick photobleaching, dramatically influences their stability and triggers certain difficulties for a precise quantification required for a long-term diagnostic process. In this case, the use of plasmonic NPs has brought a significant improvement for both radiative and non-radiative decay of fluorophores, and altered their quantum yield and lifetime.[160, 239, 240] Based on the similar mechanisms involved in the improvement of SERS platforms, when fluorophores as biomarkers for bioimaging and biosensing are placed in the field enhanced region (near the surface of the plasmonic particles), the surface-enhanced fluorescence (SEF) can be obtained due to the well-known LSPR phenomenon. The emission enhancement, calculated by ηE^2, where η is the quantum yield of fluorophore and E is the normalized electric field at the position of the fluorophore.[241] Due to the property and stability of different fluorophores, the measured enhancement factors vary a lot for each individual experiment.[239, 242]

The morphology of particles (due to concentrating the electric-field) and the spatial distance of fluorophore from the surface are crucial for SEF-based platforms. For example, fluorophore molecules must be slightly far away from the plasmonic NPs to avoid quenching of the signal because of a non-radiative deexcitation of the fluorophores. Fluorophores close to the surface (around 1-5 nm) can be affected by the electron transfer to the NPs, which will quench the fluorescent signal, while in the range of 6-20 nm (slightly far from the surface using spacers, such as SiO_X), the signal can be strongly enhanced owing to the field enhancement from the plasmon. As shown in Figure 3.14, Mei and Tang have taken advantages of controlled fluorescence quenching and enhancement mechanisms, depending on the distance between fluorophores and Au nanorods to analyze oligonucleotide detections. Simply, depending on the DNA paired or not (unfold or fold), the fluorescent signals will be respectively enhanced or quenched (Figure 3.14b). Taking advantage of the tunable dimension of nanorods (varying the aspect ratio), plasmonic spectrum can be precisely controlled to reach a match with both excitation and emission wavelength of fluorophores. Moreover, the great fluorescence enhancement can omit the limitations on the DNA detection process and greatly bring an expected accuracy for quantified results (Figure 3.14c).[93] A simultaneous utilization of different fluorophores provides a multiplex detection with fluorescent mode. Moreover, multimode imaging, for example, has been developed by combining SEF and scattering light from plasmonic NPs. Plasmonic NPs with different compositions (e.g., pure Ag and Au/Ag 50:50) coated with silica containing different fluorophores (e.g., fluorescein isothiocyanate and Rhodamine B isothiocyanate) provide a dual-mode platform for multiplexing bioimagings.[243] The combination of scatterings from plasmonic NPs and plasmonic enhanced fluorescence can significantly enlarge multiplexing opportunities by using a spectrum of biomarkers under a similar observation set up to enable quantitative analysis approaches.

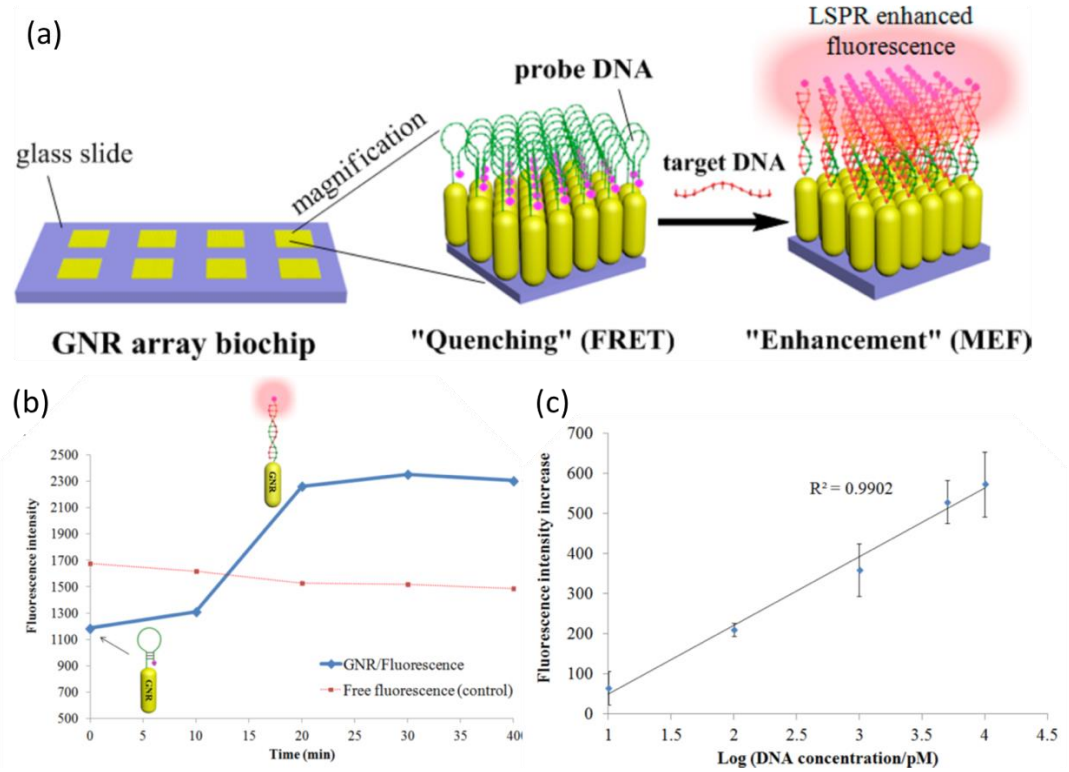

Figure 3.14. (a) Schematic of LSPR enhanced fluorescence applied in Au nanorods array chip for DNA detection, (b) fluorescent intensity comparison between free fluorescence and the one attached to Au nanorods, in quenching and enhancement modes, and (c) calibration curve of detection chip with complementary single strain DNA in different concentrations. Reproduced with permission.[93] Copyright 2017, American Chemical Society.

3.7.2 Energy Technology

Solar energy is the most sustainable green energy owing to 5000-million-year lifetime and tremendous yield of about 4000 times more than that of the global electric energy consumption in the world.[151] Therefore, many techniques, including photothermal, photovoltaic and photochemical approaches, have been developed for harvesting and converting the solar energy for various applications. One of the main challenges for a wide implantation of these developed approaches is the lack of light absorption and conversion efficiency; however, the use of metallic NPs in the energy conversion devices has shown potential to improve outcomes of these approaches.[244-249] Similar to the mechanisms involved in biomedical applications, absorption, scattering and field-enhancement play roles in different energy approaches.

Photothermal harvesting devices, the most straightforward and efficient platforms, directly convert solar energy to thermal energy. Common photothermal devices (e.g., solar thermal collectors), composed of an absorber and working fluid, are mostly assembled in flat-plate forms. These collectors employ absorbers to convert sunlight to thermal energy and transport it by using a working fluid. However, the conventional design of almost all solar thermal collectors is inefficient due to the low absorption efficiency, as well as the high losses during the energy transportation. Therefore, nanofluids, supplemented with metallic NPs (e.g., plasmonic and metallic compounds, and carbon materials) dispersed in working fluid can eliminate drawbacks of these collectors by improving the absorption efficiency and providing a localized conversion of solar energy on the spot. The performance of solar thermal collators depends on the optical absorption and concentration of particles in nanofluids.

A wide range of particles have been explored to improve the performance of photothermal harvesting devices with high absorption efficiency.[250] Compared to other nanomaterials, plasmonic NPs stand out with extraordinary large absorption cross sections, broad and adjustable absorption spectra.[251] Plasmonic NPs dispersed in the working fluid generate a localized heat at the surface that accelerates a direct and highly efficient solar steam generation. The improvement of solar thermal collectors has been applied as a pollution-free and inexhaustible approach, for example, in power generation and seawater deionization. Figure 3.15a-c illustrates Au-nanofluid based steam generation that gained a great energy conversion (more than 300 %) compared to a solar thermal collator filled with pure water as the fluid.[94] Figure 3.15d,e shows the TiO_2/Ag composites efficiently enhanced the absorption of solar energy, which helps increase the temperature of the fluid.[251] Hybrid nanomaterials composed of photocatalytic nanomaterials (e.g., Au-TiO_2, and Au-SiO_2, etc.) have also been explored due to their high permittivity and initial absorption spectrum of plasmonic components, significantly enhanced the performance of solar energy devices.[252, 253] Plasmonic nanoparticles assembled into a 3D supporting template, besides the direct dispersion in working fluids, can alternatively improve solar energy absorption up to 96 %, for example, by depositing Al NPs into the sidewall of the porous aluminum oxide membrane (a large number of NPs self-assembled in a closed-packed layer through the metal evaporation system). The assembly of plasmonic nanomaterials opens up the possibility of hieratical structure design and large-scale production, providing a feasible approach for the

utilization of solar energy in water desalination (e.g. portable plasmon-enhanced solar desalination device).[254]

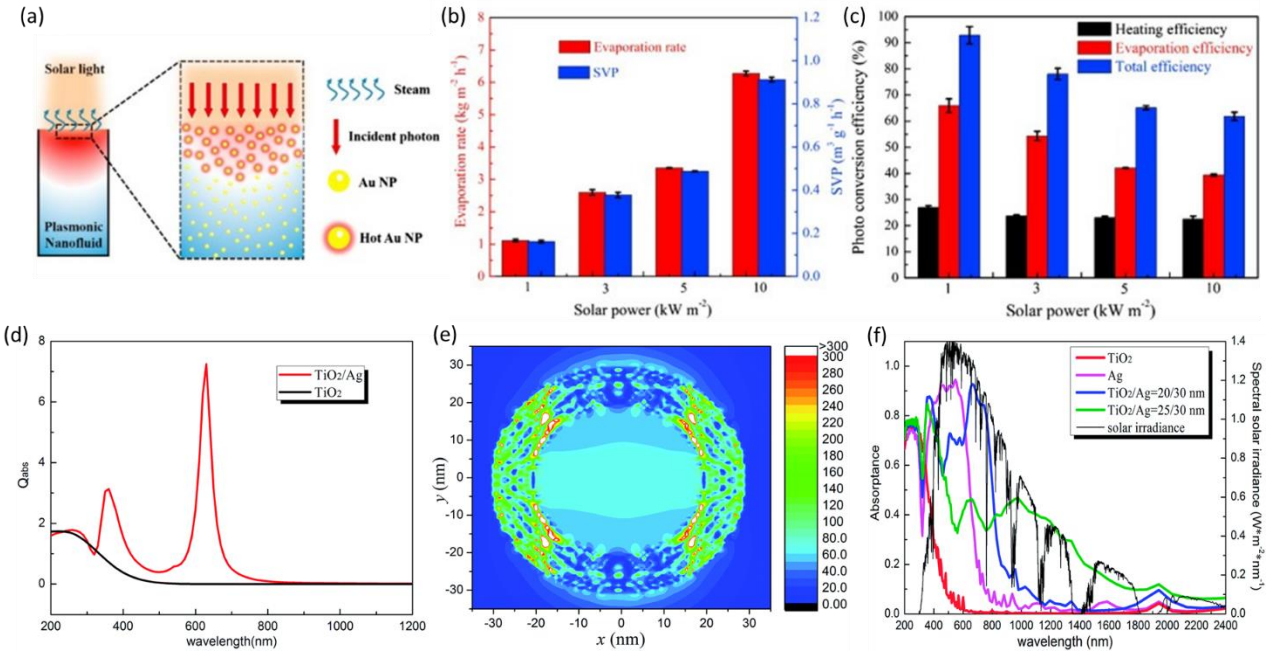

Figure 3.15 (a) Schematic of the plasmonic nanofluid enabled direct solar steam generation. The effect of solar power intensity on (b) the evaporation rate and specific vapor productivity (SVP), as well as (c) heating efficiency, evaporation efficiency, and total efficiency. Reproduced with permission.[94] Copyright 2017, Elsevier B.V. (d) Absorption efficiency (Q_{abs}) of TiO_2/Ag core/shell NPs and TiO_2 NPs, (e) simulation of the electric field of TiO_2/Ag core/shell NPs at the resonance peak (630 nm wavelength), and (f) absorptance of different nanofluids based on TiO_2, Ag and TiO_2/Ag core/shell NPs compared with the spectrum of solar irradiance. Reproduced with permission.[251] Copyright 2014, Royal Society of Chemistry.

Photovoltaic system is one of the most representative devices for cost-effectively using solar energy to directly generate electricity. Indeed, photovoltaic effect by absorbing light generates electron-hole pairs in the junction converting solar energy to electricity. During the process, two viable ways for improving efficiency are increasing light absorption and avoiding electron-hole pair recombination; however, there is a competition between these two ways as one requires thick absorption layer, while the other one requires thin one. To tackle this problem, plasmonic NPs with their unique optical properties can be employed to improve the solar cell efficiency by using i) the

large scattering cross section of particles leading to the direction change of light propagation, ii) the field enhancement at the surface of particles, and iii) carrier generation in the substrate.[255, 256]

The greater light absorption can be resulted from an effective elongating light path in the semiconductor materials due to large scattering produced by the nanoparticles.[257, 258] Indeed, plasmonic NPs deposited on the surface of the semiconductor substrate tend to scatter light (~ 96%) into the substrate with a high refractive index rather than to the air.[245, 259] When the scattered light reflected by the bottom side of the device, plasmonic NPs can reflect light back into the absorption layer and increase the amount and effective path of light in the absorption layer, thus improving the absorption efficiency. With the dominate scattering mechanism involved in plasmon-assisted photovoltaic devices, various metallic NPs (e.g., Au, Ag, Al, and Cu NPs) can effectively improve the performance of solar cells.

Due to the confined dimension of field enhancement and high-efficient light absorption, plasmonic NPs can be deposited into the ultrathin layer of solar cells. Cho et al. employed a layer of Ag nanostructures into an active layer of the textile polymer solar cells as a wearable device. The plasmonic nanostructures improve light absorption within this thin active layer of textile to achieve ~8.71 % energy conversion efficiency and 20 % improvement compared to the planar devices without the nanostructures.[260] Liu et al. synthesized Au@Ag nanocuboids (for organic photovoltaics) and tuned the thickness of Ag shell to broaden the scattering spectral range of the implemented NPs. With a broad scattering effect, nanocuboids embedded in Poly(3,4-ethylenedioxythiophene)-poly(styrenesulfonate) (PEDOT:PSS) layer (Figure 3.16a) have improved the photovoltaic performance (up to 22.8 % improvement and 10.42 % average efficiencies of solar cells), whereas nanocuboids embedded into a bulk heterojunction (BHJ) active layer (Figure 3.16b) have shown an inefficient performance due to the quenching, caused by the direct contact of Ag and heterojunctions. Au@Ag nanocuboids with different dimensions of Au core and Ag coating layer lead to various extinction spectra (Figure 3.16c). To eliminate the quenching effect, an extra silica decoration of Ag can increase the power conversion efficiency to more than 10 % for the organic photovoltaics.[90] In fact, deposition of plasmonic NPs into the active layer of organic and perovskite solar cells is a well-known strategy in which an insulating layer (e.g., silica, titania, and other oxide semiconductor) can be used to cover the deposited

plasmonic NPs and improve compatibility.[255] Metzman et al. also demonstrated the polystyrene (PS) functionalization plays an important role when AgNPs embedded into the active layer of organic photovoltaics (Figure 3.16d). Although Figure 3.16e shows a severe deterioration (67% power conversion efficiency decrease) by using the unfunctionalized AgNPs, the additional PS functionalization on AgNPs increased power conversion efficiency (≈32%) compared to reference platforms without AgNPs.[261] In most cases, dispersion of plasmonic NPs within different layers of these types of photovoltaic devices increases the light absorption and facilitates electron transportation, and improves the efficiency of photovoltaic devices.

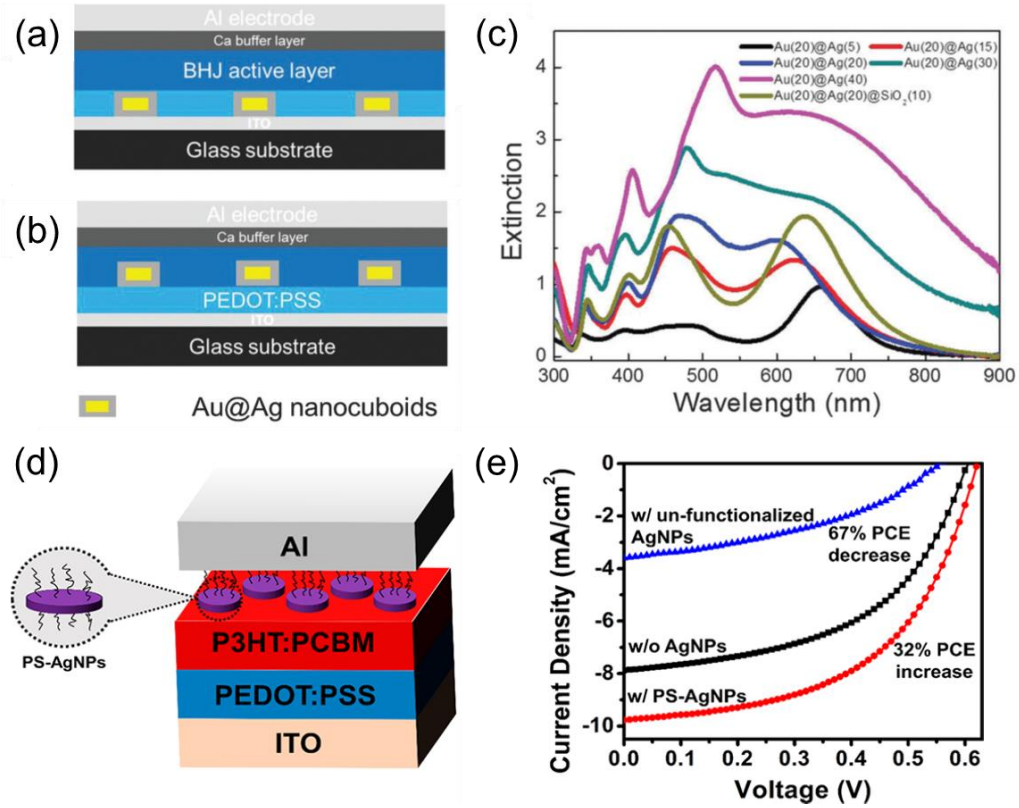

Figure 3.16. Schematic of Au@Ag nanocuboids embedded in (a) Poly(3,4-ethylenedioxythiophene)-poly(styrenesulfonate) (PEDOT:PSS) layer, and (b) bulk hererojunction (BHJ) active layer for organic photovoltaics. (c) Extinction spectrum of Au@Ag nanoboids with different Ag shell thicknesses, as indicated in the legend. Reproduced with permission.[90] Copyright 2016, Royal Society of Chemistry. (d) Schematic of organic photovoltaic device assembled by using polystyrene (PS) functionalized AgNPs. (e) The current density of the organic photovoltaic device with un-functionalized and PS functionalized AgNPs compared to a

reference device without nanostructures. Reproduced with permission.[261] Copyright 2019, American Chemical Society.

Facing energy shortage and pollution problems, semiconductor photocatalysis converts photo energy to chemical energy similar as the photosynthesis of plants. This strategy converts solar energy by using SiO_2, TiO_2, and other semiconductors, and produces clean energy (e.g., H_2, CH_4, and CO, etc.) from water and CO_2. Besides the energy conversion, solar light can also be used to induce organic decomposition, applicable for eliminating pollution. However, due to the wide-band gap/large energy barrier of these semiconductors, only a small percentage of sun light (~4% UV light) can be harvested for the conversion.[262, 263] To tackle this problem, plasmon-enhanced photocatalysis employs plasmonic NPs to increase efficiency of the oxidation reaction or reduce the energy barrier, required for the reduction reaction using visible light from the sun. The strong light-matter interaction creates resonant electrons (hot electrons) mostly similar to the mentioned processes involved in photovoltaics. These hot electrons facilitate the electron transfer not only on the surface of plasmonic NPs, but also between their interfaces with the semiconductor. For example, AuNPs can be implemented into a plasmon-enhanced photocatalysis platform to harvest methane and ethane under visible light with the surface electron transfer. Continuous-wave laser in the visible spectral range can be applied for the excitation of plasmon and the irradiated AuNP provides the hot electrons, which can activate CO_2 for the reduction. One or two electrons transferred to the absorbed CO_2 in order to be reduced to hydrocarbon products, including CH_4 and C_2H_6 (Figure 3.17a).[264] Varying excitation laser wavelength to generate higher energy excitation can form heavier hydrocarbons, for example, mostly C_2H_6 in this particular case. The production rate of each NP for generating CH_4 and C_2H_6 (the turnover frequency) strongly depends on the applied excitation wavelengths (Figure 3.17b-d). Other plasmonic NPs, provide a broad and tunable optical resonance, can also cover the whole visible spectrum facilitating the photocatalysis. Since semiconductors play an important role for photocatalysis, plasmonic doped TiO_2 and SiO_2 can efficiently tune the working range of the spectrum benefitted.[262, 263] Platinum with outstanding catalysis properties has suffered from the resonance in UV region, <300 nm. By modulating the surrounding media, Zhang et al. extended the resonance to the visible range and the absorbed light is applied to photoredox reaction by designing a three-dimensional structure with SiO_2 core coated with small platinum NPs (2-5 nm) and a thin layer of titanium dioxide. Taking

advantage of small platinum NPs with high surface-to-volume ratio, this nanostructure conserved the excellent catalysis properties suitable for the development of platinum NP-based photocatalysis.[265]

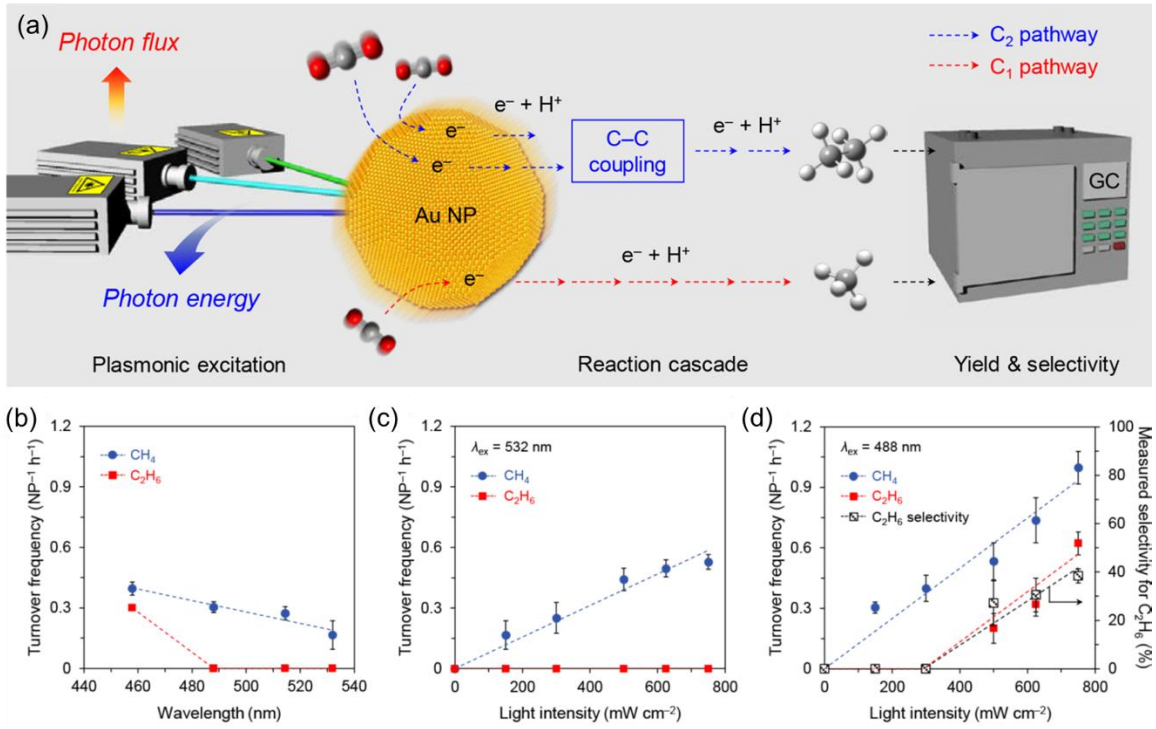

Figure 3.17. (a) Schematic of the visible-light-driven CO_2 reduction on the surface of AuNP used to produce hydrocarbons, analyzed by gas chromatography (GC). (b) Turnover frequency of CH_4 and C_2H_6 with different excitation wavelengths, and (c-d) a quantitative comparison of turnover frequency of CH_4 and C_2H_6 under 532 nm and 488 nm excitation. Reproduced with permission.[264] Copyright 2018, American Chemical Society.

3.7.3 Information Technology

Light manipulation through the modulation of plasmonic features of metallic NPs can break the diffraction limit of $\lambda/2$ in conventional optics. Overcoming the far-field diffraction limit, plasmonic NPs are able to code the information by using near-field techniques. Plasmonic-based structural color systems that create transmission filters, reflective color printing, and field-enhancement sensors are mainly based on light absorption and scattering,[266] as well as field enhancement effects. Plasmonic NPs enable color-encoding at the nanoscale and behave as a

“nanopixel”, showing advantages over the microscale dye-based systems in terms of resolution. Depending on the nano-formulation and the illumination condition, final display and detection can be controlled through the plasmonic properties of NPs, and the spectral range and polarization of light.

Instead of organic dyes, plasmonic filters based on noble metallic nanostructures, adjustable in morphology and distance between each other, are remarkably stable and these filters have been widely employed to separate specific discrete colors from white light due to their plasmonic absorption.[267, 268] Two fabrication strategies based on the plasmonic absorption mechanism have been mainly implemented by using i) an array of plasmonic NPs on substrates and ii) an array of cavity apertures.[95, 267, 269] For example, dual-state plasmonic nanopixels (full range of standard RGB region with different polarizations of white light) have been established by creating aperture arrays on Alumina film (Figure 3.18a-d). The transmission information can also be doubled by changing only the light polarization, using the same full color and polarization-dependent filter under bright field microscope. For example, Figure 3.18b-i,-ii show respectively the transmission color under x- and y-polarized white light by implementing a plasmonic-based polarization dependent filter.

The information storage technique based on the scattering effect, shape- and size-dependent LSPR and polarization (similar to the mechanisms based on the light absorption mentioned above), has frequently been employed in a reflective color printing technology.[270, 271] The ability of gap-plasmonic alumina nanodisks has been demonstrated for a saturated and dark color encoding.[95] Under varying the physical features (e.g., diameter and dimension) of nanodisks and adjusting the periodicity of nanodisks, the arrays can tune the primary color and gradually alter the color saturation. Accordingly, the color pattern “nano” with individual building blocks **(**Figure 3.18e,f) has been built, showing a wide color range. Dark color has also been obtained by combining nanodisks with different sizes in the same pixel in order to create a stronger absorption of light in the broad spectrum. In another study, Chen and Reinhard fabricated the assembled nano pixels in the visible range through a precise procedure controlling size and geometry of Au and AgNPs.[91] Various colors in a visible range can be designed due to the NP-dependent scattering spectrum. Accordingly, spherical and rod shape plasmonic NPs applied as “nano-pixel” in different

assemblies (scanning electron microscope and scattering color images as shown in Figure 3.18g) have enlarged the color generation possibility due to the multi-dimension control at the nanoscale.

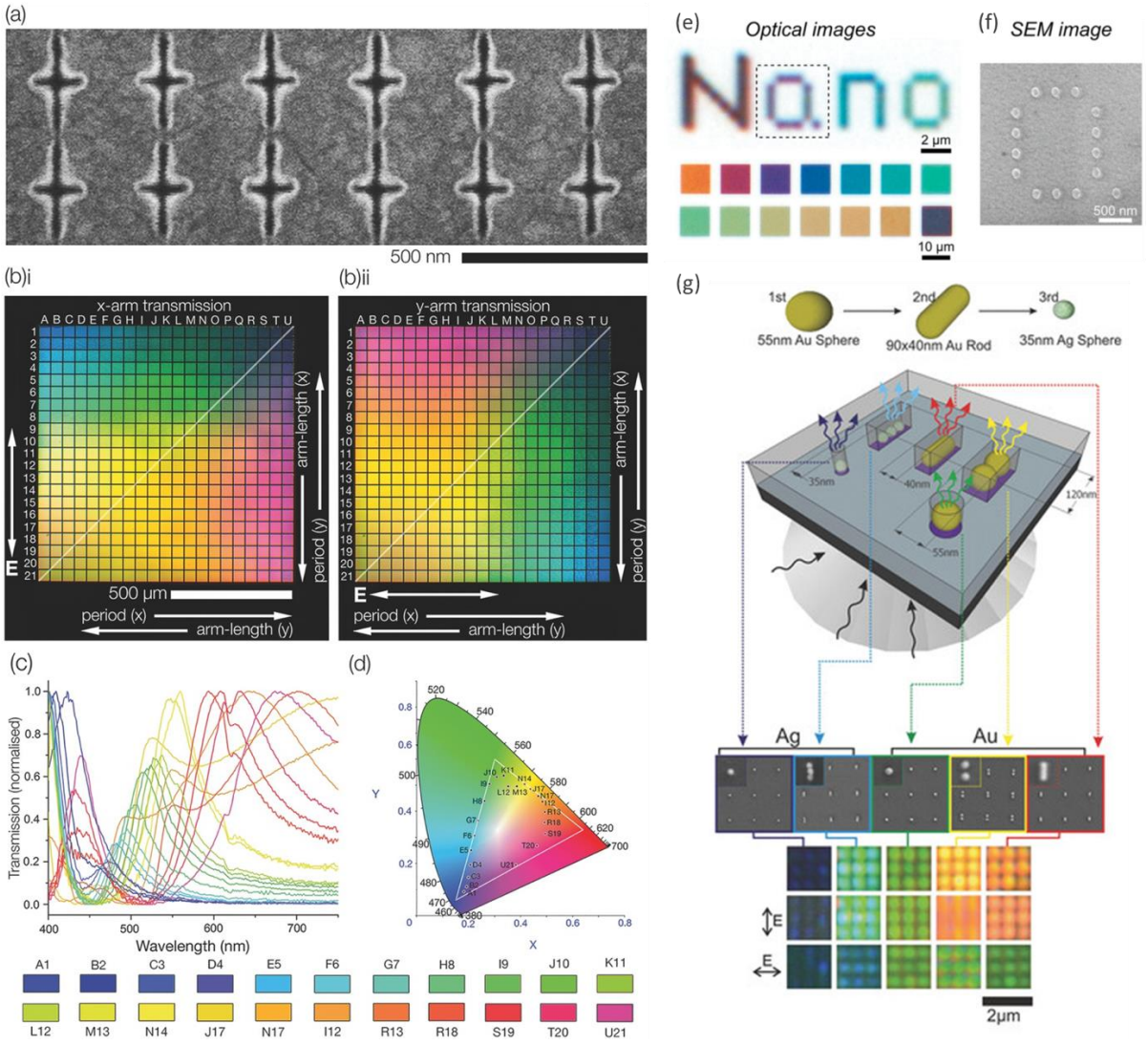

Figure 3.18 (a) SEM images of fabricated cross-structure pixel arrays, (b) transmission color of filter with varying arm-length under x (b-i) and y (b-ii) polarized white-light, as well as transmission spectra (c) and CIE XY chromaticity diagram (d) of pixel arrays labeled in (b-i). Reproduced under the terms of the CC-BY license.[117a] Copyright 2016, The authors. Published by John Wiley & Sons, Inc. Optical (e) and SEM (f) image of subwavelength color printing "Nano", with pixel in 300 nm×300 nm square, and the various colored optical image induced by varying diameter of nanodisks. Reproduced with permission.[7h] Copyright 2016, American Chemical Society. (g) Scheme of Au nanospheres, Au nanorods, and Ag nanospheres as color

pixels and their SEM and darkfield images. Reproduced with permission.[7d] Copyright 2017, John Wiley & Sons, Inc.

Due to the large absorption and scattering cross section of metallic NPs, the improved contrast can dramatically eliminate the detection limitation for writing and reading of optical information. The plasmonic nanostructures can also boost the inadequate efficiency of photodetectors through a size reduction of pixels, and meanwhile generate faster writing and reading speeds and reduce power consumption with the enhanced intensity. Furthermore, the morphology- and polarization-dependent properties of plasmonic NPs could potentially improve storage density by means of composing different well-designed nanostructures and varying illumination condition in the same area.

A combination of different SERS reporters with a specific characteristic peak can be designed for information encoding.[272] Owing to the fingerprint Raman peaks from the reporters, the encoding becomes promising for anti-counterfeiting applications. While the Raman signal is quite low, an array of plasmonic nanomaterials with the surface enhancement properties can assist to achieve high density information storage with an enough signal intensity. For example, Ag nanopillar arrays have been employed in a SERS assisted encryption through an encoding mechanism involved fluorescent and Raman reporters to achieve an information density up to 17000 ppi (pillar per inch).[273] Fluorescence and SERS were simultaneously applied in the information encoding to boost the security of the encryption. In SERS-based information storage, since the characteristic peaks are sharp, and a wide range of reporters can be chosen and combined with each other easily. The design of multi SERS reporters with different characteristic Raman shift peaks can increase the encoding capacity. High versatility and efficiency can be achieved with the combination of reporters enhanced by plasmonic NPs arrays embedded in various 2D and 3D patterns.[274]

3.8 Conclusions and Future Perspectives

Plasmonic NPs as a promising nanomaterial have been successfully applied in biomedical, energy, and information technology due to their unique plasmonic and optical features, including an extraordinary absorption, scattering, and field enhancement. This review focused on the fundamentals of optical properties of plasmonic NPs and discussed their interaction with light, and their other effective features (e.g., morphology, composition, and metal-permittivity) for a

successful development of application-oriented nanostructures. Mie theory and numerical simulations describing the phenomena have been used as a guide to verify and optimize the designed structures and properties needed to be implemented for different applications in biomedical, energy and information technologies.

Although plasmonic NPs with tunable optical properties have been rapidly developed, the large-scale utilizations are still limited probably because of i) the relatively high price of noble metals, ii) the needed precise fabrication, post-fabrication approaches and cost effectiveness, and iii) the limited chemical stability under complexed environment and unclear biological toxicity. Due to the relative costliness and low natural abundance, recycling noble metals still requires such an improvement to avoid pollution and huge energy consumption compared to that of traditional ways (e.g. aqua regia, N-bromosuccinimide, pyridine, and mixtures of thionyl chloride).[275, 276] Alternatively, deep understanding of optical properties, reducing the usage of plasmonic NPs (e.g. minimizing their weight in the platforms), and combining with other types of metals (e.g. Cu and Al materials) can remarkably assist the development of cost-effective and efficient optical platforms. In most applications, the synthesis of plasmonic NPs has to be well-controlled because of the strong dependency of their optical properties on the composition, size, morphology, and spatial distance between each other. Attention must therefore be payed to adapt the fabrication and post-fabrication technologies for achieving well-controlled and cost-effective application-oriented nanostructures. To stabilize plasmonic-metal NPs while conserve the optical properties, many efficient surface modification strategies have been successfully used by means of polymers and inorganic coatings, contributing to the chemical and biological stability. However, cytotoxicity and genotoxicity issues still remain a challenge for clinical practices (e.g., imaging, detection, and therapy), due to the long-term interaction between plasmonic nanostructures and intracellular compartments by triggering complexed biochemical and biological mechanisms. Therefore, the development of multifunctional plasmonic nanostructures for establishing a safe and efficient theranostic approach is a major breakthrough towards clinical translation.

Compared to other nanomaterials, optical properties of plasmonic NPs applicable in biomedical applications have superior advantages. The intrinsic permittivity of metals with an adjustable spectral range (e.g. UV, visible, and NIR) can facilitate the therapeutic features of plasmonic NPs for biomedical applications and future clinical translation. Even suffering from lower

biocompatibility compared to certain kinds of nanomaterials (e.g., porous silicon, lipid, and poly(lactic-co-glycolic acid) NPs), well-established functionalization techniques have been developed for plasmonic NPs to achieve long-term dispersibility, biocompatibility, and chemical stability.[277] A broad range of plasmonic nanostructures have been designed for specific absorption and scattering spectra as well as “hot-spots” for field enhancement. The large adsorption cross section of plasmonic NPs and their contrast between surrounding tissue enabled the localized photothermal effect, precise hyperthermia treatment, photoacoustic imaging and optoporation phenomena, while minimizing irreversible damages to healthy cells and tissues. Ongoing human clinical developments for cancer treatment is under actual intensive study.[176, 278] The large scattering cross section generated by plasmonic NPs made them outstanding biomarkers, with tunable color and quantification properties, for bioimaging and diagnostics. The sensitivity of surrounding media of plasmonic NPs has also induced the high-sensitive biosensing. Field-enhancement effects of plasmonic nanostructured substrates with the field-enhancement effects have also been employed for boosting Raman and fluorescent signals, which enabled enormous enhancement, creating strong signal and high sensibility, which are required in order to develop ultra-sensitive bioimaging and biosensing devices for clinical practices.

Plasmonic NPs are also considered to improve energy devices based on different technologies, including photothermal, photovoltaics, and photocatalysis. A wide range of absorption spectra, high scattering efficiency and “hot electron” generation improves the light absorption, energy transition efficiency and overcomes the energy barrier of semiconductors in such devices with a valuable improved performance.

The plasmonic NPs have also provoked creative designs for improving information technology in storage and encryption. Tunable absorption and scattering properties of plasmonic NPs, and their formulated assemblies and arrays provide a broad range of colors and saturation displays. Higher information density has been introduced by combining a well-designed and -controlled illumination spectrum and polarization. The field-enhancement of plasmonic nanostructured substrates providing such a high level of the enhancement factor has enabled a fast and sensitive information coding and detection.

Taken together, due to their chemical and optical stability, as well as their easy fabrication and functionalization strategies, plasmonic NPs with their well-known features can address critical

limitations and challenges to achieve the best performance in biomedical, energy and information technologies. Ongoing fundamental studies on plasmonics (e.g., developing practical features related to nanostructures and their properties) will open up new possibilities for designing efficient application-orientated plasmonic NPs.

3.9 Acknowledgements

This work was supported by the TransMedTech Institute, the Canada First Research Excellence Fund, the National Science and Engineering Council of Canada (NSERC), and the Canada Institutes of Health Research (CIHR). M.H. Kafshgari was supported by a TransMedTech Institute Fellowship.

CHAPTER 4 METHODOLOGY- SYNTHESIS AND OPTIMIZATION OF AU-AG NANOSPHERES

In this chapter, the details of the synthesis of spherical Au-Ag alloy NPs are described, and the kinetics and optimization during the synthesis are discussed, as well as the automatic synthesis setup. The synthesis method of Au-Ag alloy nanospheres, combining co-reduction and seeded growth, has been invented by D. Rioux and M. Meunier and a patent was obtained.[50, 279] For more efficient application and more delicate morphology design, the synthesis method of Au-Ag NPs is necessary to be optimized to achieve high quality of products. Detailed experimental description of spherical Au-Ag NPs used in the thesis is provided in this chapter. The kinetics during the co-reduction and seeded growth are discussed, and the reaction parameters are optimized accordingly for Au-Ag bimetallic nanospheres. Finally, to have better control of the process, the automatic setup is designed.

4.1 Materials

Au seeds were synthesized with the Turkevich method, named after John Turkevich who first introduced the method.[280] In detail, 30 mL water was first heated to boiling in an Erlenmeyer flask with a gentle stir. Then, the water solutions of 300 μL 30 mM $HAuCl_4$ and 200 μL 170 mM sodium citrate (NaCit) were added into the flask in sequence. After boiling with stirring for 30 min, Au seeds with a diameter of 15 ± 1 nm were synthesized. After cooling down to room temperature, the volume was adjusted to 30 mL, obtaining the Au atomic concentration of 300 μM.

4.2 Synthesis of Au-Ag nanospheres with modified method

4.2.1 Synthesis of Au seeds

Au seeds were synthesized with the Turkevich method, named after John Turkevich who first introduced the method.[280] In detail, 30 mL water was first heated to boiling in an Erlenmeyer flask with gentle stir. Then, the water solution of 300 μL 30 mM $HAuCl_4$ and 200 μL 170 mM sodium citrate (NaCit) were added into the flask in sequence. After boiling with stirring for 30 min, Au seeds with diameter of 15 ± 1 nm were synthesized. After cooling down to room temperature, the volume was adjusted to 30 mL, obtaining the Au atomic concentration of 300 μM.

4.2.2 Synthesis of Au-Ag nanospheres

The Au-Ag nanospheres are synthesized with the combination of co-reduction and seeded growth methods. $HAuCl_4$ and $AgNO_3$ as the corresponding precursors of Au and Ag were reduced simultaneously by the mild reducer, sodium citrate, which also performs as the capping agent. The concentration of Au and Ag in the growth can be adjusted by the ratio of added $HAuCl_4$ and $AgNO_3$. Meanwhile, for the size control, according to the ratio between the volume of each final NP and the seed, which has been defined as "seeding ratio" in the previously published paper,[50] the seeded growth can be separated into different stages. In order to have the controllable size and monodispersed NPs, during each stage the volume enlargement of each NP should be no more than 10, thus the step seeding ratio is limited to 10. Au seeds synthesized with the Turkevich method or other types of Au or Ag NPs can be employed as the initial seeds. If it requires more than one growth stage, the NPs after each stage of seeded growth can be applied as seeds for the next stage of growth.

In the growth stages, the total metallic atoms concentration is 150 μM, including the ones from seeds and added precursors. The precursors of Au and Ag are supposed to be thoroughly reduced and all reduced atoms are equally deposited onto the seeds to form an alloy shell. Therefore, depending on the seeds, the seeding ratio of the growth stage, composition of growth shell and volume of final NPs dispersions, the volume of seeds dispersion, dilution ratio, and amount of metal precursors can be determined.

If the ~15 nm Au seeds perform as the initial seeds, the first growth stage is usually with a seeding ratio of 10. In detail, 57 mL water was heated to 90°C in a three-necked round-bottom flask in an oil heating bath with refluxing. With vigorous stirring, 3 mL Au seeds prepared with Turkevich method were dispersed into the flask. Reducing agent NaCit (170 mM) 540 μL and metal precursors $HAuCl_4$ (30 mM) and $AgNO_3$ (30 mM) solution in total 270 μL (with the corresponding ratio of Au/Ag for the predetermined composition) was added in ten successive injections within 1 hour. After finishing the injection, the mixture was heated to 100 °C and kept stirring for 1 hour to complete the growth. After cooling down to room temperature, the dispersion volume was adjusted to 60 mL. Alloy NPs with determined composition were synthesized, with a diameter of 32 ± 2 nm.

For the following growth stage(s), the NPs synthesized in the previous stage can be applied as seeds, similar to the first growth stage.

If the 70 nm Ag-core are designed for final Au-Ag NPs in diameter of 100 nm, 70 nm Ag NPs perform as the initial seeds and the seeding ratio is 3. In this case, 40 mL water was heated to 90°C in the flask with refluxing, followed by 20 mL Ag NPs with an atomic concentration of 150 μM added into the flask with vigorous stirring. After the dilution of seeds was heated to 90 °C, 400 μL NaCit (170 mM), and 200 μL in total of $HAuCl_4$ (30 mM) and $AgNO_3$ (30 mM) solution (with the corresponding ratio of Au/Ag for the predetermined composition) were injected into the flask in ten successive injections in 1 h. After finishing the injections, the mixture was heated to 100 °C, and kept stirring for 1 h to complete the growth. After cooling down to room temperature, the volume of dispersion was adjusted to 60 mL. The ~100 nm Au-Ag NPs with Ag-core were synthesized.

There are broad choices of initial seeds for seeded growth, which provide high flexibility for the structure design. Meanwhile, the restriction of atomic concentration (150 μM) and the seeding ratio of each growth stage (≤ 10) requires more growth stages to enlarge greatly from the initial seeds to final NPs. However, the restriction combined with the stepwise co-reduction assures the quality of the seeded growth synthesis, with the coefficient of variation of less than 15 % of Au-Ag NPs between 30 – 150 nm. The co-reduction during the seeded growth provides facile control of composition for each growth stage. The composition of Au-Ag NPs can be adjusted with simple control of the added precursors, and arbitrary composition between pure Au and pure Ag can be synthesized. With controllable size and composition, the optical properties of Au-Ag NPs are adjustable according to the needs.

4.3 Kinetics during the synthesis and optimization

The co-reduction with citrate combined with seeded growth method provides a promising way to synthesize Au-Ag NPs with controllable size and composition in the aqueous colloid. Meanwhile, the kinetic control in the process is important for the spherical morphology and narrow size distribution of final bimetallic NPs. During synthesis, the reactions are complex in the system, including citrate reduction of Au and Ag precursors respectively, deposition or growth of Au and Ag atoms onto the existing seeds, the potential reaction between the two metals, and undesired

homogenous nucleation. Stepwise injection during each growth stage and control of the temperature are the main optimization that have been done. Moreover, the automatic setup has been proposed and proved improvement of dispersity.

4.3.1 Citrate reduction of Au and Ag precursors and kinetic control

The seed fabrication has been done through the Turkevich method, which has been thoroughly studied. The method has been proved with numerous experiments with a certain size and narrow dispersity under proper reaction conditions. In the synthesis of Au-Ag alloy NPs, the growth stage would be the most influential for the final size, shape, and distribution.

The theories and explanations on the citrate reduction and growth of Au NPs for the Turkevich method consider the process as reduction, nucleation, and growth. During the seeded growth of Au-Ag, the heterogeneous nucleation induces the reduced atoms growing onto the existing seeds, while the citrate reduction, as well as the growth of Au and Ag, is comparable with the mechanism of Turkevich. In the Turkevich synthesis route or the seeded growth, citrate contributes not only as reducing agent, but also stabilizer. Meanwhile, since sodium citrate (NaCit) is a weak base, its concentration and the ratio between NaCit and $HAuCl_4$ significantly influence the pH of the solution, which is critical for the size control and reaction mechanism. The Au (III) complexes vary with pH, and when pH is higher, the $[AuCl_3(OH)]^-$ with high reactivity tends to transform to $[AuCl_2(OH)_2]^-$ and $[AuCl(OH)_3]^-$ with lower reactivity. Therefore, the reduction and sequential growth will be faster with low pH (low NaCit/$HAuCl_4$ ratio), which leads to the difficulty of control. Therefore, the NaCit/$HAuCl_4$ ratio should be high to reach higher pH and maintain the equilibrium of Au (III) complexes to have lower reactivity and the growth conduct in a controllable way. With higher pH, the Au NPs tend to form spheres instead of polyhedra and ellipsoids at lower pH. Also, to balance the control in the growth and reaction time, the NaCit/$HAuCl_4$ is set around 10, and the subsequent pH is around 7.0, which is higher than the threshold (pH = 6.2-6.5) in the controllable range for seeded growth route.[281]

In the synthesis of Au-Ag alloy NPs, $AgNO_3$ is introduced into the reaction system as precursor of Ag component. The Au/Ag composition is adjusted by controlling the ratio between added $HAuCl_4$ and $AgNO_3$, leading to changes of their respective concentration, as well as the kinetics of the reaction. Besides concentration change, in contrast to $HAuCl_4$, the citrate reduction of $AgNO_3$ is

promoted at higher pH due to the reductivity of citrate. With high pH, the fast growth results in spherical NPs and some nanorods. While, at lower pH, due to the slow reduction, the NPs tend to form triangular or polygon shapes.[282] For citrate reduction of Ag NPs, the size distribution and morphology are difficult to control due to the weak reductivity and multiple roles of citrate. Therefore, the simultaneous control of spherical shape and size distribution becomes difficult. To tackle the problem, stepwise growth is proposed. Meanwhile, the coexistence of Au and Ag facilitates the spherical size and the narrow size distribution of the metallic NPs. As reported by Xia and co-workers, the Ag^+ ions not only suppress the undesired nucleation but also help reshape the polycrystal to get quasi-spheres.[283] The existence of Ag^+ regulates the buffer effect of citrate and increases the concentration of the most active $[AuCl_3(OH)]^-$, leading to higher efficiency of Au reduction and growth.

The pH is one of the key factors which affect the reaction kinetics, thus the size, shape, and polydispersity. Compared to the pH, the temperature influences the growth process slightly. The peak position slightly varies with temperature change and the polydispersity is similar between 60-100 °C.[284] Temperature adjustment affects the kinetics of growth, and there is proof about lowering the temperature to 90 °C can efficiently restrict the new nucleation.[285] Considering the reductivity of citrate and efficiency of production, the growth is set at 95 °C during the sequence of addition of reagents, and heat the mixture to boiling after the all reagents are added. Considering the synthesis efficiency, the final temperature we chose is 100 °C.

During the coreduction of Ag and Au, galvanic replacement reaction between Ag and $HAuCl_4$ induces the compositional gradient from core to shell, with Au-rich core and Ag-rich surface. Enough high citrate concentration facilitates the simultaneous reduction of Ag, without producing a hollow structure in the alloy NPs. The galvanic replacement reaction is applied for the further porous Au-Ag NPs synthesis in the following chapters.

4.3.2 Stepwise growth during each stage

The stepwise method is necessary since the concentration of NaCit, $HAuCl_4$, and $AgNO_3$ existing in the colloidal has a decisive influence on the kinetics of nucleation and growth. According to the competition between homogeneous and heterogeneous nucleation, the ratio between newly added metal monomers to the existing seed NPs, which provide heterogeneous nucleation sites, should

be relatively low to ensure the growth of NPs and avoid undesired nucleation. Stepwise addition of reagents in growth stages effectively reduces the concentration of existing NaCit, $HAuCl_4$, and $AgNO_3$, thus monomers in the colloidal, so that the undesired nucleation is restrained. Especially for the Ag-rich NPs, the shape control with narrow size distribution requires a stepwise method.

During the stepwise addition, the sequence of reagents also plays an important role. To balance the growth of Au and Ag, the precursors of the two metals are added simultaneously, and the citrate as stabilizer and pH adjuster has been added before the precursors at every step.

The use of that system results in narrow size distribution of Au-Ag NPs as well as extinction peaks with smaller full width at half maximum (FWHM), as shown in Figure 4.1. It is obvious that the NPs fabricated with that system are much more homogeneous, with fewer large rods, and newly grown NPs. The NPs are more stable compared with manual control, which is more likely to grow together. The controlled morphology and size distribution, as well as the narrow plasmonic peak, are important for further applications.

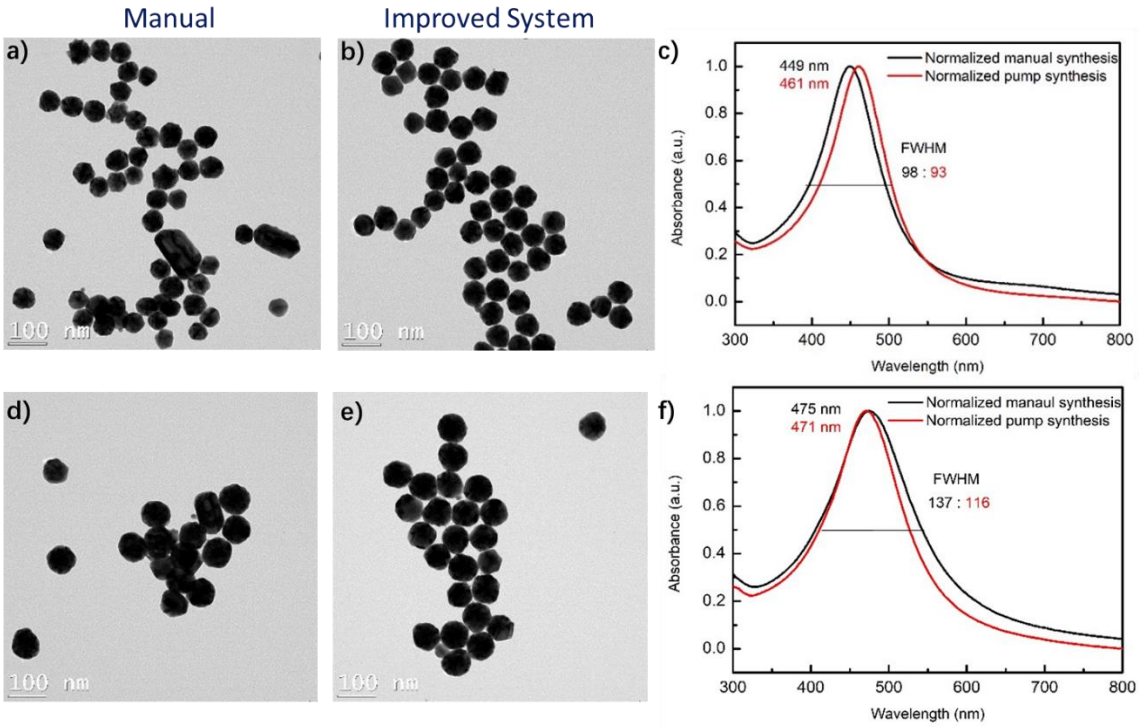

Figure 4.1 TEM (a, b, d and e) and extinction spectra (c and f) of Au/Ag 25/75 NPs synthesized with manual and improved system.

The automatic control system provides an efficient way for further exploration, such as the study of different reaction parameters, scaling up for larger batch, and even the continuous synthesis. Meanwhile, there are some details to be improved in the whole setup. The mixture in the flask with high temperature is connected with reagents via the tubes, which results in a reaction in the tube, creating deposits on the wall of tubes. The cleaning or change of tubes should be done regularly to ensure the quality of synthesized NPs.

CHAPTER 5 ARTICLE 2: DESIGNABLE NANOPLASMONIC BIOMARKERS FOR DIRECT MICROSCOPY CYTOPATHOLOGY DIAGNOSTICS

This article published in the *Journal of Biophotonics* corresponds to the design of AuAg alloy nanoparticles and their application as multiplexing biomarkers for cytopathology diagnostics. The alloy nanoparticles have been designed according to the red-green-blue LEDs and adjusted depending on the mounting medium of cell samples. Cost-effective circular side-illumination component have been invented for practical application with traditional optical microscopy. The multiplexing biomarkers of NPs and circular side-illumination components combination boosted the practical application of plasmonic biomarkers in cytopathology and enabled quantitative and efficient diagnostic.

5.1 Authors

Lu Wang, Cecile Darviot, Jennyfer Zapata-Farfan, Sergiy Patskovsky, Dominique Trudel, and Michel Meunier

5.2 Contribution of the authors

In this article, the author of this thesis, Lu Wang, performed the design and synthesis of AuAg alloy NPs. Jennyfer Zapata-Farfan assembled the side-illumination device. Cecile Darviot provided the optical calculation evaluation of the device. Cecile Darviot and Lu Wang prepared the cell samples with NPs. Lu Wang carried out the complete writing of the manuscript as well as the composition of the figures. Dominique Trudel provided the clinical point of view in the discussions. Sergiy Patskovsky discussed with Lu Wang the initial idea for the project and participated in the various associated discussions. Michel Meunier participated in the discussions as well as in the revision of the article. All authors contributed to the final review of the article.

5.3 Abstract

Direct microscopy interpretation of fine-needle biopsy cytological samples is routinely used by practicing cytopathologists. Adding the possibility to identify selective and multiplexed biomarkers on the same samples and with the same microscopy technique can greatly improve diagnostic

accuracy. In this article, we propose to use biomarkers based on designable plasmonic nanoparticles (NPs) with unique optical properties and excellent chemical stability that can satisfy the above-mentioned requirements. By finely controlling the size and composition of gold-silver alloy NPs and gold nanorods, the NPs plasmonic resonance properties, such as scattering efficiency and resonance peak spectral position, are adjusted in order to provide reliable identification and chromatic differentiation by conventional direct microscopy. Efficient darkfield NPs imaging is performed by using a novel circular side illumination adaptor that can be easily integrated into any microscopy setup while preserving the standard cytopathology visualization method. The efficiency of the proposed technology for fast visual detection and differentiation of three spectrally distinct NP-markers is demonstrated in different working media, thus confirming the potential application in conventional cytology preparations. It is worth emphasizing that the presented technology does not interfere with standard visualization with immunohistochemical staining, but should rather be considered as a second imaging modality to confirm the diagnostics.

5.4 Introduction

Recent decades have seen the bloom of development of plasmonic nanoparticles (NPs), being rapidly applied in various fields, such as catalysis,[286-288] optics,[289] and biomedicine.[143, 290] Due to their tremendous scattering efficiency, structural designability, optical tunability,[291] and surface functionalization ability,[292-295] colloidal plasmonic NPs and regular nanoplasmonic structures have brought new opportunities to a number of areas and opened doors for substantial challenges.[296] Through designing the size, shape, and composition of plasmonic NPs, various types of plasmonic NPs have been engineered with specific plasmonic properties addressing different applications.[143, 297-299]

Under illumination and detection, the noble metal NPs strongly scatter light and have 10^5-10^6 times higher scattering cross section than conventionally used fluorophores when used in bioimaging.[300, 301] Additionally, they are not subject to blinking and bleaching effects, offering an extraordinary photostability for imaging and biosensing. Optical encoding strategies of plasmonic NPs are based on dark field microscopy (DFM) methods that, in combination with hyperspectral scanning sources or cameras, allow efficient spectral differentiation, precise spatial localization, and multiplexed quantification of NPs based biological labels.[243, 302, 303]

Nowadays, there is a need for cost-effective, sensitive, and specific diagnostic methodology to overcome the limitations associated with conventional cyto- and histo-pathology based methods. Due to the high scattering efficiency and photostability of plasmonic NPs, there exist many successful applications in bioimaging.[304, 305] We think that a methodology based on a cytology protocol, where cell immunolabeling is performed by means of plasmonic NPs can drastically improve diagnostic reliability. However, to promote user adoption of this new method in cytopathology laboratories, the NPs imaging hardware should be simple and compatible with equipment currently used in laboratories. Likewise, the sample preparation and imaging procedure should not involve additional steps or risks of sample contamination compared with the existing procedures. Moreover, the practicing pathologists want to observe and differentiate multiple NPs labels directly at the eyepiece of the microscope, as well as compare and combine the images with the conventional bright field observation mode. With the aim of realizing this idea, we recently introduced a darkfield lateral illumination approach and compact device for multispectral NPs detection without the cumbersome equipment required for conventional DFM visualization.[306] We paid particular attention to the fact that the new modality should not interfere with the standard method. The proposed method was based on the chromatic differences of three NPs: Au, Ag, and Au nanorods that with consecutive illumination by means of blue, red, and green light from Red-Green-Blue (RGB) Light-emitting diodes (LED), allowed reliable plasmonic labels identification. By simply switching between lateral illumination and traditional brightfield illumination, the pathologists may opt for immunohistochemistry or immunoplasmonic imaging at their convenience. However, fast visual simultaneous NPs identification was still problematic due to the low coupling between the optimal spectral signature of the NPs and the RGB LED source.

Digital pathology appears as a promising trend for pathology, however, there are still many problems before it becomes widespread. The most concerned problems involve the variation of sample preparation and parameters in digitalization process, which requires general algorithm to compensate their influences. Moreover, digitalization is a time-consuming task, especially for obtaining more details and accurate information, which is an inevitable part of database building.[307] Therefore, most pathologists rely much more on their experience with familiar methods of sample preparation as well as the visualization. Our technique responds to the urgent

needs of direct visualization and providing at the same time a compatible way of low-cost digitalization.

In this article, we first theoretically predicted and experimentally synthesized two gold-silver (Au/Ag) alloy NPs with designed composition and sizes that together with Au nanorods NPs can be used as three spectrally distinct biomarkers optimized for direct microscopy cytopathology analysis. We then investigated the influence of three different surrounding media on the NPs parameters: PBS buffer solution for live cells detection, mounting medium solution for cytopathology tests mimicking clinical situations, and oil for the best NPs imaging contrast. We have also developed a circular side-illumination (CSI) adaptor as an improved darkfield microscopy methodology for the rapid visual multispectral identification of individual plasmonic NPs in live or fixed cell samples. We believe that the proposed technology can facilitate and accelerate the adoption of a new type of reliable and stable biomarkers for ex-vivo cytopathology analysis and diagnostics, where possible toxicity of NPs cannot drastically influence obtained results.

5.5 Materials and Methods

5.5.1 Materials

All chemical reagents were used as received, without further purification. Gold (III) chloride trihydrate ($HAuCl_4 \cdot 3H_2O$, ≥99.9%) was purchased from Sigma-Aldrich, Silver nitrate ($AgNO_3$, 99.995%) and Trisodium citrate dihydrate ($Na_3C_6H_5O_7 \bullet 2H_2O$, 99.0%) were obtained from Alfa Aesar. Before synthesis experiments, all glassware was cleaned with aqua regia and rinsed thoroughly with deionized water. All water used in this work is provided by Millipore Direct Q-UV3 water purification system, as ultrapure water with 18MΩ resistivity. Nanorods (A12-40-600 and A12-40-650) were purchased from Nanopartz. Circular glass slides and coverslip (25 mm in diameter) were used for NPs and cell samples preparation. VECTASHIELD® Vibrance™ Antifade Mounting Medium was purchased from Biolynenx Inc., which was chosen as the representative mounting medium for fixed-cell samples and is hereinafter referred as mounting medium. MDA-MB-231 cell line from ATCC® was cultured for cell samples. ‘Culture-Inserts 2 Well for self-insertion’ from Ibidi were used for culturing the cells on slides for sample preparation.

5.5.2 Synthesis of Au/Ag NPs

Spherical Au/Ag NPs of controlled size and composition were synthesized by optimizing the previously reported method (seeded growth combined with coreduction method).[50] Based on that, multiple injection in each growth stage were performed in a controlled manner in order to keep a low concentration of free ions, thus avoiding a secondary nucleation. Moreover, temperature was controlled in a dynamic way according to the ingredient injection status to regulate the rate of chemical reduction and NPs growth for precise shape control.

First, Gold (Au) seeds are synthesized through Turkevich method, as mentioned in existing work.[50, 280] In the protocol, 300 μL 30 mM $HAuCl_4$ water solution and 200 μL 170 mM $Na_3C_6H_5O_7$ (NaCit) water solution were added into 30 mL of boiling water. Keeping boiling for 15-30 minutes, Au seeds were synthesized with 15±1 nm in diameter. The volume of seeds solution was adjusted to 30 mL by adding water in order to achieve an atomic concentration of 300 μM.

Then, 2-3 growth stages were performed to reach the final size. Typically, in the first growth stage, 3 mL Au seeds achieved in initial seeds synthesis was dispersed into 57 mL 90 °C water in three-necked flask with heating bath and refluxing. Reducing agent 540 μL 170 mM NaCit and metal precursors 270 μL $HAuCl_4$ (30 mM) and $AgNO_3$ (30 mM) solution (in corresponding ratio of Au/Ag for the designed composition) was added in ten successive injections. After all injections, heating temperature was raised up to 100 °C to keep boiling for 1 hour. Then alloy NPs, with 32±2 nm diameter, were synthesized, which can be used as seeds for the next growth stage. NaCit was added before metal salts in order to adjust the pH to slow down the chemical reduction velocity, thus facilitating homogeneous growth of NPs.[282, 308, 309] For following growth stage(s), NPs synthesized in the last stage were used as seeds, and a similar process was performed to obtain the designed bioimaging labels.

In the growth stage, in order to avoid aggregation or undesired nucleation, total concentration of metal atoms should be limited to 150 μM, including Au and Ag in seeds and injected metal precursors.[50] Based on our experimental results, in each growth stage, the volume ratio of final NPs compared with the seeds should be limited to 10 to ensure that the required size distribution is less than 10 %. With the first growth stage, we obtained NPs with 32±2 nm diameter, which can

be used as seeds in the second growth stage, resulting in NPs with diameter of 69±4 nm. For even larger NPs, another growth stage will be necessary.

5.5.3 Characterization of NPs

The spectrum of colloidal NPs in water was measured with an Epoch Microplate Spectrophotometer. The morphology and size of the NPs were characterized by transmission electron microscope (TEM, JEOL 2100), and Energy-dispersive X-ray spectroscopy (EDS) was also performed on the samples to define the composition of Au/Ag alloy NPs. The samples were prepared on a Cu grid with thin carbon film (Cu-400CN, Pacific grid tech) dipped into ethanol dispersions and air-dried for every synthesized sample (Au/Ag alloy NPs).

To prepare the sample of NPs within targeting media, 3 μL of aqueous NPs solution was dropped on a microscope slide and subsequently dried with compressed nitrogen. After this procedure, 40 μL of targeting medium were deposited on the slide to cover the NPs area. A 120 μm double-sided spacer tape was set on the slide in order to cover the sample. Scattering spectrum from single NPs was then acquired through backreflection with a 100× oil objective and Andor Shamrock SR-750 imaging spectrophotometer under the illumination of an halogen lamp.[150] An inverted Nikon microscope equipped with 60× air objective combined with side illumination adaptor was employed for NPs and cells samples visualization, and the commercial camera Nikon D7500 was used for taking digital photos.

5.5.4 Cell sample preparation

MDA-MB-231 cells were used as cytology samples in this work. The cells were cultured on circular slides confined in self-insert well. When the confluence reached around 80 %, three types of NPs mixed in the culture medium were added into the well. After 2 hours of incubation, free NPs were washed three times with PBS and fixed with methanol. After another washing with PBS, the well was removed and replaced by a double-sided spacer adding the proper medium: PBS, mounting medium or oil, to subsequently use a coverslip for sealing the sample.

5.5.5 Side-illumination adaptor for dark field NPs microscopy

For this work, we designed a new microscopy adaptor where side illumination is adjusted to the circular 25 mm diameter 1 mm thick glass microscope slide with optically polished sides. The substrate is compatible with conventional 25 mm microscopy coverslips for sample preparation. As a light source, we used high-performance tricolor Cree® CLS6B LEDs with a wide viewing angle and high brightness. In the design, the narrow RGB LED array (LED size: 4.7 x 1.5 x 1.3 mm) was mounted in close optical contact with the border of the circular microscope slide, as shown schematically in Figure 5.1A. In order to provide the required precision by the scientific grade microscopes, the working prototype (Figure 5.1B) was fabricated (Vegaphoton Inc.) using aluminum CNC machining for a Nikon inverted microscope. Our tests confirmed theoretical estimation (Zemax optical software) in 3.6 times increased power in intensity and more homogeneous illumination for circular side illumination compared to the previously published rectangular configuration.[306] Another advantage of circular illumination is the minimization of the influence of the spatial orientation of such plasmonic nanomarkers as Au nanorods on the scattering spectral dependences.

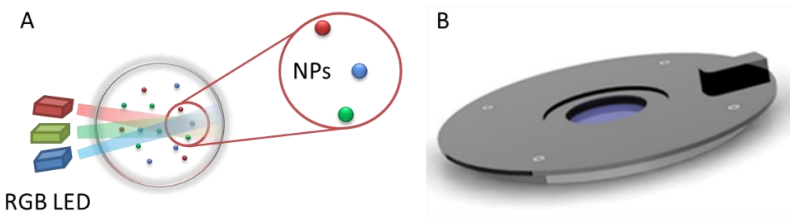

Figure 5.1 (A) Principle of circular side illumination (CSI) microscopy with RGB LED side illumination and plasmonic NPs as biomarkers; (B) experimental prototypes of CSI adaptor compatible for conventional optical microscopy.

An important property of NPs darkfield microscopy with side illumination is its compatibility with most optical microscopes commonly used by researchers and pathologists. This approach and device can be implemented with a standard protocol for cytopathology sample preparation. The visualization method allows simple switching or even combination between conventional transmission mode microscopy and side illumination dark field mode, thus providing complete and more reliable sample analysis.

RGB LED have emission peaks at 638 nm, 526 nm and 468 nm corresponding to R, G and B illumination, respectively. To provide the flexibility in the intended direct visualization microscopy, the manual control of the intensity of the individual color LED is possible. This adaptor can also be used for the realization of an automatic digital NPs microscopy where LED color, intensity, and imaging CMOS color or monochromatic camera will be controlled by the corresponding external software.

5.6 Results and Discussion

5.6.1 Design of optimized NPs for three mediums

The main goal of this project is to provide a scientist, and ultimately a practicing pathologist, a protocol and a useful tool for fast medical diagnostics based on direct visual observation of multiplexed plasmonic biomarkers. To make it possible, such plasmonic biological labels should respond to multiple criteria. First, optical labels must be clearly visible by using simplified darkfield microscopy. This requires high enough scattering efficiency, or scattering cross section, which depends on the dimension and composition of NPs.[301, 310, 311] As standing out from the literature, NPs scattering efficiency comparable to the rather large 100 nm Au NPs (~37300 nm^2) can fulfill such requirements.[204, 306] In addition, NPs are designed to target the receptors on the cell membrane. Their relatively large sizes can prevent endocytosis with living cells, which can significantly change the expression of proteins and lead to an inaccurate quantitative determination of surface receptors.[312, 313] Second, multiplexed NP markers have to be easily chromatically differentiated. Separated resonance peaks are required, which means a large difference between peak positions and small overlap for the whole spectra. This requirement is setting a limitation on the number of simultaneously detected NPs, since the spectra of the resonance peak broaden with NP size as well as the distribution of NPs size and composition. Also, the size of NPs cannot be too large to avoid the obvious quadrupole peak, which determines our choice of 100 nm Au NPs as reference for the scattering cross section and spectral shape of the plasmonic peak. Moreover, the quality control of NPs is important, to obtain a narrow distribution of size and composition. Third, the NP scattering colors should stay in the visible range for simplified direct chromatic differentiation and, at the same time, be finely tuned to the emission spectra of the commercially

available miniature RGB LED. Therefore, the exact matching of the NPs scattering peak position with the emission peak of individual LED is a required optimization condition for NPs fabrication.

Depending on the application, research and diagnostic protocols can be performed with plasmonic biomarkers in different surrounding media that influence their plasmonic and spectral properties. For example, if the 3D spatial distribution of NPs is investigated, the highest possible contrast is provided by matching refractive indexes (RI) between the glass substrate and the oil medium, as they have very close RI. A PBS solution with RI of about 1.34 is often used in the case of live cell manipulation and labeling with NP markers. Finally, conventional cytopathology samples are commonly prepared using the mounting medium to fix and preserve cells on microscope slides. All these three media: phosphate-buffered saline (PBS), cell mounting medium, and oil are of particular interest to this project and, correspondingly, all of the above requirements for NP specifications as biomarkers need to be readjusted based on the application and used medium.

The spectral position of metallic NPs plasmonic peak can be tuned in a large spectral range depending only on the size for spherical NPs. However, adjusting the NP size is not sufficient to respond to all of the above-mentioned criteria and particularly to provide similar scattering efficiency from one marker type to another. In this article, we propose to use alloy Au/Ag NPs that, as was recently shown,[50] can provide much more flexibility in fine spectral tuning by changing NP size and composition. Using Mie theory adapted to alloy NPs we have performed theoretical calculation and found the optimal alloy NP parameters to match blue (468 nm) and green (526 nm) LED illumination in different surrounding media. For future applications, if necessary, the thin biofilm of NP functionalization will be included in the optimization of the NP design and corresponding synthesis protocol.

However, alloy Au/Ag NPs tuning capabilities are limited in terms of the wavelength range. For the requirements mentioned above, the highest wavelength we can reach is around 580 nm, which corresponds to pure gold NPs of about 100 nm. Therefore, for the case of red LED lighting (638 nm), we suggest using Au nanorods, where the scattering efficiency and spectral dependences can be adjusted in accordance with our requirements. Based on Mie theory and the dielectric function for Au/Ag alloy,[120, 126] we have performed a theoretical calculation of the alloy NPs diameter and scattering cross section dependences on the Au/Ag composition for the fixed NPs resonance peak position that correspond to blue and green illumination in three working media. Figure 5.2

shows the example of obtained results for alloy NPs in PBS medium. For the reliable NPs detection, we chose as the reference a scattering cross section of the 100 nm Au NPs (the red horizontal line on the figure). Aiming at having similar scattering cross sections, one can easily obtain the composition and diameter of optimal NPs, as shown on the figure. For example, the optimal size for the "green" NPs is 99 nm with Au/Ag composition 49/51. Furthermore, the "blue" NPs calculation show that the pure Ag NPs are preferable. However, our preliminary experimental results on the stability of fabricated alloy NPs (not presented here) have shown that pure silver NPs or alloy NPs with a very low (few percent) Au concentration suffer from long-term surface oxidation leading to the resonance peak and scattered color shift. We have experimentally found that the stability of Au/Ag alloy NPs depends on the composition [314] and long-term stability can be ensured by at least 10 % of gold in the composition. This determines the choice of "blue" NPs with 10/90 composition for mounting medium and oil, instead of theoretical 2 % and 0 % of gold.

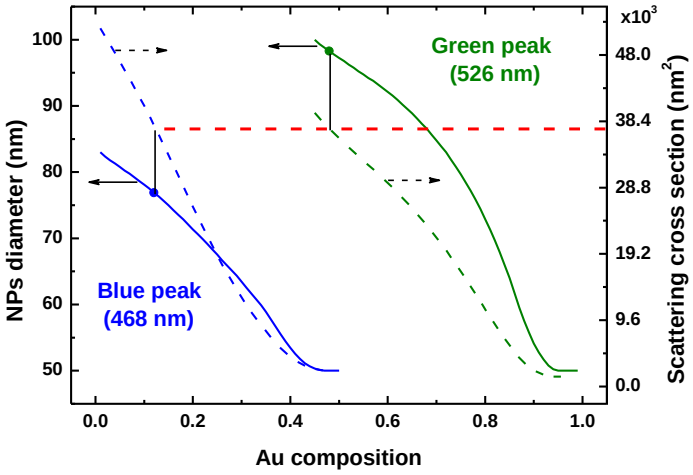

Figure 5.2 Calculation results of possible NPs diameters (solid lines) and cross sections (dashed lines) for a peak at 468 nm (blue) and at 526 nm (green) illumination in PBS. The red dashed line indicates optimization condition of a similar scattering value of 37300 nm^2.

The final result of the calculation and experimental optimization is presented in Table 5.1, including the parameters of the NPs for the other two media calculated by the similar way.

Table 5.1 Calculated composition (in atomic percent) and size of NPs designed for RGB (peak position) illumination in three media with different RI.

Medium	**RI**	**Blue (468 nm)**	**Green (526 nm)**	**Red (638 nm)**
PBS	1.34	77 nm Au/Ag 12/88[a)]	99 nm Au/Ag 49/51	76-106[b)] Au NR
Mounting medium	1.47	59 nm Au/Ag 10/90	80 nm Au/Ag 47/53	62-85 Au NR
Oil	1.51	52 nm Au/Ag 10/90	73 nm Au/Ag 49/51	55-75 Au NR

[a)] 12/88 means 12% Au and 88% Ag in composition; [b)] 76-106 means nanorods of 76 nm in diameter and 106 nm in length

A substantial spectral shift induced by the surrounding media with higher RI such as oil and mounting medium makes it impossible to have alloy NPs with a 10/90 composition at the required resonance peak and at the reference level of scattering cross section (Au 100 nm). In these cases, our choice is to use smaller NPs with lower scattering cross sections (Figure 5.3), but with stable 10/90 composition which can provide long term reliability of samples analysis. Therefore, the cross section of "blue" NPs for mounting medium and oil becomes respectively ~24800 nm^2 and ~19100 nm^2. According to that, similar scattering cross section are set for "green" and "red" NPs in the same medium. It has to be mentioned that, due to the lower loss on the medium/glass interface, these NPs are still showing sufficiently high imaging contrast. To obtain optimal parameters of Au nanorods for work in the red spectral range and in the different media we have performed a theoretical calculation using discrete dipole scattering (nanoDDSCAT) online software.[315]

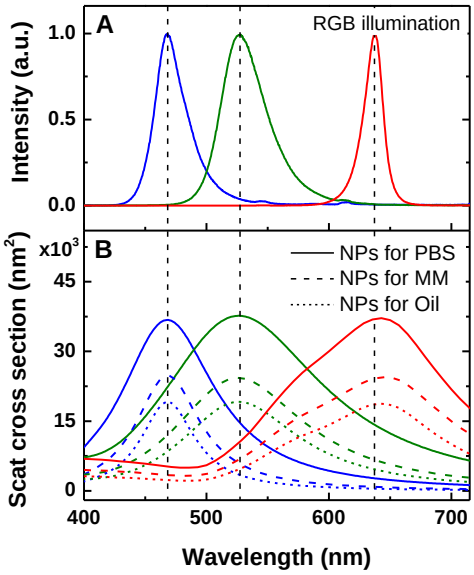

Figure 5.3 (A) Spectra of normalized CL246 LED emission as RGB illumination; (B) Scattering cross section of designed "RGB" NPs in PBS, Vectashield mounting medium (MM) and oil, respectively. The plotting in blue, green and red represents NPs designed for corresponding color/illumination.

Besides the scattered color under RGB illumination, visual or automatic differentiation of multiplexed plasmonic markers by the spectral signature also depends on the detected intensity contrast generated by these markers under single color illumination. Figure 5.4 presents the theoretical comparative scattering intensities of the three designed NPs for independent red, green, and blue illumination in each medium. Almost two times higher scattering intensities for the NPs tuned to the LED color provide adequate contrast for visual differentiation of the intended markers.[316] However, in the complex cellular environment, where additional scattering leads to a decrease of NPs contrast, multiplexing becomes much more reliable when all three nanoplasmonic markers are illuminated independently. In this case, a visual evaluation of the three consecutive images is recommended. Fast automatic LED control with corresponding image treatment software that employs multispectral differentiation method for multiplexed NPs detection is also possible.

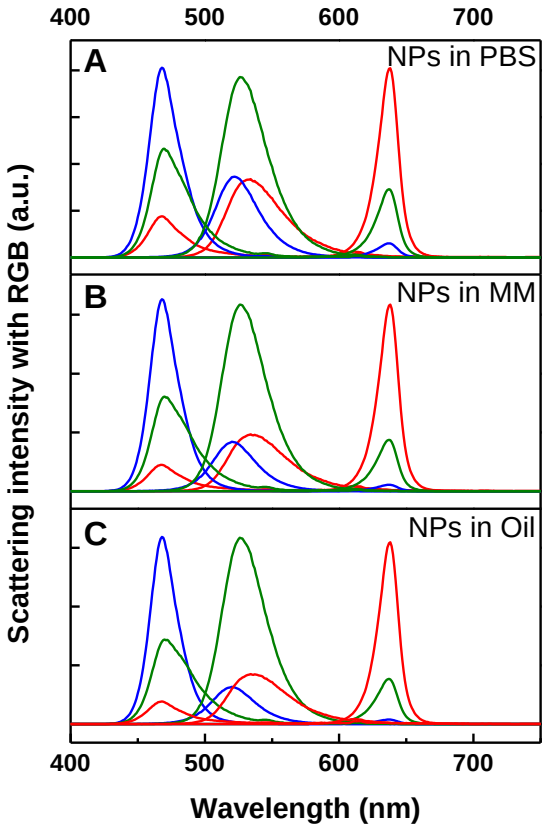

Figure 5.4 Theoretical scattering intensity of designed NPs in (A) PBS, (B) mounting medium (MM) and (C) oil, under monochromatic R, G and B illumination. The plotting in blue, green and red represents NPs designed for the corresponding color.

5.6.2 Characterization of Au/Ag alloy NPs

Au/Ag alloy NPs were synthesized in accordance with the obtained theoretical results shown in Table 1. For nanorods, we chose commercially available Au nanorods from Nanopartz with similar scattering peaks as designed: diameter-length as 40-80 nm for PBS and mounting medium and 40-68 nm for oil. Spectral and dimensional parameters of fabricated NPs were verified by performing extinction spectroscopy of the colloidal solution, TEM and EDS. Moreover, push-broom hyperspectral imaging method was used to estimate the scattering properties of individual NPs in different surrounding media. Experimental results of the UV-visible spectral dependences of the fabricated alloy NPs in aqueous solution (not presented) are in good agreement with the theoretical

prediction from Mie theory. The experimental resonance peak position stays in less than ±15 nm deviation from the theory whereas the spectral width shows higher discrepancies. This particular parameter is directly related to the NP size distribution, which was verified by TEM. Figure 5.5 shows the results for the synthesized Au/Ag alloy spherical NPs designed for three working media. All mentioned characterization methods were used to estimate NPs distribution range and reproducibility of synthesis. The coefficients of variation obtained for both NP sizes and compositions remain in the acceptance 10 % range, corresponding to the requirement of a reliable NPs differentiation spectral range deviation of about ±15 nm. Long-term stability of alloy NPs was verified after one-year storage in the fridge. The observed shift of the extinction spectrum was less than 5 nm for "blue" and "green" NPs, that is acceptable for our optical method of spectral differentiation.

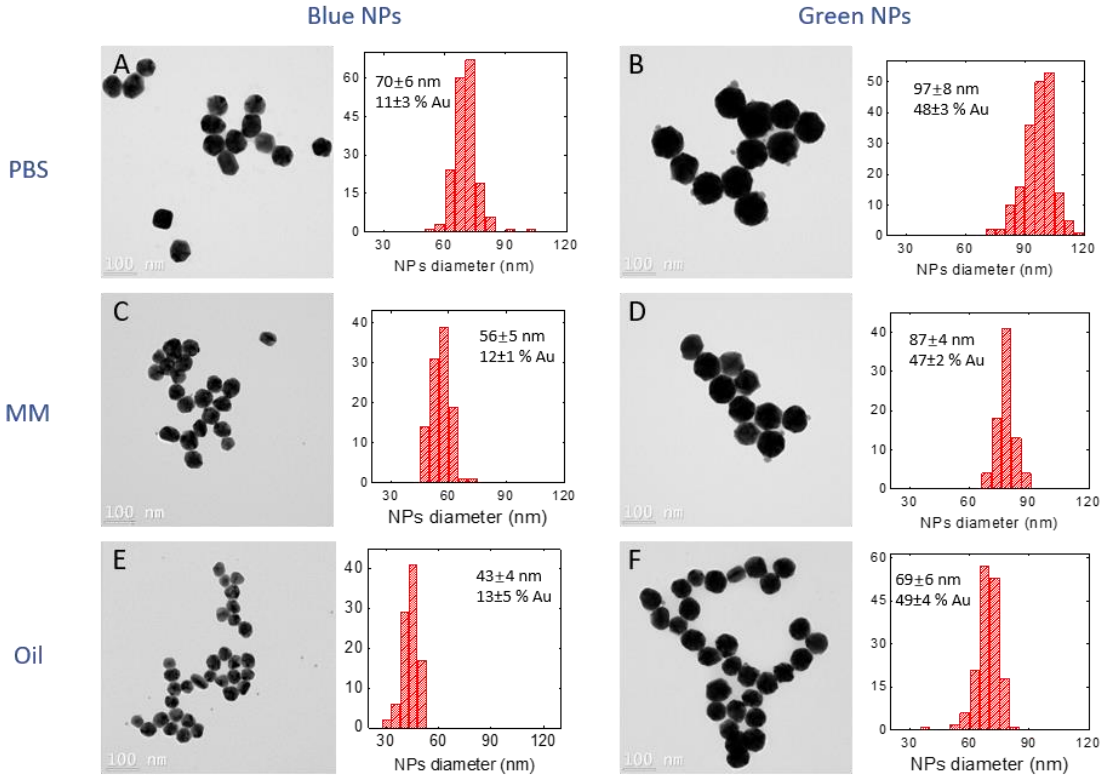

Figure 5.5 TEM images and corresponding size distribution for synthesized "blue" NPs (A, C and E) and "green" NPs (B, D and F) in PBS (A and B), mounting medium (MM) (C and D) and Oil (E and F). The size (nm), the size standard deviation (nm), the silver concentration (in %) and standard deviation are given in inset for each type of NPs.

In order to spectrally characterize the NPs in experimental conditions close to real applications, we have performed push-broom hyperspectral imaging of individual NPs placed in different media between two glass slides. Conventional Halogen 50-watt microscopy illumination was used as light source, providing a smooth spectrum in the spectral range of interest. For NPs imaging, backscattering microscopy mode with 100× 1.25NA immersion oil objective was applied in order to generate high NPs contrast and 3D spatial resolution. Experimental spectral dependences presented on Figure 5.6 confirm that NP scattering peaks are centered or close to the corresponding LED illumination. Obtained results for the morphology, composition and finally, spectral properties of tested NPs indicate the successful synthesis of plasmonic markers for the reliable detection and spectral differentiation in the multiplexing imaging.

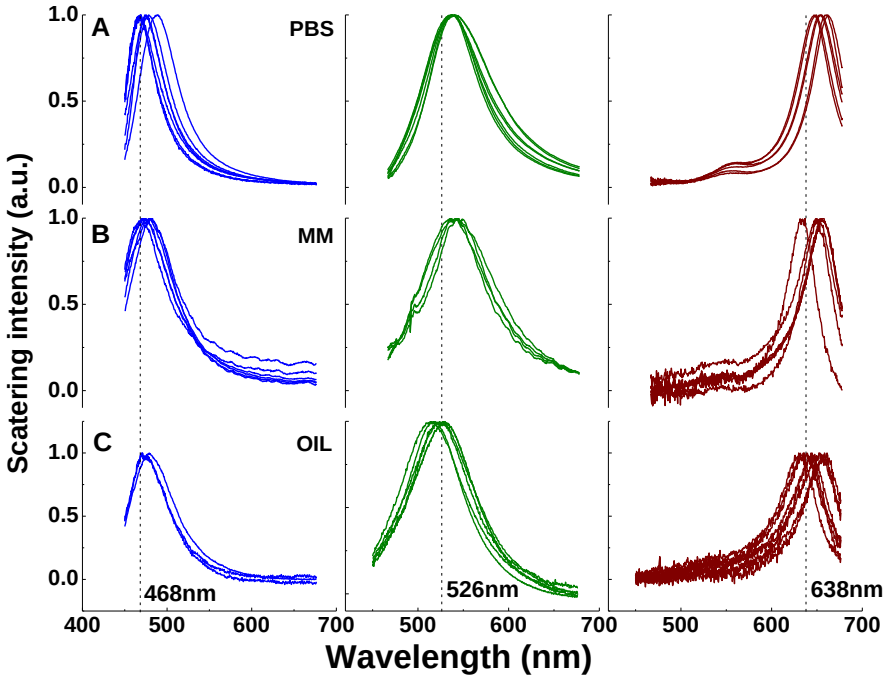

Figure 5.6 Hyperspectral examples of single NPs scattering under white (Halogen) illumination in designated medium: (A) PBS, (B) mounting medium (MM) and (C) oil, plotted in blue, green and red lines for corresponding NPs respectively. The three peak positions of RGB illumination are also indicated. For each spectrum, a sample of 5-8 nanoparticles are shown.

We have tested more than one hundred NPs for each type of NPs in each medium. For each medium, under white light illumination, most spectral peaks of "blue" and "green" NPs (≥ 85 %) are located at ±15 nm from the theoretical position. On the other hand, more than 89 % of "red" NRs have a

spectral peak position > 600 nm, as shown in Table 5.2, ensuring an efficient spectral differentiation in multiplexing. For the nanorods chosen for the red illumination, since they are commercially available ones not exactly in optimal dimension, the spectral peak distribution is relatively wider than the ones of synthesized alloy NPs, and most of them are red-shifted compared with the red illumination. Since the red illumination is the longest wavelength and the position is quite far away from blue and green illumination, the color of nanorods stays in the red. More attention on quality control of NPs is required where influence of NPs distribution can be amplified by various parameters in practical applications.

Table 5.2 Statistical results for spectral peak (in ±15 nm range around theoretical position for "blue" and "green" NPs, > 600 nm for "red" NRs) from more than 100 NPs in their targeting medium for each category.

Medium	**Blue NPs**	**Green NPs**	**Red NPs (> 600 nm)**
PBS	87.5 %	84.8 %	98.0%
Mounting medium	86.7 %	89.0 %	92.6%
Oil	86.7 %	94.0 %	89.4%

5.6.3 Multispectral plasmonic NPs imaging

Initially, multispectral plasmonic NPs imaging using dark field side illumination method with our microscopy adaptor (Figure 5.1) was performed in the homogeneous media. For this work, the CSI adaptor was installed on a Nikon inverted microscope stage (Figure 5.1B). For each used medium (PBS, mounting medium, oil) 1x1x1 mixture of corresponding "RGB" NPs (Table 5.1) was placed on a 25 mm diameter glass substrate with polished side and covered by a thin glass coverslip through a 120 μm spacer. Objective 60×, 0.70NA was used for the NPs visualization and Nikon color camera for the imaging.

On Figure 5.7A, D and G, it is possible to see NPs of three colors under the illumination of three RGB LEDs from the adaptor. In this case, NPs chromatic differentiation can be performed by the operator visual observation or by the microscope color camera. Usually "blue" and "red" NPs are readily separated, whereas differentiation of "green" NPs may sometimes be more difficult. To solve this problem, multispectral RGB imaging can be performed manually or automatically with our device. A differentiation is shown on the Figure 5.7. Under blue illumination, all "red" NPs disappear and on the contrary, under red light one cannot observe "blue" NPs. However, the "green"

NPs while decreasing in scattered intensity, are still present on the images and can be reliably identified by excluding imaging method.

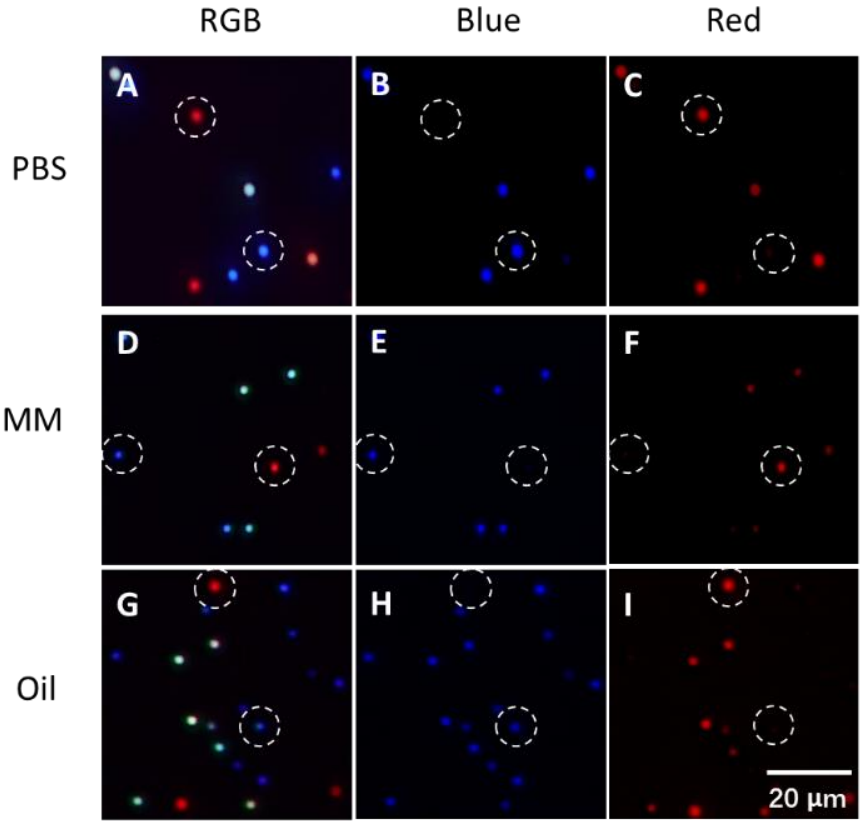

Figure 5.7 Microscopy images of NPs mixture on a glass substrate in designated medium PBS (A-C), mounting medium (MM) (D-F) and Oil (G-I) under side illumination of RGB (A, D and G), single blue (B, E and F) and single red (C, F and I). The dashed circles indicate examples of one “red” NP and one “blue” NP in each medium under different illumination.

5.6.4 Multiplex imaging of cell samples

To demonstrate the ability of our approach and tool to provide a reliable detection method for multiplexed plasmonic NPs markers in complex cellular environment, we have performed a series of experiments with MDA-MB-231 cells cytology samples. This large and adherent breast cancer cell line is highly aggressive and poorly differentiated and there exist many studies on this cell line, since it is triple negative and difficult to have effective therapeutic methods.[317, 318]

The cells were first cultured for 24 h on the glass substrate and then mixed with the three types of NPs. After incubation, they were placed in the three different media for visualization. Figure 5.8 presents the typical microscopy image of MDA-MB-231 cells decorated with the different NPs mentioned above using side illumination adaptor and 60× 0.70NA objective. Corresponding color images with higher magnification obtained in PBS, mounting medium and oil are shown in Figure 5.8C, D and E correspondingly. We can conclude from these results that direct detection and chromatic differentiation of multiple NPs in cellular environment is experimentally possible. Also, it is worth mentioning that direct microscopy visualization by human eye represents an even higher contrast in intensity and color difference than what can be shown on these figures. To further characterize plasmonic markers we have also performed a hyperspectral scan of the cells-NPs complex. With similar level of RGB illumination, the three typical spectral characteristics of NPs are shown on Figure 5.8B, from the ones in Figure 5.8D with corresponding colored circles. The spectra from each single NP are in good agreement with the one predicted by the theory (Figure 5.3). CSI provides also enhanced 3D spatial resolution for NPs detection compared to conventional transmission darkfield microscopy, as the proposed system has no intrinsic limitation on the maximum of the numerical aperture (NA) of the imaging objective. A z-scan has been taken for NPs-decorated cell with 60× 0.95NA objective, shown in the supplementary information.

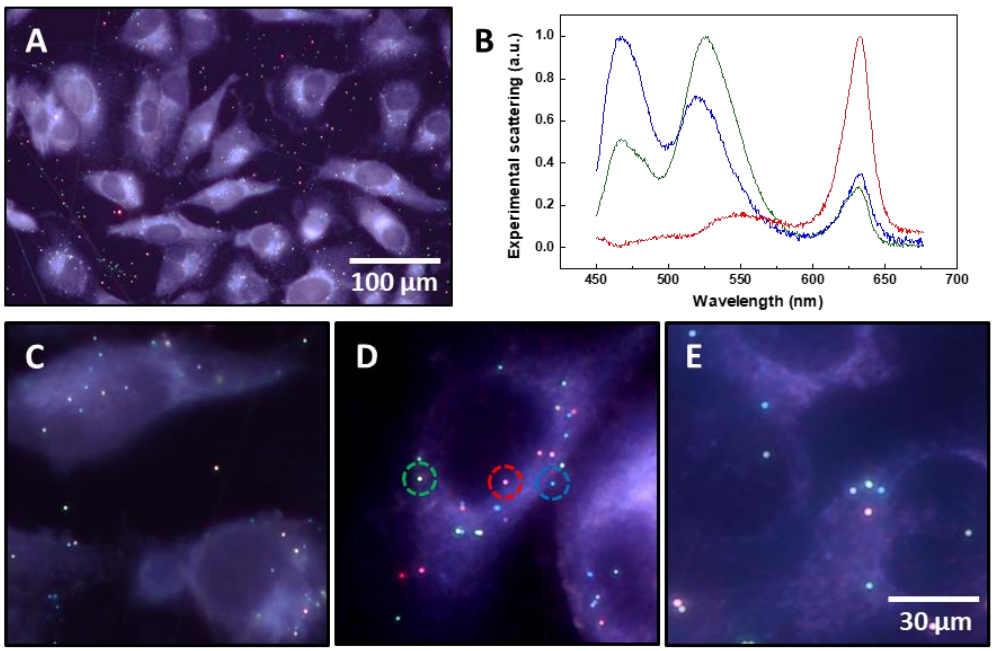

Figure 5.8 (A) CSI microscopy images of NPs mixture attached on MDA-MB-231 cells; (B) hyperspectrum of NPs for each color and detail in designated medium: (C) PBS, (D) mounting medium and (E) oil.

Depending on sensitivity of human eye on different wavelengths (CIE),[319] there is still space for optimization by playing with the combination of R, G and B illumination to obtain the "white light", under which humans are used to perceive the "real color". With the development of high-power LED of various colors, the CSI approach can be even extended to other types of biomarkers of different colors, enabling an easier way of multiplexed imaging.

The demonstrated technique offers the possibility to be easily integrated in conventional diagnostics approaches used by pathologists in clinics, as well as to provide possibility for image digitization and deep learning analysis. Indeed, CSI approach balances the need of direct microscopy visualization as most widely used for practical clinic diagnosis, and the advanced digital analysis with an economic and effective way of imaging. Adaptability in current equipment and method for clinical pathologists makes our technique convenient for distribution, thus facilitating diagnosis, with fast and reliable results.

5.7 Conclusion

Thanks to their great morphological and composition tunability, gold and gold-silver alloy nanoplasmonic biomarkers represent the potential solution for the reliable biolabeling of the cytopathology samples and efficient still simple optical detection method easily integrated on the existing microscopy setup. The synthesis method of NPs can be tailored for different scenarios depending on the final application, ensuring imaging quality and prompt direct visual analysis. The functionalization of NPs will be the next step for further use in the clinic, and will also limit non-specific attachment and aggregation.[157] Plasmonic NPs can be functionalized with various ligands, including peptides and antibodies as the most common ones for specific targeting.[157, 320] The rapidly evolving LED technology provides even more efficient and spectrally distinguishable light sources that will facilitate NPs biomarkers multiplexing with optimal image contrast. Our technology will accelerate plasmonic NPs adaptation as novel reliable and stable biological multiplexed chromatic markers for medical diagnostics.

5.8 Acknowledgements

This work was supported by the financial contributions of the Fonds de Recherche du Québec Nature et Technolgie (FRQNT), the Natural Sciences and Engineering Research Council of Canada (NSERC) and the Canadian Institutes of Health Research (CIHR) grants. Professor Dominique Trudel receives salary support from the Fonds de Recherche du Québec – Santé (FRQS) (Clinical Research Scholar, Junior 1). Technical assistance from Yves Drolet is also acknowledged.

CHAPTER 6 ARTICLE 3: POROUS AU-AG NANOPARTICLES FROM GALVANIC REPLACEMENT APPLIED AS SINGLE-PARTICLE SERS PROBE FOR QUANTITATIVE MONITORING

The article published in *Small* corresponds to the design of porous Au-Ag NPs and the application as SERS probes. The controllable porous nanostructures have been synthesized from galvanic replacement of solid AuAg alloy NPs. With the adjusting of precursor-NPs and reaction conditions, the porous NPs with red-shifted plasmon peaks, and adjustable porosity have been realized. The large accessible surface and intense field enhancement enable the Au-Ag porous NPs as SERS probe at single-particle level, exhibiting 68-fold Raman intense compared with standard Au NP. The single-particle SERS probes have demonstrated quantitative monitoring of anti-cancer drug release, showing potential for theranostic platform.

6.1 Authors

Lu Wang, Sergiy Patskovsky, Bastien Gauthier-Soumis and Michel Meunier

6.2 Contribution of the authors

The author of this thesis, Lu Wang, proposed the idea, performed all the experiments, characterization and application. Bastien Gauthier-Soumis provided the field enhancement simulation of Figure 6.9c. Lu Wang wrote the article. Sergiy Patskovsky and Michel Meunier participated in the discussions as well as in the revision of the article.

6.3 Abstract

Plasmonic nanostructures have raised the interest of biomedical applications of surface-enhanced Raman scattering (SERS). To improve the enhancement and produce sensitive SERS probes, porous Au-Ag alloy nanoparticles (NPs) have been synthesized by dealloying Au-Ag alloy NP-precursors with Au or Ag core in aqueous colloidal environment through galvanic replacement reaction. The novel designed core-shell Au-Ag alloy NP-precursors facilitates the controllable synthesis of porous nanostructure, and dealloying degree during the reaction has significant effect on the structural and spectral properties of dealloyed porous NPs. Narrow-dispersed dealloyed

nanoparticles have been obtained using NPs of Au/Ag ratio from 10/90 to 40/60 with Au and Ag core to produce solid core@porous shell and porous nanoshells, having rough surface, hollowness and porosity around 30-60 %. The clean nanostructure from colloidal synthesis exhibits a red-shifted plasmon peak up to near-infrared region and the large accessible surface induces highly localized surface plasmonic resonance and generates robust SERS activity. Thus, the porous NPs produce intensely enhanced Raman signal up to 68-fold higher than 100 nm-AuNP enhancement at single-particle level, and the estimated Raman enhancement around 7800, showing the potential for highly-sensitive SERS probes. The single-particle SERS probes are effectively demonstrated in quantitative monitoring of anti-cancer drug Doxorubicin release.

6.4 Introduction

Plasmonic nanoparticles (NPs) have been strongly considered in biomedical applications, due to their adjustable localized surface plasmon resonance (LSPR) properties.[2, 116, 246, 321] Various structured plasmonic NPs have been explored due to the strong structural dependence of their optical properties. Hollow and porous NPs are promising as multifunctional platform in theranostics owing to their unique structure with interior vacancies, and their distinctive optical properties, including the LSPR in visible-near infrared (NIR) region, and surface enhancement effect.[65, 322, 323] Especially, the porous plasmonic NPs present significant larger tunability in terms of porosity, composition, and larger specific surface area and higher hot spots density compared to the non-porous nanostructures.[324] As their plasmonic peaks can be tuned in the biological transparent window located in NIR region, the porous NPs may be implemented efficiently in biomedical applications, including bioimaging, biodetection and drug delivery, as well as the surface-enhanced Raman scattering (SERS) based applications.[64, 131, 325, 326]

For biosensing and diagnostics, SERS sensing probes are outstanding among various methods.[327-329] By highly enhancing “finger-print” Raman signal, SERS substrates and probes show promises in analytical chemistry and biochemistry detection with low detection limits.[330] The growing demand for accurate, personalized diagnosis and therapy is opening up new areas of biomedical application with SERS individual nanoprobes,[331] such as, multiplex Raman cellular detection and differentiation, or ultrasensitive multiplex quantitation of microorganisms.[226, 332] In addition, single NPs exhibit great potential in the use of SERS nanoprobes for cyto- and

histopathological diagnostics, where they can give an improvement over the existing tissue imaging system using Raman spectroscopy,[333] by providing local enhancement in spatial Raman mapping studies at the cellular and subcellular level.[334] Plasmonic NPs, especially Au-Ag NPs, provides adjustable SERS probes with high enhancement, due to their LSPR behaviors and their designable structures with high hot spots density. The rough surface, assemblies, nanoscale curvature and gap are promising structures for SERS.[335-338] However, the reproducibility and the stability remain as the main challenge for practical applications. Therefore, it becomes important to have a controllable synthetic strategy for plasmonic NPs with designed nanostructure, clean surface and aqueous dispersibility, to facilitate the wide application in biosensing.

Porous and hollow plasmonic structures have been widely explored using the galvanic replacement reaction (GRR) approach, which removes the less noble metal from the template and replaces it with more noble metal via redox process, while forming vacancies in the multimetallic structure.[58, 339-342] In nanostructures synthesized through GRR, Ag provides the most common sacrificial templates with its high reactivity, while porous structure and surface area are still difficult to control due to the nature of GRR for the fast reaction at the surface with dealloying reagents.[53, 343, 344] Recently, some efforts were made by tailoring the GRR or partially inhibiting GRR to achieve a better controlled of voids number or spherically clustered nanostructures.[57, 64, 345] However, these approaches require a polymer coating during the dealloying process, which occupies the surface, and will significantly impair the access of cargo or analytes for further applications. Another way to get porous structure is to apply a strong acid to alloyed template, thus removing the sacrificial part thoroughly.[346, 347] For example, the concentrated nitric acid, with much stronger dealloying ability than GRR, were used for dealloying the immobilized alloy arrays. However, this stabilizing and solid phase method limit the translation towards a scalable production. To tackle the difficult stabilization, and ensure the surface accessibility in colloidal synthesis, Gao's group employed a thin hollow shell of silica using a quite elaborated process to stabilize the NPs, and finally achieved porous Au-Ag with high surface accessibility.[326]

Instead of regulating GRR through an external environment and the use of organic coatings, we propose to control the final structure through carefully designing the composition of the Au-Ag NP-precursors in GRR. Indeed, as the kinetics of dealloying strongly depends on the relative Ag-

Au composition, we used our newly introduced combined seeded-growth and co-reduction synthesis approach to fabricate Au-Ag alloy NP-precursors with a fine control of both composition within 7% and size over 30 to 150 nm within 15%.[50, 89, 149]

In this paper, we report a newly facile colloidal synthesis approach for porous Au-Ag NPs, which exhibits tunable optical properties, excellent drug loading capacity, and ultrahigh SERS activity, providing single-particle level SERS detector for drug release. The GRR dealloying process is controlled by designing the composition, size, and structure of the NP-precursors. We employed our newly synthesized Au-core and Ag-core alloy-shell NPs as precursors for the GRR dealloying and synthesized the narrow-dispersed NPs, coefficient of deviation less than 15 %, of solid core@porous shell and porous nanoshells with a hollow interior. The spectral and structural evolution during dealloying and the compositional effect has been studied in detail both in colloidal solutions and on single NPs. By controlling both the core and shell size and composition, the Au-Ag alloy core-shell NP-precursors offer a great variation and easy control of final colloidal porous structures. The well-controlled synthesis approach enables to finely-tune the nanostructure, as well as their plasmonic features, including tunable red-shift of plasmon peak up to NIR region, and high-density hot spots for SERS. Thanks to the polymer-free colloidal synthesis, the NPs keep a relatively large accessible surface for SERS. Single-particle level detection is demonstrated based on the strong SERS activity to provide quantitative monitoring of drug release.

6.5 Results and Discussion

6.5.1 GRR Dealloying of Au-Ag Alloy Nanoparticles

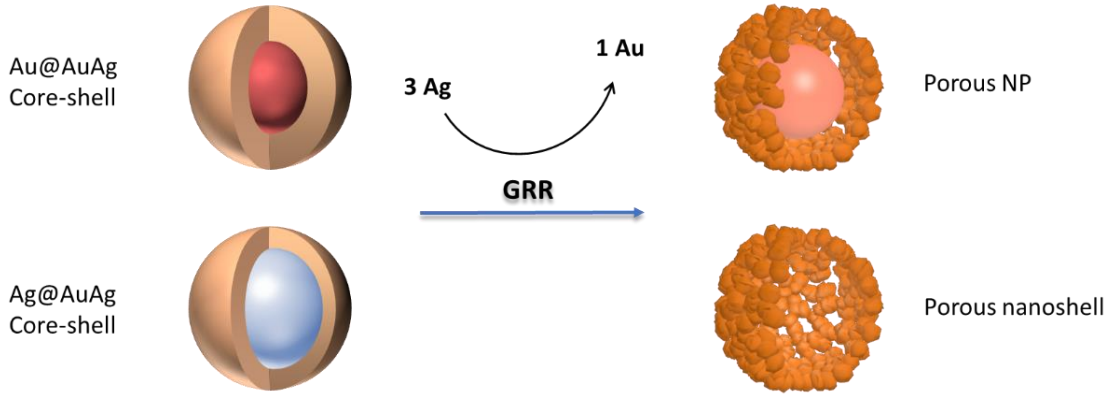

Figure 6.1 Galvanic replacement reaction on Au@Au/Ag and Ag@Au/Ag, resulting in porous shell with solid core (porous NP) or hollow interior (porous nanoshell), respectively.

Taking advantage of the different reactivity between Au and Ag, galvanic replacement reaction (GRR) was employed to remove Ag from Au-Ag alloy. Figure 6.1 illustrates that Au-Ag alloy nanoparticles (NPs) with Au- and Ag-core have been used as NP-precursors, and form porous NPs with solid core (porous NPs) and with a hollow interior (porous nanoshells), respectively. These core-shell structured NP-precursors are denoted as Au@Au/Ag and Ag@Au/Ag NPs respectively and were first synthesized using our previously published seeded-growth method.[50, 89, 149] The alloy shell can be adjusted freely in terms of thickness and composition, while maintaining the mono-dispersion of alloy NPs. Then, $HAuCl_4$ is applied for the GRR, and the dealloying process follows the chemical overall reaction:

$$3Ag(s) + AuCl_4^-(aq) \rightarrow Au(s) + 3Ag^+(aq) + 4Cl^-(aq) \qquad (1)$$

where the reduction potential over standard hydrogen electrode (SHE) of $AuCl_4^-$/Au (0.99 V vs. SHE) is higher than the one of AgCl/Ag (0.22 V vs. SHE),[54] so that each three Ag atoms are replaced by one Au atom, introducing vacancies. Combined with the concurrent Kirkendall effect, driven by the different diffusion rates between Au and Ag, GRR forms porous and hollow structure

in NPs.[53, 64, 325, 348] After dealloying, Au@Au/Ag NPs transform to solid core@porous shell nanostructures with rough surface, while Ag@Au/Au NP becomes porous shell with hollow interior as shown in Figure 6.1.

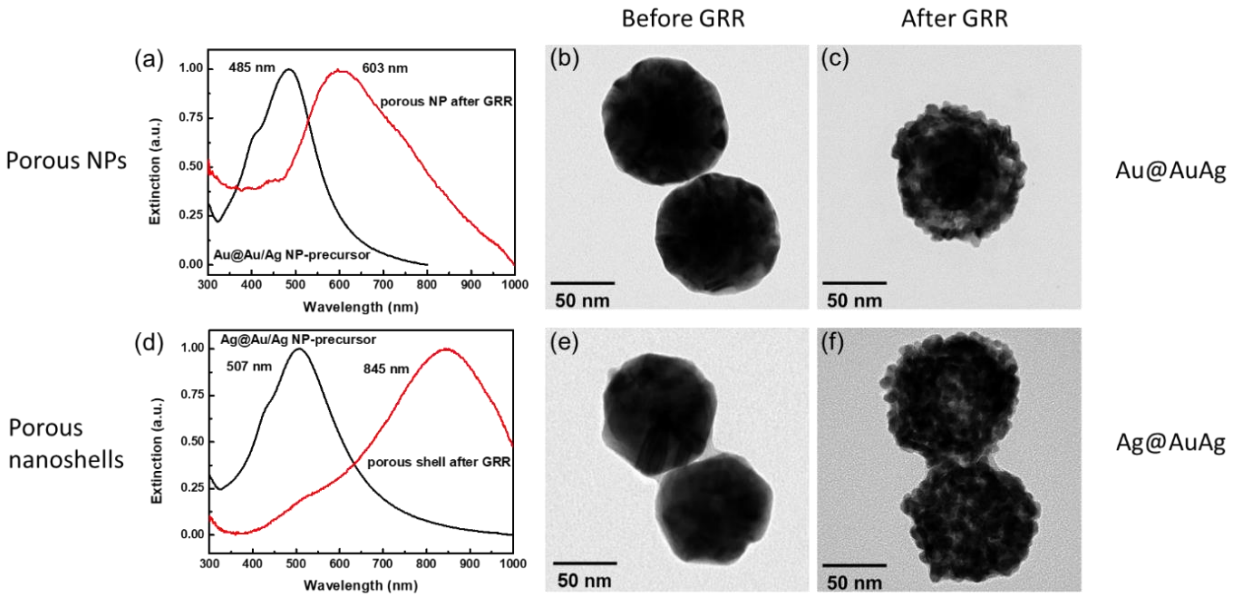

Figure 6.2 Typical extinction spectra (a, d) and TEM images of Au@Au/Ag and Ag@Au/Ag before (b, e) and after GRR (c, f).

During GRR dealloying, as $HAuCl_4$ is slowly added into the aqueous dispersion at room temperature, the NPs colloid color changes with time and its intensity decreases. To illustrate the optical and structural changes during dealloying of alloy NPs, two representative examples of the UV-visible spectra and TEM of Au@Au/Ag and Ag@Au/Ag are shown in Figure 6.2. The NP-precursors are composed of the same shell composition of Au/Ag 25/75, having respectively a 40 nm Au-core and a 60 nm Ag-core. After the GRR dealloying, the two types of precursors result in distinguishable spectra and structures. Plasmonic extinction peak of both types of NPs has red-shifted after GRR, by ~118 nm for Au-core precursors (Figure 6.2a) and by ~337 nm for Ag-core (Figure 6.2d). The large optical shifts result in an obvious color change for colloidal and single NPs, the peak of hollow nanoshells even reaches the near infrared (NIR) region, which is interesting for biomedical applications. Meanwhile, the extinction spectra broaden with the intensity decreasing, due to the porous and hollow structure, probably introducing significant phase-retardation effects.[349] During the dealloying, spherical NPs stay relatively monodispersed

while generating nanoscale rough surface and porous structure, as well as creating hollow space in the NPs. The diameter of NPs slightly increases, by < 10 %, contrary to the shrinkage in dealloying with strong acid for fixed NPs.[350, 351] Au@Au/Ag NPs transform from solid spheres to porous NPs with a rough surface and many nanoscale pits near the surface (TEM shown in Figure 6.2b,c). Note that the Ag in the shell has been partially removed, while the Au-rich core still remains. However, Ag@Au/Ag NPs reconstruct from solid spheres to porous shells with a hollow interior (Figure 6.2e,f), by removing the Ag-core. Therefore, for both structures, accessible surface and loading space increase remarkably and the rough surface creates local curvature, generating a high density of hot spots. Generally, the high surface energy limits the production of controllable and stable nanostructures which requires surface coating, based on the work of Dey and co-workers with hyperbranched polymer.[352] However, by using our monodispersed alloy precursors and by adjusting the concentration of NPs and the addition rate of dealloying reagent $HAuCl_4$, we can easily obtain through coating-free synthesis, well-dispersed final colloidal porous nanostructures with high reproducibility.

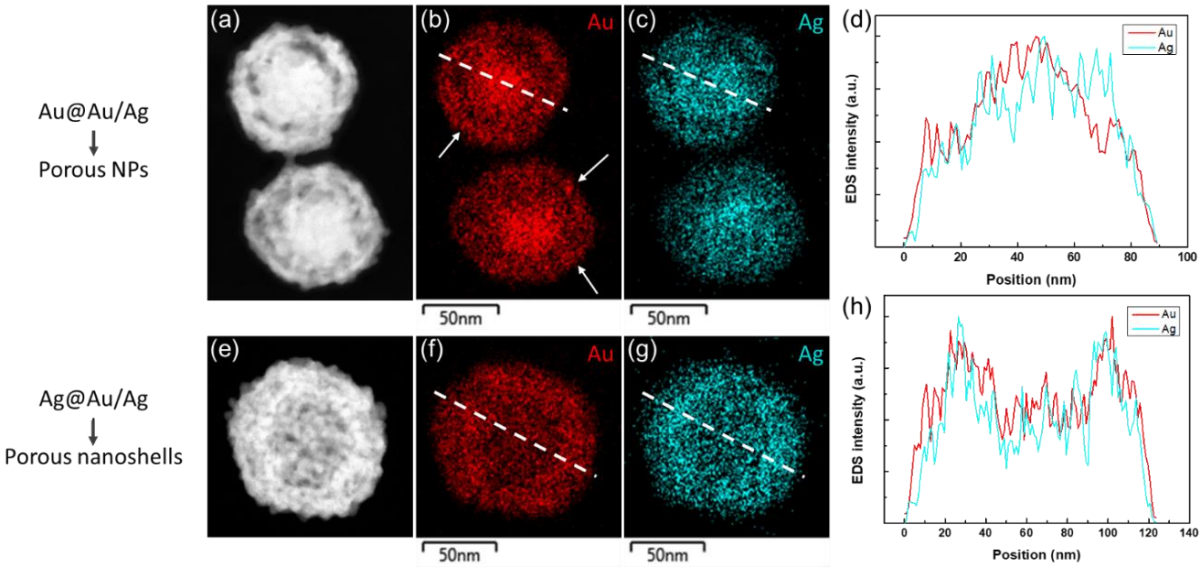

Figure 6.3 High-angle annular dark-field scanning transmission electron microscopy (HAADF-STEM) image of dealloyed NPs from (a) Au@Au/Ag, (e) Ag@Au/Ag NPs, and their respective (b,c and f,g) elemental mapping of Au and Ag. Elemental composition profile along the dashed lines (in b, c, f, and g) are shown in figures d and h.

Many details of the dealloying effect on Au-Ag alloy NPs are revealed by the high-angle annular dark field (HAADF) and energy dispersive X-ray spectroscopy (EDS) mapping under scanning transmission electron microscopy (STEM) (Figure 6.3). For the porous NPs dealloyed from Au@Au/Ag NP-precursors (Figure 6.3a-d), HAADF-STEM shows that the core remains, while large pores appear in the shell as well as a gap between the surface and core. The EDS mapping exhibits that Au accumulates near the center and at some small islands near the surface (indicated by white arrows in Figure 6.3a), and for Ag, there is an evident loss in the shell, while a significant part of Ag migrates to the core and remains after dealloying. It is reasonable that Ag atoms near the surface are easier to be selectively removed, while remaining Au atoms, along with newly grown ones gather near the forefront, especially around the pores near the surface. The line profile of Au and Ag intensities demonstrate that the Au and Ag are quite equally mixed, indicating that the Au and Ag re-alloy during the dealloying to remain thermodynamically stable.[353]

For porous nanoshells dealloyed from Ag@alloy NPs, we can clearly see the tangled ligaments near the surface from HAADF-STEM image (Figure 6.3e), and the hollow interior from the contrast between core and shell, which are created by removing large portion of the precursor, especially the Ag core. The elemental mapping and line profiles (Figure 6.3f-h) illustrate the shell structure and the homogeneous mixing of Au and Ag. Massive dealloying, especially dealloying from the core requires large interaction between the internal and external environment. The decrease near the center of the nanoshell in the line profile is a clear signature of the empty core and is in agreement with a simple geometry model of a transmission path through a shell structure shown in Figure A.1. Due to the abundant exchange in dealloying, Au and Ag are homogeneously distributed in the nanoshell, as shown in elemental mapping and line profile (Figure 6.3f-h). With different diffusion rate between Au and Ag, Kirkendall effect introduced more porous structure in the shell.[348]

By finely control the GRR reaction, even if a significant amount of Ag atoms is removed, we observed that the Au rich structure remains, preventing the collapse the final structure, and that the newly attached Au atoms on the surface slightly enlarges the diameter of final NPs. The removal of Ag and atomic diffusion during the dealloying create high curvature near the surface, pits and a gap between core and shell, as well as a hollow interior. Both Au@alloy and Ag@alloy NPs

become porous after dealloying, generating large accessible surface area, loading space, and high density of hot spots.

6.5.2 Calculation of porosity

The porosity in final NPs can be estimated from the Au and Ag composition and size of both precursor and porous NPs and the fact that the loss of each three Ag atoms is replaced by one Au atom. The vacancy 2*x* is given by:

$$\frac{Au+x}{Ag-3x} = \frac{Au'}{Ag'} \qquad (2)$$

where *Au* and *Ag* are the respective atomic percentage of Au and Ag in precursor, while *Au'* and *Ag'* are their atomic percentage in final dealloyed NPs. The removed Ag atoms and newly deposited Au atoms are quantified as 3*x* and *x*, respectively. Therefore, vacancy resulted from the loss of atoms is estimated as 2*x* in atomic percentage of NP-precursors. Due to the similar crystal structure and lattice constant of Au and Ag, 4.078 Å (Au) and 4.086 Å (Ag), we roughly consider the volume percentages as atomic ones. Besides the vacancy, Kirkendall effect during the mass transportation and accumulation of Au atoms on the surface, slightly enlarges the diameter, thus the volume of NPs. The volume enlargement (ΔV) is calculated through the diameter measured from TEM images:

$$\Delta V = V' - V = \frac{1}{6}\pi\left(D'^3 - D^3\right) \qquad (3)$$

where *D* and *D'* are the respective measured diameter of NPs before and after dealloying, as shown in Figure A.2a, taken from the average diameter of over fifty NPs from TEM images. Therefore, both the vacancy generated in GRR and volume enlargement contribute to the pore structure of the NPs. If the porosity is uniformly distributed in the whole NP, porosity equals to the percentage of pore structure in the volume of final NP, as equation (4). While in most cases, pore structure distributes in the shell, which plays the most important role in interacting with the electrolyte environment or being applied for the surface properties. Therefore, when the NPs contains a solid core (with diameter of D_{core}), we consider the pore structure distributes in the shell (with diameter of D_{shell}), as shown in Figure A.2b, and porosity in shell is expressed as equation (5).

$$porosity = \frac{2xV+\Delta V}{V'} = 1-(1-2x)\frac{V}{V'} = 1-(1-2x)\frac{D^3}{D'^3} \qquad (4)$$

Or

$$porosity\ in\ shell = \frac{2xV+\Delta V}{V_{shell}} = \frac{D_{shell}^3-(1-2x)D^3}{D_{shell}^3-D_{core}^3} \quad (5)$$

6.5.3 Effect of the dealloying degree

As dealloying reagent in GRR, the amount of $HAuCl_4$ has significant impact on the dealloying process. We define the term **dealloying degree (d_D)** to describe the amount of the added $HAuCl_4$ compared to Ag atoms in precursor NPs. When the ratio of added $HAuCl_4$ and Ag in precursors is exactly 3:1, equal to the stoichiometric ratio between $[AuCl_4]^-$ in the solution and the total number of Ag atoms in all NPs precursors in GRR, the d_D is defined as 1.0; when more $HAuCl_4$ added, d_D is higher than 1.0, otherwise, lower than 1.0. Thus, the equation is:

$$d_D = [AuCl_4]^-/3[Ag] \quad (6)$$

Dealloying degree describes the experimental condition in terms of how much dealloying reagent is added, but it does not reflect the detailed reaction, considering that the composition threshold may prevent complete dealloying, left with surplus $HAuCl_4$. The color change happens with the slow addition of $HAuCl_4$ into the precursor NPs dispersions, which directly reflects the influence from the amount of added $HAuCl_4$.

To study the influence of d_D, over a fix time of 30 min at room temperature, we dealloyed Au@Au/Ag 10/90 core-shell NPs (Au@Au/Ag NPs, constituted with 40 nm core and Au/Ag 10/90 alloy shell), at d_D = 0.5, 0.75, 1.0 and 1.5. We investigated the structural features changing with d_D through TEM and UV-visible spectrophotometer characterization as well as EDS. Figure 6.4 shows distinguishable spectral and structural changes from precursor to final NPs of different d_D. During the dealloying, the color of NPs dispersion changes abruptly from orange to blue and gray, shown in the inserted color image in Figure 6.4a. After GRR, extinction peaks show great red-shift (~170 nm) and obvious broaden at lower d_D, and the red-shift decreases with higher d_D, stabilizing after d_D > 1.0 (Figure 6.4a), showing ~110 nm red-shift compared to the precursor. The formation of gap and heterogeneous structure between core and shell induce broaden or even diverging of the peak. Moreover, the red-NIR spectral region (700-900 nm) is a signature of the presence of a thin Au-rich layer on the surface which is more pronounced at lower d_D of 0.75 and significantly

decrease with higher d_D because of the arrangement of atoms contributing to more homogeneous composition.[353]

Porous nanoparticles with d_D = 0.5 (Figure 6.4c) show mainly rough surface, and some particles begin to form the gap between core and shell, while with $d_D \geq 0.75$ (Figure 6.4d-e), NPs exhibit obvious gap between core and shell, showing similar yolk-porous shell structure. The uniformity of porous structure has been proved with low-resolution TEM images containing more porous NPs (Figure A.3). Based on the statistics from TEM images (Table A.1), we found that the core shrinks with increasing d_D. From d_D of 0.75 to 1.0, the core size stays relatively constant while the shell keeps enlarging, indicating that the dealloying process is concentrated in the shell. After the dealloying of shell, further dealloying deepens into the core at higher d_D =1.5, as the core size decreases abruptly from ~58 nm to ~49 nm, while the exterior diameter of NPs stays constant compared to d_D = 1.0. This can be explained by the collapse of microstructure resulting from the coalescing, which balances with further deposition of Au. In brief, dealloying near the surface begins at lower d_D, inducing yolk-porous shell structure, and more sufficient reagents drives the dealloying approaching the core. Figure A.4 shows the results from Au@Au/Ag 27/75 for d_D in the range of 0.25-1.5, and the spectral shift exhibits similar trend with Figure 6.4a, and the TEM show clear rough surface when $d_D \geq 0.5$.

As discussed with STEM results, dealloying occurs first near the surface and the Ag-rich (90 at. %) shell induced violent dealloying. The dealloying induces large vacancies while the inertness of left Au and Au-rich core hinder the dealloying into the core. Therefore, the gap between the core and the shell forms. The re-alloying taking place during the dealloying allows GRR to penetrate inside the NPs with higher d_D. While due to the inertness of Au core, the center of the nanostructure stays intact. The gap and porous shell induces large red-shift and the thin shell creates stronger electron-surface scattering effect, generating much wider plasmonic peak.[354]

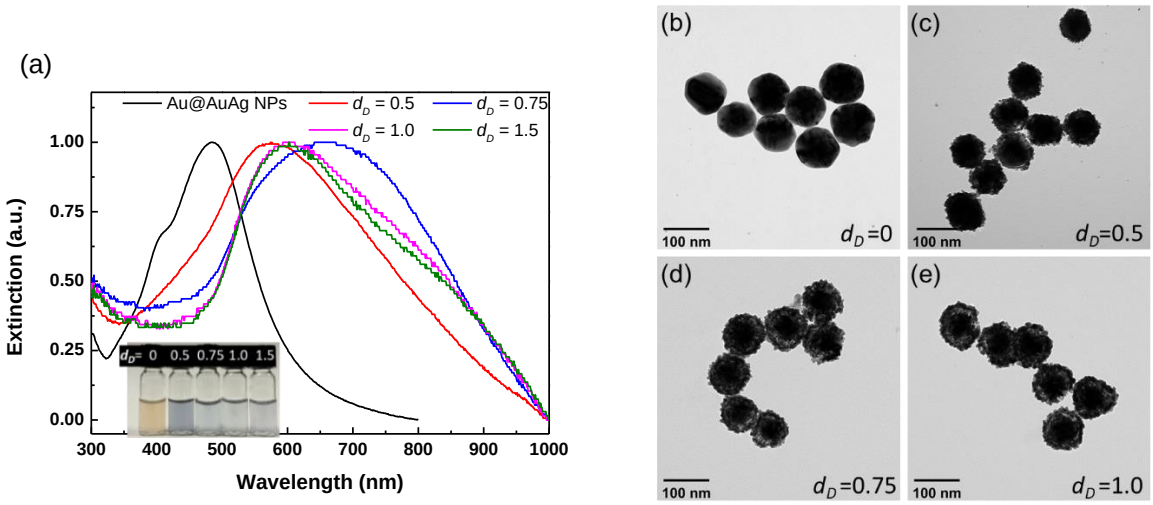

Figure 6.4 Effect of dealloying degree on the synthesis of porous NPs. (a) Extinction spectra and (b-e) TEM image of Au@Au/Ag 10/90 NP-precursor (d_D = 0) and porous NPs after GRR with dealloying degree (d_D) of 0.5 0.75, and 1.0, respectively.

Based on the statistics of the measured core and shell size, combined with compositional results from the NPs, we calculated the overall porosity and shell porosity (Figure 6.5). With increasing d_D, more Ag gets replaced by Au, and Au fraction reaches 52 % at d_D = 1.5 from 16 % in the NP-precursor. From NP-precursor to d_D = 0.75, the Au composition shows a significant increase, indicating main dealloying reaction occurs at the early stage. After that, when d_D increases, the composition change is limited, especially after d_D = 1.0. Considering the Au-core in the precursor, combined with the compositional threshold, it is difficult to have further dealloying. The overall porosity exhibits a similar trend as the Au composition of the NPs, while the shell porosity is influenced significantly by the size of the core and shell. Therefore, the shell porosity peaks at d_D = 0.5, reaching 80 %, when the dealloying only happens at the surface of NPs. Due to the dealloying penetrating into the NPs and the shell expansion, the porosity of shell drops after d_D = 0.75, reaching 44 % at d_D = 1.

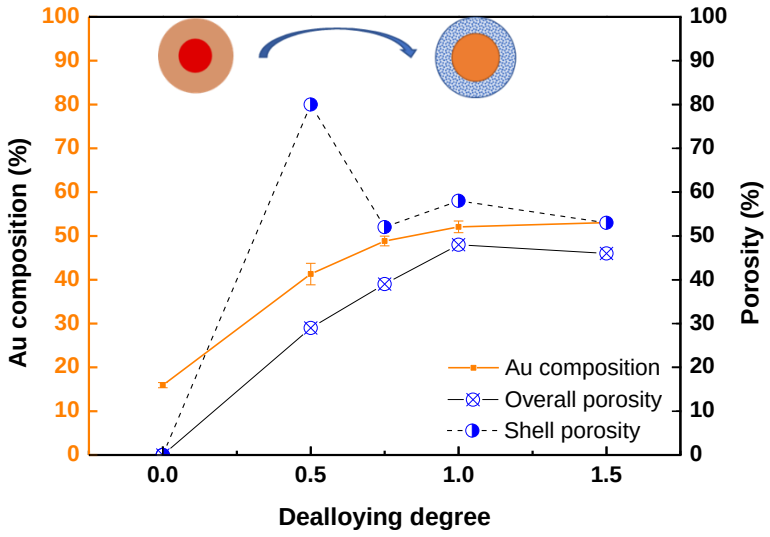

Figure 6.5 Effect of dealloying degree on the synthesis of porous NPs. The average porosity and Au composition of Au@Au/Ag 10/90 precursor and the NPs at dealloying degree d_D =0.5, 0.75, 1.0 and 1.5. The value d_D =0 is for the NPs precursor with 0 porosity. The schematics represent the size of core and exterior shell before and after dealloying.

Comparing with porous NPs from Au-core ones, Ag-core NP-precursors exhibit much larger change, including hollow interior, and plasmonic peaks of porous nanoshells shift to NIR region. To investigate the influence of d_D on Ag@AuAg precursor NPs, we performed GRR on 70 nm-Ag core and alloy shell of Au/Ag 25/75 with d_D = 0.5, 1.0 and 1.5. Due to the large amount of Ag existing in the precursors, more dealloying agent ($HAuCl_4$) is required, thus greatly affecting the structure. The extinction spectra and TEM reveal the spectral and structural changes in dealloying process (Figure 6.6). The inserted photo in Figure 6.6a shows the color of NPs dispersion change from orange to blue and pale blue-gray. Based on the extinction spectra and TEM images, the surface of NPs roughens, and the interior begins to hollow at the early stage (d_D = 0.5), resulting in a significant red-shift from 509 nm to 730 nm. With higher d_D, at 1.0, the NPs become porous nanoshells with hollow interior, and the plasmonic peak shifts further, up to NIR region. With an excess of $HAuCl_4$, at d_D = 1.5, the porous shell enlarges in different ways, the surface of the porous shells grows into large crowns or becomes thicker and solid. The extinction peak does not shift significantly compared to d_D = 1.0, which implies that the hollow interior remains intact.

Detailed statistics on the size of core and shell, composition as well as overall porosity has been listed in Table A.2. The size of porous NPs enlarges at d_D = 0.5, which indicates that the dealloying takes place near the surface, so that the deposition of Au appears on the surface, as the pores also begin to form locally. At d_D = 1.0, with more removal, the pores integrate into hollow interior, and NPs transform into porous shells. Meanwhile, the size of shell slightly shrinks, which can be the result of micro collapse during large scale removal of Ag as well as the Au deposition onto the internal frontier. From d_D of 1.0 to 1.5, the shell enlarges while the hollow interior expands slightly as well. The removal of Ag continues while more Au grows onto the surface of NP, which is in accordance with the TEM images showing a big crown or thick shell formation.

Due to the vast and fast dealloying, dealloyed NPs from Ag-core precursors exhibit larger variation, including the size of hollow interior and porous shell. Meanwhile, the overall porosity of porous shell is increasing with d_D, caused by the size enlargement at higher d_D. At d_D = 1.0, the distribution is still similar with the Au-core NP-precursors, showing finely controlled structure. Considering both porosity and dispersity, porous nanoshells at d_D = 1.0 offers high potential by demonstrating both high porosity and uniform structures.

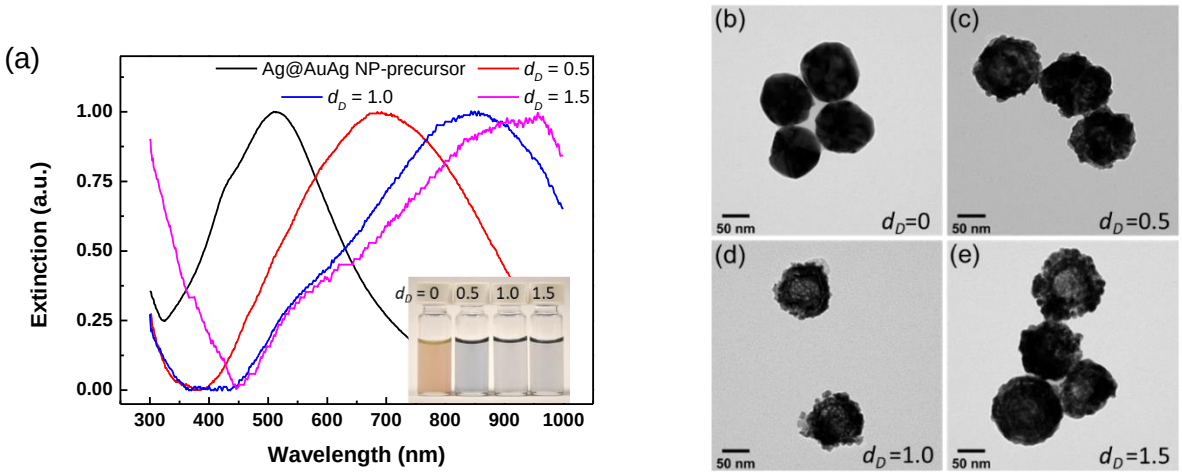

Figure 6.6 Effect of dealloying degree on the synthesis of porous nanoshells. (a) Extinction spectra and (b-e) TEM image of Ag@Au/Ag precursor and NPs after GRR with d_D of 0.5, 1.0 and 1.5.

Dealloying degree easily adjusts the reaction extent through controlling the amount of added $HAuCl_4$. Dealloying near the surface increases the shell diameter, while the further dealloying

inside NPs fine-tunes the structure, thus the optical properties. The d_D combined with the design of core-shell structure in precursor finely control the tailoring of final porous NPs.

Composition of precursors significantly affects the dealloying kinetics, due to the high reactivity of Ag and inertness of Au. Controlling the composition distribution of precursors will therefore regulate the structural, compositional, thus optical properties of final porous NPs. We employed precursors of different compositions and investigated its effect on the resulted structure after dealloying. Based on the established study on Au-Ag alloy, there exists a critical electrochemical potential for the onset of percolation dealloying, which is dependent on the composition, and the composition bound of AuAg alloy is at least ~55% Ag.[355-358]

We used Au@AuAg precursors composed of an alloy shell with composition of Au/Ag 10/90, 25/75 and 40/60, with 40 nm-Au core located at the center. Figure 6.7a shows the extinction spectra of the three kinds of NP-precursors of similar size (~90 nm) with shell composition of Au/Ag 10/90, 25/75 and 40/60, before and after d_D of 1.0. Extinction peaks broaden and show recognizable red-shift after dealloying. Some of dealloyed NPs show asymmetry, a usual signature of NPs composed of a core and a shell or heterogeneous in composition. Especially, dealloyed NPs from Au/Ag 10/90 showed broad extinction peak due to the inhomogeneous structure. Figure 6.7b shows the extinction peak shift of NPs at different d_D. Au@Au/Ag 10/90 NP-precursors (blue squares) exhibit the largest shift (over 170 nm) at d_D = 0.75, while the porous structure collapses or the porosity reduces at d_D > 1.0, with plasmon peak shifting back. Au@Au/Ag 25/75 NP-precursors (orange circles) induce gradual peak shift within a wide d_D range (up to 1.0), and demonstrate large overall shift, reaching up to 160 nm. After the almost linear shift, the peak position becomes stable after d_D = 1.0, and the further deposition of Au leads to small red-shift at d_D = 1.5. Au@Au/Ag 40/60 NP-precursors (pink triangles) yield relatively small peak shift (~60 nm) during the early stage of GRR, while there is almost no change when d_D > 0.25.

To directly compare the structure of dealloyed NPs from different compositions, we also analyzed the NPs at the same d_D = 1.0 with TEM. Figure 6.7c-e show the dealloyed NPs from Au@Au/Ag precursors with shell composition of 10/90, 25/75 and 40/60, respectively. The structure of surface and pores vary significantly with the composition. The dealloyed NPs from Au@Au/Ag 10/90 NP-precursors appear as porous shells with rough surface and the spongy interior surrounding the left core. However, the NPs dealloyed from Au@Au/Ag 25/75 precursors exhibit clear pits and holes

near the surface, forming a separation of core and shell. Moreover, the Au@Au/Ag 40/60 NPs are only slightly dealloyed at the surface, and the loss of atoms formed pits and roughened the surface, limited by the composition of 40% Au. Thus, by adjusting the composition of precursors, we produced three different structures. The plasmonic peak shifts shown in Figure 6.7a are clearly explained by the presence of pores or hollowness formed in the interior and pits with roughness of the surface.

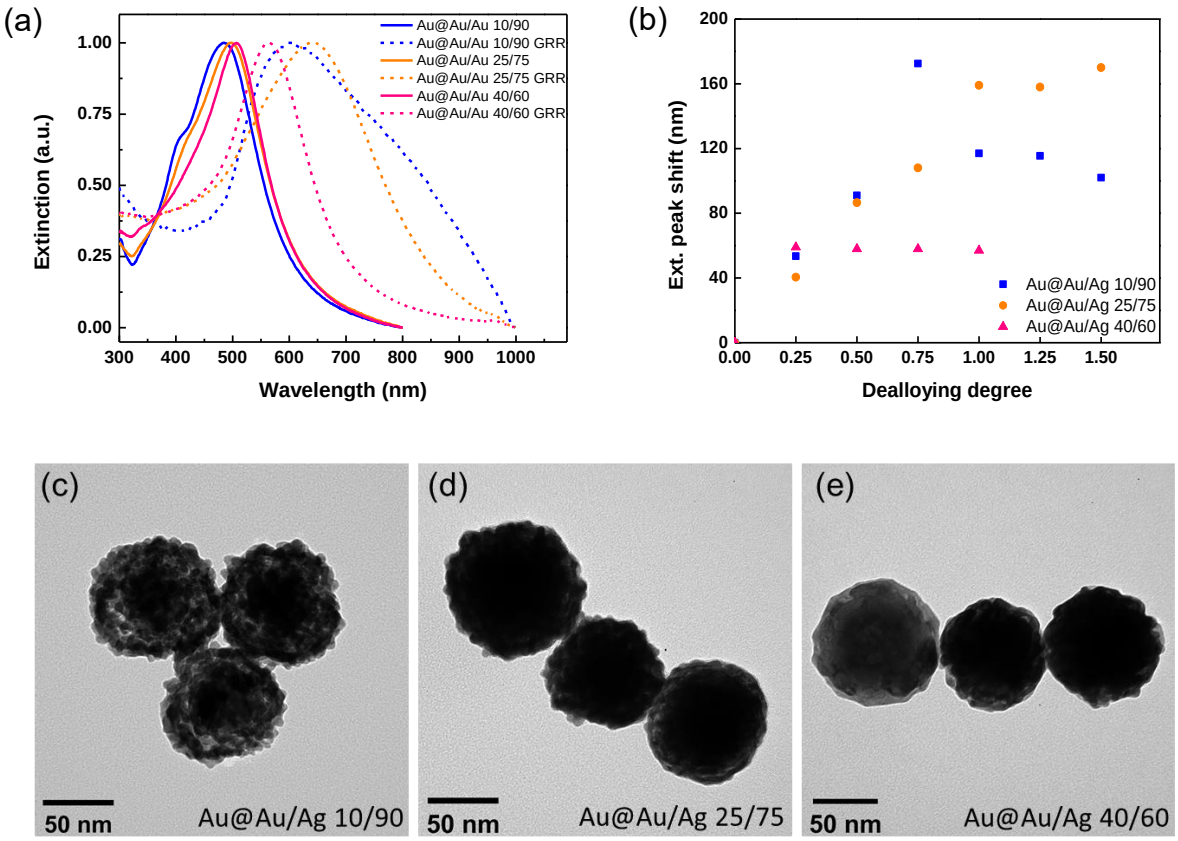

Figure 6.7 Effect of shell composition on the synthesis of porous NPs. (a) Spectra of Au@AuAg NPs with shell composition of Au/Ag 10/90, 25/75 and 40/60, three kinds of precursor NPs before and after GRR (d_D = 1.0). (b) The extinction shift of Au/Ag 10/90 (blue square), Au/Ag 25/75 (orange circle) and Au/Ag 40/60 (pink triangle) with different d_D in GRR. (c-e) TEM images of NPs at d_D = 1.0 from precursors with shell composition of Au/Ag 10/90, 25/75 and 40/60.

In bulk Au-Ag dealloying, there exist composition-dependent critical potential, which decreases with higher Ag composition.[355, 356, 359, 360] With lower critical potential, the precursor is more susceptible to dealloying. Applied in NPs under GRR, the controlled composition of the NP-precursors efficiently adjusts the removal of Ag atoms and deposition of Au atoms. The precursors with composition close to critical composition for dealloying, are limited by the compositional threshold, which means only a small number of Ag atoms can be removed until reaching the critical composition, GRR resulting in limited change of the surface roughness. Faster and more intense dealloying occurs with Ag-rich precursors, resulting in rough surfaces with higher curvature and more removal of Ag atoms and vacancies formed in the NPs as dealloying penetrates the interior of NPs. The final size, composition and the gap between core and shell are strongly dependent on the easily tunable composition of precursors, which makes the dealloyed structure predictable and enables the specific structure design. When combining with d_D, the design of the porous structure and optical properties of the dealloyed NPs can be more flexible by tuning the dimension and morphology of the core and shell.

Compositional effect not only influences the GRR process on Au-core precursors, but also on Ag-core ones. Note that it is difficult to dealloy deeper layers of the Au/Ag 40/60 shell with GRR, where only the surface layers (< 10 nm) are affected, exhibiting bumps and roughness for Au@AuAg NP-precursors. We opted to investigate the dealloying of pure Ag and Ag@Au/Ag 10/90 and Au/Ag 25/75 core-shell NPs. GRR transforms the precursors into hollow shells with different shell thicknesses and porosities. Pure Ag precursors tend to result in uniform shells, which has been widely observed before with nanocubes or nanospheres for nanocages, nanoboxes and nanoshells.[53, 361, 362] The homogeneous Au deposition in dealloying forms a thin but smooth layer on the surface of pure Ag. Only after the whole hollowing process, the alloyed shell can generate several pinholes on the surface. However, the alloy-shell precursors provide intrinsic “heterogeneous” structure with discontinuity of either Ag or Au, which creates numbers of pits and interrupts the continuous deposition over the surface during dealloying. Au islands and untouched Ag affix to each other, and their realloying occurs simultaneously with the hollowing. Rough surface and porous structure with penetrable shell are realized with the alloy shell, and the adjustable dimension of core-shell structure facilitates the size tuning in terms of hollow interior as well as the shell thickness.

6.5.4 Single NP *in situ* spectral characterization

In situ study on dealloying of plasmonic NPs has been performed to deeply understand the nanostructure evolution.[58, 363] Many researchers have used the state-of-art spectroscopic and microscopic equipment in the study, such as *in situ* optical spectroscopy and *in situ* TEM. Our recent published work on electrochemical etching of AuAg alloys NPs employed highly specialized *in situ* TEM for directly observing the nanostructure during the dealloying.[364] In this work, we combined the more accessible optical spectrometer with back-reflection mode microscopy (Figure 6.8a) to enable real-time monitoring the scattering spectra of individual NPs during the dealloying process.[150]

Similar as dealloying in colloidal, the spectra of individual NPs also exhibit red-shifting and broadening, while significant differences in details are observed among the individual NPs. Scattering spectra before and after dealloying (Figure 6.8b) are collected from identical Au@AuAg NPs with 40 nm-core and shell position of Au/Ag 25/75, and the peak position and intensity (Figure 6.8c) are tracked in real-time detection. Figure 6.8b clearly demonstrates that the peak has red-shifted accompanied with broadening. Figure 6.8c shows the real-time change, including peak position and intensity, after the addition of $HAuCl_4$. At first, peak position stabilizes around 558 nm and after 3 min, at the position of the arrow as the reaction begins, the peak has abruptly red-shifted (for around 25 nm), indicating that the fast dealloying has occurred. The early stage red-shift observed from every NP during the GRR probably comes from the surface pitting, gap forming between core and shell, compositional change as well as the surrounding of high-refractive index of AgCl (2.06 compared with 1.33 of water).[362, 365, 366] The effect of AgCl as surrounding media has not been considered in the colloidal dealloying since the amount is relatively small, especially after certain times of washing, AgCl has been essentially removed from the NPs. However, in these single NP experiments, the diffusion along with dissolution of AgCl is limited with NPs immobilized on the glass compared to the ones in vigorous stirring. After an abrupt red-shift, some NPs continue this red shifting until the end. However, some spectra as depicted in Figure 6.8c, show a small (< 10 nm) blue-shift, which can be caused by the realloying of the deposited Au surface with interior, and phase separation at the surface of NPs with AgCl due to further dealloying.[363] After stabilizing, further dealloying resumes the red-shifting. After the yolk-porous shell structure has formed, dealloying effect on peak shifting slows down

compared with the early-stage. During the dealloying, amplitude of the peak keeps decreasing until the late stage of slow red-shift.

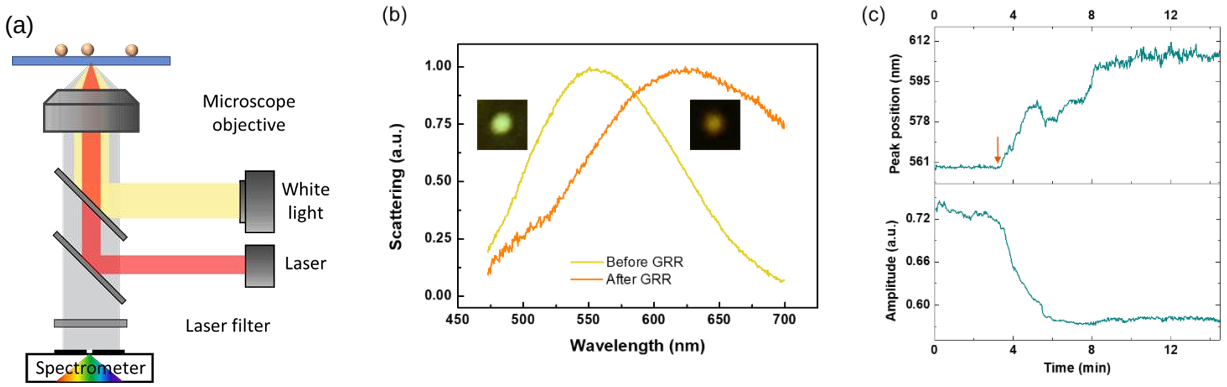

Figure 6.8 (a) Optical setup of single NP scattering and Raman detection, combination of back-reflection mode microscope and optical spectrometer. (b) Typical single NPs scattering spectra of a 40 nm Au@Au/Ag 25/75 NP before and after GRR for 30 min, inserted with the optical images and (c) *in situ* monitoring of a scattering peak shift and intensity change during the GRR, and the arrow indicates when the reaction begins.

Results from individual NPs push-broom scan and real-time monitoring are in agreement with the colloidal ones. During the dealloying process, we can clearly see the single NPs scattering color change and intensity vanishing through the microscope. From push-broom scan, the scattering spectra from many different NPs vary from each other (Figure A.5), but exhibit similar trends of red-shift and intensity decrease. The single-NP level of observation provides more details of the evolution through GRR, moreover, real-time monitoring allows us to explore the dynamics of the process.

6.5.5 Application: Single-particle SERS monitoring

The porous plasmonic structures present a robust LSPR coupling as well as a potentially high hot spots density. Due to the crevices and rough surface, porous plasmonic nanostructures are expected to provide a promising surface enhanced Raman spectroscopy (SERS) probe with high enhancement factor, enabling chemical detection with molecules at very low concentration. Porous arrays and porous single-particle as SERS substrates were designed with high sensitivity.[326, 367-369] As the anticancer drug doxorubicin (DOX) has poor solubility in water, and the typical drug

detection is in a range of 50-5000 ng with blood plasma extraction,[370] we propose to perform SERS on the DOX loaded porous NPs to detect and monitor the drug release. This proof-of-principle has been performed on single-particle SERS monitoring, where DOX represents both the drug and the Raman reporter. The optical setup is the same as the one in single-particle spectral study, shown in Figure 6.8a, and the scattering of porous NPs is employed to confirm the position of individual NPs. Figure 6.9a shows 3D-surface plot based on the images taken with the microscope under back-reflection mode (Figure A.5). For SERS measurement, the wavelength of irradiation laser is 633 nm and the Raman bands observed in SERS spectra are assigned accordingly (Table A.3). We monitored the intensity of the most intense Raman characteristic peaks from DOX at 1244 cm^{-1}, assigned to O-H vibration.[371, 372] The enhancement from single NPs is therefore compared between Au NP-DOX and porous NP-DOX (Figure 6.9b), which are dispersed onto the glass-bottom of Petri dishes. Both types of NPs are around 100 nm. The porous NP is dealloyed from Au@AuAg, whose plasmon peak is closer to the irradiation wavelength of 633 nm. The Petri dishes are filled with water, and the control signal is taken from where there is no NPs. No detectable Raman signal performed on substrate is observed while with Au-NP-DOX a very weak or even noise-level signal is detected. Note that the average field enhancement is calculated by using Mie theory to 3.9 at 633 nm from a 100 nm Au-NP leading to an estimated Raman enhancement of $(3.9)^4$ or 225 (shown in Figure A.6). The SERS signal collected from each single porous NP is intense in contrast to the very weak peak from a single Au NP. The signal collected from a porous NP can reach up to 68-fold higher than the one from a Au NP, much higher than the reported results (Table A.4),[326, 373-375] which suggests the extremely high enhancement from our porous NPs and proves the highly sensitive detection at single-particle level. The much higher enhancement compared with standard Au NPs can be explained by a high density of hot spots from the porous structure, more loaded drug molecules (by a factor of 2, see next section), and the Ag component which usually results from a higher Raman activity. As a rough estimation, the field enhancement of our porous nanostructure compared to Au NP is on the average $(68/2)^{1/4}$ or 2.41, yielding to an approximate field enhancement of $3.9 \times 2.41 = 9.4$ and to a Raman enhancement factor of approximately $(3.9 \times 2.41)^4$ or 7804. We also calculated the enhancement factor by comparing the experimental Raman signal from single porous NP with the one from DOX solution (10^{-3} mol/L) and the estimated enhancement factor is 3866. (see Supporting information)

To investigate the electromagnetic properties of porous NPs, the scattering field enhancement was simulated by using a finite element method (Figure 6.9c). The geometry of the porous structure was created by generating random holes from the surface to the solid core and controlling the porosity and the dimension of core, shell and the holes (one example shown in Figure A.7). Figure 6.9c shows the simulated results of the local field enhancement of a nanostructure having a 30 % porosity and 100 nm-diameter with 30 nm-solid core, which is close to the porous NP dealloyed from Au@AuAg NP-precursor. Hot spots with simulated field enhancement values ranging from 8 to 10 may lead to an estimated Raman enhancement factor between 4000 and 10000, which is in agreement with experimental estimations.

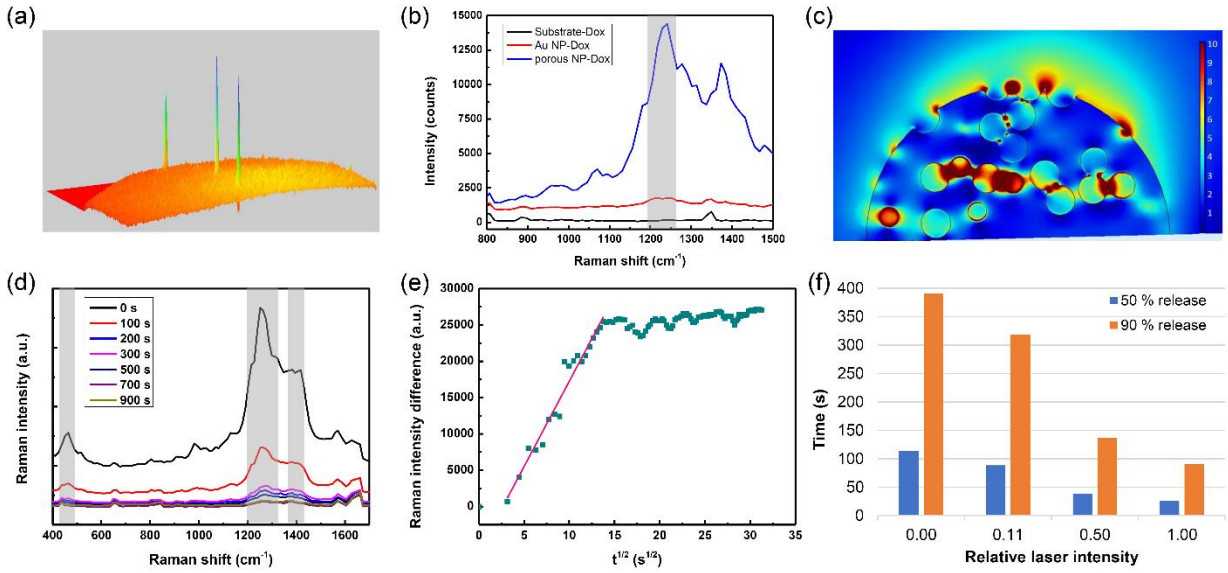

Figure 6.9 (a) 3D-surface plot of individual porous NPs scattering observed by back-reflection mode microscopy. (b) Raman signals from glass substrate, DOX-loaded single 100 nm-Au NP and 96 nm-porous NP deposited on the glass substrate. (c) The simulated local field enhancement of porous NP under the irradiation of 633 nm laser. (d) SERS spectra obtained from DOX-loaded porous Au-Ag NPs with a focused laser after the irradiation time, (e) the intensity at the peak around 1250 cm^{-1} decays in 1000 s at a step of 10 s over the square root of time and (f) the time of 50 % and 90 % DOX release under different laser intensity (The relative value of 1.0 correspond to 7.7×10^4 W/cm^2).

6.5.6 Application: Drug loading

The anticancer DOX is used as the drug model. To load the drug into the nanostructures, the aqueous dispersion of NPs and DOX mixture is under shaking at room temperature overnight. DOX has a characterized absorbance peak at 480 nm, which serves as the evaluation for its concentration in the solution. The loading capacity of NPs is determined by measuring the unloaded DOX in the supernatant after centrifugation. Since NPs are stabilized with citrate, which makes the NPs negatively charged, the positively charged DOX attaches to the NPs through electrostatic interaction.[376, 377]

To investigate the loading capacity, we employed 100 nm Au nanospheres for comparison. The Au NPs, porous NPs and porous nanoshells of similar size and same concentration of NPs are incubated with the same amount of DOX, at low and high concentration, respectively (Table 6.1). At low DOX concentration (30 uM), more than 2-fold loading exhibits the potential of porous structures, which provide more effective surface for the attachment of drug molecules. At high DOX concentration (90 uM), the porous shells induced almost 3-fold loading capacity over the spherical NPs. The increase is contributed by not only larger specific area from the porous structure, but also less weight of each NP. The drug loading test proved that the significant Raman enhancement from porous NPs over solid Au NP is mainly contributed by the porous structure and only slightly by the loading amount. Furthermore, from the optical spectra before and after drug loading, the plasmon peaks have not really shifted, indicating that the chemical composition and porous structure have not significantly changed and that the porous NPs are stable for drug loading.

Table 6.1 Drug loading capacity of different NPs with low and high concentration of DOX solution.

DOX loading	**Solid NPs [mg/mg]**	**Porous NPs [mg/mg]**	**Porous nanoshells [mg/mg]**
Low concentration	0.17	0.37	0.43
High concentration	0.73	1.24	2.15

With the single-particle level SERS from porous NP, we observed the quantitative monitoring of drug release during the laser irradiation. Three relative intense characteristic peaks are noted in

Figure 6.9d, namely the peak near 1413 cm^{-1}, assigned to the ring stretch; the most intense bands from C-O and O-H in the range of 1200-1300 cm^{-1}, and the ones at 436 and 465 cm^{-1}, deformation peaks corresponding to C=O.[370-372] The intensity of Raman signal decreases with continuous laser irradiation, and the intensity change of the peak around 1244 cm^{-1} were plotted over the square root of time in Figure 6.9e. A clear decay indicates the release of DOX triggered by laser, which fits well with the most accepted Higuchi model,[378-380] in which the released amount Q follow the equation:

$$Q_t = K_H t^{1/2} \quad (7)$$

where K_H is the release constant for Higuchi model. The plot of the Raman intensity decrease as a function of $t^{1/2}$ indicates a two-stage release, one is a linear fit ($R^2 = 0.96$) at the beginning, in the first 200 s, and after the fast release that can reach > 92 % loaded drug, another gentle slope implies a much moderate release over t > 200 s. The release constant K_H is related to how the molecules are strongly bonded to the NPs and the actual porosity and pore tortuosity of the nanostructure.[381] In our case, the used porous NP has a solid core and porous shell, containing heterogeneous pores including inter-connected pores near the surface, as well as the voids that penetrated into the core. The first faster step with $K_H = 2351\ s^{-1/2}$ probably relates to the faster diffusion of DOX from the porous structure near surface, while the long-time release with $K_H = 147\ s^{-1/2}$ much lower diffusion rate is primarily due to the small partial of DOX loaded deep into the NPs or in some narrow porous structure which creates barriers for the DOX release. The laser-stimuli release can be explained by a thermal effect of porous Au-Ag NPs, which absorbs laser light, thus inducing a local temperature increase. The thermal effect accelerates the diffusion of DOX molecules, and stimulates their release. Figure 6.9f exhibits the release of DOX under different laser intensity, showing the higher intensity inducing faster drug release.

It is worth noting that the irradiation laser power density is 7.7×10^4 W/cm^2, and focused by a 100× oil objective with a spot size of 244 nm. The small spot size assures the single NP under irradiation and eliminates the collective effect from multi heating source. The temperature rise has been estimated with the simplified equation:[382]

$$\Delta T(r) = \frac{\sigma(\omega)P}{4\pi\kappa r} \text{ , for } r > \text{NPs radius} \quad (8)$$

where σ is the absorption cross section at the irradiation wavelength (633 nm), P is the power density in W/m^2, κ is the thermal conductivity of water as the surrounding medium, and r is the distance from the center of the NP. The optical cross sections of porous NPs have been simulated based on Mie theory and Bruggeman's model of effective medium approximations (Figure A.8). The NPs are modeled with an alloy core and a porous shell with calculated porosity (discussed in the section of **Effect of Dealloying degree**), and in this case, the σ = 1.2×10^4 nm^2, P = 7.7×10^8 W/m^2, and κ (water) = 0.6 W/(m K). Since the NP is 96 nm in diameter, the surface temperature is estimated to be ΔT (r = 48 nm) = 25 K. The laser irradiation generates a thermal effect within and on the surface of the porous NP, which stimulates the DOX molecules and assists their release. Meanwhile, this moderate temperature increase is tolerable since the NPs structure up to 100-250°C, and the DOX solution has shown no effect from temperature up to 70 °C.[382, 383] Porous NPs provide not only a drug carrier, but also an active SERS substrate at single-particle level, with highly intense enhancement effect. The high enhancement plus analytical monitoring provides large prospect in biomedical applications.

6.6 Conclusions

This work demonstrates a versatile method to synthesize designable porous Au-Ag nanoparticles, with rough surface, and adjustable hollowness, as promising SERS probes. Au or Ag core@Au-Ag alloy shell NPs provide monodispersed precursors and regulate GRR dealloying in colloidal to produce solid core@porous shell or porous nanoshells with hollow interior. The aqueous colloidal synthesis without polymer coating provides a promising approach for large-scale production of porous NPs with accessible surface. We characterized the morphology, composition and optical properties to understand the dealloying mechanism. Through designing the composition and its distribution in alloy precursor and adjust the parameters in GRR process, we manage to tailor the hollowness and porosity, as well as plasmonic properties of final nanoparticles. Due to the rough surface and strong LSPR coupling, porous nanoparticles possess high density of hot spots and exhibit up to 68-fold higher Raman enhancement compared to Au nanospheres at single-particle level, with estimated Raman enhancement factor reaching up to 7804. The porous plasmonic nanostructure demonstrates high loading capacity with DOX as anticancer drug model, 2 to 3 times increase compared to solid nanospheres. The porous Au-Ag nanoparticles provide potential

multifunctional platform, as cargo carrier and SERS probe. Accommodating composition distribution of Au-Ag alloy NP-precursors in colloidal GRR dealloying enlarges the possibility of porous structure design, as well as potential applications.

6.7 Experimental Section

Chemicals and Materials: Gold (III) chloride trihydrate ($HAuCl_4 \cdot 3H_2O$, Sigma-Aldrich), silver nitrate ($AgNO_3$, Alfa Aesar) and trisodium citrate dihydrate ($Na_3C_6H_5O_7 \cdot 2H_2O$, Alfa Aesar), Doxorubicin hydrochloride (DOX, Sigma-Aldrich), 4-Mercaptophenylacetic acid (4-MPAA, Sigma-Aldrich), and 70 nm silver nanoparticles (no. AGCN70, nanoComposix) were received from the indicated suppliers, and used without further purification. Deionized water used in all experiments was purified by Milli-Q water purification system (Millipore) to 18.2 MΩ resistivity.

Synthesis of NP-precursors: Au@Au/Ag alloy core-shell precursor NPs were prepared using the previously reported optimized seeded-growth method by our group.[50, 89, 149] In brief, Au seeds were firstly prepared with the Turkevich method, followed by an alloy shell growth with Au and Ag coreduction in multi-stages until final alloy precursors. The Turkevich method usually produces Au NPs with diameter of ~15 nm, which are used as seeds in the following growth stage. According to the size and composition of precursors, Au-Ag alloy growth is adjusted by the amount and ratio of $HAuCl_4$ and $AgNO_3$ in the growth stages. To adjust the size of Au-core, a growth stage of pure Au is performed before the growth of alloy. To obtain Ag@Au/Ag alloy core-shell precursor NPs, we used Ag NPs purchased from nanoComposix as seeds, for further growth. Similar as Au@Au/Ag NPs, a layer of pure Ag can be grown onto seeds to adjust the size of Ag core, and finally the growth of the alloy shell is performed to achieve the precursor NPs.

Taking precursors of ~90 nm (in diameter) Au@Au/Ag as an example, which is composed of a 40 nm Au core and a Au/Ag 10/90 shell: 3 mL Au seeds dispersion from Turkevich method was mixed with 57 mL water while stirring in a three-neck flask in 90 °C heating bath; 540 µL 170 mM sodium citrate and 270 µL 30 mM $HAuCl_4$ solution were simultaneously added into the refluxed flask in ten steps during one hour and then the mixture was heated up to 100 °C; after 1 h, ~32 nm Au NPs were synthesized. After cooling to room temperature, 31.5 mL synthesized Au NPs were left in the three-neck flask as seeds for next growth stage. Then, 28.5 mL water was added, and the mixture

was heated to 90 °C under vigorous stirring. The solution of 284 µL 170 mM sodium citrate and simultaneously 142 µL $HAuCl_4$ of 30 mM were added into the refluxed flask in ten steps during one hour, and the mixture was stirred at 100°C. After one hour, ~40 nm Au NPs were obtained, which provide the seeds for alloy shell growth. After cooling down, 6 mL synthesized Au NPs were left in the flask, and 54 mL of water was added in the flask, and the dispersion was heated up to 90 °C under vigorous stirring. Then, 540 µL 170 mM sodium citrate were added in ten steps during one hour and each step followed by 27 µL 3 mM $HAuCl_4$ and 27 µL 30 mM $AgNO_3$ solution added simultaneously. After adding all the solution, the mixture was refluxed at 100 °C for 1 h to complete the growth.

GRR dealloying: Precursor NPs dispersion was centrifugated at 5000g, and 80 % supernatant was replaced by water to remove the excess citrate. Then the NPs dispersion was 3-fold diluted by water. $HAuCl_4$ as dealloying agent was slowly injected into the precursor dispersion under vigorous stirring, at a speed of 40 mL/h. The dealloying was allowed for 30 min at room temperature, and then the porous NPs were washed with water through centrifugation at 7000 g. Finally, the porous NPs are dispersed in water for further use.

Drug loading and SERS reporter integration: DOX was applied as anticancer drug in the loading analysis for the prepared porous NPs. Each 1 mL NPs were incubated with certain volume (20 - 50 µL) of 1 mM DOX solution, and shaken under dark environment for 20 h. After loading, the excess DOX supernatants were measured after centrifugation at 7000 g. The unloaded DOX was measured by UV-vis spectrophotometer, quantified by the intensity at the absorbance peak of 480 nm.

Characterization: The extinction spectra of colloidal precursors and porous nanoparticles were characterized by Epoch Microplate Spectrophotometer. The size, morphology and composition were characterized by JEOL 2100 Transmission electron microscope (TEM) and Oxford energy-dispersive X-ray spectroscopy (EDS) attached to it. The TEM and the high-angle-annular-dark-field (HAADF) scanning transmission electron microscope (STEM) measurements were performed at an accelerating voltage of 200 kV. Thin carbon film coated Cu grids (Electron Microscopy Sciences) were used for sample preparation, which were dipped in NPs ethanol dispersion and air-dried. Andor Shamrock SR-750 imaging spectrophotometer combined

with an invert Nikon microscope were employed in hyperspectral measuring scattering spectra from individual nanoparticles. The sample were prepared in glass-bottom petri dish (MatTek), 10 µL NPs were spread onto the bottom and 4 mL of water was added. The measurements were performed with 100× oil objective through backreflection mode under illumination of a Halogen lamp. Similar setup and sample preparation were used in SERS measurements, instead of the halogen lamp, a focused 633 nm laser was employed as the excitation at 5.2×10^4 W/cm^2 and a beam spot size of 594 nm. A filter to cut the laser wavelength was implemented before the Andor imaging spectrophotometer, and FVB mode is applied in the measuring Andor software.

6.8 Supporting Information

Supporting Information is available from the Wiley Online Library or from the author.

6.9 Acknowledgements

This work was supported by the Natural Sciences and Engineering Council of Canada. The authors would like to thank Jean-Philippe Masse at the Center for Characterization and Microscopy of Materials (CM^2) for the help with the HRTEM measurements.

CHAPTER 7 GENERAL DISCUSSION

In this thesis, we have discussed the synthesis and bioimaging application of spherical Au-Ag NPs, and based on the spherical NPs, we successfully synthesized porous Au-Ag NPs, and explored the application as the drug carrier and SERS probe at single-particle level.

In this chapter, several important aspects are discussed, which are not mentioned in the previous chapters. First, slight modifications on the dealloying process are further explored. Then, the porous Au-Ag NPs are tested as SERS probes in *in vitro* application, and surface modification is discussed, which will be necessary for further study and application. Finally, more possible applications of porous Au-Ag nanoparticles are proposed in the field of energy and information technology.

7.1 Discussion on the dealloying process

In Chapter 6, we reported the method to synthesize Au-Ag porous NPs, through mild GRR dealloying from well-controlled Au-Ag NPs precursors. By adjusting the composition and Au/Ag distribution in the precursors, we succeeded in tuning the structure and their optical properties of final NPs. However, during dealloying Au-Ag alloy NPs, other aspects have not been explored, such as temperature control, and further reaction, including higher dealloying degree and removal of residual Ag components.

7.1.1 Temperature control in GRR

The temperature during dealloying has great influence on the GRR, re-alloying and Kirkendall effect, thus the final structure and optical properties are temperature-dependent. Considering that the NPs are capped by a certain amount of citrate, it can induce obvious reduction and growing process, especially at high temperature. Before GRR, we removed most citrate in the NPs suspension, and reduced its concentration to 0.3 mM to avoid growth while keeping the NPs stable. At room temperature, the reduction is limited due to the low reducing ability of citrate. However, when temperature rises, the reducing ability increases, reduction of $HAuCl_4$ can result in further growth of Au onto the NPs instead of dealloying Ag atoms.

Meanwhile, at higher temperature, the interdiffusion of Au and Ag is accelerated, as well as the voids diffusion. Therefore, the Au and Ag components tends to form homogeneous alloy and the small pores or the overall porous structure may converge into large hollow structure or NPs may collapse into solid structure. High temperature facilitates the thermodynamic control on the structure, leading to less pores as well as smoother surface. On the other hand, when lowering the temperature, the GRR can be more controllable in kinetics with lower reaction rate, while the efficiency of reaction can be limited. The reducing ability of citrate is also limited under low temperature. Re-alloying and Kirkendall effect will be reduced, and slow dealloying reaction can be limited by the composition at the front. The limited exchange may impede the dealloying penetrating into the core of NPs.

Min and co-worker explored GRR at different temperatures between 4-100 °C applied to Ag nanospheres.[64] They reported that smooth hollow nanoshells developed at the high-temperature (≥ 40 °C) while rough structure formed under low temperature (≤ 20 °C). The spongelike structure with increased pores and surface-to-volume has been successfully synthesized with a temperature control on GRR. Since the low temperature induced fast deposition of AgCl, it locally impeded further GRR, and lead to rough Au islands surrounding the surface. To get porous structure, sequential etching of Ag and AgCl has been implemented after the inhibited GRR with the assistance of polymer coating. Finally, the spherically clustered porous nanoparticles were used in drug delivery, exhibiting 10 times higher loading capacity compared to conventional nanoshells.

When combining the temperature control with adjustable Au-Ag alloy NPs, the flexibility of GRR is potentially increasing. Furthermore, considering NP-precursors with tunable composition shell with Au-core and Ag-core, the temperature of each step for dealloying different layers can be adjusted, according to the reaction penetration from surface to the core. The coordination of NP-precursors and reaction conditions is enabling more finely controlled structures.

7.1.2 High dealloying degree

In GRR, we also introduced the concept of dealloying degree to quantify the relative amount of $HAuCl_4$ added to react with Ag in the precursors. While to preserve analogous structure as the precursors, the dealloying degree has been limited under 2.0 in the synthesize of porous Au-Ag NPs. Actually, with more $HAuCl_4$, or higher dealloying degree, even up to 10, there would be more

opportunities for other types of structures. The unpublished results with dealloying degree of 10 shows that the NPs can lose their original structure, and become nanowires connected with core and linked arms, as seen in Figure 7.1. Similar core-satellite with nanobranches assemblies have been reported by other researchers, with potential for SERS and photothermal therapy.[338] Dey and coworkers applied special polymer linker to assemble multiple 5 nm Au NPs with 15 nm Au NP core, which brought complexity of controlling the attachment between different NPs. While with our proposed NP-precursors with GRR, the morphology of final assemblies can be easily adjusted by the size of core and shell, as well as the composition. Within simple colloidal system, the unexpected varieties can be avoided, allowing synthesis with high yield, control and purity, and polymer-free reaction ensures more accessible surface for further SERS detection and loading capacity.

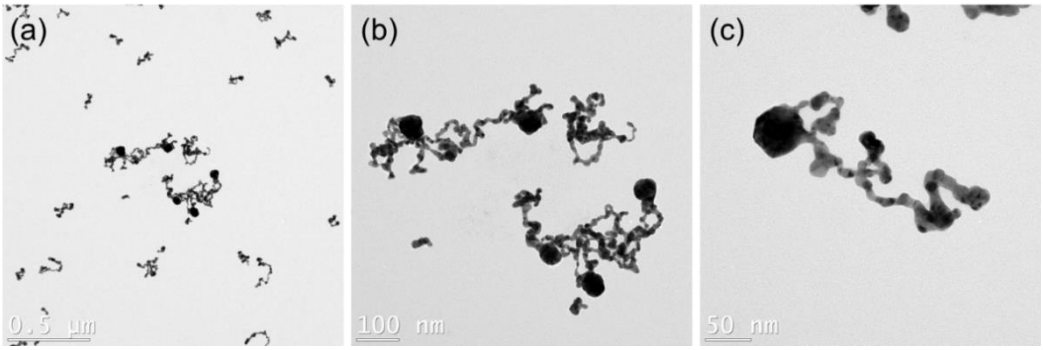

Figure 7.1 TEM of nanowire assemblies at different scale dealloyed from Au@AuAg NPs with dealloying degree of 10.

The result is preliminary and more elaborated structure and dispersion is of great potential with further research. The dealloying degree in a broad range enlarges the flexibility of dealloying, combining GRR with further growth and the transformation of structure. The plasmonic behavior can be adjusted accordingly in terms of peak position and field enhancement.

7.1.3 Removal of Ag

Etching Ag is involved in most of the cases for building porous Au-Ag structures. Due to the limited oxidizing ability of $HAuCl_4$, and compositional threshold (~55 % Ag) of dealloying, there remain Ag components after GRR. Due to the limitation with stability or toxicity of Ag, as well as the adjustability of alloy structures, removal of residual Ag in the nanostructures is beneficial.

Many studies have been carried out for the Ag etching after GRR, employing etchants such as H_2O_2, NH_4OH, $Fe(NO_3)_3$, and HNO_3.[63, 384, 385] The etching can remove the remaining Ag and AgCl to achieve higher porosity and result in a larger red-shift for the plasmonic peak. Improved loading capacity is expected and plasmon peak in near-infrared range with etching. To control the morphology, anisotropic etching has been explored by adjusting the etching ability and reaction conditions, inducing more intraparticle gaps, and strong localized surface plasmons.[368] The anisotropic etching can introduce more edges and corners and generate more hot spots. Polymers are usually involved in the anisotropic etching, to protect certain facets and keep the etching direction. Generally, during the etching process, polymer coating becomes necessary to keep the NPs stable, to avoid agglomeration under the extreme environment with etchants.

7.2 *In vitro* SERS sensing and surface functionalization

Porous Au-Ag NPs have been applied as SERS probes, with high enhancement at single-particle level. The SERS probes can be also applied for *in vitro* sensing. Due to the excellent Raman enhancement behavior, porous Au-Ag NPs provide promising biosensors with high sensibility. Since Raman spectroscopy is a robust analytical technique for chemicals with fingerprint characteristics, the biosensing with our proposed porous Au-Ag NPs for diagnostics is of great promise. SERS-based studies on live cells or tissues have made great progress, exploring the microenvironment for disease assessment, especially plasmonic substrate-assisted cancer diagnostics.[386] Their biomedical applications of SERS technology are typically in two categories: label-free sensor or Raman biomarker. Both ways are developed based on the plasmonic nanostructures, the localized surface plasmon provides high enhancement as SERS substrates. The label-free sensor is for enhancing Raman signals from intrinsic chemical molecules in the analytes, and the Raman biomarkers are assembled with Raman reporter molecules before targeting the bio samples.

According to the differences in the metabolites or environment from mitosis or other physiological activities of healthy and malignant cells, enhanced Raman signal exhibits different peaks or intensities of the peaks. Analyzing the complex signal allows the study of cytopathology and theranostic approaches developments. To test the *in vitro* application as label-free biosensors, our bare porous Au-Ag NPs have been incubated with cancer cells and healthy cells respectively. By

employing the side-illumination component with back-reflected mode microscopy and spectrophotometer, we can easily locate the NPs on certain cells and perform SERS measurements.

Raman biomarkers are another important biomedical application of plasmon-based SERS techniques. The plasmonic NPs are firstly coated by a layer of reporter molecules with distinguishable Raman peaks, which eliminates the difficulty of differentiating signals in analyzing. Large fluorophore molecules are easily detected due to their intense Raman signal, in addition, small molecules self-assembly for SERS biomarker also play an important role, considering the full coverage over the surface, facile assemble process, and simple Raman peaks. Subsequently, a coating layer will probably be implemented to keep the reporters stable and improve the stability and biocompatibility of NPs. The coating layer is not only useful for SERS biomarker but also necessary for cargo delivery to avoid leaking. Silica, polymer, or liposome capping are very popular coating layers due to their great biocompatibility and ease to be functionalized. Some of them also include smart functions, for instance, co-polymer with proper transition temperature can be applied for temperature stimulated drug release. Moreover, biofunctionalization for specific targeting and detection is crucial for high efficiency and accuracy in applications. Specific antibodies, peptides, and aptamers are potential choices for bio-conjugation according to the targets.

7.3 Future application of porous Au-Ag nanoparticles

In the previous sections, we discussed the biomedical applications of porous Au-Ag NPs, but meanwhile, the NPs are promising for broader applications in the energy field and information technology. Porous Au-Ag NPs are of great interests with their special structural and optical properties, including high surface-to-volume ratio, broad and adjustable plasmon spectra in visible and near-infrared range, and high localized field enhancement through whole NPs.

7.3.1 Porous Au-Ag NPs in energy field

Plasmonic NPs are attractive in energy conversion applications, due to their unique optical properties. Moreover, with the outstanding large surface, our porous NPs are suitable for photovoltaic and catalysis.

In photovoltaic, porous NPs with a broad scattering spectrum instead of a narrow peak from regular shapes, increase the absorption of the broad solar spectrum. Also, surface field enhancement and a

large number of hot electrons will probably greatly improve the efficiency by increasing the carrier generation and avoiding electron-hole pair combination.

In catalysis for energy transition, the porous structure provides large accessible interface. For photocatalysis, the interface between NPs with semiconductors facilitates the transfer of hot electrons, lowering down the barrier, therefore, increasing the efficiency of the energy transition. In most oxidation reactions, due to the gaps and curvatures in the porous structure, there exists a high density of active surface steps and kinks, which are active for the chemical reactions.[387] Moreover, the alloy NPs allows the adjustment of composition, benefiting the optimization of catalyst. Ag components in the Au-Ag alloy NPs are more active, and in the case of future application, Pt or Cu can also be included for higher catalytic activities.

7.3.2 Porous Au-Ag NPs in information field

As mentioned in the literature review chapter, optical properties of plasmonic nanostructures are widely applied in different fields, and information technology is an important area. The intrinsic color from NPs, like scattering or absorption, can be an option, and the surface-enhanced fluorescence (SEF) and SERS with special fluorescent color or Raman peaks is another way of information storage or encryption. Our porous Au-Ag NPs with high localized field enhancement are promising SERS and SEF substrates. The fluorescent and Raman signals can also be combined in the information code to increase the information storage efficiency as well as the security of encryption. Since Raman peaks are sharp and characteristic for different chemicals, the capacity to combine various reporters and the accuracy of the encoding is reliable.

CHAPTER 8 CONCLUSION AND RECOMMANDATIONS

The Au-Ag alloy NPs with unique optical properties have proven their potential in biomedical applications including multiplexing bioimaging and SERS probing. The optical properties of plasmonic nanomaterials have induced great applicability in theranostics, as well as in the fields of energy and information technologies. The optical properties and application examples have been summarized in our review published in *Advanced Functional Materials* and in Chapter 3.

In the thesis, we have focused the research on the principal objectives:

1. Understanding and optimizing the colloidal synthesis of Au-Ag alloy nanospheres;
2. Facilitating the multiplexing bioimaging with Au-Ag alloy NPs for cytopathology;
3. New structure design based on Au-Ag alloy for SERS probe.

The first objective of the thesis is understanding the colloidal synthesis of solid Au-Ag alloy nanospheres and optimizing the process for more precise control, which has been done, as shown in Chapter 4. The methodology of synthesis has been studied in detail, including the temperature and pH effects. The kinetics of the whole synthesis process has been discussed, from the Turkevich method in seeds fabrication to seeded growth stages for larger NPs. The improved setup has been proposed for higher automation and reproducibility. The NPs produced with this setup exhibit narrower distribution compared with the ones from manual control. With the understanding of seeded growth and coreduction, more types of metal precursors can be applied, such as Pt, Cu, or Al, enriching the alloy types and enlarging the LSPR range. The capping agents or shape-directing agents can be included for non-spherical structures, resulting in spectra with different shapes.

The second part of the doctorate thesis has applied the Au-Ag alloy NPs in multiplexing for cytopathology, shown in Chapter 5, published in the *Journal of Biophotonics*. Theoretically, plasmon peaks of Au-Ag alloy NPs can be fine-tunned in the range of the ones of pure Ag and pure Au NPs. The circular side-illumination microscopic component provides a cost-effective and easily installed illumination solution with an adjustable red-green-blue (RGB) LED. Accordingly, we have designed RGB Au-Ag NPs with similar scattering peak positions with the illumination spectra. The RGB NP kits have been proposed for three kinds of mounting media of cell samples, which are representative of various situations. Through theoretical calculation based on Mie theory, we designed the exact RGB NPs according to different refractive indexes of mounting media, and

to provide reliable identification and differentiation and in each medium, RGB NPs exhibit similar intensity. With finely controlling the size and composition of Au-Ag NPs, we have succeeded in developing the multiplexing kits and in vitro test with side-illumination component proved the quantitative chromatic biolabeling compatible with traditional cytopathology and illustrated the potential for digitalization diagnostics. The flexible plasmonic properties of Au-Ag NPs in the range of visible light have facilitated the multiplexing bioimaging, promoting efficient and advanced cytopathology. Further biofunctionalization with high efficiency and stability can be valuable for specific targeting to certain types of cells, and facilitating clinical use.

The third object of the thesis to design new structures based on Au-Ag NPs for SERS probes has been completed in Chapter 6, published in *Small*. Porous structured Au-Ag NPs have been produced through dealloying solid Au-Ag NPs. The flexibly adjusted Au-Ag NPs provide proper NP-precursors for the galvanic replacement reaction, applied as a dealloying method, and the dealloying has delicately controlled the porous structure and optical properties of the final NPs. Stable and controllable porous NPs with solid core and hollow interior have been dealloyed from Au-core and Ag-core alloy NPs, respectively. The dealloying process has been carefully studied on structure and properties, based on the variation of composition of NP-precursors and dealloying conditions. The porous Au-Ag NPs exhibit a large red-shift compared to solid ones, the rough surface generates high density of hot spots, and the pores create loading capacity. High localized surface enhancement has enabled SERS at single-particle level, and the release of the loaded anticancer drug has been quantitatively monitored on-site. The porous Au-Ag NPs with promising SERS behavior combined with improved loading capability, provide a promising multifunctional theranostic platform. In future sensing applications, bare SERS probes can be either in colloid or on the surface, directly detecting the signal through attached sample. For theranostics, further surface modification can be designed for controllable release of the loaded cargo, while the SERS substrate can be covered with small molecules as Raman reporter by self-assembly. Combination with IR or ultrasound imaging is possible for more situations.

In summary, the research in this doctorate thesis has covered different aspects, including chemistry, materials engineering, optics, biology, and medicine. We proved the potential of Au-Ag alloy NPs in various biomedical applications, and in the future, more applications in broad fields are encouraged.

REFERENCES

[1] D. J. de Aberasturi, A. B. Serrano-Montes, and L. M. Liz-Marzán, "Modern Applications of Plasmonic Nanoparticles: From Energy to Health," *Advanced Optical Materials,* vol. 3, pp. 602-617, 2015.

[2] L. Wang, M. Hasanzadeh Kafshgari, and M. Meunier, "Optical Properties and Applications of Plasmonic-Metal Nanoparticles," *Advanced Functional Materials,* vol. 30, p. 2005400, 2020.

[3] U. Kreibig and M. Vollmer, *Optical properties of metal clusters* vol. 25: Springer Science & Business Media, 2013.

[4] G. Yu, S. Yu, M. L. Saha, J. Zhou, T. R. Cook, B. C. Yung, *et al.*, "A discrete organoplatinum(II) metallacage as a multimodality theranostic platform for cancer photochemotherapy," *Nature Communications,* vol. 9, p. 4335, 2018/10/18 2018.

[5] H. Chen, W. Zhang, G. Zhu, J. Xie, and X. Chen, "Rethinking cancer nanotheranostics," *Nature Reviews Materials,* vol. 2, p. 17024, 2017/05/09 2017.

[6] G. Chen, H. Qiu, P. N. Prasad, and X. Chen, "Upconversion Nanoparticles: Design, Nanochemistry, and Applications in Theranostics," *Chemical Reviews,* vol. 114, pp. 5161-5214, 2014/05/28 2014.

[7] T. A. Tabish, P. Dey, S. Mosca, M. Salimi, F. Palombo, P. Matousek, *et al.*, "Smart Gold Nanostructures for Light Mediated Cancer Theranostics: Combining Optical Diagnostics with Photothermal Therapy," *Advanced Science,* vol. 7, p. 1903441, 2020.

[8] N. E. Motl, A. F. Smith, C. J. DeSantis, and S. E. Skrabalak, "Engineering plasmonic metal colloids through composition and structural design," *Chemical Society Reviews,* vol. 43, pp. 3823-3834, 2014.

[9] P. Yang, J. Zheng, Y. Xu, Q. Zhang, and L. Jiang, "Colloidal Synthesis and Applications of Plasmonic Metal Nanoparticles," *Advanced Materials,* vol. 28, pp. 10508-10517, 2016.

[10] P. R. West, S. Ishii, G. V. Naik, N. K. Emani, V. M. Shalaev, and A. Boltasseva, "Searching for better plasmonic materials," *Laser & Photonics Reviews,* vol. 4, pp. 795-808, 2010.

[11] G. V. Hartland, "Optical studies of dynamics in noble metal nanostructures," *Chemical reviews,* vol. 111, pp. 3858-3887, 2011.

[12] E. Cottancin, N. Del Fatti, and V. Halté, "Optical, Structural and Magneto-Optical Properties of Metal Clusters and Nanoparticles," in *Nanoalloys,* ed: Springer, 2012, pp. 331-368.

[13] K. L. Kelly, E. Coronado, L. L. Zhao, and G. C. Schatz, "The optical properties of metal nanoparticles: the influence of size, shape, and dielectric environment," ed, 2003.

[14] S. M. Amini, "Gold nanostructures absorption capacities of various energy forms for thermal therapy applications," *Journal of Thermal Biology,* vol. 79, pp. 81-84, Jan 2019.

[15] Y. Liu, Z. Liu, D. Huang, M. Cheng, G. Zeng, C. Lai, *et al.*, "Metal or metal-containing nanoparticle@MOF nanocomposites as a promising type of photocatalyst," *Coordination Chemistry Reviews,* vol. 388, pp. 63-78, 2019/06/01/ 2019.

[16] X. Duan, S. Kamin, and N. Liu, "Dynamic plasmonic colour display," *Nature Communications,* vol. 8, p. 14606, 2017/02/24 2017.

[17] C. Zong, M. Xu, L.-J. Xu, T. Wei, X. Ma, X.-S. Zheng, *et al.*, "Surface-Enhanced Raman Spectroscopy for Bioanalysis: Reliability and Challenges," *Chemical Reviews,* vol. 118, pp. 4946-4980, 2018/05/23 2018.

[18] J. Prakash, S. H. Sun, H. C. Swart, and R. K. Gupta, "Noble metals-TiO2 nanocomposites: From fundamental mechanisms to photocatalysis, surface enhanced Raman scattering and antibacterial applications," *Applied Materials Today,* vol. 11, pp. 82-135, Jun 2018.

[19] J. S. DuChene, G. Tagliabue, A. J. Welch, W. H. Cheng, and H. A. Atwater, "Hot Hole Collection and Photoelectrochemical CO2 Reduction with Plasmonic Au/p-GaN Photocathodes," *Nano Letters,* vol. 18, pp. 2545-2550, Apr 2018.

[20] J. Shu, Z. Qiu, S. Lv, K. Zhang, and D. Tang, "Plasmonic Enhancement Coupling with Defect-Engineered TiO2–x: A Mode for Sensitive Photoelectrochemical Biosensing," *Analytical Chemistry,* vol. 90, pp. 2425-2429, 2018/02/20 2018.

[21] L. Jauffred, A. Samadi, H. Klingberg, P. M. Bendix, and L. B. Oddershede, "Plasmonic Heating of Nanostructures," *Chemical Reviews,* vol. 119, pp. 8087-8130, Jul 2019.

[22] Z. Xi, H. Ye, and X. Xia, "Engineered Noble-Metal Nanostructures for in Vitro Diagnostics," *Chemistry of Materials,* vol. 30, pp. 8391-8414, 2018/12/11 2018.

[23] S. H. Lee and B. H. Jun, "Silver Nanoparticles: Synthesis and Application for Nanomedicine," *International Journal of Molecular Sciences,* vol. 20, Feb 2019.

[24] K. Kluczyk, C. David, J. Jacak, and W. Jacak, "On Modeling of Plasmon-Induced Enhancement of the Efficiency of Solar Cells Modified by Metallic Nano-Particles," *Nanomaterials,* vol. 9, Jan 2019.

[25] H. Kang, J. T. Buchman, R. S. Rodriguez, H. L. Ring, J. Y. He, K. C. Bantz, *et al.*, "Stabilization of Silver and Gold Nanoparticles: Preservation and Improvement of Plasmonic Functionalities," *Chemical Reviews,* vol. 119, pp. 664-699, Jan 2019.

[26] A. M. Wilson, J. Mazzaferri, É. Bergeron, S. Patskovsky, P. Marcoux-Valiquette, S. Costantino, *et al.*, "In Vivo Laser-Mediated Retinal Ganglion Cell Optoporation Using KV1.1 Conjugated Gold Nanoparticles," *Nano Letters,* vol. 18, pp. 6981-6988, 2018/11/14 2018.

[27] L. Wang, C. Darviot, J. Zapata-Farfan, S. Patskovsky, D. Trudel, and M. Meunier, "Designable nanoplasmonic biomarkers for direct microscopy cytopathology diagnostics," *Journal of Biophotonics,* vol. 12, p. e201900166, 2019.

[28] S. Liu, R. Jiang, P. You, X. Zhu, J. Wang, and F. Yan, "Au/Ag core–shell nanocuboids for high-efficiency organic solar cells with broadband plasmonic enhancement," *Energy & Environmental Science,* vol. 9, pp. 898-905, 2016.

[29] T. Chen and B. M. Reinhard, "Assembling Color on the Nanoscale: Multichromatic Switchable Pixels from Plasmonic Atoms and Molecules," *Advanced Materials,* vol. 28, pp. 3522-3527, 2016.

[30] T. Köker, N. Tang, C. Tian, W. Zhang, X. Wang, R. Martel, *et al.*, "Cellular imaging by targeted assembly of hot-spot SERS and photoacoustic nanoprobes using split-fluorescent protein scaffolds," *Nature Communications,* vol. 9, p. 607, 2018/02/09 2018.

[31] Z. Mei and L. Tang, "Surface-Plasmon-Coupled Fluorescence Enhancement Based on Ordered Gold Nanorod Array Biochip for Ultrasensitive DNA Analysis," *Analytical Chemistry,* vol. 89, pp. 633-639, Jan 2017.

[32] X. Wang, Y. He, X. Liu, L. Shi, and J. Zhu, "Investigation of photothermal heating enabled by plasmonic nanofluids for direct solar steam generation," *Solar Energy,* vol. 157, pp. 35-46, 2017/11/15/ 2017.

[33] M. Miyata, H. Hatada, and J. Takahara, "Full-Color Subwavelength Printing with Gap-Plasmonic Optical Antennas," *Nano Letters,* vol. 16, pp. 3166-3172, 2016/05/11 2016.

[34] G. V. Naik, V. M. Shalaev, and A. Boltasseva, "Alternative Plasmonic Materials: Beyond Gold and Silver," *Advanced Materials,* vol. 25, pp. 3264-3294, 2013.

[35] U. Guler, V. M. Shalaev, and A. Boltasseva, "Nanoparticle plasmonics: going practical with transition metal nitrides," *Materials Today,* vol. 18, pp. 227-237, May 2015.

[36] A. Comin and L. Manna, "New materials for tunable plasmonic colloidal nanocrystals," *Chemical Society Reviews,* vol. 43, pp. 3957-3975, 2014.

[37] I. Alessandri and J. R. Lombardi, "Enhanced Raman Scattering with Dielectrics," *Chemical Reviews,* vol. 116, pp. 14921-14981, Dec 2016.

[38] A. Agrawal, S. H. Cho, O. Zandi, S. Ghosh, R. W. Johns, and D. J. Milliron, "Localized Surface Plasmon Resonance in Semiconductor Nanocrystals," *Chemical Reviews,* vol. 118, pp. 3121-3207, 2018/03/28 2018.

[39] Y. Li, Z. Li, C. Chi, H. Shan, L. Zheng, and Z. Fang, "Plasmonics of 2D Nanomaterials: Properties and Applications," *Advanced Science,* vol. 4, p. 1600430, 2017.

[40] A. Naldoni, U. Guler, Z. Wang, M. Marelli, F. Malara, X. Meng, *et al.*, "Broadband Hot-Electron Collection for Solar Water Splitting with Plasmonic Titanium Nitride," *Advanced Optical Materials,* vol. 5, p. 1601031, 2017.

[41] Y. Zhao, H. Pan, Y. Lou, X. Qiu, J. Zhu, and C. Burda, "Plasmonic Cu2−xS Nanocrystals: Optical and Structural Properties of Copper-Deficient Copper(I) Sulfides," *Journal of the American Chemical Society,* vol. 131, pp. 4253-4261, 2009/04/01 2009.

[42] L. Zhou, Z. Liu, Z. Guan, B. Tian, L. Wang, Y. Zhou, *et al.*, "0D/2D plasmonic Cu2-xS/g-C3N4 nanosheets harnessing UV-vis-NIR broad spectrum for photocatalytic degradation of antibiotic pollutant," *Applied Catalysis B: Environmental,* vol. 263, p. 118326, 2020/04/01/ 2020.

[43] X. Liu, X. Wang, B. Zhou, W. C. Law, A. N. Cartwright, and M. T. Swihart, "Size‐controlled synthesis of Cu2‐xE (E= S, Se) nanocrystals with strong tunable near‐infrared localized surface plasmon resonance and high conductivity in thin films," *Advanced Functional Materials,* vol. 23, pp. 1256-1264, 2013.

[44] D. Dorfs, T. Härtling, K. Miszta, N. C. Bigall, M. R. Kim, A. Genovese, *et al.*, "Reversible Tunability of the Near-Infrared Valence Band Plasmon Resonance in Cu2–x Se

Nanocrystals," *Journal of the American Chemical Society,* vol. 133, pp. 11175-11180, 2011.

[45] E. A. Hernandez-Pagan, E. H. Robinson, A. D. La Croix, and J. E. Macdonald, "Direct Synthesis of Novel Cu2-xSe Wurtzite Phase," *Chemistry of Materials,* vol. 31, pp. 4619-4624, Jun 2019.

[46] M. Kanehara, H. Koike, T. Yoshinaga, and T. Teranishi, "Indium Tin Oxide Nanoparticles with Compositionally Tunable Surface Plasmon Resonance Frequencies in the Near-IR Region," *Journal of the American Chemical Society,* vol. 131, pp. 17736-17737, 2009/12/16 2009.

[47] Q. Hao, W. Li, H. Xu, J. Wang, Y. Yin, H. Wang, *et al.*, "VO2/TiN Plasmonic Thermochromic Smart Coatings for Room-Temperature Applications," *Advanced Materials,* vol. 30, p. 1705421, 2018.

[48] M. Ono, M. Hata, M. Tsunekawa, K. Nozaki, H. Sumikura, H. Chiba, *et al.*, "Ultrafast and energy-efficient all-optical switching with graphene-loaded deep-subwavelength plasmonic waveguides," *Nature Photonics,* vol. 14, pp. 37-+, Jan 2020.

[49] K. Khaliji, S. R. Biswas, H. Hu, X. Yang, Q. Dai, S.-H. Oh, *et al.*, "Plasmonic Gas Sensing with Graphene Nanoribbons," *Physical Review Applied,* vol. 13, p. 011002, 01/22/ 2020.

[50] J. Guo, S. Li, Z. He, Y. Li, Z. Lei, Y. Liu, *et al.*, "Near-infrared photodetector based on few-layer MoS2 with sensitivity enhanced by localized surface plasmon resonance," *Applied Surface Science,* vol. 483, pp. 1037-1043, 2019/07/31/ 2019.

[51] S. A. Ghopry, M. A. Alamri, R. Goul, R. Sakidja, and J. Z. Wu, "Extraordinary Sensitivity of Surface-Enhanced Raman Spectroscopy of Molecules on MoS2 (WS2) Nanodomes/Graphene van der Waals Heterostructure Substrates," *Advanced Optical Materials,* vol. 7, p. 1801249, 2019.

[52] S. Chen, E. S. H. Kang, M. Shiran Chaharsoughi, V. Stanishev, P. Kühne, H. Sun, *et al.*, "Conductive polymer nanoantennas for dynamic organic plasmonics," *Nature Nanotechnology,* vol. 15, pp. 35-40, 2020/01/01 2020.

[53] J. Olson, S. Dominguez-Medina, A. Hoggard, L.-Y. Wang, W.-S. Chang, and S. Link, "Optical characterization of single plasmonic nanoparticles," *Chemical Society Reviews,* vol. 44, pp. 40-57, 2015.

[54] P. K. Jain, X. H. Huang, I. H. El-Sayed, and M. A. El-Sayed, "Noble Metals on the Nanoscale: Optical and Photothermal Properties and Some Applications in Imaging, Sensing, Biology, and Medicine," *Accounts of Chemical Research,* vol. 41, pp. 1578-1586, Dec 2008.

[55] A. Espinosa, J. Reguera, A. Curcio, Á. Muñoz-Noval, C. Kuttner, A. Van de Walle, *et al.*, "Janus Magnetic-Plasmonic Nanoparticles for Magnetically Guided and Thermally Activated Cancer Therapy," *Small,* vol. 16, p. 1904960, 2020.

[56] A. I. Henry, J. M. Bingham, E. Ringe, L. D. Marks, G. C. Schatz, and R. P. Van Duyne, "Correlated Structure and Optical Property Studies of Plasmonic Nanoparticles," *Journal of Physical Chemistry C,* vol. 115, pp. 9291-9305, May 2011.

[57] L. A. Austin, M. A. Mackey, E. C. Dreaden, and M. A. El-Sayed, "The optical, photothermal, and facile surface chemical properties of gold and silver nanoparticles in biodiagnostics, therapy, and drug delivery," *Archives of Toxicology*, vol. 88, pp. 1391-1417, Jul 2014.

[58] D. Rioux, S. Vallières, S. Besner, P. Muñoz, E. Mazur, and M. Meunier, "An analytic model for the dielectric function of Au, Ag, and their alloys," *Advanced Optical Materials*, vol. 2, pp. 176-182, 2014.

[59] P. B. Johnson and R. W. Christy, "Optical Constants of the Noble Metals," *Physical Review B*, vol. 6, pp. 4370-4379, 12/15/ 1972.

[60] E. D. Palik, *Handbook of optical constants of solids* vol. 3: Academic press, 1998.

[61] N. Ascroft and D. Mermin, "Solid State physics (Holt, Rinehart and Winston)," 1976.

[62] E. A. Coronado and G. C. Schatz, "Surface plasmon broadening for arbitrary shape nanoparticles: A geometrical probability approach," *The Journal of Chemical Physics*, vol. 119, pp. 3926-3934, 2003.

[63] M. B. Cortie and A. M. McDonagh, "Synthesis and Optical Properties of Hybrid and Alloy Plasmonic Nanoparticles," *Chemical Reviews*, vol. 111, pp. 3713-3735, 2011/06/08 2011.

[64] G. Mie, "Beiträge zur Optik trüber Medien, speziell kolloidaler Metallösungen," *Annalen der physik*, vol. 330, pp. 377-445, 1908.

[65] M. Rycenga, C. M. Cobley, J. Zeng, W. Li, C. H. Moran, Q. Zhang, *et al.*, "Controlling the Synthesis and Assembly of Silver Nanostructures for Plasmonic Applications," *Chemical Reviews*, vol. 111, pp. 3669-3712, 2011/06/08 2011.

[66] D. Rioux, "Synthèse et modélisation des propriétés optiques de nanoparticules d'alliage or-argent et leur application en imagerie hyperspectrale," École Polytechnique de Montréal, 2015.

[67] LP2L. (2020). *Numerical tools -- NFMie program*. Available: https://www.polymtl.ca/lp2l/?q=en/outils-num%C3%A9riques

[68] W. Zhang, P. Gu, Z. Wang, B. Ai, Z. Zhou, Z. Zhao, *et al.*, "Integrated "Hot Spots": Tunable Sub-10 nm Crescent Nanogap Arrays," *Advanced Optical Materials*, vol. 7, p. 1901337, 2019.

[69] H. K. Lee, Y. H. Lee, Q. Zhang, I. Y. Phang, J. M. R. Tan, Y. Cui, *et al.*, "Superhydrophobic Surface-Enhanced Raman Scattering Platform Fabricated by Assembly of Ag Nanocubes for Trace Molecular Sensing," *ACS Applied Materials & Interfaces*, vol. 5, pp. 11409-11418, 2013/11/13 2013.

[70] Q. Zhang, N. Large, P. Nordlander, and H. Wang, "Porous Au Nanoparticles with Tunable Plasmon Resonances and Intense Field Enhancements for Single-Particle SERS," *The Journal of Physical Chemistry Letters*, vol. 5, pp. 370-374, 2014/01/16 2014.

[71] J. Reguera, J. Langer, D. J. de Aberasturi, and L. M. Liz-Marzan, "Anisotropic metal nanoparticles for surface enhanced Raman scattering," *Chemical Society Reviews*, vol. 46, pp. 3866-3885, Jul 2017.

[72] H. H. Jeong, A. G. Mark, M. Alarcon-Correa, I. Kim, P. Oswald, T. C. Lee, *et al.*, "Dispersion and shape engineered plasmonic nanosensors," *Nature Communications,* vol. 7, Apr 2016.

[73] A. Bansal and S. Verma, "Optical properties of bimetallic (Ag-Cu) core-noble metal shell nanoparticles," *Journal of Optics,* vol. 45, pp. 7-10, 2016.

[74] E. R. Encina and E. A. Coronado, "Size optimization of iron oxide@ noble metal core–shell nanohybrids for photothermal applications," *The Journal of Physical Chemistry C,* vol. 120, pp. 5630-5639, 2016.

[75] C. Loo, A. Lin, L. Hirsch, M.-H. Lee, J. Barton, N. Halas, *et al.*, "Nanoshell-enabled photonics-based imaging and therapy of cancer," *Technology in cancer research & treatment,* vol. 3, pp. 33-40, 2004.

[76] X. Huang, S. Neretina, and M. A. El ‐ Sayed, "Gold nanorods: from synthesis and properties to biological and biomedical applications," *Advanced Materials,* vol. 21, pp. 4880-4910, 2009.

[77] H. J. Chen, L. Shao, Q. Li, and J. F. Wang, "Gold nanorods and their plasmonic properties," *Chemical Society Reviews,* vol. 42, pp. 2679-2724, 2013.

[78] R. v. Gans, "Form of ultramicroscopic particles of silver," *Ann. Phys,* vol. 47, pp. 270-284, 1915.

[79] M. Yorulmaz, S. Nizzero, A. Hoggard, L.-Y. Wang, Y.-Y. Cai, M.-N. Su, *et al.*, "Single-Particle Absorption Spectroscopy by Photothermal Contrast," *Nano Letters,* vol. 15, pp. 3041-3047, 2015/05/13 2015.

[80] J. He, C. He, C. Zheng, Q. Wang, and J. Ye, "Plasmonic nanoparticle simulations and inverse design using machine learning," *Nanoscale,* vol. 11, pp. 17444-17459, 2019.

[81] J. Zhao, A. O. Pinchuk, J. M. McMahon, S. Li, L. K. Ausman, A. L. Atkinson, *et al.*, "Methods for Describing the Electromagnetic Properties of Silver and Gold Nanoparticles," *Accounts of Chemical Research,* vol. 41, pp. 1710-1720, 2008/12/16 2008.

[82] M. Hu, J. Chen, Z.-Y. Li, L. Au, G. V. Hartland, X. Li, *et al.*, "Gold nanostructures: engineering their plasmonic properties for biomedical applications," *Chemical Society Reviews,* vol. 35, pp. 1084-1094, 2006.

[83] J. P. Kottmann, O. J. F. Martin, R. S. David, and S. Sheldon, "Field polarization and polarization charge distributions in plasmon resonant nanoparticles," *New Journal of Physics,* vol. 2, p. 27, 2000.

[84] E. J. Zeman and G. C. Schatz, "An accurate electromagnetic theory study of surface enhancement factors for silver, gold, copper, lithium, sodium, aluminum, gallium, indium, zinc, and cadmium," *Journal of Physical Chemistry,* vol. 91, pp. 634-643, 1987.

[85] S. Kim, J. M. Kim, J. E. Park, and J. M. Nam, "Nonnoble ‐ Metal ‐ Based Plasmonic Nanomaterials: Recent Advances and Future Perspectives," *Advanced Materials,* vol. 30, 2018.

[86] U. Aslam and S. Linic, "Kinetic Trapping of Immiscible Metal Atoms into Bimetallic Nanoparticles through Plasmonic Visible Light-Mediated Reduction of a Bimetallic Oxide

Precursor: Case Study of Ag–Pt Nanoparticle Synthesis," *Chemistry of Materials*, vol. 28, pp. 8289-8295, 2016/11/22 2016.

[87] L. Huang, J. Zou, J.-Y. Ye, Z.-Y. Zhou, Z. Lin, X. Kang, *et al.*, "Synergy between Plasmonic and Electrocatalytic Activation of Methanol Oxidation on Palladium–Silver Alloy Nanotubes," *Angewandte Chemie*, vol. 131, pp. 8886-8890, 2019.

[88] D. Rioux and M. Meunier, "Seeded Growth Synthesis of Composition and Size-Controlled Gold–Silver Alloy Nanoparticles," *The Journal of Physical Chemistry C*, vol. 119, pp. 13160-13168, 2015/06/11 2015.

[89] D. Rioux and M. Meunier, "Alloy nanoparticles, process for their preparation and use thereof," ed: Google Patents, 2016.

[90] S. Patskovsky, E. Bergeron, D. Rioux, M. Simard, and M. Meunier, "Hyperspectral reflected light microscopy of plasmonic Au/Ag alloy nanoparticles incubated as multiplex chromatic biomarkers with cancer cells," *Analyst*, vol. 139, pp. 5247-5253, Oct 2014.

[91] M. A. García, "Surface plasmons in metallic nanoparticles: fundamentals and applications," *Journal of Physics D: Applied Physics*, vol. 44, p. 283001, 2011.

[92] E. Prodan, P. Nordlander, and N. Halas, "Effects of dielectric screening on the optical properties of metallic nanoshells," *Chemical Physics Letters*, vol. 368, pp. 94-101, 2003.

[93] R. Bardhan, S. Mukherjee, N. A. Mirin, S. D. Levit, P. Nordlander, and N. J. Halas, "Nanosphere-in-a-nanoshell: a simple nanomatryushka," *The Journal of Physical Chemistry C*, vol. 114, pp. 7378-7383, 2009.

[94] J. Zhu, J. J. Li, and J. W. Zhao, "Frequency-Dependent Polarization Properties of Local Electric Field in Gold-Dielectric Multi-Nanoshells," *Plasmonics*, vol. 8, pp. 417-424, Jun 2013.

[95] J. A. I. Acapulco, S. Hong, S. K. Kim, and S. Park, "Controlling optical properties of metallic multi-shell nanoparticles through suppressed surface plasmon resonance," *Journal of Colloid and Interface Science*, vol. 461, pp. 376-382, Jan 2016.

[96] I. Pastoriza-Santos, C. Kinnear, J. Pérez-Juste, P. Mulvaney, and L. M. Liz-Marzán, "Plasmonic polymer nanocomposites," *Nature Reviews Materials*, vol. 3, pp. 375-391, 2018/10/01 2018.

[97] E. Bergeron, C. Boutopoulos, R. Martel, A. Torres, C. Rodriguez, J. Niskanen, *et al.*, "Cell-specific optoporation with near-infrared ultrafast laser and functionalized gold nanoparticles," *Nanoscale*, vol. 7, pp. 17836-17847, 2015.

[98] E. Chaffin, R. T. O'Connor, J. Barr, X. Huang, and Y. Wang, "Dependence of SERS enhancement on the chemical composition and structure of Ag/Au hybrid nanoparticles," *The Journal of Chemical Physics*, vol. 145, p. 054706, 2016.

[99] S. Schlücker, "Surface-Enhanced Raman Spectroscopy: Concepts and Chemical Applications," *Angewandte Chemie International Edition*, vol. 53, pp. 4756-4795, 2014.

[100] K. Kim, Y. M. Lee, J. W. Lee, and K. S. Shin, "Metal-Enhanced Fluorescence of Rhodamine B Isothiocyanate from Micrometer-Sized Silver Powders," *Langmuir*, vol. 25, pp. 2641-2645, 2009/03/03 2009.

[101] X. Y. Duan, S. Kamin, and N. Liu, "Dynamic plasmonic colour display," *Nature Communications,* vol. 8, Feb 2017.

[102] A. Bucharskaya, G. Maslyakova, G. Terentyuk, A. Yakunin, Y. Avetisyan, O. Bibikova, *et al.*, "Towards effective photothermal/photodynamic treatment using plasmonic gold nanoparticles," *International journal of molecular sciences,* vol. 17, p. 1295, 2016.

[103] D. Yang, G. Yang, P. Yang, R. Lv, S. Gai, C. Li, *et al.*, "Assembly of Au Plasmonic Photothermal Agent and Iron Oxide Nanoparticles on Ultrathin Black Phosphorus for Targeted Photothermal and Photodynamic Cancer Therapy," *Advanced Functional Materials,* vol. 27, p. 1700371, 2017.

[104] Z. Qin and J. C. Bischof, "Thermophysical and biological responses of gold nanoparticle laser heating," *Chemical Society Reviews,* vol. 41, pp. 1191-1217, 2012.

[105] C. Darviot, P. Hardy, and M. Meunier, "Laser-induced plasmon-mediated treatment of retinoblastoma in viscous vitreous phantom," *Journal of Biophotonics,* vol. 12, p. e201900193, 2019.

[106] P. Yuan, X. Ding, Y. Y. Yang, and Q.-H. Xu, "Metal Nanoparticles for Diagnosis and Therapy of Bacterial Infection," *Advanced Healthcare Materials,* vol. 7, p. 1701392, 2018.

[107] D. Wang, S. C. Pillai, S.-H. Ho, J. Zeng, Y. Li, and D. D. Dionysiou, "Plasmonic-based nanomaterials for environmental remediation," *Applied Catalysis B: Environmental,* vol. 237, pp. 721-741, 2018/12/05/ 2018.

[108] P. C. Ray, S. A. Khan, A. K. Singh, D. Senapati, and Z. Fan, "Nanomaterials for targeted detection and photothermal killing of bacteria," *Chemical Society Reviews,* vol. 41, pp. 3193-3209, 2012.

[109] M.-F. Tsai, S.-H. G. Chang, F.-Y. Cheng, V. Shanmugam, Y.-S. Cheng, C.-H. Su, *et al.*, "Au Nanorod Design as Light-Absorber in the First and Second Biological Near-Infrared Windows for in Vivo Photothermal Therapy," *ACS Nano,* vol. 7, pp. 5330-5342, 2013/06/25 2013.

[110] T. Yata, Y. Takahashi, M. M. Tan, H. Nakatsuji, S. Ohtsuki, T. Murakami, *et al.*, "DNA nanotechnology-based composite-type gold nanoparticle-immunostimulatory DNA hydrogel for tumor photothermal immunotherapy," *Biomaterials,* vol. 146, pp. 136-145, Nov 2017.

[111] J. Beik, Z. Abed, F. S. Ghoreishi, S. Hosseini-Nami, S. Mehrzadi, A. Shakeri-Zadeh, *et al.*, "Nanotechnology in hyperthermia cancer therapy: From fundamental principles to advanced applications," *Journal of Controlled Release,* vol. 235, pp. 205-221, Aug 2016.

[112] X. Huang, I. H. El-Sayed, W. Qian, and M. A. El-Sayed, "Cancer cell imaging and photothermal therapy in the near-infrared region by using gold nanorods," *Journal of the American Chemical Society,* vol. 128, pp. 2115-2120, 2006.

[113] S. M. Fothergill, C. Joyce, and F. Xie, "Metal enhanced fluorescence biosensing: from ultra-violet towards second near-infrared window," *Nanoscale,* vol. 10, pp. 20914-20929, Dec 2018.

[114] J.-E. Park, M. Kim, J.-H. Hwang, and J.-M. Nam, "Golden Opportunities: Plasmonic Gold Nanostructures for Biomedical Applications based on the Second Near-Infrared Window," *Small Methods,* vol. 1, p. 1600032, 2017.

[115] C. Song, F. Li, X. Guo, W. Chen, C. Dong, J. Zhang, *et al.*, "Gold nanostars for cancer cell-targeted SERS-imaging and NIR light-triggered plasmonic photothermal therapy (PPTT) in the first and second biological windows," *Journal of Materials Chemistry B,* vol. 7, pp. 2001-2008, 2019.

[116] A. R. Rastinehad, H. Anastos, E. Wajswol, J. S. Winoker, J. P. Sfakianos, S. K. Doppalapudi, *et al.*, "Gold nanoshell-localized photothermal ablation of prostate tumors in a clinical pilot device study," *Proceedings of the National Academy of Sciences,* vol. 116, pp. 18590-18596, 2019.

[117] H. Sun, J. Su, Q. Meng, Q. Yin, L. Chen, W. Gu, *et al.*, "Cancer Cell Membrane-Coated Gold Nanocages with Hyperthermia-Triggered Drug Release and Homotypic Target Inhibit Growth and Metastasis of Breast Cancer," *Advanced Functional Materials,* vol. 27, p. 1604300, 2017.

[118] L. Luo, H. He, C. Li, Y. He, Z. Hao, S. Wang, *et al.*, "Near-Infrared Responsive Bimetallic Nanovesicles for Enhanced Synergistic Chemophotothermal Therapy," *ACS Biomaterials Science & Engineering,* vol. 5, pp. 1321-1331, 2019/03/11 2019.

[119] Y. Li, J. Jin, D. Wang, J. Lv, K. Hou, Y. Liu, *et al.*, "Coordination-responsive drug release inside gold nanorod@metal-organic framework core–shell nanostructures for near-infrared-induced synergistic chemo-photothermal therapy," *Nano Research,* vol. 11, pp. 3294-3305, 2018/06/01 2018.

[120] R. Cheheltani, R. M. Ezzibdeh, P. Chhour, K. Pulaparthi, J. Kim, M. Jurcova, *et al.*, "Tunable, biodegradable gold nanoparticles as contrast agents for computed tomography and photoacoustic imaging," *Biomaterials,* vol. 102, pp. 87-97, Sep 2016.

[121] Z. Yang, J. Song, Y. Dai, J. Chen, F. Wang, L. Lin, *et al.*, "Self-Assembly of Semiconducting-Plasmonic Gold Nanoparticles with Enhanced Optical Property for Photoacoustic Imaging and Photothermal Therapy," *Theranostics,* vol. 7, pp. 2177-2185, 2017.

[122] X. Ge, B. Chen, T. Liu, L. Wei, L. Tong, Q. Ma, *et al.*, "Active targeting drug-gold nanorod hybrid nanoparticles for amplifying photoacoustic signal and enhancing anticancer efficacy," *RSC Advances,* vol. 9, pp. 13494-13502, 2019.

[123] M. Xu and L. V. Wang, "Photoacoustic imaging in biomedicine," *Review of Scientific Instruments,* vol. 77, p. 041101, 2006.

[124] P. K. Upputuri, C. Yang, S. Huang, K. Wang, M. Wang, and M. Pramanik, "Contrast-enhanced photoacoustic imaging in the second near-infrared window using semiconducting polymer nanoparticles," *Journal of Biomedical Optics,* vol. 24, p. 031002, 2018.

[125] A. Hatef, B. Darvish, A. Dagallier, Y. R. Davletshin, W. Johnston, J. C. Kumaradas, *et al.*, "Analysis of Photoacoustic Response from Gold–Silver Alloy Nanoparticles Irradiated by Short Pulsed Laser in Water," *The Journal of Physical Chemistry C,* vol. 119, pp. 24075-24080, 2015/10/22 2015.

[126] M. R. Jones, K. D. Osberg, R. J. Macfarlane, M. R. Langille, and C. A. Mirkin, "Templated Techniques for the Synthesis and Assembly of Plasmonic Nanostructures," *Chemical Reviews,* vol. 111, pp. 3736-3827, 2011/06/08 2011.

[127] W. Li and X. Chen, "Gold nanoparticles for photoacoustic imaging," *Nanomedicine,* vol. 10, pp. 299-320, 2015.

[128] L. Nie, S. Wang, X. Wang, P. Rong, Y. Ma, G. Liu, *et al.*, "In Vivo Volumetric Photoacoustic Molecular Angiography and Therapeutic Monitoring with Targeted Plasmonic Nanostars," *Small,* vol. 10, pp. 1585-1593, 2014.

[129] A. Chekkoury, J. Gateau, W. Driessen, P. Symvoulidis, N. Bézière, A. Feuchtinger, *et al.*, "Optical mesoscopy without the scatter: broadband multispectral optoacoustic mesoscopy," *Biomedical Optics Express,* vol. 6, pp. 3134-3148, 2015/09/01 2015.

[130] L. Cavigli, S. Centi, C. Borri, P. Tortoli, I. Panettieri, I. Streit, *et al.*, "1064-nm-resonant gold nanorods for photoacoustic theranostics within permissible exposure limits," *Journal of Biophotonics,* vol. 12, Oct 2019.

[131] J. Baumgart, L. Humbert, É. Boulais, R. Lachaine, J.-J. Lebrun, and M. Meunier, "Off-resonance plasmonic enhanced femtosecond laser optoporation and transfection of cancer cells," *Biomaterials,* vol. 33, pp. 2345-2350, 2012/03/01/ 2012.

[132] T. K. Kim and J. H. Eberwine, "Mammalian cell transfection: the present and the future," *Analytical and Bioanalytical Chemistry,* vol. 397, pp. 3173-3178, August 01 2010.

[133] C. Boutopoulos, E. Bergeron, and M. Meunier, "Cell perforation mediated by plasmonic bubbles generated by a single near infrared femtosecond laser pulse," *Journal of Biophotonics,* vol. 9, pp. 26-31, 2016.

[134] E. Boulais, R. Lachaine, A. Hatef, and M. Meunier, "Plasmonics for pulsed-laser cell nanosurgery: Fundamentals and applications," *Journal of Photochemistry and Photobiology C: Photochemistry Reviews,* vol. 17, pp. 26-49, 2013/12/01/ 2013.

[135] M. Schomaker, D. Heinemann, S. Kalies, S. Willenbrock, S. Wagner, I. Nolte, *et al.*, "Characterization of nanoparticle mediated laser transfection by femtosecond laser pulses for applications in molecular medicine," *Journal of Nanobiotechnology,* vol. 13, Feb 2015.

[136] R. Lachaine, É. Boulais, D. Rioux, C. Boutopoulos, and M. Meunier, "Computational Design of Durable Spherical Nanoparticles with Optimal Material, Shape, and Size for Ultrafast Plasmon-Enhanced Nanocavitation," *ACS Photonics,* vol. 3, pp. 2158-2169, 2016/11/16 2016.

[137] Y. Umebayashi, Y. Miyamoto, M. Wakita, A. Kobayashi, and T. Nishisaka, "Elevation of Plasma Membrane Permeability on Laser Irradiation of Extracellular Latex Particles," *The Journal of Biochemistry,* vol. 134, pp. 219-224, 2003.

[138] C. M. Pitsillides, E. K. Joe, X. Wei, R. R. Anderson, and C. P. Lin, "Selective Cell Targeting with Light-Absorbing Microparticles and Nanoparticles," *Biophysical Journal,* vol. 84, pp. 4023-4032, 2003/06/01/ 2003.

[139] D. Heinemann, M. Schomaker, S. Kalies, M. Schieck, R. Carlson, H. M. Escobar, *et al.*, "Gold nanoparticle mediated laser transfection for efficient siRNA mediated gene knock down," *Plos one,* vol. 8, p. e58604, 2013.

[140] R. Lachaine, C. Boutopoulos, P.-Y. Lajoie, É. Boulais, and M. Meunier, "Rational Design of Plasmonic Nanoparticles for Enhanced Cavitation and Cell Perforation," *Nano Letters,* vol. 16, pp. 3187-3194, 2016/05/11 2016.

[141] Y. Feng, G. Wang, Y. Chang, Y. Cheng, B. Sun, L. Wang, *et al.*, "Electron Compensation Effect Suppressed Silver Ion Release and Contributed Safety of Au@Ag Core–Shell Nanoparticles," *Nano Letters,* vol. 19, pp. 4478-4489, 2019/07/10 2019.

[142] E. S. Melby, S. E. Lohse, J. E. Park, A. M. Vartanian, R. A. Putans, H. B. Abbott, *et al.*, "Cascading Effects of Nanoparticle Coatings: Surface Functionalization Dictates the Assemblage of Complexed Proteins and Subsequent Interaction with Model Cell Membranes," *Acs Nano,* vol. 11, pp. 5489-5499, Jun 2017.

[143] K. A. Willets, A. J. Wilson, V. Sundaresan, and P. B. Joshi, "Super-Resolution Imaging and Plasmonics," *Chemical Reviews,* vol. 117, pp. 7538-7582, 2017/06/14 2017.

[144] S. Patskovsky, E. Bergeron, and M. Meunier, "Hyperspectral darkfield microscopy of PEGylated gold nanoparticles targeting CD44-expressing cancer cells," *Journal of Biophotonics,* vol. 8, pp. 162-167, 2015.

[145] S. Patskovsky, E. Bergeron, D. Rioux, and M. Meunier, "Wide‐field hyperspectral 3D imaging of functionalized gold nanoparticles targeting cancer cells by reflected light microscopy," *Journal of biophotonics,* vol. 8, pp. 401-407, 2015.

[146] É. Bergeron, S. Patskovsky, D. Rioux, and M. Meunier, "3D multiplexed immunoplasmonics microscopy," *Nanoscale,* vol. 8, pp. 13263-13272, 2016.

[147] K. Seekell, M. Crow, A. Chilkoti, A. Wax, S. Marinakos, and J. Ostrander, "Hyperspectral molecular imaging of multiple receptors using immunolabeled plasmonic nanoparticles," *Journal of Biomedical Optics,* vol. 16, p. 116003, 2011.

[148] H. Xu, Q. Li, L. Wang, Y. He, J. Shi, B. Tang, *et al.*, "Nanoscale optical probes for cellular imaging," *Chemical Society Reviews,* vol. 43, pp. 2650-2661, 2014.

[149] M. Imai, K. Mine, H. Tomonari, J. Uchiyama, S. Matuzaki, Y. Niko, *et al.*, "Dark-Field Microscopic Detection of Bacteria using Bacteriophage-Immobilized SiO2@AuNP Core-Shell Nanoparticles," *Analytical Chemistry,* vol. 91, pp. 12352-12357, Oct 2019.

[150] N. Khlebtsov, V. Bogatyrev, L. Dykman, B. Khlebtsov, S. Staroverov, A. Shirokov, *et al.*, "Analytical and Theranostic Applications of Gold Nanoparticles and Multifunctional Nanocomposites," *Theranostics,* vol. 3, pp. 167-180, 2013.

[151] S. E. Ochmann, C. Vietz, K. Trofymchuk, G. P. Acuna, B. Lalkens, and P. Tinnefeld, "Optical Nanoantenna for Single Molecule-Based Detection of Zika Virus Nucleic Acids without Molecular Multiplication," *Analytical Chemistry,* vol. 89, pp. 13000-13007, Dec 2017.

[152] A. R. Halpern, J. B. Wood, Y. Wang, and R. M. Corn, "Single-Nanoparticle Near-Infrared Surface Plasmon Resonance Microscopy for Real-Time Measurements of DNA Hybridization Adsorption," *ACS Nano,* vol. 8, pp. 1022-1030, 2014/01/28 2014.

[153] X. Liu, Y. Wang, P. Chen, A. McCadden, A. Palaniappan, J. Zhang, *et al.*, "Peptide Functionalized Gold Nanoparticles with Optimized Particle Size and Concentration for

Colorimetric Assay Development: Detection of Cardiac Troponin I," *ACS Sensors,* vol. 1, pp. 1416-1422, 2016/12/23 2016.

[154] Z. Gao, H. Ye, D. Tang, J. Tao, S. Habibi, A. Minerick, *et al.*, "Platinum-Decorated Gold Nanoparticles with Dual Functionalities for Ultrasensitive Colorimetric in Vitro Diagnostics," *Nano Letters,* vol. 17, pp. 5572-5579, 2017/09/13 2017.

[155] H. B. Jeon, P. V. Tsalu, and J. W. Ha, "Shape Effect on the Refractive Index Sensitivity at Localized Surface Plasmon Resonance Inflection Points of Single Gold Nanocubes with Vertices," *Scientific Reports,* vol. 9, p. 13635, 2019/09/20 2019.

[156] C. Zhang, D. Paria, S. Semancik, and I. Barman, "Composite‐Scattering Plasmonic Nanoprobes for Label‐Free, Quantitative Biomolecular Sensing," *Small,* vol. 15, 2019.

[157] P. Chen, N. T. Tran, X. Wen, Q. Xiong, and B. Liedberg, "Inflection Point of the Localized Surface Plasmon Resonance Peak: A General Method to Improve the Sensitivity," *ACS Sensors,* vol. 2, pp. 235-242, 2017/02/24 2017.

[158] P. Chen and B. Liedberg, "Curvature of the localized surface plasmon resonance peak," *Analytical chemistry,* vol. 86, pp. 7399-7405, 2014.

[159] M. Fleischmann, P. J. Hendra, and A. J. McQuillan, "Raman spectra of pyridine adsorbed at a silver electrode," *Chemical Physics Letters,* vol. 26, pp. 163-166, 1974/05/15/ 1974.

[160] S. Nie and S. R. Emory, "Probing Single Molecules and Single Nanoparticles by Surface-Enhanced Raman Scattering," *Science,* vol. 275, pp. 1102-1106, 1997.

[161] C. Zong, R. Premasiri, H. N. Lin, Y. M. Huang, C. Zhang, C. Yang, *et al.*, "Plasmon-enhanced stimulated Raman scattering microscopy with single-molecule detection sensitivity," *Nature Communications,* vol. 10, Nov 2019.

[162] M. Rycenga, M. H. Kim, P. H. Camargo, C. Cobley, Z.-Y. Li, and Y. Xia, "Surface-enhanced Raman scattering: comparison of three different molecules on single-crystal nanocubes and nanospheres of silver," *The Journal of Physical Chemistry A,* vol. 113, pp. 3932-3939, 2009.

[163] J.-H. Lee, J.-W. Oh, S. H. Nam, Y. S. Cha, G.-H. Kim, W.-K. Rhim, *et al.*, "Synthesis, Optical Properties, and Multiplexed Raman Bio-Imaging of Surface Roughness-Controlled Nanobridged Nanogap Particles," *Small,* vol. 12, pp. 4726-4734, 2016.

[164] J. M. McLellan, Z.-Y. Li, A. R. Siekkinen, and Y. Xia, "The SERS activity of a supported Ag nanocube strongly depends on its orientation relative to laser polarization," *Nano letters,* vol. 7, pp. 1013-1017, 2007.

[165] B. Kuestner, M. Gellner, M. Schuetz, F. Schoeppler, A. Marx, P. Stroebel, *et al.*, "SERS labels for red laser excitation: Silica‐encapsulated SAMs on tunable gold/silver nanoshells," *Angewandte Chemie International Edition,* vol. 48, pp. 1950-1953, 2009.

[166] N. Pazos-Perez, J. M. Fitzgerald, V. Giannini, L. Guerrini, and R. A. Alvarez-Puebla, "Modular assembly of plasmonic core–satellite structures as highly brilliant SERS-encoded nanoparticles," *Nanoscale Advances,* vol. 1, pp. 122-131, 2019.

[167] J. Liu, J. Guo, G. Meng, and D. Fan, "Superstructural Raman Nanosensors with Integrated Dual Functions for Ultrasensitive Detection and Tunable Release of Molecules," *Chemistry of Materials,* vol. 30, pp. 5256-5263, 2018.

[168] Z. Fusco, R. Bo, Y. Wang, N. Motta, H. Chen, and A. Tricoli, "Self-assembly of Au nano-islands with tuneable organized disorder for highly sensitive SERS," *Journal of Materials Chemistry C,* vol. 7, pp. 6308-6316, 2019.

[169] B. G. M. Vieira, N. S. Mueller, E. B. Barros, and S. Reich, "Plasmonic Properties of Close-Packed Metallic Nanoparticle Mono- and Bilayers," *The Journal of Physical Chemistry C,* vol. 123, pp. 17951-17960, 2019/07/25 2019.

[170] H. Dies, A. Bottomley, D. L. Nicholls, K. Stamplecoskie, C. Escobedo, and A. Docoslis, "Electrokinetically-Driven Assembly of Gold Colloids into Nanostructures for Surface-Enhanced Raman Scattering," *Nanomaterials,* vol. 10, p. 661, 2020.

[171] R. Schreiber, J. Do, E.-M. Roller, T. Zhang, V. J. Schüller, P. C. Nickels, *et al.*, "Hierarchical assembly of metal nanoparticles, quantum dots and organic dyes using DNA origami scaffolds," *Nature Nanotechnology,* vol. 9, pp. 74-78, 2014/01/01 2014.

[172] G. Chen, K. J. Gibson, D. Liu, H. C. Rees, J.-H. Lee, W. Xia, *et al.*, "Regioselective surface encoding of nanoparticles for programmable self-assembly," *Nature Materials,* vol. 18, pp. 169-174, 2019/02/01 2019.

[173] M. Wang, J. Dong, C. Zhou, H. Xie, W. Ni, S. Wang, *et al.*, "Reconfigurable Plasmonic Diastereomers Assembled by DNA Origami," *ACS Nano,* vol. 13, pp. 13702-13708, 2019/12/24 2019.

[174] V. V. Thacker, L. O. Herrmann, D. O. Sigle, T. Zhang, T. Liedl, J. J. Baumberg, *et al.*, "DNA origami based assembly of gold nanoparticle dimers for surface-enhanced Raman scattering," *Nature Communications,* vol. 5, p. 3448, 2014/03/13 2014.

[175] M. D. Baaske, M. R. Foreman, and F. Vollmer, "Single-molecule nucleic acid interactions monitored on a label-free microcavity biosensor platform," *Nature nanotechnology,* vol. 9, pp. 933-939, 2014.

[176] H.-N. Wang, J. K. Register, A. M. Fales, N. Gandra, E. H. Cho, A. Boico, *et al.*, "Surface-enhanced Raman scattering nanosensors for in vivo detection of nucleic acid targets in a large animal model," *Nano Research,* vol. 11, pp. 4005-4016, August 01 2018.

[177] U. S. Dinish, G. Balasundaram, Y.-T. Chang, and M. Olivo, "Actively Targeted In Vivo Multiplex Detection of Intrinsic Cancer Biomarkers Using Biocompatible SERS Nanotags," *Scientific Reports,* vol. 4, p. 4075, 02/12/online 2014.

[178] K. Wang, S. Li, M. Petersen, S. Wang, and X. Lu, "Detection and Characterization of Antibiotic-Resistant Bacteria Using Surface-Enhanced Raman Spectroscopy," *Nanomaterials,* vol. 8, p. 762, 2018.

[179] M. Bauch, K. Toma, M. Toma, Q. Zhang, and J. Dostalek, "Plasmon-enhanced fluorescence biosensors: a review," *Plasmonics,* vol. 9, pp. 781-799, 2014.

[180] S.-H. Guo, S.-J. Tsai, H.-C. Kan, D.-H. Tsai, M. R. Zachariah, and R. J. Phaneuf, "The Effect of an Active Substrate on Nanoparticle-Enhanced Fluorescence," *Advanced Materials,* vol. 20, pp. 1424-1428, 2008.

[181] J.-W. Liaw, J.-H. Chen, C.-S. Chen, and M.-K. Kuo, "Purcell effect of nanoshell dimer on single molecule's fluorescence," *Optics express,* vol. 17, pp. 13532-13540, 2009.

[182] J.-F. Li, C.-Y. Li, and R. F. Aroca, "Plasmon-enhanced fluorescence spectroscopy," *Chemical Society Reviews,* vol. 46, pp. 3962-3979, 2017.

[183] S. Tu, D. Rioux, J. Perreault, D. Brouard, and M. Meunier, "Fluorescence and Scattering Dual-Mode Multiplexed Imaging with Gold–Silver Alloy Core Silica Shell Nanoparticles," *The Journal of Physical Chemistry C,* vol. 121, pp. 8944-8951, 2017/04/27 2017.

[184] H. A. Atwater and A. Polman, "Plasmonics for improved photovoltaic devices," *Nat Mater,* vol. 9, pp. 205-213, 03//print 2010.

[185] S. Pillai and M. A. Green, "Plasmonics for photovoltaic applications," *Solar Energy Materials and Solar Cells,* vol. 94, pp. 1481-1486, 2010/09/01/ 2010.

[186] S. Linic, P. Christopher, and D. B. Ingram, "Plasmonic-metal nanostructures for efficient conversion of solar to chemical energy," *Nature materials,* vol. 10, pp. 911-921, 2011.

[187] M. J. Kale, T. Avanesian, and P. Christopher, "Direct Photocatalysis by Plasmonic Nanostructures," *Acs Catalysis,* vol. 4, pp. 116-128, Jan 2014.

[188] A. Furube and S. Hashimoto, "Insight into plasmonic hot-electron transfer and plasmon molecular drive: new dimensions in energy conversion and nanofabrication," *Npg Asia Materials,* vol. 9, Dec 2017.

[189] L. Zhou, S. Zhuang, C. He, Y. Tan, Z. Wang, and J. Zhu, "Self-assembled spectrum selective plasmonic absorbers with tunable bandwidth for solar energy conversion," *Nano Energy,* vol. 32, pp. 195-200, 2017/02/01/ 2017.

[190] H. Ren, M. Tang, B. Guan, K. Wang, J. Yang, F. Wang, *et al.*, "Hierarchical Graphene Foam for Efficient Omnidirectional Solar–Thermal Energy Conversion," *Advanced Materials,* vol. 29, p. 1702590, 2017.

[191] Y. Xuan, H. Duan, and Q. Li, "Enhancement of solar energy absorption using a plasmonic nanofluid based on TiO 2/Ag composite nanoparticles," *RSC Advances,* vol. 4, pp. 16206-16213, 2014.

[192] L. Yi, S. Ci, S. Luo, P. Shao, Y. Hou, and Z. Wen, "Scalable and low-cost synthesis of black amorphous Al-Ti-O nanostructure for high-efficient photothermal desalination," *Nano Energy,* vol. 41, pp. 600-608, 2017/11/01/ 2017.

[193] H. Duan, L. Tang, Y. Zheng, and C. Xu, "Effect of plasmonic nanoshell-based nanofluid on efficiency of direct solar thermal collector," *Applied Thermal Engineering,* vol. 133, pp. 188-193, 2018/03/25/ 2018.

[194] L. Zhou, Y. Tan, J. Wang, W. Xu, Y. Yuan, W. Cai, *et al.*, "3D self-assembly of aluminium nanoparticles for plasmon-enhanced solar desalination," *Nature Photonics,* vol. 10, pp. 393-398, 2016/06/01 2016.

[195] K. Yao, H. J. Zhong, Z. L. Liu, M. Xiong, S. F. Leng, J. Zhang, *et al.*, "Plasmonic Metal Nanoparticles with Core-Bishell Structure for High-Performance Organic and Perovskite Solar Cells," *Acs Nano,* vol. 13, pp. 5397-5409, May 2019.

[196] X. Chen and M. Gu, "Hole Blocking Layer-Free Perovskite Solar Cells with High Efficiencies and Stabilities by Integrating Subwavelength-Sized Plasmonic Alloy Nanoparticles," *Acs Applied Energy Materials,* vol. 2, pp. 2094-2103, Mar 2019.

[197] S. H. Jeong, H. Choi, J. Y. Kim, and T. W. Lee, "Silver-Based Nanoparticles for Surface Plasmon Resonance in Organic Optoelectronics," *Particle & Particle Systems Characterization,* vol. 32, pp. 164-175, Feb 2015.

[198] S. W. Baek, G. Park, J. Noh, C. Cho, C. H. Lee, M. K. Seo, *et al.*, "Au@Ag Core-Shell Nanocubes for Efficient Plasmonic Light Scattering Effect in Low Bandgap Organic Solar Cells," *Acs Nano,* vol. 8, pp. 3302-3312, Apr 2014.

[199] K. R. Catchpole and A. Polman, "Plasmonic solar cells," *Optics Express,* vol. 16, pp. 21793-21800, 2008/12/22 2008.

[200] S. H. Cho, J. Lee, M. J. Lee, H. J. Kim, S.-M. Lee, and K. C. Choi, "Plasmonically Engineered Textile Polymer Solar Cells for High-Performance, Wearable Photovoltaics," *ACS Applied Materials & Interfaces,* vol. 11, pp. 20864-20872, 2019/06/12 2019.

[201] J. S. Metzman, A. U. Khan, B. A. Magill, G. A. Khodaparast, J. R. Heflin, and G. Liu, "Critical Role of Polystyrene Layer on Plasmonic Silver Nanoplates in Organic Photovoltaics," *ACS Applied Energy Materials,* vol. 2, pp. 2475-2485, 2019/04/22 2019.

[202] V. Kumaravel, S. Mathew, J. Bartlett, and S. C. Pillai, "Photocatalytic hydrogen production using metal doped TiO2: A review of recent advances," *Applied Catalysis B: Environmental,* vol. 244, pp. 1021-1064, 2019/05/05/ 2019.

[203] C. P. Li, P. Wang, H. J. Li, M. M. Wang, J. Zhang, G. H. Qi, *et al.*, "Plasmon-driven water splitting enhancement on plasmonic metal-insulator-semiconductor hetero-nanostructures: unraveling the crucial role of interfacial engineering," *Nanoscale,* vol. 10, pp. 14290-14297, Aug 2018.

[204] S. Yu, A. J. Wilson, J. Heo, and P. K. Jain, "Plasmonic Control of Multi-Electron Transfer and C–C Coupling in Visible-Light-Driven CO2 Reduction on Au Nanoparticles," *Nano Letters,* vol. 18, pp. 2189-2194, 2018/04/11 2018.

[205] N. Zhang, C. Han, Y.-J. Xu, J. J. Foley Iv, D. Zhang, J. Codrington, *et al.*, "Near-field dielectric scattering promotes optical absorption by platinum nanoparticles," *Nature Photonics,* vol. 10, pp. 473-482, 2016/07/01 2016.

[206] S. J. Tan, L. Zhang, D. Zhu, X. M. Goh, Y. M. Wang, K. Kumar, *et al.*, "Plasmonic Color Palettes for Photorealistic Printing with Aluminum Nanostructures," *Nano Letters,* vol. 14, pp. 4023-4029, 2014/07/09 2014.

[207] E. Heydari, J. R. Sperling, S. L. Neale, and A. W. Clark, "Plasmonic Color Filters as Dual-State Nanopixels for High-Density Microimage Encoding," *Advanced Functional Materials,* vol. 27, pp. 1701866-n/a, 2017.

[208] C. S. H. Hwang, M. S. Ahn, Y. Lee, T. Chung, and K. H. Jeong, "Ag/Au Alloyed Nanoislands for Wafer-Level Plasmonic Color Filter Arrays," *Scientific Reports,* vol. 9, Jun 2019.

[209] A. Gentile, F. Ruffino, and M. Grimaldi, "Complex-Morphology Metal-Based Nanostructures: Fabrication, Characterization, and Applications," *Nanomaterials,* vol. 6, p. 110, 2016.

[210] Y. Gu, L. Zhang, J. K. W. Yang, S. P. Yeo, and C.-W. Qiu, "Color generation via subwavelength plasmonic nanostructures," *Nanoscale,* vol. 7, pp. 6409-6419, 2015.

[211] J. Feng, F. Yang, X. Wang, F. Lyu, Z. Li, and Y. Yin, "Self-Aligned Anisotropic Plasmonic Nanostructures," *Advanced Materials,* vol. 31, p. 1900789, 2019.

[212] Z. Wang, S. Zong, L. Wu, D. Zhu, and Y. Cui, "SERS-Activated Platforms for Immunoassay: Probes, Encoding Methods, and Applications," *Chemical Reviews,* vol. 117, pp. 7910-7963, 2017/06/28 2017.

[213] Y. Liu, Y. H. Lee, Q. Zhang, Y. Cui, and X. Y. Ling, "Plasmonic nanopillar arrays encoded with multiplex molecular information for anti-counterfeiting applications," *Journal of Materials Chemistry C,* vol. 4, pp. 4312-4319, 2016.

[214] Y. Liu, Y. H. Lee, M. R. Lee, Y. Yang, and X. Y. Ling, "Flexible Three-Dimensional Anticounterfeiting Plasmonic Security Labels: Utilizing Z-Axis-Dependent SERS Readouts to Encode Multilayered Molecular Information," *ACS Photonics,* vol. 4, pp. 2529-2536, 2017/10/18 2017.

[215] W. Lin, R.-W. Zhang, S.-S. Jang, C.-P. Wong, and J.-I. Hong, "“Organic Aqua Regia”—Powerful Liquids for Dissolving Noble Metals," *Angewandte Chemie International Edition,* vol. 49, pp. 7929-7932, 2010.

[216] C. Yue, H. Sun, W.-J. Liu, B. Guan, X. Deng, X. Zhang, *et al.*, "Environmentally Benign, Rapid, and Selective Extraction of Gold from Ores and Waste Electronic Materials," *Angewandte Chemie International Edition,* vol. 56, pp. 9331-9335, 2017.

[217] J.-L. Do, D. Tan, and T. Friščić, "Oxidative Mechanochemistry: Direct, Room-Temperature, Solvent-Free Conversion of Palladium and Gold Metals into Soluble Salts and Coordination Complexes," *Angewandte Chemie International Edition,* vol. 57, pp. 2667-2671, 2018.

[218] M. R. K. Ali, Y. Wu, and M. A. El-Sayed, "Gold-Nanoparticle-Assisted Plasmonic Photothermal Therapy Advances Toward Clinical Application," *The Journal of Physical Chemistry C,* vol. 123, pp. 15375-15393, 2019/06/27 2019.

[219] K. D. Gilroy, A. Ruditskiy, H.-C. Peng, D. Qin, and Y. Xia, "Bimetallic Nanocrystals: Syntheses, Properties, and Applications," *Chemical Reviews,* vol. 116, pp. 10414-10472, 2016/09/28 2016.

[220] M. Zhou, C. Li, and J. Fang, "Noble-Metal Based Random Alloy and Intermetallic Nanocrystals: Syntheses and Applications," *Chemical Reviews,* vol. 121, pp. 736-795, 2021/01/27 2021.

[221] X.-F. Zhang, Z.-G. Liu, W. Shen, and S. Gurunathan, "Silver nanoparticles: synthesis, characterization, properties, applications, and therapeutic approaches," *International journal of molecular sciences,* vol. 17, p. 1534, 2016.

[222] M. Tréguer-Delapierre, J. Majimel, S. Mornet, E. Duguet, and S. Ravaine, "Synthesis of non-spherical gold nanoparticles," *Gold Bulletin,* vol. 41, pp. 195-207, June 01 2008.

[223] A. Guerrero-Martínez, S. Barbosa, I. Pastoriza-Santos, and L. M. Liz-Marzán, "Nanostars shine bright for you: colloidal synthesis, properties and applications of branched metallic nanoparticles," *Current Opinion in Colloid & Interface Science,* vol. 16, pp. 118-127, 2011.

[224] D. Wang and Y. Li, "Bimetallic Nanocrystals: Liquid-Phase Synthesis and Catalytic Applications," *Advanced Materials,* vol. 23, pp. 1044-1060, 2011.

[225] T. Wen, L. N. Brush, and K. M. Krishnan, "A generalized diffusion model for growth of nanoparticles synthesized by colloidal methods," *Journal of Colloid and Interface Science,* vol. 419, pp. 79-85, 2014/04/01/ 2014.

[226] V. K. L. Mer, "Nucleation in Phase Transitions," *Industrial & Engineering Chemistry,* vol. 44, pp. 1270-1277, 1952.

[227] V. K. LaMer and R. H. Dinegar, "Theory, production and mechanism of formation of monodispersed hydrosols," *Journal of the American Chemical Society,* vol. 72, pp. 4847-4854, 1950.

[228] L. Vitos, A. V. Ruban, H. L. Skriver, and J. Kollár, "The surface energy of metals," *Surface Science,* vol. 411, pp. 186-202, 1998/08/11/ 1998.

[229] S. Link, Z. L. Wang, and M. A. El-Sayed, "Alloy Formation of Gold−Silver Nanoparticles and the Dependence of the Plasmon Absorption on Their Composition," *The Journal of Physical Chemistry B,* vol. 103, pp. 3529-3533, 1999/05/01 1999.

[230] C. Moreira Da Silva, A. Girard, M. Dufond, F. Fossard, A. Andrieux-Ledier, V. Huc, *et al.*, "Nickel platinum (NixPt1−x) nanoalloy monodisperse particles without the core–shell structure by colloidal synthesis," *Nanoscale Advances,* vol. 2, pp. 3882-3889, 2020.

[231] L. Zhang, H. Su, M. Sun, Y. Wang, W. Wu, T. Yu, *et al.*, "Concave Cu-Pd bimetallic nanocrystals: Ligand-based Co-reduction and mechanistic study," *Nano Research,* vol. 8, pp. 2415-2430, 2015/07/01 2015.

[232] Y. Yu, W. Yang, X. Sun, W. Zhu, X. Z. Li, D. J. Sellmyer, *et al.*, "Monodisperse MPt (M = Fe, Co, Ni, Cu, Zn) Nanoparticles Prepared from a Facile Oleylamine Reduction of Metal Salts," *Nano Letters,* vol. 14, pp. 2778-2782, 2014/05/14 2014.

[233] N. Pokhrel, P. K. Vabbina, and N. Pala, "Sonochemistry: Science and Engineering," *Ultrasonics Sonochemistry,* vol. 29, pp. 104-128, 2016/03/01/ 2016.

[234] J. J. Hinman and K. S. Suslick, "Nanostructured Materials Synthesis Using Ultrasound," *Topics in Current Chemistry,* vol. 375, p. 12, 2017/01/11 2017.

[235] Y.-J. Zhu and F. Chen, "Microwave-Assisted Preparation of Inorganic Nanostructures in Liquid Phase," *Chemical Reviews,* vol. 114, pp. 6462-6555, 2014/06/25 2014.

[236] C. Gümeci, D. U. Cearnaigh, D. J. Casadonte, and C. Korzeniewski, "Synthesis of PtCu3 bimetallic nanoparticles as oxygen reduction catalysts via a sonochemical method," *Journal of Materials Chemistry A,* vol. 1, pp. 2322-2330, 2013.

[237] M. A. Matin, J.-H. Jang, and Y.-U. Kwon, "PdM nanoparticles (M = Ni, Co, Fe, Mn) with high activity and stability in formic acid oxidation synthesized by sonochemical reactions," *Journal of Power Sources,* vol. 262, pp. 356-363, 2014/09/15/ 2014.

[238] M. Kalyva, M. F. Sunding, A. E. Gunnæs, S. Diplas, and E. A. Redekop, "Correlation between surface chemistry and morphology of PtCu and Pt nanoparticles during oxidation-reduction cycle," *Applied Surface Science*, vol. 532, p. 147369, 2020/12/01/ 2020.

[239] I. Bilecka and M. Niederberger, "Microwave chemistry for inorganic nanomaterials synthesis," *Nanoscale*, vol. 2, pp. 1358-1374, 2010.

[240] Y. Xiang, X. Wu, D. Liu, Z. Li, W. Chu, L. Feng, *et al.*, "Gold Nanorod-Seeded Growth of Silver Nanostructures: From Homogeneous Coating to Anisotropic Coating," *Langmuir*, vol. 24, pp. 3465-3470, 2008/04/01 2008.

[241] M. Jin, H. Zhang, J. Wang, X. Zhong, N. Lu, Z. Li, *et al.*, "Copper Can Still Be Epitaxially Deposited on Palladium Nanocrystals To Generate Core–Shell Nanocubes Despite Their Large Lattice Mismatch," *ACS Nano*, vol. 6, pp. 2566-2573, 2012/03/27 2012.

[242] H. Guo, Y. Chen, H. Ping, J. Jin, and D.-L. Peng, "Facile synthesis of Cu and Cu@Cu–Ni nanocubes and nanowires in hydrophobic solution in the presence of nickel and chloride ions," *Nanoscale*, vol. 5, pp. 2394-2402, 2013.

[243] L. Wang, Y. Nemoto, and Y. Yamauchi, "Direct Synthesis of Spatially-Controlled Pt-on-Pd Bimetallic Nanodendrites with Superior Electrocatalytic Activity," *Journal of the American Chemical Society*, vol. 133, pp. 9674-9677, 2011/06/29 2011.

[244] C.-C. Huang, Z. Yang, and H.-T. Chang, "Synthesis of Dumbbell-Shaped Au−Ag Core−Shell Nanorods by Seed-Mediated Growth under Alkaline Conditions," *Langmuir*, vol. 20, pp. 6089-6092, 2004/07/01 2004.

[245] F.-R. Fan, D.-Y. Liu, Y.-F. Wu, S. Duan, Z.-X. Xie, Z.-Y. Jiang, *et al.*, "Epitaxial Growth of Heterogeneous Metal Nanocrystals: From Gold Nano-octahedra to Palladium and Silver Nanocubes," *Journal of the American Chemical Society*, vol. 130, pp. 6949-6951, 2008/06/01 2008.

[246] C. Tan, J. Chen, X.-J. Wu, and H. Zhang, "Epitaxial growth of hybrid nanostructures," *Nature Reviews Materials*, vol. 3, p. 17089, 2018/01/23 2018.

[247] W. L. Weng, C. Y. Hsu, J. S. Lee, H. H. Fan, and C. N. Liao, "Twin-mediated epitaxial growth of highly latticemis-matched Cu/Ag core-shell nanowires," *Nanoscale*, vol. 10, pp. 9862-9866, Jun 2018.

[248] D. Dutta, R. M. Sankaran, and V. R. Bhethanabotla, "Predicting the Chiral Enrichment of Metallic SWCNTs on Ni-Cu Bimetallic Surfaces," *Chemistry of Materials*, vol. 26, pp. 4943-4950, Sep 2014.

[249] B. Lim, J. G. Wang, P. H. C. Camargo, M. J. Jiang, M. J. Kim, and Y. N. Xia, "Facile synthesis of bimetallic nanoplates consisting of Pd cores and Pt shells through seeded epitaxial growth," *Nano Letters*, vol. 8, pp. 2535-2540, Aug 2008.

[250] K. D. Gilroy, R. A. Hughes, and S. Neretina, "Kinetically Controlled Nucleation of Silver on Surfactant-Free Gold Seeds," *Journal of the American Chemical Society*, vol. 136, pp. 15337-15345, 2014/10/29 2014.

[251] Z. Wang, Z. Chen, H. Zhang, Z. Zhang, H. Wu, M. Jin, *et al.*, "Lattice-Mismatch-Induced Twinning for Seeded Growth of Anisotropic Nanostructures," *ACS Nano*, vol. 9, pp. 3307-3313, 2015/03/24 2015.

[252] S. E. Habas, H. Lee, V. Radmilovic, G. A. Somorjai, and P. Yang, "Shaping binary metal nanocrystals through epitaxial seeded growth," *Nature Materials,* vol. 6, pp. 692-697, 2007/09/01 2007.

[253] S. Chen, S. V. Jenkins, J. Tao, Y. Zhu, and J. Chen, "Anisotropic Seeded Growth of Cu–M (M = Au, Pt, or Pd) Bimetallic Nanorods with Tunable Optical and Catalytic Properties," *The Journal of Physical Chemistry C,* vol. 117, pp. 8924-8932, 2013/05/02 2013.

[254] M. R. Langille, J. Zhang, and C. A. Mirkin, "Plasmon-Mediated Synthesis of Heterometallic Nanorods and Icosahedra," *Angewandte Chemie International Edition,* vol. 50, pp. 3543-3547, 2011.

[255] R. G. Weiner, M. R. Kunz, and S. E. Skrabalak, "Seeding a New Kind of Garden: Synthesis of Architecturally Defined Multimetallic Nanostructures by Seed-Mediated Co-Reduction," *Accounts of Chemical Research,* vol. 48, pp. 2688-2695, 2015/10/20 2015.

[256] M. R. Kunz, S. M. McClain, D. P. Chen, K. M. Koczkur, R. G. Weiner, and S. E. Skrabalak, "Seed-mediated co-reduction in a large lattice mismatch system: synthesis of Pd–Cu nanostructures," *Nanoscale,* vol. 9, pp. 7570-7576, 2017.

[257] Y. Xia, X. Xia, and H.-C. Peng, "Shape-Controlled Synthesis of Colloidal Metal Nanocrystals: Thermodynamic versus Kinetic Products," *Journal of the American Chemical Society,* vol. 137, pp. 7947-7966, 2015/07/01 2015.

[258] A. M. El-Toni, M. A. Habila, J. P. Labis, A. L. ZA, M. Alhoshan, A. A. Elzatahry, *et al.*, "Design, synthesis and applications of core-shell, hollow core, and nanorattle multifunctional nanostructures," *Nanoscale,* vol. 8, pp. 2510-31, Feb 7 2016.

[259] X. Xia, Y. Wang, A. Ruditskiy, and Y. Xia, "25th Anniversary Article: Galvanic Replacement: A Simple and Versatile Route to Hollow Nanostructures with Tunable and Well-Controlled Properties," *Advanced Materials,* vol. 25, pp. 6313-6333, 2013.

[260] S. W. Chee, S. F. Tan, Z. Baraissov, M. Bosman, and U. Mirsaidov, "Direct observation of the nanoscale Kirkendall effect during galvanic replacement reactions," *Nature Communications,* vol. 8, p. 1224, 2017/10/31 2017.

[261] H. Jing and H. Wang, "Structural Evolution of Ag–Pd Bimetallic Nanoparticles through Controlled Galvanic Replacement: Effects of Mild Reducing Agents," *Chemistry of Materials,* vol. 27, pp. 2172-2180, 2015/03/24 2015.

[262] A. N. Chen, S. M. McClain, S. D. House, J. C. Yang, and S. E. Skrabalak, "Mechanistic Study of Galvanic Replacement of Chemically Heterogeneous Templates," *Chemistry of Materials,* vol. 31, pp. 1344-1351, 2019/02/26 2019.

[263] W. Zhang, J. Yang, and X. Lu, "Tailoring Galvanic Replacement Reaction for the Preparation of Pt/Ag Bimetallic Hollow Nanostructures with Controlled Number of Voids," *ACS Nano,* vol. 6, pp. 7397-7405, 2012/08/28 2012.

[264] G. G. Li, Z. Wang, and H. Wang, "Complementing Nanoscale Galvanic Exchange with Redox Manipulation toward Architectural Control of Multimetallic Hollow Nanostructures," *ChemNanoMat,* vol. 6, pp. 998-1013, 2020.

[265] R. Liu and A. Sen, "Unified Synthetic Approach to Silver Nanostructures by Galvanic Displacement Reaction on Copper: From Nanobelts to Nanoshells," *Chemistry of Materials,* vol. 24, pp. 48-54, 2012/01/10 2012.

[266] Y. Kobayashi, Z. Cai, G. Chang, Y. He, and M. Oyama, "Palladium Deposition on Nickel Microparticles by a Galvanic Replacement Reaction for Electrocatalytic Oxidation of Ethanol," *ACS Applied Energy Materials,* vol. 2, pp. 6023-6030, 2019/08/26 2019.

[267] B. Zhao, Y. Li, Q. Zeng, L. Wang, J. Ding, R. Zhang, *et al.*, "Galvanic Replacement Reaction Involving Core–Shell Magnetic Chains and Orientation-Tunable Microwave Absorption Properties," *Small,* vol. 16, p. 2003502, 2020.

[268] A. G. M. da Silva, T. S. Rodrigues, S. J. Haigh, and P. H. C. Camargo, "Galvanic replacement reaction: recent developments for engineering metal nanostructures towards catalytic applications," *Chemical Communications,* vol. 53, pp. 7135-7148, 2017.

[269] X. Lu, L. Au, J. McLellan, Z.-Y. Li, M. Marquez, and Y. Xia, "Fabrication of Cubic Nanocages and Nanoframes by Dealloying Au/Ag Alloy Nanoboxes with an Aqueous Etchant Based on Fe(NO3)3 or NH4OH," *Nano Letters,* vol. 7, pp. 1764-1769, 2007/06/01 2007.

[270] H. Jang and D.-H. Min, "Spherically-Clustered Porous Au–Ag Alloy Nanoparticle Prepared by Partial Inhibition of Galvanic Replacement and Its Application for Efficient Multimodal Therapy," *ACS Nano,* vol. 9, pp. 2696-2703, 2015/03/24 2015.

[271] D. Wan, X. Xia, Y. Wang, and Y. Xia, "Robust Synthesis of Gold Cubic Nanoframes through a Combination of Galvanic Replacement, Gold Deposition, and Silver Dealloying," *Small,* vol. 9, pp. 3111-3117, 2013.

[272] E. González, J. Arbiol, and V. F. Puntes, "Carving at the Nanoscale: Sequential Galvanic Exchange and Kirkendall Growth at Room Temperature," *Science,* vol. 334, pp. 1377-1380, 2011.

[273] B. Zhao, X. Guo, W. Zhao, J. Deng, B. Fan, G. Shao, *et al.*, "Facile synthesis of yolk–shell Ni@void@SnO2(Ni3Sn2) ternary composites via galvanic replacement/Kirkendall effect and their enhanced microwave absorption properties," *Nano Research,* vol. 10, pp. 331-343, 2017/01/01 2017.

[274] H. Zhang, M. Jin, H. Liu, J. Wang, M. J. Kim, D. Yang, *et al.*, "Facile Synthesis of Pd–Pt Alloy Nanocages and Their Enhanced Performance for Preferential Oxidation of CO in Excess Hydrogen," *ACS Nano,* vol. 5, pp. 8212-8222, 2011/10/25 2011.

[275] L. Xu, Z. Luo, Z. Fan, X. Zhang, C. Tan, H. Li, *et al.*, "Triangular Ag–Pd alloy nanoprisms: rational synthesis with high-efficiency for electrocatalytic oxygen reduction," *Nanoscale,* vol. 6, pp. 11738-11743, 2014.

[276] Y. Kuang, Y. Zhang, Z. Cai, G. Feng, Y. Jiang, C. Jin, *et al.*, "Single-crystalline dendritic bimetallic and multimetallic nanocubes," *Chemical Science,* vol. 6, pp. 7122-7129, 2015.

[277] Y. Yang, Q. Zhang, Z.-W. Fu, and D. Qin, "Transformation of Ag Nanocubes into Ag–Au Hollow Nanostructures with Enriched Ag Contents to Improve SERS Activity and Chemical Stability," *ACS Applied Materials & Interfaces,* vol. 6, pp. 3750-3757, 2014/03/12 2014.

[278] X. Yue, J. Hou, H. Zhao, P. Wu, Y. Guo, Q. Shi, *et al.*, "Au–Ag alloy nanoparticles with tunable cavity for plasmon-enhanced photocatalytic H2 evolution," *Journal of Energy Chemistry*, vol. 49, pp. 1-7, 2020/10/01/ 2020.

[279] D. Rioux and M. Meunier, "Alloy nanoparticles, process for their preparation and use thereof," ed: Google Patents, 2019.

[280] J. Turkevich, P. C. Stevenson, and J. Hillier, "A study of the nucleation and growth processes in the synthesis of colloidal gold," *Discussions of the Faraday Society*, vol. 11, pp. 55-75, 1951.

[281] X. Ji, X. Song, J. Li, Y. Bai, W. Yang, and X. Peng, "Size Control of Gold Nanocrystals in Citrate Reduction: The Third Role of Citrate," *Journal of the American Chemical Society*, vol. 129, pp. 13939-13948, 2007/11/01 2007.

[282] X. Dong, X. Ji, H. Wu, L. Zhao, J. Li, and W. Yang, "Shape Control of Silver Nanoparticles by Stepwise Citrate Reduction," *The Journal of Physical Chemistry C*, vol. 113, pp. 6573-6576, 2009/04/23 2009.

[283] H. Xia, S. Bai, J. Hartmann, and D. Wang, "Synthesis of Monodisperse Quasi-Spherical Gold Nanoparticles in Water via Silver(I)-Assisted Citrate Reduction," *Langmuir*, vol. 26, pp. 3585-3589, 2010/03/02 2010.

[284] M. Tran, R. DePenning, M. Turner, and S. Padalkar, "Effect of citrate ratio and temperature on gold nanoparticle size and morphology," *Materials Research Express*, vol. 3, p. 105027, 2016/10/12 2016.

[285] N. G. Bastús, F. Merkoçi, J. Piella, and V. Puntes, "Synthesis of Highly Monodisperse Citrate-Stabilized Silver Nanoparticles of up to 200 nm: Kinetic Control and Catalytic Properties," *Chemistry of Materials*, vol. 26, pp. 2836-2846, 2014/05/13 2014.

[286] U. Aslam, S. Chavez, and S. Linic, "Controlling energy flow in multimetallic nanostructures for plasmonic catalysis," *Nature Nanotechnology*, vol. 12, p. 1000, 07/17/online 2017.

[287] H. Tong, S. X. Ouyang, Y. P. Bi, N. Umezawa, M. Oshikiri, and J. H. Ye, "Nano-photocatalytic Materials: Possibilities and Challenges," *Advanced Materials*, vol. 24, pp. 229-251, Jan 2012.

[288] Q. Z. Zhang, X. Jin, Z. H. Xu, J. M. Zhang, U. F. Rendon, L. Razzari, *et al.*, "Plasmonic Au-Loaded Hierarchical Hollow Porous TiO2 Spheres: Synergistic Catalysts for Nitroaromatic Reduction," *Journal of Physical Chemistry Letters*, vol. 9, pp. 5317-5326, Sep 2018.

[289] H. Ditlbacher, J. R. Krenn, B. Lamprecht, A. Leitner, and F. R. Aussenegg, "Spectrally coded optical data storage by metal nanoparticles," *Optics Letters*, vol. 25, pp. 563-565, 2000/04/15 2000.

[290] H. W. Liao, C. L. Nehl, and J. H. Hafner, "Biomedical applications of plasmon resonant metal nanoparticles," *Nanomedicine*, vol. 1, pp. 201-208, Aug 2006.

[291] N. J. Halas, S. Lal, W.-S. Chang, S. Link, and P. Nordlander, "Plasmons in Strongly Coupled Metallic Nanostructures," *Chemical Reviews*, vol. 111, pp. 3913-3961, 2011/06/08 2011.

[292] N. G. Khlebtsov and L. A. Dykman, "Optical properties and biomedical applications of plasmonic nanoparticles," *Journal of Quantitative Spectroscopy & Radiative Transfer,* vol. 111, pp. 1-35, Jan 2010.

[293] W. Q. Zhu and K. B. Crozier, "Quantum mechanical limit to plasmonic enhancement as observed by surface-enhanced Raman scattering," *Nature Communications,* vol. 5, Oct 2014.

[294] X. Huang, W. Qian, I. H. El-Sayed, and M. A. El-Sayed, "The potential use of the enhanced nonlinear properties of gold nanospheres in photothermal cancer therapy," *Lasers in Surgery and Medicine,* vol. 39, pp. 747-753, Oct 2007.

[295] R. C. Jin, "Atomically precise metal nanoclusters: stable sizes and optical properties," *Nanoscale,* vol. 7, pp. 1549-1565, 2015.

[296] X. Sun, L. Huang, R. Zhang, W. Xu, J. Huang, D. D. Gurav, *et al.*, "Metabolic Fingerprinting on a Plasmonic Gold Chip for Mass Spectrometry Based in Vitro Diagnostics," *ACS Central Science,* vol. 4, pp. 223-229, 2018/02/28 2018.

[297] X. H. Huang, S. Neretina, and M. A. El-Sayed, "Gold Nanorods: From Synthesis and Properties to Biological and Biomedical Applications," *Advanced Materials,* vol. 21, pp. 4880-4910, Dec 2009.

[298] A. J. Mieszawska, W. J. M. Mulder, Z. A. Fayad, and D. P. Cormode, "Multifunctional Gold Nanoparticles for Diagnosis and Therapy of Disease," *Molecular Pharmaceutics,* vol. 10, pp. 831-847, Mar 2013.

[299] L. Huang, J. Wan, X. Wei, Y. Liu, J. Huang, X. Sun, *et al.*, "Plasmonic silver nanoshells for drug and metabolite detection," *Nature Communications,* vol. 8, p. 220, 2017/08/09 2017.

[300] N. G. Khlebtsov and L. A. Dykman, "Optical properties and biomedical applications of plasmonic nanoparticles," *Journal of Quantitative Spectroscopy and Radiative Transfer,* vol. 111, pp. 1-35, 2010/01/01/ 2010.

[301] P. K. Jain, K. S. Lee, I. H. El-Sayed, and M. A. El-Sayed, "Calculated Absorption and Scattering Properties of Gold Nanoparticles of Different Size, Shape, and Composition: Applications in Biological Imaging and Biomedicine," *The Journal of Physical Chemistry B,* vol. 110, pp. 7238-7248, 2006/04/01 2006.

[302] B. Sepulveda, P. C. Angelome, L. M. Lechuga, and L. M. Liz-Marzan, "LSPR-based nanobiosensors," *Nano Today,* vol. 4, pp. 244-251, Jun 2009.

[303] Y. Park, C. Depeursinge, and G. Popescu, "Quantitative phase imaging in biomedicine," *Nature Photonics,* vol. 12, pp. 578-589, 2018/10/01 2018.

[304] J. A. Webb and R. Bardhan, "Emerging advances in nanomedicine with engineered gold nanostructures," *Nanoscale,* vol. 6, pp. 2502-2530, 2014.

[305] W. Chen, S. Zhang, Y. Yu, H. Zhang, and Q. He, "Structural-Engineering Rationales of Gold Nanoparticles for Cancer Theranostics," *Advanced Materials,* vol. 28, pp. 8567-8585, 2016.

[306] M. Qi, C. Darviot, S. Patskovsky, and M. Meunier, "Cost-effective side-illumination darkfield nanoplasmonic marker microscopy," *Analyst,* 2019.

[307] A. Madabhushi and G. Lee, "Image analysis and machine learning in digital pathology: Challenges and opportunities," *Medical Image Analysis,* vol. 33, pp. 170-175, 2016/10/01/ 2016.

[308] N. G. Bastús, F. Merkoçi, J. Piella, and V. Puntes, "Synthesis of highly monodisperse citrate-stabilized silver nanoparticles of up to 200 nm: kinetic control and catalytic properties," *Chemistry of Materials,* vol. 26, pp. 2836-2846, 2014.

[309] R. Baber, L. Mazzei, N. T. K. Thanh, and A. Gavriilidis, "An engineering approach to synthesis of gold and silver nanoparticles by controlling hydrodynamics and mixing based on a coaxial flow reactor," *Nanoscale,* vol. 9, pp. 14149-14161, 2017.

[310] G. Doria, J. Conde, B. Veigas, L. Giestas, C. Almeida, M. Assuncao, *et al.*, "Noble Metal Nanoparticles for Biosensing Applications," *Sensors,* vol. 12, pp. 1657-1687, Feb 2012.

[311] T. L. Doane and C. Burda, "The unique role of nanoparticles in nanomedicine: imaging, drug delivery and therapy," *Chemical Society Reviews,* vol. 41, pp. 2885-2911, 2012.

[312] S. Zhang, J. Li, G. Lykotrafitis, G. Bao, and S. Suresh, "Size-Dependent Endocytosis of Nanoparticles," *Advanced Materials,* vol. 21, pp. 419-424, 2009.

[313] R. Garcia-Alvarez, M. Hadjidemetriou, A. Sanchez-Iglesias, L. M. Liz-Marzan, and K. Kostarelos, "In vivo formation of protein corona on gold nanoparticles. The effect of their size and shape," *Nanoscale,* vol. 10, pp. 1256-1264, Jan 2018.

[314] C. Gao, Y. Hu, M. Wang, M. Chi, and Y. Yin, "Fully Alloyed Ag/Au Nanospheres: Combining the Plasmonic Property of Ag with the Stability of Au," *Journal of the American Chemical Society,* vol. 136, pp. 7474-7479, 2014/05/21 2014.

[315] P. K. Jain, N. Sobh, J. Smith, A. N. Sobh, S. White, J. Faucheaux, *et al.*, "nanoDDSCAT," ed, 2014.

[316] A. Rose, "The Sensitivity Performance of the Human Eye on an Absolute Scale*," *Journal of the Optical Society of America,* vol. 38, pp. 196-208, 1948/02/01 1948.

[317] H. S. Jung, J. Han, H. Shi, S. Koo, H. Singh, H.-J. Kim, *et al.*, "Overcoming the Limits of Hypoxia in Photodynamic Therapy: A Carbonic Anhydrase IX-Targeted Approach," *Journal of the American Chemical Society,* vol. 139, pp. 7595-7602, 2017/06/07 2017.

[318] M. Milczarek, K. Wiktorska, L. Mielczarek, M. Koronkiewicz, A. Dąbrowska, K. Lubelska, *et al.*, "Autophagic cell death and premature senescence: New mechanism of 5-fluorouracil and sulforaphane synergistic anticancer effect in MDA-MB-231 triple negative breast cancer cell line," *Food and Chemical Toxicology,* vol. 111, pp. 1-8, 2018/01/01/ 2018.

[319] T. Smith and J. Guild, "The C.I.E. colorimetric standards and their use," *Transactions of the Optical Society,* vol. 33, pp. 73-134, 1931/01/01 1931.

[320] S. Monti, G. Barcaro, L. Sementa, V. Carravetta, and H. Ågren, "Dynamics and self-assembly of bio-functionalized gold nanoparticles in solution: Reactive molecular dynamics simulations," *Nano Research,* vol. 11, pp. 1757-1767, April 01 2018.

[321] J. N. Anker, W. P. Hall, O. Lyandres, N. C. Shah, J. Zhao, and R. P. Van Duyne, "Biosensing with plasmonic nanosensors," *Nature Materials,* vol. 7, pp. 442-453, Jun 2008.

[322] M. Hu, J. Y. Chen, Z. Y. Li, L. Au, G. V. Hartland, X. D. Li, *et al.*, "Gold nanostructures: engineering their plasmonic properties for biomedical applications," *Chemical Society Reviews*, vol. 35, pp. 1084-1094, 2006.

[323] J. Wang, J. Sun, Y. Wang, T. Chou, Q. Zhang, B. Zhang, *et al.*, "Gold Nanoframeworks with Mesopores for Raman–Photoacoustic Imaging and Photo-Chemo Tumor Therapy in the Second Near-Infrared Biowindow," *Advanced Functional Materials*, vol. 30, p. 1908825, 2020.

[324] A. N. Koya, X. Zhu, N. Ohannesian, A. A. Yanik, A. Alabastri, R. Proietti Zaccaria, *et al.*, "Nanoporous Metals: From Plasmonic Properties to Applications in Enhanced Spectroscopy and Photocatalysis," *ACS Nano*, vol. 15, pp. 6038-6060, 2021/04/27 2021.

[325] W. J. Lee, E. Y. Park, D. Choi, D. Lee, J. Koo, J. G. Min, *et al.*, "Colloidal Porous AuAg Alloyed Nanoparticles for Enhanced Photoacoustic Imaging," *ACS Appl Mater Interfaces*, vol. 12, pp. 32270-32277, Jul 22 2020.

[326] K. Liu, Y. Bai, L. Zhang, Z. Yang, Q. Fan, H. Zheng, *et al.*, "Porous Au–Ag Nanospheres with High-Density and Highly Accessible Hotspots for SERS Analysis," *Nano Letters*, vol. 16, pp. 3675-3681, 2016/06/08 2016.

[327] M. F. Cardinal, E. V. Ende, R. A. Hackler, M. O. McAnally, P. C. Stair, G. C. Schatz, *et al.*, "Expanding applications of SERS through versatile nanomaterials engineering," *Chemical Society Reviews*, vol. 46, pp. 3886-3903, Jul 2017.

[328] T. Vo-Dinh, H. N. Wang, and J. Scaffidi, "Plasmonic nanoprobes for SERS biosensing and bioimaging," *Journal of Biophotonics*, vol. 3, pp. 89-102, Jan 2010.

[329] J. Langer, D. Jimenez de Aberasturi, J. Aizpurua, R. A. Alvarez-Puebla, B. Auguié, J. J. Baumberg, *et al.*, "Present and Future of Surface-Enhanced Raman Scattering," *ACS Nano*, vol. 14, pp. 28-117, 2020/01/28 2020.

[330] Y. Huang, W. Liu, Z. Gong, W. Wu, M. Fan, D. Wang, *et al.*, "Detection of Buried Explosives Using a Surface-Enhanced Raman Scattering (SERS) Substrate Tailored for Miniaturized Spectrometers," *ACS Sensors*, vol. 5, pp. 2933-2939, 2020/09/25 2020.

[331] Y. Q. Zhang, Y. Q. Gu, J. He, B. D. Thackray, and J. Ye, "Ultrabright gap-enhanced Raman tags for high-speed bioimaging," *Nature Communications*, vol. 10, Aug 29 2019.

[332] W.-J. Kim, S. Kim, A. R. Kim, and D. J. Yoo, "Direct Detection System for Escherichia coli Using Au–Ag Alloy Microchips," *Industrial & Engineering Chemistry Research*, vol. 52, pp. 7282-7288, 2013/06/05 2013.

[333] K. Aubertin, J. Desroches, M. Jermyn, V. Q. Trinh, F. Saad, D. Trudel, *et al.*, "Combining high wavenumber and fingerprint Raman spectroscopy for the detection of prostate cancer during radical prostatectomy," *Biomedical Optics Express*, vol. 9, pp. 4294-4305, Sep 1 2018.

[334] K. Dardir, H. Wang, B. E. Martin, M. Atzampou, C. B. Brooke, and L. Fabris, "SERS Nanoprobe for Intracellular Monitoring of Viral Mutations," *Journal of Physical Chemistry C*, vol. 124, pp. 3211-3217, Feb 6 2020.

[335] J. Kim, K. Sim, S. Cha, J.-W. Oh, and J.-M. Nam, "Single-Particle Analysis on Plasmonic Nanogap Systems for Quantitative SERS," *Journal of Raman Spectroscopy,* vol. 52, pp. 375-385, 2021.

[336] J. Ma, W. Liu, Z. Ma, P. Song, Y. Zhao, F. Yang, *et al.*, "Rapidly fabricating a large area nanotip microstructure for high-sensitivity SERS applications," *Nanoscale,* vol. 11, pp. 20194-20198, 2019.

[337] N. C. Lindquist and A. G. Brolo, "Ultra-High-Speed Dynamics in Surface-Enhanced Raman Scattering," *The Journal of Physical Chemistry C,* vol. 125, pp. 7523-7532, 2021/04/15 2021.

[338] P. Dey, T. A. Tabish, S. Mosca, F. Palombo, P. Matousek, and N. Stone, "Plasmonic Nanoassemblies: Tentacles Beat Satellites for Boosting Broadband NIR Plasmon Coupling Providing a Novel Candidate for SERS and Photothermal Therapy," *Small,* vol. 16, p. 1906780, 2020.

[339] Y. Sun, B. T. Mayers, and Y. Xia, "Template-Engaged Replacement Reaction: A One-Step Approach to the Large-Scale Synthesis of Metal Nanostructures with Hollow Interiors," *Nano Letters,* vol. 2, pp. 481-485, 2002/05/01 2002.

[340] K. D. Gilroy, A. Ruditskiy, H. C. Peng, D. Qin, and Y. N. Xia, "Bimetallic Nanocrystals: Syntheses, Properties, and Applications," *Chemical Reviews,* vol. 116, pp. 10414-10472, Sep 2016.

[341] S. E. Skrabalak, J. Y. Chen, Y. G. Sun, X. M. Lu, L. Au, C. M. Cobley, *et al.*, "Gold Nanocages: Synthesis, Properties, and Applications," *Accounts of Chemical Research,* vol. 41, pp. 1587-1595, Dec 2008.

[342] S. E. Skrabalak, L. Au, X. D. Li, and Y. N. Xia, "Facile synthesis of Ag nanocubes and Au nanocages," *Nature Protocols,* vol. 2, pp. 2182-2190, 2007.

[343] J. G. Smith, Q. Yang, and P. K. Jain, "Identification of a Critical Intermediate in Galvanic Exchange Reactions by Single-Nanoparticle-Resolved Kinetics," *Angewandte Chemie International Edition,* vol. 53, pp. 2867-2872, 2014.

[344] J. G. Smith, X. Zhang, and P. K. Jain, "Galvanic reactions at the single-nanoparticle level: tuning between mechanistic extremes," *Journal of Materials Chemistry A,* vol. 5, pp. 11940-11948, 2017.

[345] H. Liu, K. Liu, P. Zhong, J. Qi, J. Bian, Q. Fan, *et al.*, "Ultrathin Pt–Ag Alloy Nanotubes with Regular Nanopores for Enhanced Electrocatalytic Activity," *Chemistry of Materials,* vol. 30, pp. 7744-7751, 2018/11/13 2018.

[346] T. Zheng, G. G. Li, F. Zhou, R. Wu, J.-J. Zhu, and H. Wang, "Gold-Nanosponge-Based Multistimuli-Responsive Drug Vehicles for Targeted Chemo-Photothermal Therapy," *Advanced Materials,* vol. 28, pp. 8218-8226, 2016.

[347] C. Zhu, D. Du, A. Eychmüller, and Y. Lin, "Engineering Ordered and Nonordered Porous Noble Metal Nanostructures: Synthesis, Assembly, and Their Applications in Electrochemistry," *Chemical Reviews,* vol. 115, pp. 8896-8943, 2015/08/26 2015.

[348] S. W. Chee, Z. M. Wong, Z. Baraissov, S. F. Tan, T. L. Tan, and U. Mirsaidov, "Interface-mediated Kirkendall effect and nanoscale void migration in bimetallic nanoparticles during interdiffusion," *Nature Communications,* vol. 10, p. 2831, 2019/06/27 2019.

[349] H. Wang and N. J. Halas, "Mesoscopic Au “Meatball” Particles," *Advanced Materials,* vol. 20, pp. 820-825, 2008.

[350] D. Wang and P. Schaaf, "Nanoporous gold nanoparticles," *Journal of Materials Chemistry,* vol. 22, pp. 5344-5348, 2012.

[351] Y.-c. K. Chen-Wiegart, R. Harder, D. C. Dunand, and I. McNulty, "Evolution of dealloying induced strain in nanoporous gold crystals," *Nanoscale,* vol. 9, pp. 5686-5693, 2017.

[352] P. Dey, S. Zhu, K. J. Thurecht, P. M. Fredericks, and I. Blakey, "Self assembly of plasmonic core–satellite nano-assemblies mediated by hyperbranched polymer linkers," *Journal of Materials Chemistry B,* vol. 2, pp. 2827-2837, 2014.

[353] Y. Sun and Y. Xia, "Alloying and Dealloying Processes Involved in the Preparation of Metal Nanoshells through a Galvanic Replacement Reaction," *Nano Letters,* vol. 3, pp. 1569-1572, 2003/11/01 2003.

[354] M. Hu, H. Petrova, A. R. Sekkinen, J. Chen, J. M. McLellan, Z.-Y. Li, *et al.*, "Optical Properties of Au−Ag Nanoboxes Studied by Single Nanoparticle Spectroscopy," *The Journal of Physical Chemistry B,* vol. 110, pp. 19923-19928, 2006/10/01 2006.

[355] K. Sieradzki, N. Dimitrov, D. Movrin, C. McCall, N. Vasiljevic, and J. Erlebacher, "The Dealloying Critical Potential," *Journal of The Electrochemical Society,* vol. 149, p. B370, 2002.

[356] J. Erlebacher, "An Atomistic Description of Dealloying," *Journal of The Electrochemical Society,* vol. 151, p. C614, 2004.

[357] L. Burr, I. Schubert, W. Sigle, C. Trautmann, and M. E. Toimil-Molares, "Surface Enrichment in Au–Ag Alloy Nanowires and Investigation of the Dealloying Process," *The Journal of Physical Chemistry C,* vol. 119, pp. 20949-20956, 2015/09/10 2015.

[358] G. G. Li and H. Wang, "Dealloyed Nanoporous Gold Catalysts: From Macroscopic Foams to Nanoparticulate Architectures," *ChemNanoMat,* vol. 4, pp. 897-908, 2018.

[359] D. Artymowicz, R. Newman, and J. Erlebacher, "Insights into the Parting Limit for De-Alloying from Reconsideration of Atomistic Considerations," *ECS Transactions,* vol. 3, pp. 499-506, 2019/12/21 2019.

[360] J. Erlebacher, M. J. Aziz, A. Karma, N. Dimitrov, and K. Sieradzki, "Evolution of nanoporosity in dealloying," *Nature,* vol. 410, pp. 450-453, 2001/03/01 2001.

[361] X. Sun, J. Kim, K. D. Gilroy, J. Liu, T. A. F. König, and D. Qin, "Gold-Based Cubic Nanoboxes with Well-Defined Openings at the Corners and Ultrathin Walls Less Than Two Nanometers Thick," *ACS Nano,* vol. 10, pp. 8019-8025, 2016/08/23 2016.

[362] L. Russo, F. Merkoçi, J. Patarroyo, J. Piella, A. Merkoçi, N. G. Bastús, *et al.*, "Time- and Size-Resolved Plasmonic Evolution with nm Resolution of Galvanic Replacement Reaction in AuAg Nanoshells Synthesis," *Chemistry of Materials,* vol. 30, pp. 5098-5107, 2018/08/14 2018.

[363] J. G. Smith, I. Chakraborty, and P. K. Jain, "In Situ Single-Nanoparticle Spectroscopy Study of Bimetallic Nanostructure Formation," *Angewandte Chemie International Edition,* vol. 55, pp. 9979-9983, 2016.

[364] Y. Jiang, L. Wang, M. Meunier, and U. Mirsaidov, "Formation Pathways of Porous Alloy Nanoparticles through Selective Chemical and Electrochemical Etching," *Small,* vol. 17, p. 2006953, 2021.

[365] V. Vongsavat, B. M. Vittur, W. W. Bryan, J.-H. Kim, and T. R. Lee, "Ultrasmall Hollow Gold–Silver Nanoshells with Extinctions Strongly Red-Shifted to the Near-Infrared," *ACS Applied Materials & Interfaces,* vol. 3, pp. 3616-3624, 2011/09/28 2011.

[366] A. Genç, J. Patarroyo, J. Sancho-Parramon, R. Arenal, M. Duchamp, E. E. Gonzalez, *et al.*, "Tuning the Plasmonic Response up: Hollow Cuboid Metal Nanostructures," *ACS Photonics,* vol. 3, pp. 770-779, 2016/05/18 2016.

[367] B. Chen, G. Meng, Q. Huang, Z. Huang, Q. Xu, C. Zhu, *et al.*, "Green Synthesis of Large-Scale Highly Ordered Core@Shell Nanoporous Au@Ag Nanorod Arrays as Sensitive and Reproducible 3D SERS Substrates," *ACS Applied Materials & Interfaces,* vol. 6, pp. 15667-15675, 2014/09/24 2014.

[368] M. J. Mulvihill, X. Y. Ling, J. Henzie, and P. Yang, "Anisotropic Etching of Silver Nanoparticles for Plasmonic Structures Capable of Single-Particle SERS," *Journal of the American Chemical Society,* vol. 132, pp. 268-274, 2010/01/13 2010.

[369] T. Zhang, Y. Sun, L. Hang, H. Li, G. Liu, X. Zhang, *et al.*, "Periodic Porous Alloyed Au–Ag Nanosphere Arrays and Their Highly Sensitive SERS Performance with Good Reproducibility and High Density of Hotspots," *ACS Applied Materials & Interfaces,* vol. 10, pp. 9792-9801, 2018/03/21 2018.

[370] Z. Farhane, F. Bonnier, A. Casey, and H. J. Byrne, "Raman micro spectroscopy for in vitro drug screening: subcellular localisation and interactions of doxorubicin," *Analyst,* vol. 140, pp. 4212-4223, 2015.

[371] H. Cao, Y. Yang, X. Chen, and Z. Shao, "Intelligent Janus nanoparticles for intracellular real-time monitoring of dual drug release," *Nanoscale,* vol. 8, pp. 6754-6760, 2016.

[372] N. Strekal, A. German, G. Gachko, A. Maskevich, and S. Maskevich, "The study of the doxorubicin adsorbed onto chemically modified silver films by surface-enhanced spectroscopy," *Journal of Molecular Structure,* vol. 563-564, pp. 183-191, 2001/05/28/ 2001.

[373] T. Y. Olson, A. M. Schwartzberg, C. A. Orme, C. E. Talley, B. O'Connell, and J. Z. Zhang, "Hollow Gold−Silver Double-Shell Nanospheres: Structure, Optical Absorption, and Surface-Enhanced Raman Scattering," *The Journal of Physical Chemistry C,* vol. 112, pp. 6319-6329, 2008/04/01 2008.

[374] P. Singh, T. A. F. König, and A. Jaiswal, "NIR-Active Plasmonic Gold Nanocapsules Synthesized Using Thermally Induced Seed Twinning for Surface-Enhanced Raman Scattering Applications," *ACS Applied Materials & Interfaces,* vol. 10, pp. 39380-39390, 2018/11/14 2018.

[375] H. Chang, Y. Y. Lee, H. E. Lee, H.-Y. Ahn, E. Ko, K. T. Nam, *et al.*, "Size-controllable and uniform gold bumpy nanocubes for single-particle-level surface-enhanced Raman scattering sensitivity," *Physical Chemistry Chemical Physics*, vol. 21, pp. 9044-9051, 2019.

[376] S. Suarasan, M. Focsan, M. Potara, O. Soritau, A. Florea, D. Maniu, *et al.*, "Doxorubicin-Incorporated Nanotherapeutic Delivery System Based on Gelatin-Coated Gold Nanoparticles: Formulation, Drug Release, and Multimodal Imaging of Cellular Internalization," *ACS Applied Materials & Interfaces*, vol. 8, pp. 22900-22913, 2016/09/07 2016.

[377] J. You, G. Zhang, and C. Li, "Exceptionally High Payload of Doxorubicin in Hollow Gold Nanospheres for Near-Infrared Light-Triggered Drug Release," *ACS Nano*, vol. 4, pp. 1033-1041, 2010/02/23 2010.

[378] E. Aznar, M. D. Marcos, R. Martínez-Máñez, F. Sancenón, J. Soto, P. Amorós, *et al.*, "pH- and Photo-Switched Release of Guest Molecules from Mesoporous Silica Supports," *Journal of the American Chemical Society*, vol. 131, pp. 6833-6843, 2009/05/20 2009.

[379] T. Higuchi, "Rate of Release of Medicaments from Ointment Bases Containing Drugs in Suspension," *Journal of Pharmaceutical Sciences*, vol. 50, pp. 874-875, 1961/10/01/ 1961.

[380] W. I. Higuchi, "Analysis of Data on the Medicament Release from Ointments," *Journal of Pharmaceutical Sciences*, vol. 51, pp. 802-804, 1962/08/01/ 1962.

[381] M. Otsuka, H. Nakagawa, A. Ito, and W. I. Higuchi, "Effect of geometrical structure on drug release rate of a three-dimensionally perforated porous apatite/collagen composite cement," *Journal of Pharmaceutical Sciences*, vol. 99, pp. 286-292, 2010.

[382] G. Baffou, *Thermoplasmonics: Heating Metal Nanoparticles Using Light*. Cambridge: Cambridge University Press, 2017.

[383] J. H. Beijnen, O. A. G. J. van der Houwen, and W. J. M. Underberg, "Aspects of the degradation kinetics of doxorubicin in aqueous solution," *International Journal of Pharmaceutics*, vol. 32, pp. 123-131, 1986/10/01/ 1986.

[384] Q. Zhang, C. M. Cobley, J. Zeng, L.-P. Wen, J. Chen, and Y. Xia, "Dissolving Ag from Au−Ag Alloy Nanoboxes with H2O2: A Method for Both Tailoring the Optical Properties and Measuring the H2O2 Concentration," *The Journal of Physical Chemistry C*, vol. 114, pp. 6396-6400, 2010/04/15 2010.

[385] X. Gu, L. Xu, F. Tian, and Y. Ding, "Au-Ag alloy nanoporous nanotubes," *Nano Research*, vol. 2, pp. 386-393, 2009/05/01 2009.

[386] D. Cialla-May, X. S. Zheng, K. Weber, and J. Popp, "Recent progress in surface-enhanced Raman spectroscopy for biological and biomedical applications: from cells to clinics," *Chemical Society Reviews*, vol. 46, pp. 3945-3961, 2017.

[387] T. Fujita, P. Guan, K. McKenna, X. Lang, A. Hirata, L. Zhang, *et al.*, "Atomic origins of the high catalytic activity of nanoporous gold," *Nature Materials*, vol. 11, pp. 775-780, 2012/09/01 2012.

[388] C. Eliasson, A. Lorén, K. V. G. K. Murty, M. Josefson, M. Käll, J. Abrahamsson, *et al.*, "Multivariate evaluation of doxorubicin surface-enhanced Raman spectra," *Spectrochimica*

Acta Part A: Molecular and Biomolecular Spectroscopy, vol. 57, pp. 1907-1915, 2001/08/01/ 2001.

APPENDIX A POROUS AU-AG NANOPARTICLES FROM GALVANIC REPLACEMENT APPLIED AS SINGLE-PARTICLE SERS PROBE FOR QUANTITATIVE MONITORING: SUPPORTING INFORMATION

This appendix presents the supporting information for the article transcribed in Chapter 5. It contains some additional figures and tables demonstrating the structure of the Au-Ag porous nanoparticles and the characterization results of dealloyed Au-Ag NPs. It also contains information on the simulation results of field enhancement of Au NP, and the geometry for porous structure field simulation as well as the calculation result of optical cross section of porous NP.

Theoretical electron transmission in scanning transmission electron microscopy

For elemental mapping of porous nanoshell, the theoretical transmission path is expressed as:

$$transmission\ path = \ 2\sqrt{R_{shell}^2 - x^2} - \ 2\sqrt{R_{core}^2 - x^2} \quad for\ \ |x| < R_{core}$$

$$= 2\ \sqrt{R_{shell}^2 - x^2}\ \ for\ \ R_{core} \leq |x| < R_{shell} \qquad \text{(S1)}$$

where x is the distance from the center of nanoshell (see Figure A. 1a). With known dimensions of hollow core and porous shell, the electron transmission path or the intensity of EDS can be easily simulated and is shown in Figure A.1b.

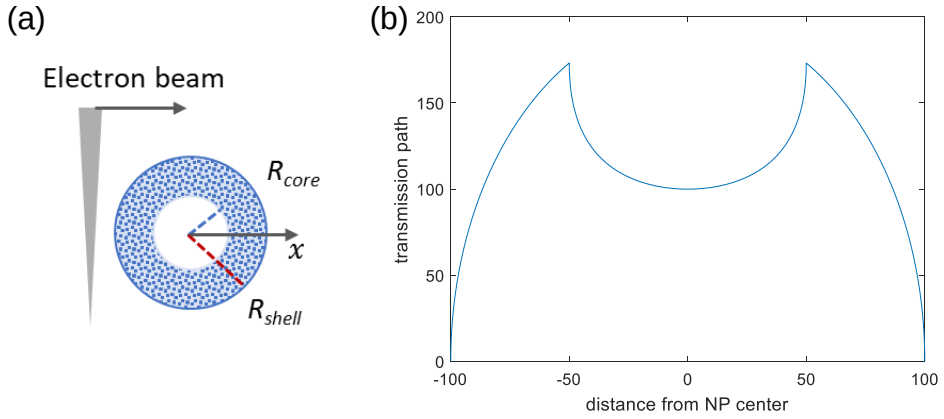

Figure A.1 Schematics (a) and theoretical plot (b) of transmission path in elemental mapping for nanoshell.

The general trend of line plot (Figure 6.3h) from measurement in STEM is very similar with the theoretical transmission path, thus confirming the presence of the hollow interior geometry.

Schematics of NPs for porosity calculation

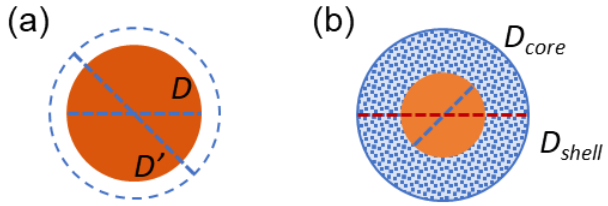

Figure A.2 Schematics of (a) the diameter of NPs before (D) and after (D') GRR with size expanding, and (b) the diameter of core (Dcore) and shell (Dshell) after GRR.

Additional results of low-resolution of porous NPs

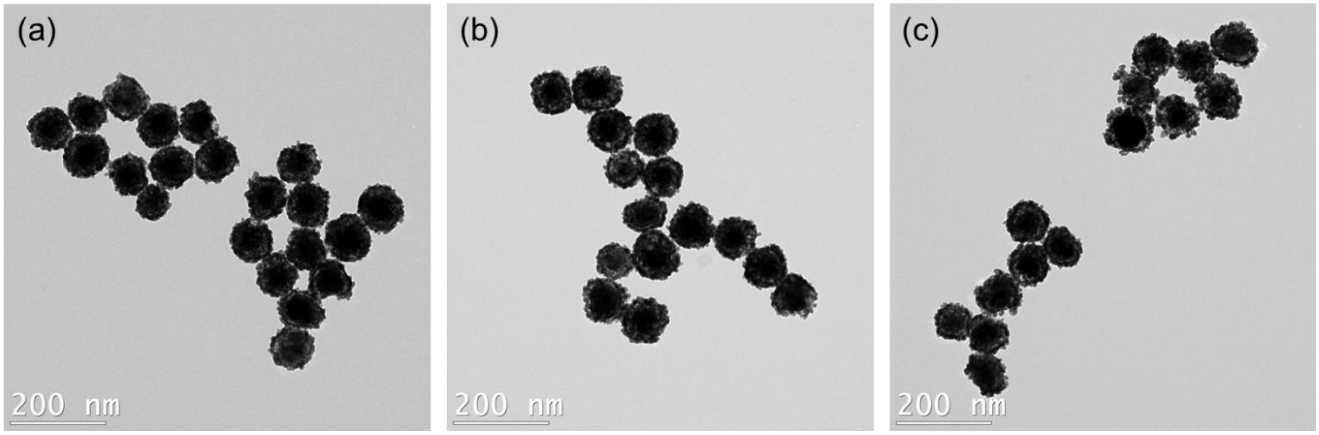

Figure A.3 Low-resolution TEM image of porous NPs dealloyed from Au@Au/Ag 10/90 NP-precursors with dealloying degree (dD) of (a) 0.75, (b) 1.0 and (c) 1.5, respectively.

Additional results of porous NPs for various d_D

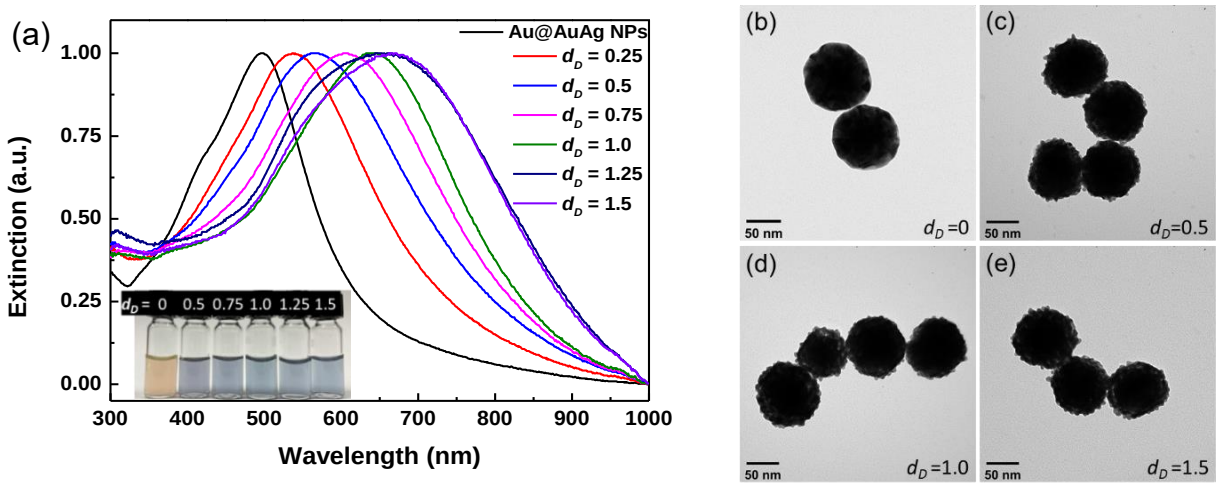

Figure A.4 (a) Extinction spectra and (b-e) TEM image of Au@Au/Ag 25/75 precursor and porous NPs after GRR with dealloying degree (d_D) of 0.5, 1.0 and 1.5, respectively.

Statistics of porous NP and porous nanoshells

Table A.1 Diameter of solid core (d_{core}) and exterior shell (D_{shell}) from Au@Au/Ag 10/90 precursor and the NPs at dealloying degree (d_D) of 0.5, 0.75, 1.0 and 1.5. Data are obtained by analysing 50 porous NPs.

Dealloying degree	**d_{core}/D_{shell}**	**Au/Ag at.%**	**Overall porosity**	**Porosity in shell**
0	90	16/84	/	/
0.5	78/91	41/59	29%	80 %
0.75	59/93	48/52	39 %	52 %
1.0	58/96	52/48	48 %	58 %
1.5	49/96	52/48	46 %	53 %

Table A.2 Diameter of hollow core (d_{core}) and exterior shell (D_{shell}) from Ag@Au/Ag 25/75 precursor and the NPs at dealloying degree (d_D) of 0.5, 1.0 and 1.5. Data are obtained by analysing 50 porous NPs.

Dealloying degree	d_{core} (nm)	D_{shell} (nm)	Au/Ag at.%	Overall porosity
0	70±4	102±8	13/87	/
0.5	/	113±13	29/71	42 %
1.0	51±7	110±7	54/46	52 %
1.5	57±9	120±11	56/44	64 %

Real-time dealloying single-particle characterization

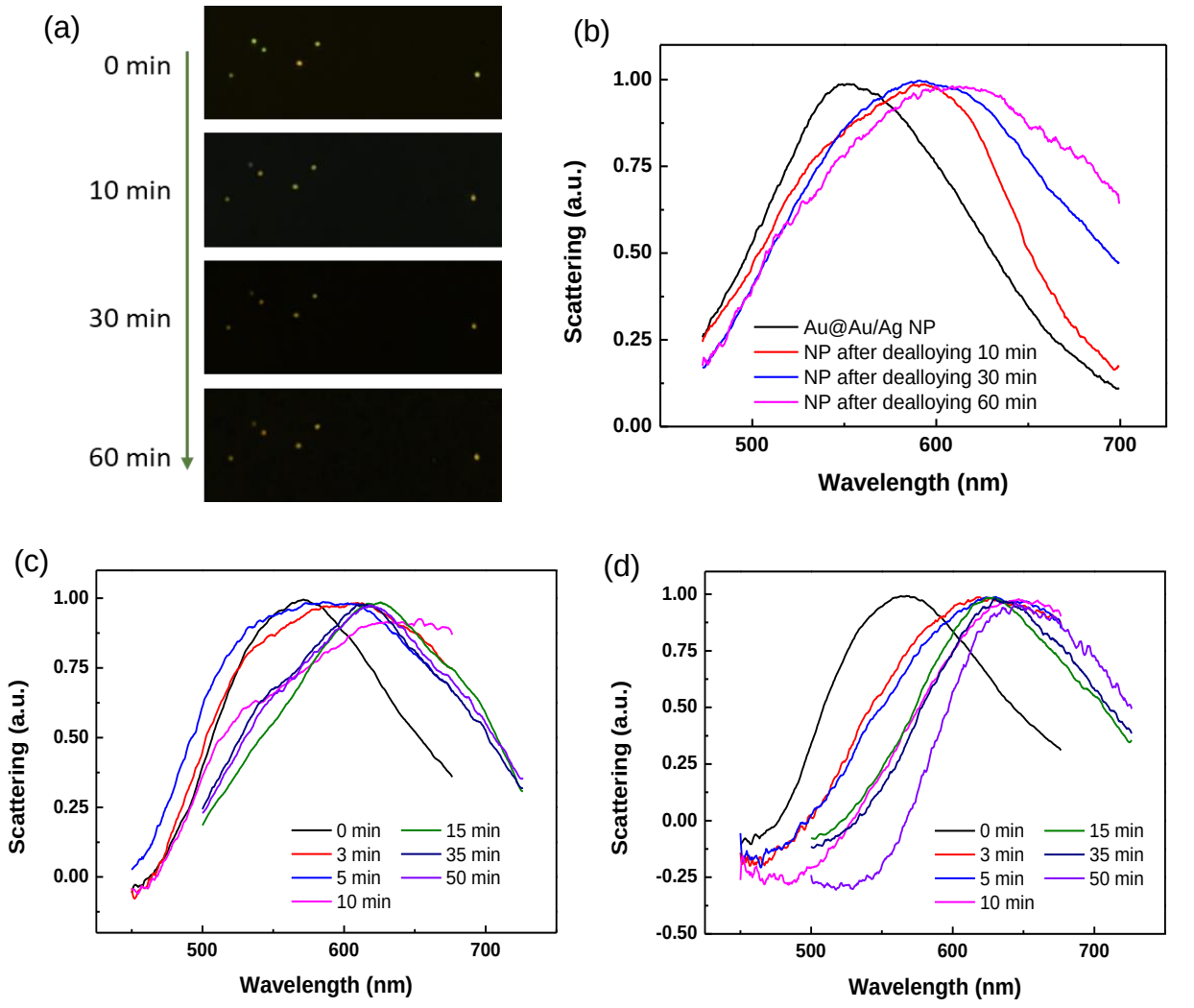

Figure A.5 (a) Images of Au@Au/Ag 25/75 NPs scattering and (b-d) real-time monitoring the dealloying of three different NPs scattering spectra during 1h.

Raman spectra analysis

Table A.3 Raman bands in SERS spectra of DOX.

Raman shift (cm^{-1})	Assignment[371, 372, 388]
436	δ (C=O)
465	δ (C=O)
990	Ring breath
1207	δ (O-H)
1244	δ (O-H)
1304	ν(C-O)
1413	Ring stretch
1553	ν(C=N)
1574	Ring stretch
1657	ν(C=N)

Field enhancement of 100 nm AuNP

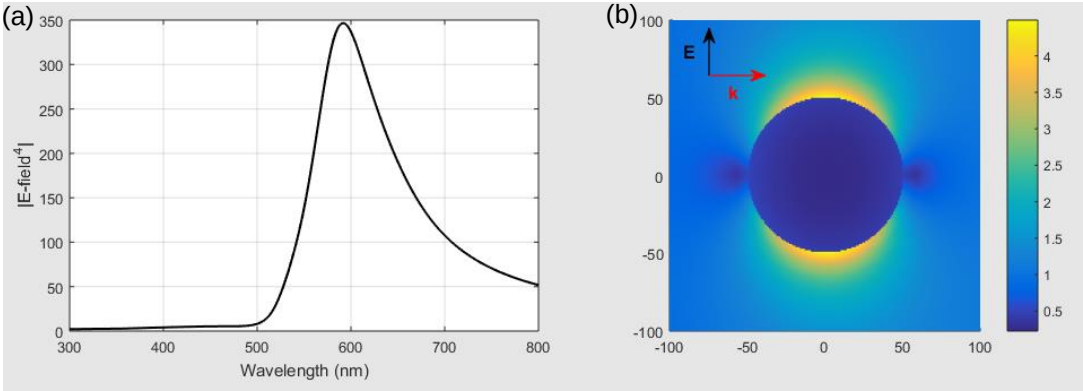

Figure A.6 (a) The electric-field enhancement calculation of 100 nm AuNP and (b) the field enhancement at 633 nm from NFMie program.[128] At the irradiation wavelength of 633 nm, the Raman enhancement factor $E^4 = 225$.

Reported single-particle Raman enhancement effect

Table A.4 Raman enhancement improvement compared with Au NPs.

Nanostructure of SERS substrate	Raman enhancement over Au NPs	Reference
Porous AuAg@void@SiO2 yolk/shell nanostructures	17-20-fold over AuNP	[326]
Hollow gold-silver double-shell nanospheres	4-5-fold over hollow AuNPs	[373]
Au-beads@Ag nanorods	11 times over Au-bead nanoparticles	[374]
gold bumpy nanocubes	15-18-fold over Au nanocubes	[375]

Raman enhancement factor calculation

The enhancement factor of a single porous particle can be also estimated by comparing with the Raman measurement from 1mM DOX solution, with the following calculation:

$$EF = \frac{I(single\ particle)/N(single\ particle)}{I(solution)/N(solution)} \qquad \text{(S2)}$$

where *I* stand for Raman intensity and *N* for the number of Raman reporter molecules (DOX). Raman signal *I*(single particle) from a single porous NP was 555 counts/s at laser intensity of $7.7*10^4$ W/cm^2. Raman signal from solution was measured using a 40x air objective, with a laser intensity of $1.53*10^5$ W/cm^2. The *I*(solution) was 134 counts/s, corresponding to 67 counts/s at intensity of $7.7*10^4$ W/cm^2.

According to the drug loading results, each porous NP is loaded with *N*(single particle) = $2.4*10^6$. To estimate the number of DOX in solution with a concentration of 10^{-3} mol/L, the interaction with the laser beam was simplified as molecules in a cylinder with cross section of the spot size of diameter 487 nm, and a lenght of 1cm. Therefore, the molecules numbers are estimated with the equation:

$$N(solution) = N_A \times C(DOX) \times V(solution)$$

$$= 6.02 \times 10^{23} mol^{-1} \times 1 \times 10^{-3} mol/L \times \left(\pi \left(\frac{487\ nm}{2}\right)^2 \times 1cm\right) = 1.12 \times 10^9 \qquad \text{(S3)}$$

So that the enhancement factor of single porous NP is:

$$EF = \frac{555/(2.4\times10^{6})}{67/(1.12\times10^{9})} = 3866 \qquad \text{(S4)}$$

Geometry model for field enhancement simulation

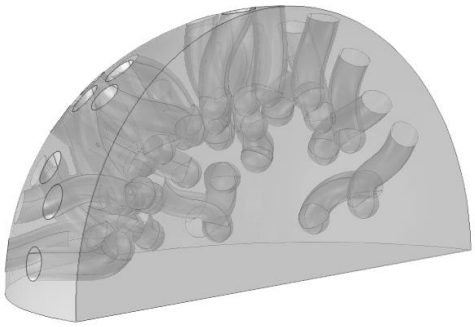

Figure A.7 One example of a porous geometry generated for the field enhancement simulation. Only a quarter of the sphere is shown.

Optical cross section simulation

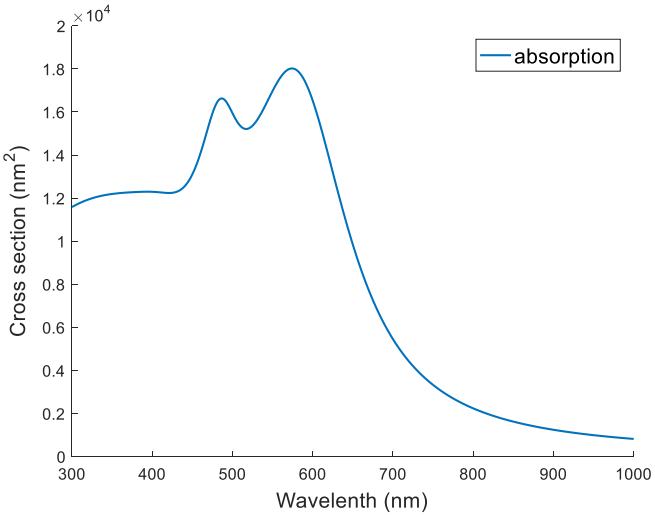

Figure A.8 Simulated absorption plot of porous NP applied as SERS substrate. Absorption cross section is 12349 nm^2 at the excitation wavelength of 633 nm.

APPENDIX B LIST OF PUBLICATIONS BY LU WANG

Peer-reviewed journal publications

1. **Wang, L.**, Patskovsky S., Gauthier-Soumis B., & Meunier, M. (2021). Porous Au-Ag Nanoparticles from Galvanic Replacement Applied as Single-particle SERS Probe for Quantitative Monitoring. *Small*, 2105209.
2. **Wang, L.**, Hasanzadeh Kafshgari, M., & Meunier, M. (2020). Optical Properties and Applications of Plasmonic‐Metal Nanoparticles. *Advanced Functional Materials*, 30(51), 2005400.
3. **Wang, L.**, Darviot, C., Zapata‐Farfan, J., Patskovsky, S., Trudel, D., & Meunier, M. (2019). Designable nanoplasmonic biomarkers for direct microscopy cytopathology diagnostics. *Journal of Biophotonics*, 12(11), 201900166.
4. Jiang, Y., **Wang, L.**, Meunier, M., & Mirsaidov, U. (2021). Formation Pathways of Porous Alloy Nanoparticles through Selective Chemical and Electrochemical Etching. *Small*, 17(17), 2006953.
5. Nsamela Matombi, A., Hasanzadeh Kafshgari, M., **Wang, L.**, Patskovsky, S., Trudel, D., & Meunier, M. (2020). Sensitive and Rapid Cancer Diagnosis with Immunoplasmonic Assay Based on Plasmonic Nanoparticles: Toward Fine-Needle Aspiration Cytology. *ACS Applied Nano Materials*, 3(5), 4171-4177.
6. Marcoux-Valiquette, P., Darviot, C., **Wang, L.**, Grosset, A. A., Hasanzadeh Kafshgari, M., Birela, M., ... & Meunier, M. (2021). Multiplexed Plasmonic Nano-Labeling for Bioimaging of Cytological Stained Samples. *Cancers*, 13(14), 3509.

Presentations in conferences

1. **L. Wang**, S. Patskovsky, M. H. Kafshgari and M. Meunier, “Porous AuAg nanoparticles synthesis and their theranostic application”, *SPIE Photonics West* (2020).

2. **L. Wang**, S. Patskovsky and M. Meunier, “Synthesis of Reproducible Plasmonic AuAg Alloy Porous Nanoparticles”, *SPIE Photonics North* (2018).
3. **L. Wang**, D. Rioux, E. Bergeron, S. Patskovsky, M. Meunier “Gold-Silver Nanoparticles for Specific-targeting Bioimaging Applications”, *GRSTB* (2017).
4. **L. Wang**, S. Patskovsky and M. Meunier, “Synthesis of porous AuAg nanoparticles with tunable porosity, cavity size and optical properties”, *SPIE Photonics West* (2019).
5. S. Patskovsky, M. Qi, C. Darviot, **L. Wang**, A. Nsamela, D. Tomasso and M. Meunier, “Cytopathology diagnosis by multiplexed plasmonic biomarkers”, *SPIE Photonics West* (2019).